



**ENVIRONMENTAL DEGRADATION OF NICKEL-BASED SUPERALLOYS
DUE TO GYPSIFEROUS DESERT DUSTS**

DISSERTATION

Matthew B. Krisak, Major, USAF

AFIT-ENY-DS-15-S-066

**DEPARTMENT OF THE AIR FORCE
AIR UNIVERSITY**

AIR FORCE INSTITUTE OF TECHNOLOGY

Wright-Patterson Air Force Base, Ohio

DISTRIBUTION STATEMENT A:
APPROVED FOR PUBLIC RELEASE; DISTRIBUTION UNLIMITED

The views expressed in this dissertation are those of the author and do not reflect the official policy or position of the United States Air Force, the Department of Defense, or the United States Government.

This material is declared a work of the U.S. Government and is not subject to copyright protection in the United States.

AFIT-ENY-DS-15-S-066

ENVIRONMENTAL DEGRADATION OF NICKEL-BASED SUPERALLOYS
DUE TO GYPSIFEROUS DESERT DUSTS

DISSERTATION

Presented to the Faculty
Graduate School of Engineering and Management
Air Force Institute of Technology
Air University
Air Education and Training Command
in Partial Fulfillment of the Requirements for the
Degree of Doctor of Philosophy in Materials Science and Engineering

Matthew B. Krisak, M.S. ESM, B.S. ChE
Major, USAF

September 2015

DISTRIBUTION STATEMENT A:
APPROVED FOR PUBLIC RELEASE; DISTRIBUTION UNLIMITED

ENVIRONMENTAL DEGRADATION OF NICKEL-BASED SUPERALLOYS
DUE TO GYPSIFEROUS DESERT DUSTS

Matthew B. Krisak, M.S. ESM, B.S. ChE
Major, USAF

Committee Membership:

Capt Brook I. Bentley, PhD
Chair

Alex G. Li, PhD
Member

Marc D. Polanka, PhD
Member

Timothy C. Radsick, PhD
Member

Andrew W. Phelps, PhD
Member

ADEDEJI B. BADIRU, Ph.D.
Dean, Graduate School of Engineering
and Management

Abstract

More than twenty-five years of continuous operation in the dusty environments of Southwest Asia have shown that degradation of gas turbine engine components due to particle ingestion is a serious threat to operations. In particular, the continued push for higher engine operating temperatures has brought a new emphasis to the damage mechanisms (for example CMAS glass formation and hot corrosion) caused by ingested particles forming molten deposits on engine components. Despite decades of research little progress has been made to mitigate the effects of CMAS and hot corrosion degradation to engine components.

This research focused on hot corrosion specifically. A ground-up review of real-world incidents of hot corrosion revealed that the chemical species (sodium sulfate), cited as the cause of hot corrosion in all current academic study, is not present in any natural environment where hot corrosion is an issue. This fact alone raises serious concerns as to the real-world applicability of more than 40 years of laboratory study. An alternative species (gypsum) was identified which is abundant across the globe, and in particular is found in the locations the DoD has reported hot corrosion. Testing proved that gypsum is molten at the same temperatures as sands from a location known to cause significant hot corrosion degradation. Gypsum was proven to initiate hot corrosion at temperatures associated with modern gas turbine engine operation, which are beyond the range at which sodium sulfate can cause degradation.

A first-of-its-kind model was developed to predict degradation caused by gypsiferous dusts as a function of temperature, sulfate concentration, and time. The model was based on kinetic rate law equations and was validated by comparison to additional laboratory runs. The model suggests a minimum concentration of sulfate is necessary to cause hot corrosion, beyond which temperature and time-at-temperature become the chief predictors of degradation. The model also predicted that gypsum could cause degradation at temperatures lower than studied in this effort (750 to 1000°C). This prediction is important because an alternate cause of hot corrosion is also necessary at lower temperatures given that sodium sulfate is not present in DoD environments to cause any form of hot corrosion.

*To my wife who supported me in this endeavor over the countless hours
when I could not be present physically or mentally.*

*To my children who provided much needed escapes from the constant struggle,
now that this is over you'll learn that daddy is good at more than just working.*

Acknowledgements

I would like to thank Capt Brook Bentley for his mentorship and direction over the past year. Despite coming on board half-way through this effort, he truly committed to the project and provided sound advise and motivation each time everything went wrong. Second I would like to thank Dr. Andy Phelps, my day-to-day go-to expert at AFRL. I appreciate the countless hours you listened to my theories and the fact that always pointed me towards further readings as opposed to answers. Requiring me to find the answers myself only made my solutions stronger. I must also thank Lynne Pfladderer of AFRL who brought me into the fold and provided the financial support which made this research possible.

I am also extremely thankful to Dr. Timothy Radsick who was my first research advisor up until he retired. Thank you for dealing with the outside struggles which attempted to derail this project before it could even start. You truly dealt with more issues than any advisor should have had to. Thank you to Adam Long and Randy Corns who opened their labs to me and taught me how to use all the good tools. In addition, I greatly appreciate the time and patience of Dr. Alex Li and Dr. Marc Polanka who provided outside voices to help clarify this project. Finally I would like to thank Col Tim Lawrence, not only for providing me with the motivation and opportunity to pursue my doctorate, but also for helping me find a research project with real-world implications far beyond the laboratory.

Matthew B. Krisak

Table of Contents

	Page
Abstract	iv
Dedication	v
Acknowledgements	vi
Table of Contents	vii
List of Figures	x
List of Tables	xiv
List of Chemical Formula of Select Minerals and Compounds	xvi
List of Acronyms	xvii
 I. Introduction	 1
1.1 The Real World Phenomenon	1
1.1.1 Conditions of the Operating Environment	4
1.1.2 Conditions within the GTE Affected	7
1.1.3 Summary of Real World Findings	8
1.2 Motivation for Research	8
1.3 Problem Statement	10
1.4 Organization of Paper	11
 II. Background and Relevant Research into Failure Due to Molten Deposits	 13
2.1 The Gas Turbine Engine	13
2.1.1 Inlet	14
2.1.2 Compressor	14
2.1.3 Combustor	15
2.1.4 Turbine	15
2.1.5 Exhaust	16
2.2 Nickel-based Superalloys	16
2.2.1 Structure	16
2.2.2 Benefits of Current Superalloys	18
2.2.3 Issues with Current Superalloys	20
2.2.4 Consideration as an Engine Component	21
2.3 Academic Studies of Artificial CMAS Glass	23
2.3.1 Select CMAS studies	24

	Page
2.3.2 Interpolation of Results to Real-World Application	26
2.4 Academic Studies of Hot Corrosion	29
2.4.1 Interpolation of HC Initiation to the Real-World	33
2.4.1.1 Na ₂ SO ₄ as Product of Fuel Sulfur Reactions	34
2.4.1.2 Na ₂ SO ₄ Ingested From the Environment	36
2.5 Real-World CMAS and HC	41
2.5.1 CMAS - Melting of Real Dusts	41
2.5.2 HC - An Environmental Initiator	46
2.5.3 Potential Overlap Between CMAS and HC initiation	47
2.6 Conclusion	48
III. Materials and Facilities	50
3.1 Materials Studied	50
3.1.1 Desert Dusts and Surrogates	50
3.1.2 Substrates	53
3.2 Test Apparatus	54
3.2.1 UDRI Static Furnace	54
3.2.2 AFRL Box Furnace	56
3.2.3 Major Analysis Equipment	56
IV. Characterization of Desert Dust Chemistry	59
4.1 Crucible Tests of Desert Dusts	59
4.1.1 Methodology	59
4.1.2 Results	62
4.1.3 Discussion	66
4.1.3.1 Glass Formation	66
4.1.3.2 Mass Loss	73
4.2 DSC of Desert Dusts	78
4.2.1 Results - Single-Source Dusts	79
4.2.2 Results - Modified Dusts	85
4.3 Objective 1 Summary	91
V. Quantification of Substrate Attack	94
5.1 Static Reducing Furnace Flat Coupons	94
5.1.1 Development of Loading Method	96
5.1.2 Static Furnace Methodology	100
5.1.3 Results and Observations	102
5.1.3.1 Appearance	102
5.1.3.2 Cross-Section Analysis	105
5.1.3.3 Extent of Degradation	107
5.2 Static Oxidizing Furnace Flat Coupons	122
5.2.1 Oxidizing Furnace Methodology	122

	Page
5.2.2 Results and Observations	123
5.2.2.1 Appearance	123
5.2.2.2 Extent of Degradation	125
5.2.3 Comparison to Static Reducing Tests	129
5.3 Objective 2 Summary	135
VI. Sulfate Attack Model	138
6.1 Initial Model Development	138
6.1.1 Position	139
6.1.2 Peak Temperature Soak Time	140
6.1.3 Temperature Dependence	141
6.1.4 Sulfur Dependence	143
6.1.5 Thickness of Degradation in a Reducing Environment	143
6.1.6 Thickness of Degradation in an Oxidizing Environment	145
6.1.7 Mass Loss in an Oxidizing Environment	147
6.2 Final Model Development	149
6.2.1 Thickness of Degradation in a Reducing Environment - Nickel	151
6.2.2 Thickness of Degradation in a Reducing Environment - Superalloy	155
6.2.3 Thickness of Degradation in an Oxidizing Environment - Superalloy	159
6.3 Model Validation	163
6.3.1 Methodology	164
6.3.2 Results	165
6.3.3 Discussion	171
6.4 Summary of Findings from Objective 3 and 4	172
VII. Concluding Remarks	174
7.1 Contributions	174
7.2 Future Work	177
Bibliography	181

List of Figures

Figure	Page
1.1 Soil sample sites on Arabian Peninsula and primary constituents	5
1.2 Soil sample sites in Afghanistan and primary constituents	6
1.3 Soil sample sites in Saudi Arabia and primary constituents	7
2.1 Gas-stream temperature profile in high-bypass GTE	14
2.2 Schematic of the air flow in the combustor section	15
2.3 Two-phase microstructure of a typical superalloy	17
2.4 Representative yield behavior of a nickel-based superalloy	19
2.5 Rafting of γ' precipitates in a nickel-based superalloy	20
2.6 SEM image of a typical profile within an EB-PVD deposited TBC	21
2.7 SEM image of a typical profile within an overlay EBC	22
2.8 Wellman's samples after heat treatment	25
2.9 Top-level timeline of CMAS degradation within the GTE	27
2.10 Relative corrosion rates on superalloys as a function of temperature	30
2.11 Representative HTHC degradation as seen on Inconel 718 alloy	33
2.12 Effect of initial sodium chloride concentration on the sulphidation reaction	36
2.13 Example of a baseline shift in a DSC curve	43
2.14 DSC curves of select sands collected in Saudi Arabia	45
2.15 DSC curves of select sands collected in Afghanistan	46
3.1 UDRI furnace	55
3.2 UDRI furnace thermocouple versus pyrometer readings	56
3.3 UDRI furnace thermocouple versus pyrometer readings for each testing block	58
4.1 Loaded crucibles in graphite cup	60
4.2 Static furnace amperage setting and temperature profile for a typical SR run	60
4.3 Onset of sticking for GB1 at 850°C	63
4.4 Onset of fusion for GB1 at 1150°C	64

Figure	Page
4.5 Static Furnace temperature profile for TP#1	67
4.6 Transmitted light images of thin-section GB1 pellet after 1200°C run	69
4.7 Initial processed image showing glass regions of a GB1 thin-section	69
4.8 Final image showing glass regions of thin-sectioned GB1 pellet from a 1200°C run . .	70
4.9 Sample melt fraction with and without inclusion of mullite formations	72
4.10 Static Furnace temperature profile for TP#2	73
4.11 Average mass loss versus peak temperature in crucible testing	75
4.12 Average mass loss versus peak temperature in crucible testing	77
4.13 Result of a Na ₂ SO ₄ /salt mixture deliquescing	79
4.14 DSC plot for gypsum	80
4.15 DSC plot for sodium sulfate	81
4.16 DSC plot for Oxide Mix	82
4.17 DSC plot for PTI A2	83
4.18 DSC plot for YPG	83
4.19 DSC plot for AFRL02 and GB1	84
4.20 DSC plot comparing fired versus unfired CMAS mixtures from 300-600°C	86
4.21 DSC plot comparing fired versus unfired CMAS mixtures from 1150-1350°C	87
4.22 Change in CMAS DSC plot due to increasing gypsum content from 100-500°C	88
4.23 Change in CMAS DSC plot due to increasing gypsum content from 1200-1350°C . . .	89
4.24 Effect of 5% NaCl added to various test dusts from 100-500°C	90
4.25 Effect of 5% NaCl added to various test dusts from 1200-1350°C	90
4.26 Difference in PTI A2 and Aramco DSC behavior from 900-1400°C	91
4.27 DSC plot comparing gypsum and GB1 from 1000-1500°C	92
5.1 Dust wafer pressing set-up	95
5.2 Gypsum samples on EN coupons	97
5.3 Sample mass loss for loading test runs	98
5.4 Depth profile for gypsum attack on EN coupon at 1200°C	100

Figure	Page
5.5 Surface image of representative coupon showing wafer and cross-section locations . . .	106
5.6 Chemical phases from degradation of a superalloy coupon in SR testing	107
5.7 Measurement of sulfur-phase thickness for coupons tested in a SR environment	109
5.8 Degradation thickness in nickel tested in a SR environment at 16 cycles	111
5.9 Degradation thickness in nickel tested in a SR environment at eight cycles	112
5.10 Degradation thickness in nickel tested in a SR environment at four cycles	112
5.11 Degradation thickness in nickel tested in a SR environment at two cycles	113
5.12 Reduction of radial data-points to a single thickness measurement with error	114
5.13 Degradation in SR nickel coupons plotted versus cycle time	114
5.14 Degradation thickness in superalloy tested in a SR environment at 16 cycles	116
5.15 Degradation thickness in superalloy tested in a SR environment at eight cycles	116
5.16 Degradation thickness in superalloy tested in a SR environment at two cycles	117
5.17 Degradation in SR superalloy coupons plotted versus cycle time	118
5.18 Measurement of area of chemical shift for coupons tested in a SR environment	119
5.19 Area of degradation in nickel tested in a SR environment at 1300°C	120
5.20 Area of degradation in nickel tested in a SR environment at 1150 and 1250°C	120
5.21 Area of degradation in superalloy tested in a SR environment at 1300°C	121
5.22 Area of degradation in superalloy tested in a SR environment at 1150 and 1250°C . . .	121
5.23 Measurement of degradation thickness for coupons tested in a SO environment	126
5.24 Degradation thickness in superalloy tested in a SO environment at 16 cycles	127
5.25 Degradation thickness in superalloy tested in a SO environment at eight cycles	128
5.26 Degradation thickness in superalloy tested in a SO environment at two cycles	128
5.27 Representative melted wafers from SR and SO testing	129
5.28 Coupon mass as a function of cycles for SR environment set-points	130
5.29 Coupon mass as a function of cycles for SO environment set-points	131
5.30 Determination of Avrami constants for SO-H1 and SO-H5	133
5.31 Degradation in SO superalloy coupons plotted versus cycle time	134

Figure	Page
5.32 Comparison of sulfur degradation on Ni-Cr superalloys	135
6.1 Example sequence of events for degradation due to gypsiferous desert dust ingestion	138
6.2 Relationship between fraction melt formed and normalized temperature	142
6.3 Predicted thickness of sulfur phase due to .5CMAS loading in SR testing	145
6.4 Predicted thickness of sulfur phase due to .5CMAS loading in SO testing	146
6.5 Predicted coupon mass loss .5CMAS loading in SO testing	149
6.6 Plot of predicted thickness of degradation from 900 to 1300°C	150
6.7 Arrhenius plots for nickel degradation at various sulfate concentrations	152
6.8 Plot of the final model of degradation thickness of nickel in a SR environment	153
6.9 Comparison between measured and predicted degradation for nickel in SR testing	154
6.10 Calculation of the rate constant for chromium	156
6.11 Plot of the final model of degradation thickness of superalloy in a SR environment	157
6.12 Comparison between measured and predicted degradation for superalloy in SR testing	158
6.13 Relationship between T_c and dust sulfate concentration	160
6.14 Plot of the final model of degradation in a SO environment	161
6.15 Comparison between measured and predicted degradation in SO testing	162
6.16 Plot of Avrami melt curves for SO-H1 and SO-H5 set-points	163
6.17 Change in appearance and SEM image of coupon for the SR-MG test	165
6.18 Plot of the degradation thickness for SR-MG testing	167
6.19 Change in appearance and SEM image of coupon for the SR-MY test	168
6.20 Plot of the degradation thickness for SR-MY testing	169
6.21 Change in appearance and SEM image of coupon for the SO-H3 test	170
6.22 Plot of the degradation thickness for SO-H3 testing	170
6.23 Sulfate contribution to degradation at 1250°C	171

List of Tables

Table	Page
1.1 Relative intensity of EDS peaks of T700 vane deposit studied by Smialek	1
2.1 Nominal composition of various second generation superalloys	17
2.2 Oxide weight percents of various lab mixtures used in select CMAS glass studies . . .	24
2.3 Major ion composition of seawater	37
2.4 Order of precipitation of salts from seawater at 40°C	38
2.5 Major salts left from evaporated seawater	39
2.6 Major minerals found in sedimentary rocks	40
2.7 Major reserves of natural Na ₂ SO ₄	41
2.8 Select events which can cause DSC peaks	42
3.1 Composition of test samples - Part 1	52
3.2 Composition of test samples - Part 2	53
4.1 Temperatures of operational significant physical states identified in crucible testing . .	65
4.2 Sample appearance after heating under TP#1 versus 1000 and 1250°C	68
4.3 Percent of glass phase present in each thin-section as determined by GIMP	71
4.4 Percent of melted phase present in each thin-section as determined by GIMP	72
4.5 Fraction mass loss of sample after heating under TP#2 versus 1000 and 1250°C	74
4.6 Samples subjected to DSC testing	79
5.1 Profiles used for loading method determination	97
5.2 Static Reducing furnace testing set-points	101
5.3 Change in appearance of coupons for SR-L1 test runs	102
5.4 Change in appearance of coupons for SR-L5 test runs	103
5.5 Change in appearance of coupons for SR-M3 test runs	104
5.6 Change in appearance of coupons for SR-H1 test runs	104
5.7 Change in appearance of coupons for SR-H5 test runs	105
5.8 Static Oxidizing furnace testing set-points	123

Table	Page
5.9 Change in appearance of coupons for SO-L1 test runs	124
5.10 Change in appearance of coupons for SO-L5 test runs	124
5.11 Change in appearance of coupons for SO-M3 test runs	124
5.12 Change in appearance of coupons for SO-H1 test runs	125
5.13 Change in appearance of coupons for SO-H5 test runs	125
6.1 \hat{D} calculated for each SR set-point	140
6.2 \hat{D} calculated for each SO set-point	140
6.3 Data points used to develop melting relationship of select dusts	142
6.4 Constants for degradation thickness in a SR environment	144
6.5 Constants for degradation thickness in superalloy coupons in a SO environment	146
6.6 Constants for mass loss in superalloy coupons in a SO environment	148
6.7 Set-points used for validation testing of SR and SO models	164

List of Chemical Formula of Select Minerals and Compounds

Mineral	Formula
Alumina	Al_2O_3
Calcia	CaO
Calcite	CaCO_3
Calcium Sulfate	
Anhydrite	CaSO_4
Basinite	$\text{CaSO}_4 \cdot .5\text{H}_2\text{O}$
Gypsum	$\text{CaSO}_4 \cdot 2\text{H}_2\text{O}$
Chromia	Cr_2O_3
Dolomite	$\text{CaMg}(\text{CO}_3)_2$
Feldspars	
Albite	$\text{NaAlSi}_3\text{O}_8$
Anorthite	$\text{CaAl}_2\text{Si}_2\text{O}_8$
Microcline	KAlSi_3O_8
Hornblende (general formula)	$(\text{Ca}, \text{Na})_{23}(\text{Mg}, \text{Fe}, \text{Al})_5(\text{Al}, \text{Si})_8\text{O}_{22}(\text{OH}, \text{F})_2$
Magnesia	MgO
Magnesium Sulfate	MgSO_4
Mica (biotite)	$\text{K}(\text{Mg}, \text{Fe})_3(\text{AlSi}_3\text{O}_{10})(\text{F}, \text{OH})_2$
Pyrite	FeS_2
Quartz	$\alpha\text{-SiO}_2$
Sodium Sulfate	
Mirabilite	$\text{Na}_2\text{SO}_4 \cdot 10\text{H}_2\text{O}$
Thenardite	Na_2SO_4
Wollastinite	CaSiO_3

List of Acronyms

Acronym	Definition
AFRL	Air Force Research Laboratory
APS	air plasma spray
ASTM	American Society for Testing and Materials
BC	bond coat
BSE	Back-scatter electron
CC	conventionally-cast
CMAS	calcium magnesium alumina silicate
CTE	coefficient of thermal expansion
DO	dynamic oxidizing
DoD	Department of Defense
DoE	Department of Energy
DS	directionally-solidified
DSC	differential scanning calorimetry
EBC	environmental barrier coating
EB-PVD	electron beam physical vapor deposition
EDS	energy-dispersive x-ray spectroscopy
EN	Electroless nickel
FCC	face-centered cubic
GE	General Electric
GTE	gas turbine engine
GIMP	GNU Image Manipulation Program
HC	hot corrosion
HPC	high-pressure compressor
HPT	high-pressure turbine
HTHC	high-temperature hot corrosion

Acronym	Definition
IPS	inertial particle separator
LOF	lack-of-fit
LPC	low-pressure compressor
LPT	low-pressure turbine
LTHC	low-temperature hot corrosion
MSDS	material safety data sheet
NASA	National Aeronautics and Space Administration
NMAB	National Material Advisory Board
PTI	Powder Technology Inc
P&W	Pratt and Whitney
RMSE	root-mean-square error
SEM	Scanning electron microscopy
SO	static oxidizing
SR	static reducing
SX	single-crystal
TBC	thermal barrier coating
TC	top coat
TCP	topologically close-packed
TGO	thermally grown oxide
TIT	turbine inlet temperature
UDRI	University of Dayton Research Institute
XRF	x-ray fluorescence
YPG	Yuma Proving Grounds
YSZ	yttria-stabilized zirconia

ENVIRONMENTAL DEGRADATION OF NICKEL-BASED SUPERALLOYS DUE TO GYPSIFEROUS DESERT DUSTS

I. Introduction

1.1 The Real World Phenomenon

The Department of Defense (DoD)'s current emphasis on molten deposits in aviation gas turbine engine (GTE) began with the Persian Gulf War. United States military operations started in August of 1990 and by December, Black Hawk helicopters operating along the Saudi Arabia/Iraqi border began to show significant performance losses [101]. Engine tear-down revealed significant cooling passage blockage, extensive erosion damage, and a glassy build-up on the leading edges of vanes of the high-pressure turbine (HPT) vanes which had not previously been found during engine maintenance [101]. Smialek performed one of the initial studies of this glassy deposit. Smialek's energy-dispersive x-ray spectroscopy (EDS) analysis of the glassy deposit gave the elemental composition shown in Table 1.1.

Table 1.1: Relative intensity of EDS peaks of T700 vane deposit studied by Smialek [101]. The deposit consisted of two phases and also contained significant sulfur. (NA=not analyzed)

Deposit Section	Si	Ca	Al	Fe	Mg	S	O
Glassy Surface (Exterior)	0.50	0.19	0.11	0.03	0.04	0.00	0.13
Uniform Granules (Interior)	0.18	0.19	0.08	0.05	0.02	0.25	0.09
Bulk Analysis	0.47	0.21	0.10	0.12	0.09	NA	NA

The deposit analyzed in Smialek's study would eventually be identified as a calcium magnesium alumina silicate (CMAS) glass. CMAS glass had long been studied in ceramic sciences and as a by-product slag in steel production, but the discovery of CMAS glass in the Black Hawks brought attention to CMAS as a potential operational concern for aircraft GTE. Smialek

also identified CaSO_4 alongside the glassy deposit. The vanes Smialek studied did not show any corrosive attack, which Smialek attributed to the low operating temperatures of the particular engine. However, in subsequent laboratory testing, Smialek was able to show that a CaSO_4 deposit could cause corrosion on a nickel-aluminide alloy at temperatures above 1000°C . At 1200°C , both CaSO_4 and river band sand (rich in carbonates and gypsum) collected near the operating location of the affected Black Hawks caused excessive corrosion with a porous, flaky outer nickel oxide layer. The corrosion damage was similar to that associated with high-temperature hot corrosion (HTHC) which will be discussed in Section 2.4 [101].

Between 2008 and 2011, Braue and Mechnic published several papers studying ex-service first stage high pressure airfoils which had substantial deposits of both CaSO_4 and a CMAS glass. The CMAS glass they analyzed had a significant amount of iron, just as with Smialek's CMAS glass, but they were also able to identify titanium in the glass deposit [18, 19]. Their study showed that CaSO_4 can react with yttria in yttria-stabilized zirconia (YSZ), destabilizing its structure, at temperatures as low as 1100°C [18]. In addition, Braue and Mechnic identified CaSO_4 infiltration into the complete depth of columnar structure of the electron beam physical vapor deposition (EB-PVD) top coat (TC) of a field-retained HPT blade, but only found YSZ degradation at the surface. The lack of degradation suggests only the surface of the TC exceeded 1100°C . Further, it suggests a mechanism by which CaSO_4 was molten at temperatures below 1100°C allowing infiltration without TC degradation.

Vidal-Setif's 2012 study of ex-service HPT blades revealed the presence of two distinct CMAS formations. A porous, inhomogeneous CMAS formed at the leading edge of the blade while the "typical" homogeneous, fully-dense CMAS deposit presented in other studies to be discussed in Section 2.3 was found along the hottest section of the pressure-side of the blade [112]. The same ingested sand caused two unique glass deposits, showing that temperature has a significant effect on the morphology of the glass which forms.

A series of canal and agricultural projects initiated by the British in 1952 began the draining of natural marshland at the intersection of the Tigris and Euphrates Rivers near Basra in Iraq. Saddam Hussein accelerated the draining of the marshlands as a political move against the marsh Arabs

after the Persian Gulf War. These actions resulted in the desertification of 7500 of the original 7700 square miles of marshland. Millennia of accumulated sedimentary and evaporate deposits from the Tigris and Euphrates have been added to the dust profile of the area. Due to the desertification of marshland in the area, molten deposits are currently a significant problem for aviation GTE operated around Basra.

More than twenty years after the first reports of degradation due to molten deposits in GTE operating in Saudi Arabia, CMAS is still an issue for military aircraft operating there. One current maintenance issue in particular provides an interesting data point to CMAS formation. Two squadrons of the same aircraft, with the same GTE, and similar maintenance procedures are experiencing vastly different levels of CMAS-related degradation [84]. The major difference between the two squadrons appears to be geographic location which suggests that the specific mix of ingested sand may have an important effect on CMAS formation and degradation mechanisms.

At the same time in Afghanistan, various rotor-wing aircraft have been showing a marked decrease in performance due to substantial glass deposits in the first stage turbine of T700 GTEs. The current issues in Afghanistan have led to a tri-service test event to qualify a new test media for sand ingestion qualification testing of all DoD GTEs.

The most recent news from the field is that various GTE rotor blades are now showing signs of sulfur attack in the blade root. The blade root is not exposed to combustion gases, therefore the sulfur degradation must be attributed to ingested sand flowing through the internal cooling passages of the engine.

As aviation GTEs have achieved higher performance, and higher operating temperatures, and as operations have expanded in Southwest Asia since the First Gulf War, CMAS deposits and their effects on aviation GTE components have been an increasing focus of research by academia and industry. Much of the research into CMAS has been funded by the DoD and Department of Energy (DoE). The history of sulfur degradation dates back to the GTEs used for industrial power generation beginning as early as the 1950s. The DoE and DoD have also funded large amounts of research into hot corrosion (HC). However, as the preceding examples demonstrate, despite decades of research, CMAS glass formation and sulfur attack in aviation GTEs remain serious

problems with huge operational impacts. To date, the only link identified in literature between the two is that they result from molten deposits formed in GTEs as the result of ingested environmental materials. Therefore, it is important to understand the dusts which could be ingested in the operating environments molten deposits have been reported, and the operating parameters of affected GTEs.

1.1.1 Conditions of the Operating Environment.

As will be introduced in Chapter 2, the mechanisms of molten deposit infiltration and/or attack of GTE components and their coatings is highly dependent upon the composition of the ingested material and surface properties of the component. Composition of ingested material is tied to geographic location of attack. When DoD Black Hawks began experiencing issues in 1990, analysis of sand from the region near Dharhan, Saudi Arabia (where the affected helicopters were operating) showed the sand chemistry varied by location, but mostly consisted of a calcium-aluminum-silicate glass, quartz, dolomite, calcite, and salt [101]. Interestingly, the same study found that the concentration of each varied with the sample's mean particle size. For example, "as-collected" desert sand comprised 91% silicon oxides. However, when sieved to 20 μm , silicon oxides only accounted for about 50% of the sample [101]. This change in composition has significant implications. The drop in SiO_2 content and particle size both allow the ingested material to melt at a lower temperature than would be expected for the "as-collected" sand.

Just two years before the Black Hawks began to experience performance losses due to ingested desert sands, Toriz presented a paper which briefly mentioned TC degradation on commercial aircraft operated out of several airports in the Middle East due to molten deposits formed at component temperatures exceeding 1150°C [111]. In an effort to better understand the possible degradation noted in Toriz's work, Wet and Stott collected sands from four different airports on the Arabian Peninsula. A map of the airports and principal minerals found in each sample are presented in Figure 1.1. They found that sand collected from Sinaiyah melted at 1200°C, Bahrain between 1250 and 1275°C, and Doha at 1275°C [107]. In addition, it should be noted that the sands at Doha cannot form a CMAS glass as they lack an alumina-containing species. This fact has important implications to the study of degradation that may be caused by glass deposits at Doha. In particular, the use of a generic CMAS glass to study thermochemical degradation may be applicable to Bahrain

and Sinaiyah, but will have questionable applicability to the degradation which could be caused at Doha since the Doha glass will have significantly different chemistry from the other two locations. As an aside, the tables in Figures 1.1 - 1.3 are arranged to highlight the natural minerals at each location that could form CMAS glasses. Additional constituents have been omitted.

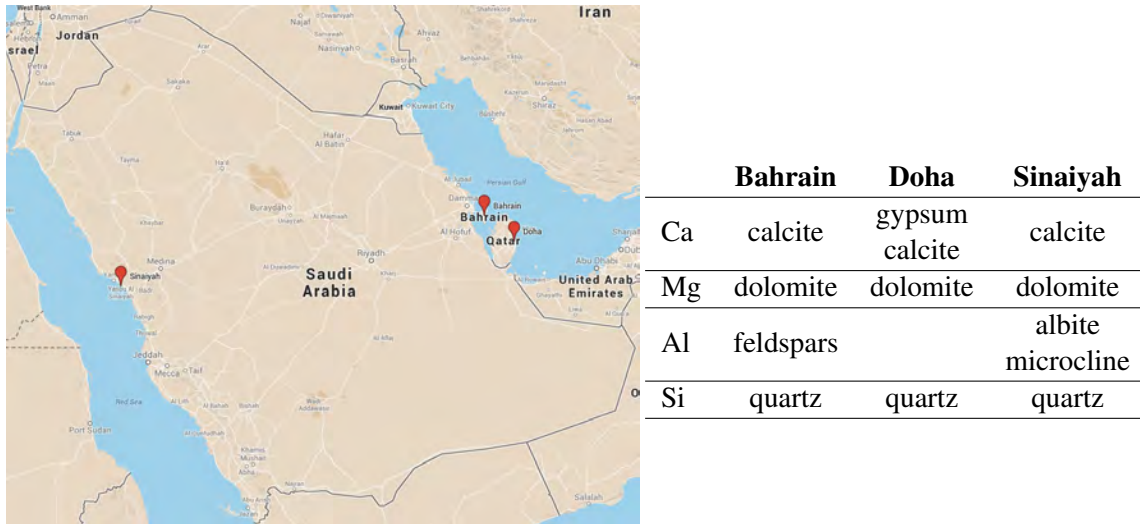


Figure 1.1: Soil sample sites on Arabian Peninsula and primary constituents which could contribute to CMAS glass formation [107]. Constituents which do not contribute to CMAS glass formation have been omitted.

A study by the Desert Research Institute in 2004 found sulfate in all seven ground samples and both vehicle dust samples collected in the area around the former marshlands at Basra [68]. Five of the nine sulfates were specifically identified as calcium sulfates (gypsum or bassanite). The other four sulfate samples were not attributed to any specific sulfate salt. In addition, the study noted that the dust collected from vehicles was most likely to be clay ($<3 \mu\text{m}$) or silt ($3\text{-}15 \mu\text{m}$) sized. As discussed above, the dust size has significant implications to the specific composition of an ingested dust, and by extension, the possible molten deposit which could form.

More recently, due to extended operations in Afghanistan, the Army Corps of Engineers have been collecting petrological information of various locations in the country. Figure 1.2 shows the location of sample sites. The Corps of Engineers data is not yet publicly available, instead soil compositions reported by previous studies are shown. Of note, while gypsum can be found in trace amounts in undisturbed soil throughout Afghanistan, it is only found in significant quantities in the

Helmand Basin. Serpentine and pyroxene are complex iron-containing silicate blends which may have calcium, aluminum, or magnesium.

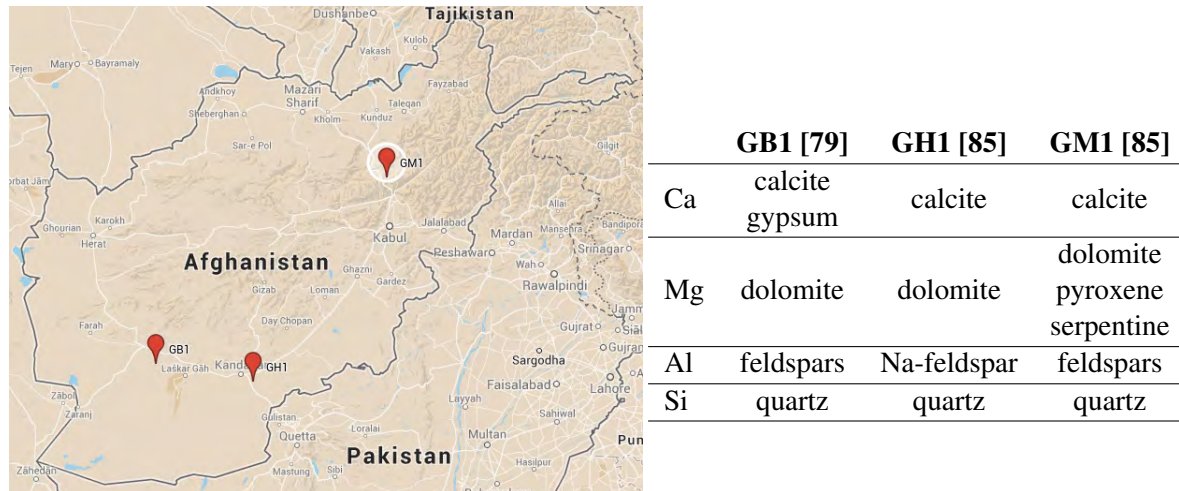


Figure 1.2: Soil sample sites in Afghanistan and primary constituents which could contribute to CMAS glass formation. Constituents which do not contribute to CMAS glass formation have been omitted. The samples have similar constituents except for GB1 which is reported to have significant amounts of gypsum also.

Similar information has been collected at various other locations of DoD interest. Locations of study by the Air Force Research Laboratory (AFRL) as well as composition at those sites are shown in Figure 1.3. As can be seen in the map in Figure 1.3, the western region of Saudi Arabia is dominated by the Arabian Shield while the eastern region is dominated by the Arabian Platform. Current operational experience has shown that despite the area having the necessary soil ingredients, aircraft stationed in eastern Saudi Arabia experience fewer problems due to CMAS formation compared to aircraft stationed and operating in western Saudi Arabia. This difference may be partially explained by the presence of mica in western sands versus dolomite in eastern sands. As a pure component, mica begins to melt at approximately 1300°C while dolomite melts in excess of 2300°C. The substitution of lower melting mica may lead to a lower bulk melting point.

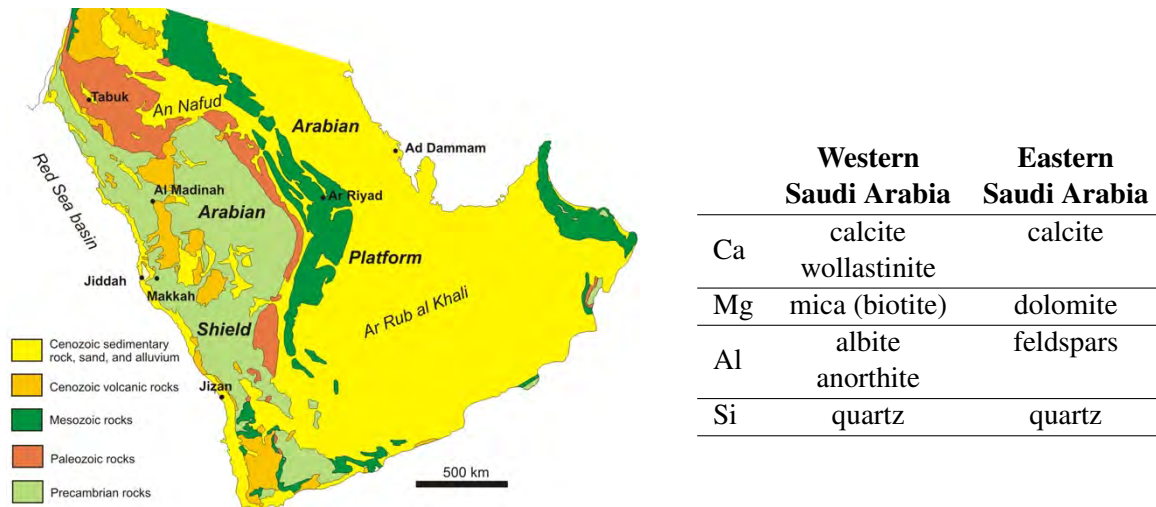


Figure 1.3: Soil sample sites in Saudi Arabia and primary constituents which could contribute to CMAS glass formation [20]. Constituents which do not contribute to CMAS glass formation have been omitted. The primary difference between the two samples is that the western sand contains mica (melting point $\sim 1300^{\circ}\text{C}$) instead of dolomite (melting point $> 2300^{\circ}\text{C}$). Image courtesy of the Saudi Geological Survey [95].

1.1.2 Conditions within the GTE Affected.

The ingestion of material into aviation GTE is unavoidable even with the use of air filtering. An inertial particle separator (IPS) can be highly effective (85-97%) at filtering large particles (0-1000 μm with 200 μm average size) but is only 60-70% efficient at filtering fine sand (0-80 μm with 8 μm average size) [63]. Even with good filtering efficiency, the huge amount of air moved by a GTE results in the potential for a large mass of particulate flowing over internal GTE components. Further, as was mentioned in Section 1.1.1, the removal of large particles from a sample can allow the remaining sample to melt at lower temperatures than the original would have. Therefore, while the removal of large particles by IPS is desirable to limit erosion damage of GTE components, it increases the likelihood of attack by molten deposits.

While there are likely other GTE affected, open literature lists examples of the T55, T58, T700, AE1107, and F100 experiencing sulfur attack when operated in many of the regions already discussed. In addition, CMAS deposits have been reported in both the T700 and F100 GTE. The first four engines can be found on various commercial and military rotor-wing aircraft. The F100 has been used on various models of F-15 and F-16. The fact that the F100 is affected shows that

sand ingestion is not just a problem for aircraft performing low altitude sorties where sand ingestion is expected, it is also an issue for aircraft operating at high altitude. Based on engine operating specifications provided by Mattingly, for the GTE listed above, sulfur attack is a known issue for DoD GTEs operating with turbine inlet temperature (TIT)s as low as 744°C (T58) [67]. Further, both CMAS and sulfur attack are known issues for DoD GTEs operating with TITs ranging from 851°C (T700) to 1482°C (F100). It should be noted that TIT is the gas-stream temperature entering the turbine. Surface temperatures of components in the hot section are typically lower than the TIT (up to 70-150°C lower due to the employment of film cooling and protective coatings) [43].

1.1.3 Summary of Real World Findings.

Several important observations come from the preceding discussion. First, HC attack is found both on surfaces exposed to the combustion gas stream, and surfaces never exposed to combustion gases. Therefore, any mechanism for HC must not be limited only to the combustion stream. Second, gypsum is often found in dust samples taken at operating locations where CMAS glass has been found in aviation GTE. Not surprisingly, CMAS glass deposits and HC degradation have been found side-by-side on aviation GTE components. While this does not mean they are caused by the same mechanism, any mechanism proposed to explain either CMAS glass deposit formation or HC initiation should not require the two to be mutually exclusive. Lastly, with specific regard to CMAS glass formation, similar inputs do not necessarily cause similar results. The case of western versus eastern Saudi Arabia showed that an ingested dust containing all four required components for CMAS does not guarantee a CMAS glass will form. Vidal-Setif's analysis showed with the exact same input, different glasses could form depending on temperature at the deposition site. These two examples illustrate how CMAS glass formation is dependent on a complex process of many variables.

1.2 Motivation for Research

Degradation of coating systems and component substrates within GTE can be classified into two overarching categories: intrinsic failures (dominated by factors inherent in the chemistry and processing of the material) and extrinsic failures (controlled by factors external to the material). Common intrinsic failures include coefficient of thermal expansion (CTE) mismatch [9, 40],

interdiffusion [31, 39, 40, 64], and thermally grown oxide (TGO) growth [6, 25, 38–40, 43, 53, 54, 115]. Common extrinsic failures typically initiate with the ingestion of particulate from the environment and include erosion [8, 10, 24, 49, 51, 75, 86, 108] , oxidation [10, 37, 86, 98, 99] , and degradation due to molten deposits [33–35, 55, 59, 72, 81, 94, 113].

While all these degradation mechanisms continue to be of great concern within GTE, more than twenty-five years of continuous operation in the dusty environments of Southwest Asia have shown that degradation of GTE components due to particle ingestion is a serious threat to operations. In particular, the consistent push for higher GTE operating temperatures has brought a new focus to the problems caused when ingested particles become molten and deposit on GTE components. Specifically, the aviation community is focused on the “new” molten deposit phenomena of CMAS glass formation and sulfate salt induced HC attack in aircraft GTE despite the fact that these two phenomena have been known and studied in other fields for decades.

As will be discussed in Chapter 2 of this document, numerous studies have been accomplished in academia, as well as industry, to assess the impact of molten deposits on GTE components. While these studies have contributed toward a general understanding of degradation caused by CMAS and HC, this knowledge is predicated on starting assumptions made decades ago which have never been validated to the realities of real-world DoD observations. In the case of HC attack caused by sulfate salt deposition, more than sixty years of research are based on the deposition of a particular salt, sodium sulfate (Na_2SO_4), which is not found in the operating locations where HC is occurring in DoD aviation GTEs. Current CMAS research has completely neglected how natural CMAS glass actually forms, focusing instead on an artificial CMAS composition which melts above the expected surface temperatures of currently fielded DoD hardware.

To date, no lifing models have been developed at component or system level to account for the degradation caused by CMAS or sulfate salt deposits. Undoubtedly some of the reason for the lack of lifing models can be attributed to academic studies which do not attempt to replicate the real-world phenomenon. Without proper lifing models, decisions affecting maintenance, sustainment, and design are overly cautious causing substantially higher safety factors not only in design and testing, but in operations, to be implemented. The result is greatly increased acquisition,

logistics, and operating costs within the aerospace industry and DoD. A better understanding of the mechanisms of molten CMAS glass formation and sulfate salt deposition within aviation GTE could lead to not only better GTE design but significant cost savings in a wide range of connected disciplines.

This research effort focused on sulfur attack due to molten deposits caused by ingested desert dusts. While sulfur attack is the main focus of this research, as will be discussed in Chapter 2, the desert dusts likely to cause sulfur attack are also likely to cause CMAS glass formation. Therefore the test dusts used in this study were designed so that degradation due to CMAS glass formation was not ignored. In order to develop an accurate understanding of sulfate attack in DoD GTE, it will be necessary to: (1) Identify parameters, such as the operating conditions of affected engines and composition of ingested dusts at locations of attack, which can lead to sulfate attack in the real-world and (2) determine the mechanisms of sulfate attack in a representative laboratory environment. The long term goal behind this work is to provide key inputs to an improved lifing model which will allow better informed design, deployment, and sustainment.

1.3 Problem Statement

As stated in Section 1.1, and will be further detailed in Chapter 2, a body of knowledge of sulfate attack exists based on empirical observations from the field. A second body of knowledge, which will be described in Sections 2.3 and 2.4, exists based completely on laboratory observations. These two bodies of knowledge are distinct from each other. This research was an initial attempt at rectifying the disconnect by re-examining the assumptions upon which current research has been built, and by studying the problems of CMAS formation and HC attack caused by media likely to be ingested in current DoD operating environments.

The objective of this effort was four-fold. First, the evolution of select desert dusts and common artificial surrogates was studied as a function of temperature. Specifically, the dusts were characterized with regard to glass phase formation and presence of sulfur compounds which could initiate HC attack. Glass phase formation was analyzed following soaks at various temperatures. differential scanning calorimetry (DSC) was used to supplement furnace data for phase change determination.

The second objective was to quantify the degradation of representative aviation GTE materials caused by a gypsiferous artificial dust. The artificial dust was used to limit competing effects attributable to the various compounds found in natural desert dusts. The artificial dust was designed to cause CMAS glass formation at temperatures similar to current CMAS studies, but with CaO replaced by gypsum in set ratios to allow HC study. To quantify the degradation caused by this artificial dust, it was first necessary to develop a loading method for static furnace testing. Once the loading method was determined, degradation was measured with regard to depth of attack and reaction products on coupons of pure nickel and a currently fielded NiCr superalloy to represent materials used in current DoD aviation GTE. Degradation was measured as a function of temperature, dust sulfate concentration, and exposure time.

The third objective was to develop a model of sulfate attack based upon the work completed in the previous objectives. The model was developed in two phases. First a mathematical model was developed to predict degradation within the range of test variables. The mathematical fit was then used to develop a chemical attack model with broader applicability beyond the range of test variables used in this study. The final objective was to test the model developed from a simple artificial dust against complex natural dusts. The accuracy of the model was analyzed to determine future variables to be studied.

The following problem statement summarizes the objectives of this research:

Characterize the evolution of select desert dusts and surrogates from loose powder to glass as a function of temperature. Quantify the degradation of representative aviation GTE materials as caused by a sulfur-containing artificial dust. Develop a model for sulfur attack on superalloy components. Finally, evaluate the efficacy of the model using select natural desert dusts.

1.4 Organization of Paper

The second chapter of this document begins with a brief overview of current GTE design and the role of nickel-based superalloys in the engines. However, the main focus of the chapter is a comparison of the differences between academic studies of CMAS glass and HC degradation and real-world observations introduced in Section 1.1. The third chapter outlines the materials and research facilities used in this study. The fourth chapter provides an explanation of the methods used

to characterize various desert sands and surrogates along with discussion of relevant results. The fifth chapter focuses on the methods used to characterize CMAS and HC attack in both reducing and oxidizing environments. The sixth chapter discusses the development of a model to predict severity of attack on superalloy components along with validation methods for the model. Concluding remarks are offered in the seventh chapter.

II. Background and Relevant Research into Failure Due to Molten Deposits

The purpose of this chapter is to provide a relevant framework in which the proposed research was built. The chapter begins with a brief overview of the GTE, nickel-based superalloys, and the component coatings which are required for current aerospace operations. Next, an overview of current academic research into degradation caused by molten deposits in GTE is included. This chapter concludes with a discussion of the issues with current academic research in regard to the real-world examples highlighted in Chapter 1. Finally, the relevance of this particular work shall be explained in light of these issues.

2.1 The Gas Turbine Engine

The modern GTE, other than a few refinements which have garnered huge improvements in efficiency, power, and reliability, has changed little since its adoption into the military and civil aviation inventories in the 1940s and 1950s. Among those refinements are superalloys and their associated environmental and thermal barrier coatings (environmental barrier coating (EBC)s and thermal barrier coating (TBC)s respectively) which have enabled tremendous increases in engine gas flow temperature. GTE thermodynamic efficiency (η_{th}) is primarily determined by the ratio of TIT to compressor inlet temperature, commonly referred to as T_4/T_2 [29]. For a given pressure ratio, higher ratios of T_4/T_2 indicate improved efficiency. Accordingly, improved GTE efficiency can be obtained by increasing T_4 or decreasing T_2 . Since compressor inlet temperature is largely determined by ambient conditions, from a design and operations point-of-view, T_4 (TIT) is the important variable [29]. Increased thermodynamic efficiency due to higher TIT allows higher fuel economy, reduced emissions of carbon monoxide and hydrocarbons, and increased performance capability [36, 52]. A typical bypass GTE and associated temperature profile can be seen in Figure 2.1. The main sections shown in the figure will be discussed in the following paragraphs. While Figure 2.1 is a schematic of a high-bypass turbofan GTE, the main sections to be discussed are common to most GTE variants.

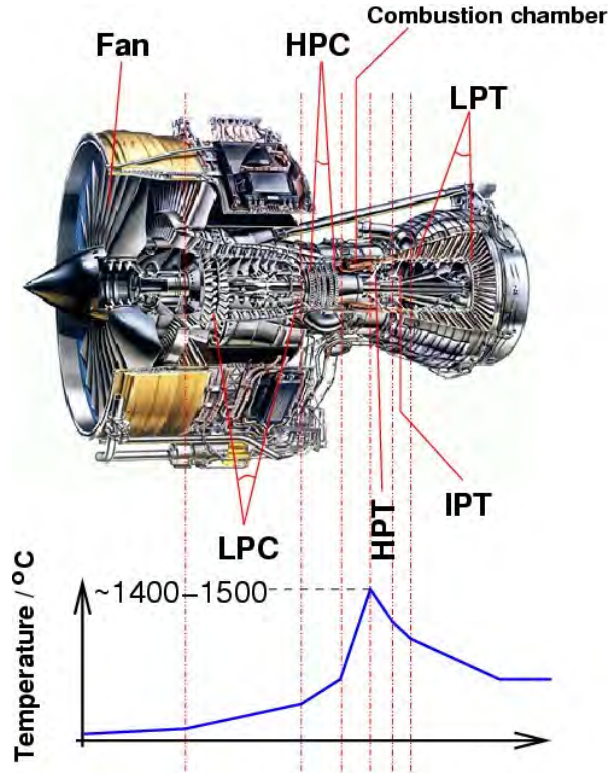


Figure 2.1: Gas-stream temperature profile in high-bypass GTE. Some heating occurs due to compression of the gas-stream, however the largest increase in temperature is due to the burning of fuel in the combustor. Special materials and coatings are required in the combustor and early turbine stages. Adapted from [103]

2.1.1 Inlet.

As mentioned in Section 2.1, thermodynamic efficiency is largely determined by T_4/T_1 . However, overall efficiency of the GTE is calculated by $\eta = \eta_{th}\eta_p$ where η_p is the propulsive efficiency which is largely determined by the mass of air accelerated by the GTE [29]. The inlet not only provides the feed air to the GTE compressor, but, in the case of bypass engines, allows a larger mass of motive air therefore increasing η_p .

2.1.2 Compressor.

The compressor section consists of alternating rows of rotating blades followed by stationary vanes. A single ring of blades comprises a rotor, while a single ring of vanes is a stator. A single rotor and stator pair is known as a stage. A typical turbofan GTE has between six and eighteen compressor stages [1, 17] which may be divided into a high-pressure compressor (HPC) and a low-pressure compressor (LPC) in a two shaft design. The blades serve to speed gas flow while the

vanes transform a portion of the increased gas velocity into increased static pressure. The result is an incremental increase in gas flow velocity and total pressure as the gas passes through each stage. This compression increases the temperature of the gas flow up to $\sim 650^{\circ}\text{C}$ by the final compressor stage [17]. The relatively cool temperatures of the compressor section allow the use of uncoated titanium for compressor components in current GTE design.

2.1.3 *Combustor.*

In the combustor, some of the compressed gas is mixed with fuel for combustion. However, as seen in Figure 2.2, the majority of gas flow from the compressor is used to control the flame shape, provide additional downstream mass to the combustion gas, and provide cooling air within the combustor and turbine sections [28]. The full flame temperature, which can approach 1900°C [28, 29, 35], does not reach the combustor walls due to the cooling air, however temperatures in this section are still high enough that the combustor liner is typically formed from superalloy sheet material [51].

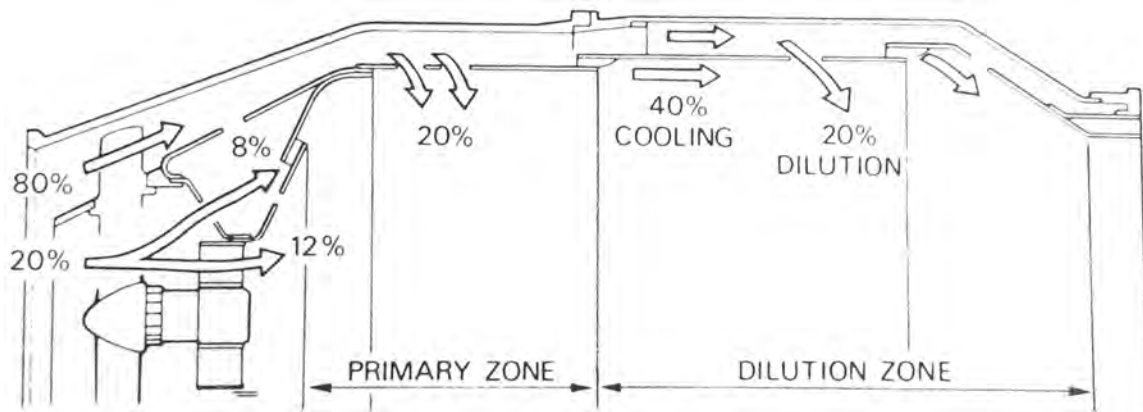


Figure 2.2: Schematic of the air flow in the combustor section [29] Only a small portion of air from the compressor section is used for combustion. The remainder is used to cool the combustor and provide additional motive air mass to the combustion gas-stream.

2.1.4 *Turbine.*

The turbine section consists of stages comprising stators followed by rotors (the opposite order of the compressor section). The turbine converts the thermal energy of the combustion products into mechanical energy which drives the compressor. Gas at high temperature and pressure, but low

velocity, enters the turbine section and leaves as a low temperature and pressure, but high velocity, stream which, along with any engine bypass from the inlet, provides thrust [28]. A typical turbofan GTE may have between two and eight stages [1]. The high temperature, harsh reactive environment, and high mechanical loading within the turbine requires the use of specialized materials and coatings (see Section 2.2) for turbine components. The first stage of the turbine is exposed to the full TIT requiring the use of cast superalloy components. Vanes in this section will typically be directionally-solidified (DS), while the significant mechanical stresses, particularly creep, developed by rotation of the rotor blades requires the use of single-crystal (SX) superalloy [51]. Lower temperatures and loading in successive stage components may allow the use of DS or even conventionally-cast (CC) stator and rotor components. Due to several design limitations, which will be discussed in Section 2.2.4, these superalloy components are typically covered with a protective coating.

In a two spool arrangement, the turbine may be divided into a HPT and a low-pressure turbine (LPT). The HPT will be connected to the HPC via one shaft while and LPT is connected through a second shaft to the LPC. The two shaft configuration allows the higher pressure sections of the engine to operate at different speeds than the lower pressure sections which improves engine efficiency.

2.1.5 Exhaust.

The gas flow is discharged after being further accelerated by the converging shape of the exhaust. Some higher performance engines may have an afterburner in this section to achieve additional thrust by burning additional fuel.

2.2 Nickel-based Superalloys

Though other superalloys exist (for example iron- and cobalt-based) this research will focus on nickel-based superalloys. Unless specifically noted otherwise, all use of the term “superalloy” in this paper will be in reference to nickel-based superalloys.

2.2.1 Structure.

The typical microstructure of a two-phase superalloy is shown in Figure 2.3. The microstructure consists of a γ' cuboidal precipitate phase, nominally of Ni_3Al , surrounded by a γ matrix of nickel and the refractory alloying elements of the specific formulation [37, 89]. The γ'

phase typically constitutes 60-70% of the crystal structure by volume [37, 97]. Both phases are face-centered cubic (FCC) and together form a single coherent crystal structure. The two-phase structure is stronger than either the γ or the γ' phase alone.

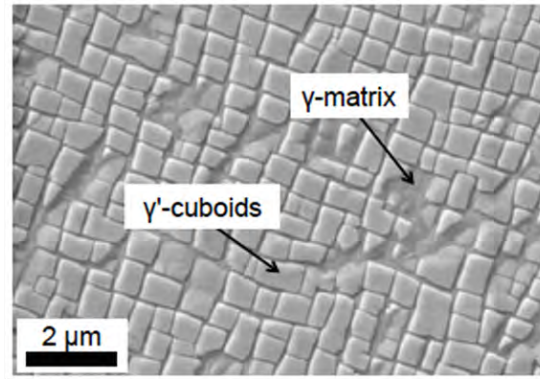


Figure 2.3: Two-phase microstructure of a typical superalloy which is responsible for the unique mechanical properties of the superalloy [97]. The γ' phase is primarily Ni_3Al while the γ phase is nickel and the additional alloying elements shown in Table 2.1.

Nominal compositions of two standard SX superalloys used in current DoD GTEs (General Electric (GE)'s René N5 and Pratt and Whitney (P&W)'s PWA 1484) are listed in Table 2.1. A third SX superalloy commonly used in industrial turbines and some Rolls-Royce aviation GTE (CMSX-4) is also included for comparison.

Table 2.1: Nominal composition (Ni in balance) of various second generation superalloys used to produce SX components [87, 97]. Polycrystalline superalloys use similar alloying elements however also require other elements, such as carbon, boron, and yttrium, which strengthen grain boundaries but may also reduce the superalloy's melting point.

Alloy	Co	Cr	Mo	W	Ta	Re	Al	Hf	Ti
René N5	7.5	7	1.5	5	6.5	3	6.2	0.15	0
PWA 1484	10	5	2	6	9	3	5.6	0.1	0
CMSX-4	9.6	6.4	0.6	6.4	0	2.9	5.6	0.1	1.0

All generations of SX, as well as CC and DS superalloys, include additional refractory alloying elements to improve mechanical properties. The refractory elements promote adhesion of the oxide

scale and also act as impurity scavengers, preventing impurities such as sulfur from diffusing to the oxide scales [98]. Both aluminum and chromium provide oxidation resistance by forming oxide scales (Al_2O_3 and Cr_2O_3 respectively). However, the oxidation rate of superalloy components becomes a significant concern at temperatures above 1000°C [86] where Cr_2O_3 readily oxidizes to CrO_3 which is highly volatile [98]. Formation of CrO_3 causes appreciable loss of oxide scale, so superalloys are predominately dependent on Al_2O_3 for oxidation protection at high temperatures. Therefore, oxidation resistance of GTE components operated at high temperatures is best improved with high aluminum, low chromium alumina-forming superalloys or EBCs [37, 99]. As a secondary benefit, the higher aluminum content increases γ' formation thereby increasing superalloy strength. Also, minimizing chromium content prevents the formation of topologically close-packed (TCP) phases in γ' phase [31, 47, 97]. Phase boundaries between the desired γ/γ' structure of the superalloy and the TCP phase cannot tolerate deformation which leads to crack formation within the superalloy structure under loading [31]. Therefore, TCP formation ultimately leads to a decrease in creep-rupture strength [37].

2.2.2 Benefits of Current Superalloys.

Nickel-based superalloys offer unique material properties which make them well suited for use in modern GTEs. First, superalloys can have yield strengths of 900-1300 MPa [87] at the high operating temperatures within the GTE hot sections which are greater than ordinary steels at room temperature. Superalloys experience what is known as a yielding anomaly. Yield strength of superalloys increases with temperature, whereas the typical material response is for yield strength to decrease with increasing temperature. Figure 2.4 is a simple depiction of the yielding anomaly. For nickel-based superalloys the yielding anomaly typically holds up to temperatures approaching 800°C [97], after which yield strength rapidly decreases.

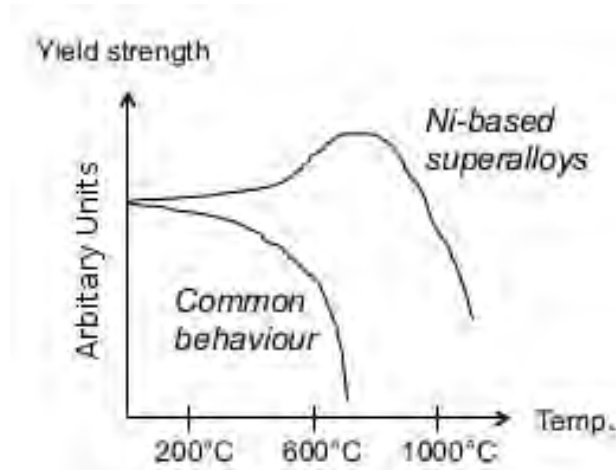


Figure 2.4: Representative yield behavior of a nickel-based superalloy. Superalloys show increasing yield strength until temperatures approaching 800°C. This is anomalous to typical materials which show monotonically decreasing yield strength with increasing temperature. Adapted from [97]

Second, superalloys have high creep resistance. The tight tolerances in GTEs require materials which will exhibit minimal creep deformation when subjected to the high centrifugal forces turbine blades may experience for many hours at a time. Excessive elongation due to creep could cause the blade to contact the engine housing causing serious damage. The high volume fraction of γ' phase which is key to the creep behavior of the superalloy [87]. The γ' phase provides increasing shear resistance, which leads to increased creep resistance, as temperature increases [104]. Among the crystallographic orientations possible, the $\langle 001 \rangle$ direction was found to have the highest creep resistance under tension. The increased creep resistance in the $\langle 001 \rangle$ direction is due to a unidirectional γ' coarsening called rafting. If rafting is parallel to the applied load as shown in Figure 2.5 creep resistance improves [50, 97]. Since creep resistance in tension is of most concern for rotating components in the GTE, DS and SX components are cast so the $\langle 001 \rangle$ crystallographic direction is parallel to the applied load.

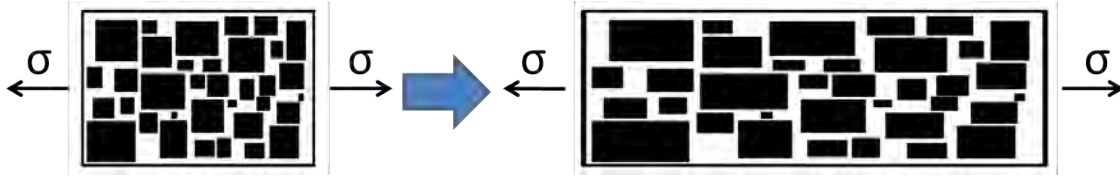


Figure 2.5: Rafting of γ' precipitates in a nickel-based superalloy. Creep elongation can be minimized by orienting the structure so applied load (denoted σ) is parallel to γ' rafting.

Slow diffusing elements in the recipe, such as rhenium, ruthenium, tungsten, and molybdenum, also add to the creep resistance of the superalloy [87]. The already substantial creep resistance of superalloys has been further improved with the advent of single crystal castings. The removal of grain boundaries removes any possibility of grain boundary slip thereby removing a key creep mechanism [97]. The lack of grain boundaries has also improved the oxidation resistance of the superalloy by presenting fewer nucleation points for oxidation to initiate.

Finally, the second generation SX superalloys widely used in DoD aviation GTE were designed to operate at average surface temperatures of $\sim 1050^{\circ}\text{C}$ with occasional excursions exceeding 1200°C [12, 52, 87]. Depending on the superalloy's specific recipe, the alloy's melting temperature is $\sim 1450^{\circ}\text{C}$ [37, 52, 87, 97]. No other class of structural material is currently known to allow sustained operation at such a high fraction of its melting temperature.

2.2.3 Issues with Current Superalloys.

Currently employed superalloys are expensive and nearly twice the density of titanium alloys used in other GTE components, such as compressor blades. Therefore, superalloys are typically reserved for just the hottest operating sections of the GTE. In addition, engines are typically run lean to ensure complete combustion. The high air-to-fuel ratio leads to a large excess of oxygen which creates an oxidizing environment. The environment within the GTE can also be made more oxidizing by contaminants in the fuel and the ingestion of sulfur and/or chlorine containing particles from the environment. Therefore, superalloys must have high oxidation resistance to withstand the highly oxidative engine environment. However, superalloy recipes have largely been developed focusing on mechanical properties at the expense of oxidation resistance.

2.2.4 Consideration as an Engine Component.

The first stage of the turbine sees the most severe conditions within the engine, making it the limiting factor to increasing TIT and, by extension, engine efficiency and performance. Currently, to achieve the desired TIT, internal cooling air and TBCs must be used. The typical TBC system consists of three primary layers: a bond coat (BC), a TGO layer, and the TC, as shown in Figure 2.6. Zirconia was the first candidate TC picked in the 1980s, and testing of various stabilizing dopants by researchers at the National Aeronautics and Space Administration (NASA) identified zirconia partially stabilized with 6-8 wt% yttria (YSZ) as having the best thermal cycle life [26, 30, 38]. YSZ has been the TC of choice since. YSZ has a melting temperature of $\sim 2700^{\circ}\text{C}$ and a bulk thermal conductivity of only 1-2 W/mK [30, 40, 43, 56, 64] which is basically invariant of temperature [27, 30, 40, 43].

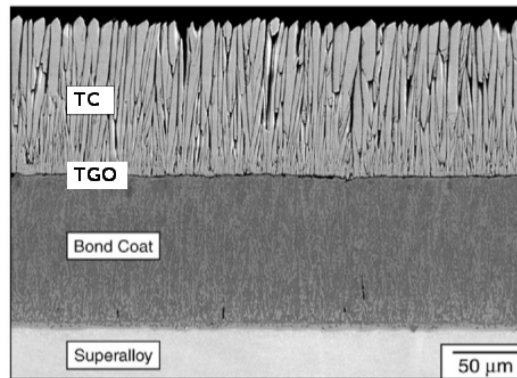


Figure 2.6: SEM image of a typical profile within an EB-PVD deposited TBC. The porous top coat provides thermal protection but cannot provide environmental protection. Therefore the bond coat doubles as an EBC. The TGO grows from oxidation of aluminum in the bond coat and provides adhesion between the top coat and bond coat. Adapted from [38]

Modern TCs based on YSZ have been improved by the strategic use of voids to lower thermal conductivity below values which would be expected for the bulk ceramic. The porous structure of the TC also increases the ceramic's strain tolerance [30, 40, 66] which is important given an operating temperature range exceeding 1200°C [38]. However, the porous structure which gives the TC its necessary thermal conductivity also allows ready transportation of oxygen and other reactive species through the TC. The porous TC structure is a key reason to use EBCs, which will

be discussed shortly, as the BC in the TBC. The TGO layer is the result of aluminum in the BC oxidizing the form a dense alumina (Al_2O_3) protective layer at the surface of the BC [30, 35, 43, 88].

Current superalloys have been optimized to provide increased strength and creep resistance at high operating temperatures. However, the optimization of mechanical properties has primarily been achieved by lowering chromium and aluminum content below levels which have been found to be optimal for intrinsic oxidation and HC resistance of the superalloy [89]. Therefore, EBCs are required to provide protection to counter the lack of intrinsic environmental resistance of current superalloys.

There are two primary categories of EBCs. The first is a diffusion layer based on platinum-modified aluminide such as NiAl. While NiAl coatings have been in use since the 1940s, the addition of platinum to the coating was not introduced until the 1970s [46]. The second category is based on overlay coatings originally developed by P&W in the 1960s. The typical overlay EBC, as shown in Figure 2.7, is based on the MCrAlY system, where M can be nickel, cobalt, or a combination of the two [46, 86, 88, 89].

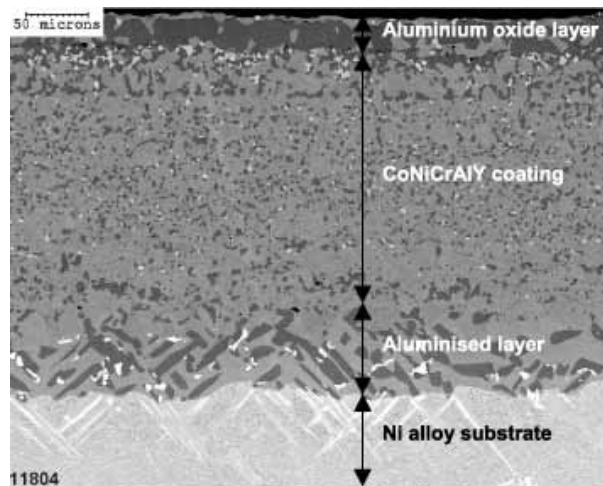


Figure 2.7: SEM image of a typical profile within an overlay EBC [38]. The aluminised layer provides adhesion between the EBC and superalloy. The aluminised layer also acts as a source of aluminum to slow leaching of aluminum from the superalloy into the EBC as the EBC becomes depleted in aluminum due to TGO growth.

Both EBC systems are designed to be fully dense to prevent easy transport of oxidizing agents to the substrate. However, diffusion coatings primarily provide only oxidation resistance to the superalloy. Overlays can provide both oxidation and HC protection and can be tailored to the environment in which they will operate [88]. The EBC must also be devoid of segregants, such as sulfur, carbon, and titanium, which can diminish adhesion between the TGO and EBC by as much as a factor of ten [30, 43, 46, 88].

Protective coating systems which include aluminum and/or chromium have been shown to provide excellent resistance to sulfate attack as long as the coating remains intact. Once the coating is compromised the resistance of the component to sulfate attack depends entirely on the resistance of the substrate [47] which, as was mentioned in Section 2.2.1, has been greatly diminished, by the removal of chromium, to allow greater mechanical properties.

Any of the failure mechanisms listed in Section 1.2 can compromise the protective EBCs and TBCs causing the superalloy substrate to be exposed to conditions it was not designed to tolerate. Unfortunately, the effects of these failure mechanisms are not yet fully understood due to the complex operating conditions the coatings can be exposed to, and a lack of accurate predictive models. As mentioned in Section 1.1, due to the push for ever-increasing TIT and prolonged operations in dusty environments, degradation due to molten deposits have been a growing focus within the DoD since the Persian Gulf War. In particular, two distinct (as currently studied) forms of molten deposit will be discussed in detail: CMAS glass (Section 2.3) and HC (Section 2.4).

2.3 Academic Studies of Artificial CMAS Glass

Smialek's work in 1992 characterized newly discovered CMAS glass deposits on turbine vanes in relation to the local mineralogy. In various papers authored between 1992 and 1994 [105–107], Stott and Wet expanded Smialek's work to the laboratory study of CMAS glass degradation of TBC caused by various natural sands collected from across the Arabian Peninsula. Stott and Wet also attempted to correlate the effects of these natural sands to various simple silicate glasses they produced by mixing Na_2O , SiO_2 , and CaO [107]. Their choice of artificial glass is interesting for a study of CMAS, as lacking aluminum and magnesium the test media could not be classified as CMAS glass. Following in this vane, in 1996 Borom studied the glasses formed by dirt from various

locations in the Near East, Far East, and southwest United States. He determined “the composition of the [glass] was similar irrespective of geographic location, severity of operating conditions, or degree of exposure to dust [16].” Since that time, studies of CMAS and its effects on components within the aviation GTE have focused almost exclusively on degradation caused *after* the formation of CMAS on a component. As such, the media used for testing is a homogeneously prepared artificial glass, manufactured from pure reagent-grade oxides of calcium, magnesium, aluminum, and silicon (typically CaO, MgO, Al₂O₃, SiO₂).

2.3.1 Select CMAS studies.

Table 2.2 shows the oxide content of ingested sands studied by Smialek and Borom followed by the oxide content of artificial CMAS glasses used in several studies over the last decade.

Table 2.2: Pure oxide weight percents of various lab mixtures used in select CMAS glass studies. The studies focus on pure oxides as opposed to naturally occurring oxides. The studies also ignore other volatiles and fluxing agents which could affect the type of glass formed and the process of glass formation.

	Smialek [101]	Borom [16]	Krämer [59]	Wellman [113]	Drexler [34]	Drexler [33]
Year	1992	1996	2006	2010	2010	2012
CaO	17.73	28.7	29.6	32.9	35.2	37.1
MgO	5.77	6.4	5.8	6.8	3.3	3.5
Al ₂ O ₃	11.65	11.1	21.2	12.0	6.7	7.1
SiO ₂	43.44	43.7	43.3	48.4	49.6	52.3
TiO ₂	2.18					
Fe ₂ O ₃	11.43	8.3			2.6	
Na ₂ O	1.41				1.0	
K ₂ O					1.6	
NiO		1.9				

Krämer’s glass study [59] was based on the sand oxide composition presented by Borom but without iron or nickel oxides. The omission of iron and nickel oxides was because Krämer believed these oxides came from upstream in the GTE, not as ingested material. Krämer produced his glass by mixing the appropriate amounts of reagent-grade oxides then milling them to form a thick paste. For his study, he applied the paste to TBC coupons at a concentration of ~40 mg/cm² then heated

the coupons at 1400°C and several temperatures between 1200 and 1300°C for four hours. He noted partial melting began at 1235°C with complete melt by 1240°C.

Wellman's study [113] attempted to determine a minimum CMAS dosage to initiate degradation of TBCs. He applied various masses of artificial CMAS on TBC samples and heated them at 1300°C for four hours. He performed an interesting secondary test during his study, but only offered a brief discussion of its results. In addition to coating the samples with his crushed artificial CMAS glass, he also coated several coupons with a mixture of the four oxides shown in Table 2.2 without first melting them into a glass. As shown in Figure 2.8, after heat treatment, the TBC sample under the crushed artificial CMAS glass showed no damage but the TBC sample under the unfired oxide mixture showed substantial cracking.

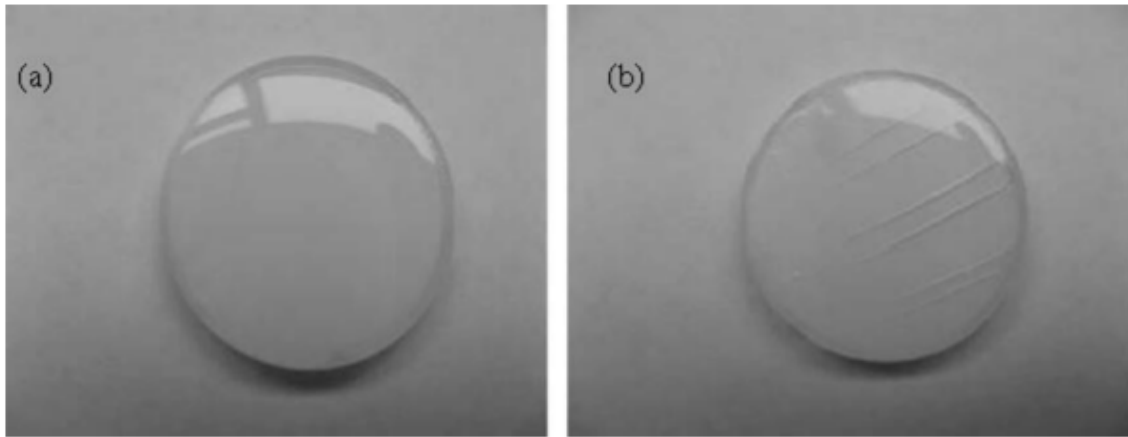


Figure 2.8: Final melt appearance of crushed, previously-melted CMAS glass (left) and pure oxides which weren't previously melted (right) from Wellman's study [113]. While the final glass formed in each case was the same, the different process of glass formation the two powders experienced resulted in damage to the TBC substrate in the right image which was not found in the left image.

Wellman's analysis of the TBC under the two deposits showed similar chemical structure and physical degradation to the TC at the interface with the deposit. However, the TC under the unfired oxides showed a larger shift toward the monoclinic phase. The 3-9% volume change associated with the transformation from t' - to m -phase YSZ [11, 30, 43, 70, 107] likely accounts for the cracking shown in the right picture of Figure 2.8.

Drexler's 2010 study [34] looked at air plasma spray (APS) TBCs resistant to CMAS attack. For this study she specifically chose not to use actual sand because "uncertainties in the oxides-mixture case are expected in the melting behavior and the homogeneity of the resulting CMAS glass" [34]. Instead she produced an artificial CMAS glass frit by mixing reagent-grade dry powders of SiO₂, CaCO₃, MgO, Al₂O₃, Na₂CO₃, K₂CO₃ and Fe₂O₃. The mixture was then heated at 1550°C for four hours, crushed, and reheated at 1550°C for another four hours before being milled and screened through a #500 mesh sieve [4]. The resulting homogeneous glass powder was then mixed with ethanol and applied to test samples as a thick paste. The CMAS paste was applied at a concentration of 35 mg/cm² and the samples were heat treated at 1200°C for 24 hours.

Drexler's 2012 study [33] examined the effect of additions of various solute ions to YSZ to make a TC more resistant to CMAS attack. As shown in Table 2.2, this study used a simpler artificial CMAS glass to limit side reactions due to the minor iron, sodium, and potassium oxides use in her 2010 study. The artificial CMAS glass was produced by the same heating procedure as her 2010 study, however, the final artificial CMAS glass was not milled into a powder in this study. Instead, wafers of the CMAS glass were placed directly on test samples for heat treatment at 1200°C for 24 hours.

2.3.2 Interpolation of Results to Real-World Application.

Three important questions must be answered in order to determine the relevance of current lab results to the real-world CMAS problem. The first question is: *Are the chemistries studied representative of the real world?* The artificial CMAS used for current studies is a "dry" chemistry. The oxides used are already chemically exhausted, in addition there is no influence from water vapor, there are no volatiles to off-gas during gas formation, and there are no salts. Reactive species, water, volatiles, and salts all cause depression of melting temperature in sand mixes. Reactive species, water, volatiles, and salts are all also readily found in naturally occurring sands (see Figures 1.1 - 1.3). Therefore, the temperature reported for initiation of CMAS attack is likely too high.

The second question rises as an artifact of the specific surrogate CMAS glass used in current studies: *How do the temperatures used in the studies correlate to real-world operational*

temperatures? The conclusion of most current academic research into CMAS degradation is that CMAS attack and infiltration begins at $\sim 1240^{\circ}\text{C}$. This is because the artificial CMAS glass used in most current academic research melts at that temperature. As mentioned in Section 1.1, Toriz found evidence of molten deposit infiltration into the TBC at 1150°C . A recently completed study by Opie found certain Afghan sands infiltrating TBC at temperatures as low as 1100°C [79]. The difference in melt temperature between laboratory studies and the real-world phenomenon is that the laboratory CMAS lacks reactive species.

However, the most important question raised by trying to interpolate current CMAS studies to real-world application is: *How much of the phenomenon do the studies capture?* The four studies cited are indicative of a significant issue in the current body of research into CMAS degradation of GTEs: the research is predominately focused on the end effect of CMAS glass deposition while ignoring how CMAS glass deposits form in the first place. While the damage caused to the TBC by a specific CMAS glass mixture, at a small range of temperatures has been well studied, little is known as to how long it takes to get to a CMAS attack situation. Further, little is known about how that TBC degradation translates to a loss of GTE performance in an operational sense. The lack of translation from laboratory study to operational impact is a key roadblock for the development of useful lifing models. Figure 2.9 helps to illustrate this point.

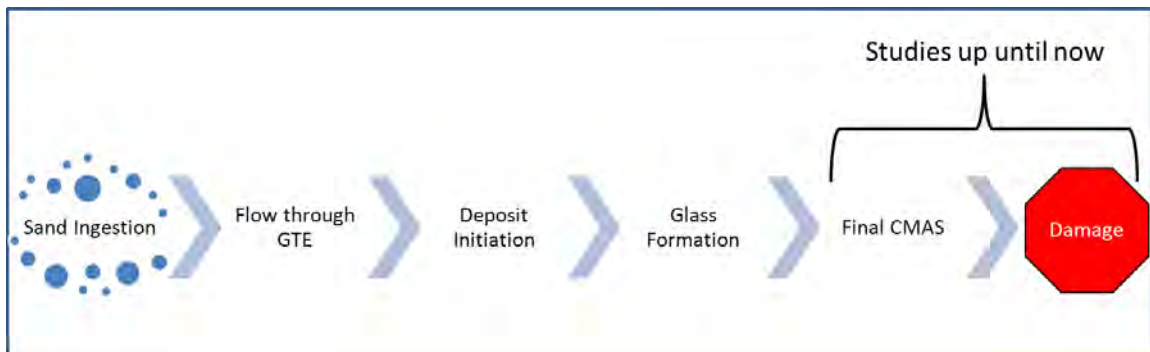


Figure 2.9: Top-level timeline of CMAS degradation within the GTE. Current literature has focused on the final CMAS glass under the assumption that damage is the result of this final glass. In reality the final CMAS glass formed is just a function of all the steps before it in the timeline. Damage may occur at any of the steps.

- **Sand Ingestion** As has been shown by real-world experience, not all ingested dusts lead to the formation of CMAS deposits. Some dusts simply lack the required components. In addition, not all ingested dusts which contain calcium, magnesium, alumina, and silicate will form CMAS glass at current operating temperatures, as was shown in the example from Saudi Arabia in Chapter 1.
- **Flow Through GTE** Smialek showed that filtering “as-collected” dusts to a smaller size changed the chemistry of the sample. This filtering process happens in the GTE as well, most obviously through the use of filters and IPSs. Both techniques are used to lower the likelihood and severity of particle erosion within the GTE, but may also affect the chemistry of what makes it to the hot sections of the GTE. Even ignoring any potential change in chemical composition, the dust that gets past filtration will melt at a lower temperature due to a much lower particle size distribution than the “as-collected” dust would have. The cold section can also work as a “pulverizer” producing a smaller particle distribution, and therefore lower melting dust.
- **Deposit Initiation** Current CMAS studies use a homogeneous oxide mixture which melts at a predictable and narrow range. However, real-world deposits are likely to occur in a piecewise function as certain minerals, namely salts and evaporates, melt or soften at different temperatures. This piecewise deposition process would greatly expand the temperature range over which attack occurs, and likely allow degradation to begin before the final CMAS glass forms.
- **Glass Formation** Glass formation is a complex process which is a function of chemistry, time, and temperature. A glass formed from natural materials will go through many phase and compositional changes as different species liquefy, react, or off-gas. With each change, a different glass can be formed with different chemical and mechanical properties.
- **Final CMAS** The CMAS glass used in current studies only represents a small fraction of the total timeline described above, yet it remains the focus of current research. The final glass is devoid of the most reactive species from the initial ingested dust, so the mechanisms

with which the final CMAS can cause damage are limited in comparison to the mechanisms possible while the glass is forming and reactive species are still present.

The “Damage” stage is not included in the list above, because without study of the entire CMAS timeline presented in Figure 2.9 there is no way of knowing when damage actually occurs. Thermomechanical damage may happen during the initial glass formation process and be irreversible before the final CMAS glass even forms. Thermochemical damage would logically be more likely to occur while reactive species are still present during initial deposition as opposed to after a glass of chemically-exhausted oxides forms. Real-world differences between CMAS glassing in Saudi Arabia, as well as differences in CMAS damage caused by fired versus unfired oxides in Wellman’s laboratory study show the fallacy of using Borom’s conclusion that the final CMAS is the same regardless of inputs, to assume that the inputs don’t matter. Changing the starting point slightly can have a pronounced effect of the results seen, yet the design of all current CMAS studies ignore the starting point.

2.4 Academic Studies of Hot Corrosion

Oxidation¹ was discussed in Section 2.2.1 as being a key concern at temperatures above approximately 1000°C. However, according to current literature, at lower temperatures a corrosion mechanism known as HC attacks superalloys. HC can be considered an accelerated form of oxidation involving the deposition of a liquid or solid containing salts of sulfur, vanadium, or chlorine. Figure 2.10 shows the relative occurrence of oxidation and two distinct mechanisms of HC as currently studied: HTHC and low-temperature hot corrosion (LTHC). HC has been found to be more severe in GTEs operated along coastal areas and in desert or active volcanic regions [36].

¹Oxidation is an electrochemical reaction which may be initiated by several oxidative species including oxygen, sulfur, bromine, fluorine, chlorine, and iodine [10]. The other species can produce worse oxidative degradation than oxygen. However, the term “oxidation” as used here, and the remainder of this paper, refers to the common usage of the term which implies oxygen-induced oxidation.

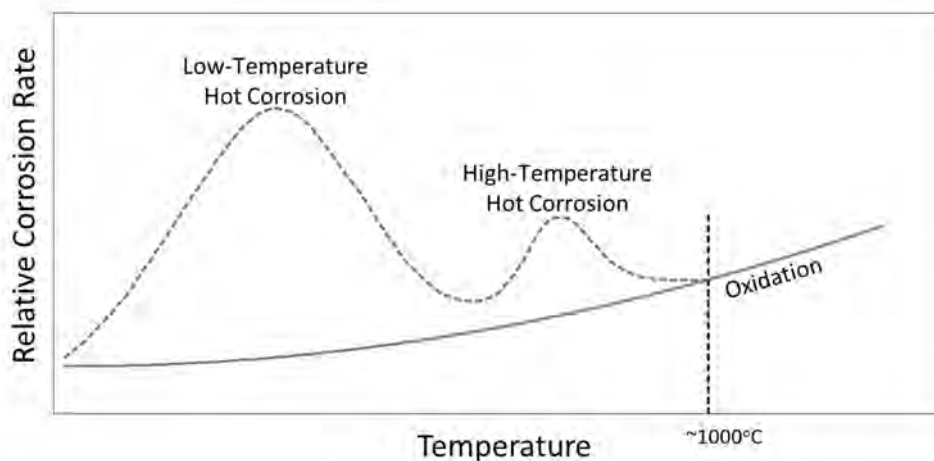


Figure 2.10: Relative corrosion rates on superalloys, as a function of temperature, assuming sodium sulfate as the cause of HC [86]. Given sodium sulfate as the cause of HC, oxidation is the primary concern for damage at temperatures exceeding 1000°C because HC is minimal at these temperatures.

HTHC, also known as Type I HC, has been a recognized problem for power generation GTEs since the 1950s [21, 55]. However, the DoD's interest began in the late 1960s as military aircraft operating over seawater during Vietnam began to experience severe corrosion of GTE components [94]. HTHC is variously reported as being prevalent between 750-1000°C [35, 55, 58, 89, 94, 98], though the presence of certain other reactive species within the GTE gas flow may expand the temperature range for attack. A second form of HC, LTHC, or Type II HC, was discovered around 1975 [55] attacking components at temperatures of 600-850°C [35, 46, 55, 58, 89, 94] which is below those associated with HTHC. Surprisingly, the affected components had been coated with the MCrAlY EBCs which had been designed to prevent HTHC [46]. It has been suggested LTHC requires a high partial pressure of SO_3 to initiate [35, 55]. Therefore, LTHC is unlikely in current aviation GTE running modern fuels which produce little SO_3 [42]. As such, only HTHC will be discussed further and the term HC will be used to refer to hot corrosion in general.

Within the HTHC mechanism, once a sulfate salt has deposited on a GTE component, there is an incubation period as the molten salt fluxes away any protective oxide. Eliaz has suggested that the incubation period diminishes with increasing NaCl [35]. The reduction in incubation period occurs because chloride ions in molten deposits make the protective Al_2O_3 or Cr_2O_3 layer more susceptible to cracking or spallation [81] enabling sulfate access directly to the underlying superalloy. Two

mechanisms have been proposed for the fluxing of the protective oxide layer: acidic and basic fluxing.

Much of the development of the two fluxing mechanisms was accomplished by Goebel and Pettit [8, 44, 45, 81]. According to Pettit, the corrosion-causing deposits found on fielded hardware often contain sulfates of calcium, potassium, sodium, and magnesium. While Pettit's work focused primarily on sodium sulfate (as most studies before and after have) but stated "consideration of other deposits would not change the content [of the mechanism]...but only present variations [81]." Despite the broad applicability of the accepted HC mechanism to all sulfate salts, little research could be found examining sulfate salts other than sodium sulfate. One master's thesis was found examining gypsum attack on various nickel alloys at temperatures from 850 to 1100°C [2]. The study found gypsum to cause damage comparable to that accepted as HC. The remaining research which mentioned gypsum sought to downplay gypsum's role in HC on nickel-based superalloys via one of two arguments: (1.) Gypsum does not cause as severe damage as sodium sulfate; and (2.) Gypsum melts at too high of a temperature to cause HC. Therefore, in keeping with current literature, and for simplicity, the following discussion will focus on Na_2SO_4 as the sulfate salt. A full discussion of Na_2SO_4 as *the* initiator of HC will be discussed in Section 2.4.1.

The idea of separate acidic and basic fluxing mechanisms arises from the dissociation of Na_2SO_4 into a base (Na_2O) and an acid (SO_3) [98]. Regardless of fluxing mechanism, the development of a protective oxide layer is inhibited by the salt deposit blocking oxygen transport to the substrate surface [81]. In acidic fluxing, protective oxide scales (if present) are broken down by SO_3 . In basic fluxing, the oxide scales are attacked by Na_2O (assuming Na_2SO_4 as the initiator). Acidic fluxing results in degradation more severe than basic fluxing, however basic fluxing is more favorable than acidic fluxing at temperatures exceeding 900°C, in environments high in oxygen, and on alloys with less than 10-12% aluminum content. In other words, current DoD aviation GTE are perfectly suited for basic fluxing in the presence of sulfate salts.

Assuming Na_2SO_4 as the HC initiator, in the basic fluxing mechanism, Na_2O attacks the protective chromium or aluminum oxide at the substrate/deposit interface to form a Na-(Cr, Al)-oxide which reprecipitates at the deposit/gas stream interface as a non-protective oxide [13]. In the

case of a protective Cr_2O_3 layer, CrO_3 eventually forms at the deposit/gas stream interface, where it off-gases and is transported away in the gas stream, resulting in a chromium-depleted substrate. The initiation phase of basic fluxing (removal of the protective oxide layer) can only proceed as long as the Na_2O source is renewed [35, 81].

The propagation phase begins once the protective oxide layer is removed. During the propagation phase, the SO_3 formed by dissociation of the sulfate salt in the basic fluxing mechanism releases sulfur to react with the underlying substrate [58]. Once through the protective oxide, sulfur preferentially reacts with chromium remaining in the superalloy to form Cr_2S_3 . At temperatures above $\sim 850^\circ\text{C}$, Cr_2S_3 further reacts to form Cr_2O_3 which then oxidizes to a volatile species CrO_3 [89] which, just as in the initiation phase, evaporates from the surface resulting in further chromium depletion. The oxidation of chromium sulfide releases sulfur back into the superalloy to propagate the reaction front. In this manner, the initial attacking sulfur is “freed” to attack again, making the propagation phase “autocatalytic” [58].

Once chromium is sufficiently depleted in the superalloy, sulfur begins to react with the base nickel to form NiS and NiO [94]. NiS , which becomes molten at 645°C , well below the range for HTHC [89], escapes to the superalloy surface. NiO forms a porous, non-protective, oxide layer on the surface of the structure. The resulting structure caused by the HTHC reaction mechanism is readily seen in the cross-section in Figure 2.11 below. Zone 1 shows the porous, nickel-rich, non-protective oxide outer layer. Zone 2 is a sulfur-rich layer depleted of chromium. Zone 3 shows the unaffected superalloy.

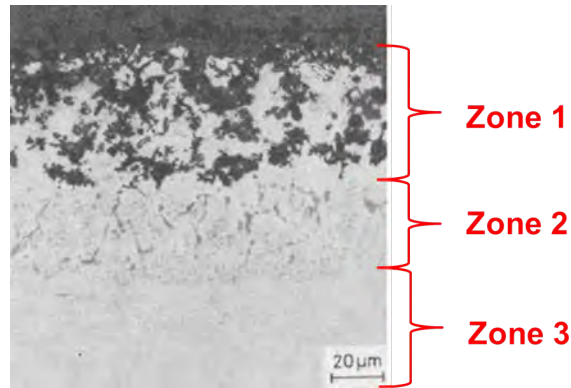


Figure 2.11: Representative HTHC degradation as seen on Inconel 718 alloy. HC causes a Cr-depleted region (Zone 2) at the surface of the unaffected superalloy (Zone 3). Oxidation of sulfides formed in Zone 2 cause substrate metal (predominantly nickel and chromium) to flux into the molten sulfate salt deposit forming a porous, non-protective metal oxide outer layer (Zone 1). Adapted from [96]

Refractory alloying elements such as vanadium, tungsten, and molybdenum added to improve the mechanical properties of the superalloy make it more susceptible to HTHC. Oxides of these elements are acidic and aid in the removal of protective chromium and aluminum oxides and also form mixtures with the sulfate salt with lower melting points than the pure sulfate salt. These low melting point salt mixtures, allow initiation of HTHC at lower temperatures. It has been determined that 15% chromium in the superalloy is necessary to combat HTHC [21, 35, 72]. However, as noted in Table 2.1, the current recipes for second generation SX superalloys have considerably less chromium than 15% chromium. To overcome the lack of intrinsic HTHC resistance, a MCrAlY EBC with 25% chromium, 12% aluminum can be used. Interestingly, the high chromium, low aluminum recipe is the exact opposite of what was discussed in Section 2.2.1 as necessary for oxidation resistance. The conflict between a proper recipe design for HC resistance versus oxidation resistance shows the importance of tailoring the EBC to the operating conditions to which the coated component will be subjected. Therefore, the current state of understanding of molten deposits, which will be discussed in Section 2.4.1, is particularly important to the proper design of GTE components.

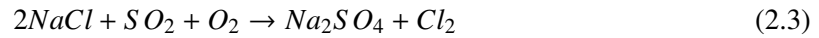
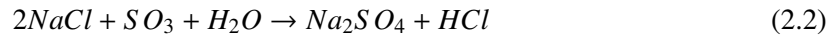
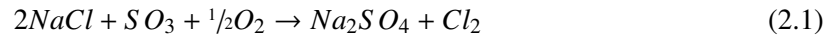
2.4.1 Interpolation of HC Initiation to the Real-World.

The discussion of HC in the previous section focused on what happens *after* a molten salt deposits on a superalloy GTE component. When HC was originally found in aviation GTE, the

assumptions and explanations developed for HC in industrial turbines were adopted to explain HC in aviation GTE. The current sulfate salt accepted as the cause of HC by the majority of HC researchers is sodium sulfate (Na_2SO_4). This section will review the accepted views of how sodium sulfate forms as a molten deposit in GTE and discuss several issues with the hypothesis of sodium sulfate as the cause of HC in DoD aviation GTE.

2.4.1.1 Na_2SO_4 as Product of Fuel Sulfur Reactions.

HC was initially identified as a problem within GTE used for industrial power generation in the 1950s. It was originally deduced from three common observations that NaCl from ingested sea water reacted with sulfur oxide combustion by-products to form Na_2SO_4 , which could then deposit on GTE components to initiate HC attack. (1.) Analysis of deposits on affected components showed the presence of sodium and sulfur. (2.) The most severe cases of HC were found in maritime regions (3.) using fuels (coal or low-grade kerosene) with high sulfur content. The following reaction mechanisms are most commonly cited for the formation of Na_2SO_4 in the GTE.



The predominant sulfur compound formed by combustion at the lean fuel-to-air ratios used in aviation GTE is SO_2 . In fact, SO_2 accounts for more than 99% of sulfurous combustion by-products [42]. Even at high fuel-to-air ratios, the formation of SO_3 is only a few percent of SO_2 . Therefore, while each reaction mechanism shown above is thermodynamically feasible, only Equation (2.3) is likely to occur in an aviation GTEs.

Early developmental studies of the HC mechanism relied on a molten salt for ion transport in the corrosive process and also as a means of transporting metal sulfides of aluminum, chromium, and nickel away from the substrate. The transport of sulfides away from the substrate is responsible for the resulting structure for HTHC shown in Figure 2.11. Therefore, the presence of a liquid salt

was essential. The fact that many initial reports of HC fell into a temperature range bracketed by Na_2SO_4 's melting point and dew point (when sodium sulfate is liquid), helped corroborate sodium sulfate as the cause of HC.

However, laboratory studies of Na_2SO_4 attack on various superalloys of the time would reveal that Na_2SO_4 itself is not corrosive to nickel alloys [32, 47]. It was hypothesized, and later proven in the lab, that NaCl (which had not reacted to form Na_2SO_4) was necessary to initiate HC attack by Na_2SO_4 . The addition of NaCl to the attack mechanism, and later acknowledgement of other impurities present in the real-world, would expand the accepted range of this form of HC to temperatures below the melting point of Na_2SO_4 .

To this date, Na_2SO_4 formed by reaction in the fuel stream, remains the primary accepted cause of what has now been renamed HTHC [21, 35, 46, 72, 99, 102]. The use of the term HTHC became necessary after the discovery of another form of HC (LTHC) occurring at temperatures far below Na_2SO_4 's melting point.

However, while the reaction of NaCl with SO_2 to form Na_2SO_4 is *thermodynamically* possible in a lab environment, it is *kinetically* improbable in a real-world aviation GTE combustion environment. Birks was able to show that the conversion of NaCl to sodium sulfate is most likely to occur by gas-stream reaction at temperatures exceeding 650°C [13]. However, Hanby [48] showed (as seen in Figure 2.12) that at residence times <16 ms, less than $\sim 8.5\%$ conversion of NaCl to Na_2SO_4 is possible via gas-stream reaction. Hanby conducted his experiment at 1190, 1302, and 1350°C and found that as temperature was increased, the conversion of NaCl decreased. Figure 2.12 shows that for a 5-10 ms residence time, cited by Hanby as typical for a GTE hot section, the amount of Na_2SO_4 formed in the combustor to cause a deposit by the first HPT stage is no more than 2% of the ingested NaCl concentration.

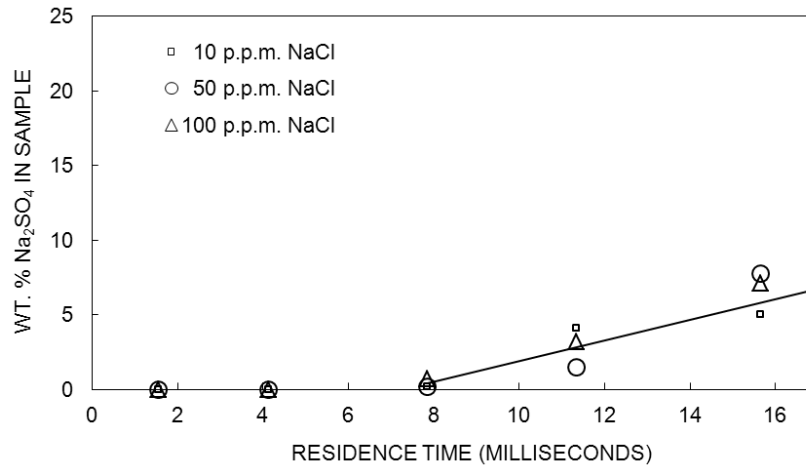


Figure 2.12: Effect of initial sodium chloride concentration on the sulphidation reaction [48]. For the hot section residence time of 5-10 ms cited by Hanby, less than 2% conversion of NaCl to sodium sulfate occurs regardless of NaCl or fuel sulfur concentration. Hanby found conversion of NaCl decreases with increasing temperature.

2.4.1.2 *Na₂SO₄ Ingested From the Environment.*

An alternate theory for the initiation of HC is that Na₂SO₄ is ingested directly from the operating environment. This theory becomes more attractive considering the high air-to-fuel ratios employed in modern aviation GTE. A National Material Advisory Board (NMAB) report on HC made the case for direct ingestion of sodium sulfate with a simple example: at an air-to-fuel ratio of 50:1, 1 ppm of ingested sulfate salt would be the equivalent of 50 ppm sulfate salt formed by fuel-stream reaction [72]. Based on the logic presented by the NMAB, the issues raised in the previous section are moot, as it would not matter how little Na₂SO₄ did or did not form in the combustion process. The possibility of directly ingested Na₂SO₄ would far outweigh fuel-produced Na₂SO₄. However, direct ingestion is occasionally treated as a secondary source of Na₂SO₄ [72], and only rarely cited as a primary source [35] (compared to the many sources cited in Section 2.4.1.1 for the formation of Na₂SO₄ via reaction).

2.4.1.2.1 Maritime Environments. Table 2.3 shows the relative abundance of the primary ions which account for greater than 99% of the salinity of seawater. Those who reference seawater ingestion as a source of Na₂SO₄ for HC have used these percentages to claim Na₂SO₄ is the second most abundant salt formed from seawater at nearly 11% of sea salt. In theory 11% sodium sulfate

precipitating from seawater would provide ample Na_2SO_4 to initiate HC and is in fact far more Na_2SO_4 than could be produced by reaction within the GTE according to Hanby [48].

Table 2.3: Major ion composition of seawater [71]. Salts formed by dehydration of salt water will be combinations of the cations and anions depicted in this table. The exact salts formed by precipitation depend on the activities and solubility of all potential salt combinations as the ion concentration changes over time.

Ion		wt %
Chloride	Cl^-	1.9353
Sodium	Na^+	1.0760
Sulfate	SO_4^{2-}	0.2712
Magnesium	Mg^{2+}	0.1294
Calcium	Ca^{2+}	0.0413
Potassium	K^+	0.0387

The idea of $\sim 10\%$ Na_2SO_4 is further promulgated by American Society for Testing and Materials (ASTM) standards. As early as 1961, Philips Petroleum Company was referencing ASTM D655-60 as part of their test protocol for new jet engine fuels. The synthetic seawater Phillips used in accordance with ASTM D655-60 contained 9.75% Na_2SO_4 in the manufactured sea salt [109]. ASTM D1141-98 (adopted in 1998 and re-approved in 2013) is the current standard for the preparation of a “substitute sea water” for lab use. ASTM D1141-98 produces a sea salt consisting of 11.35% Na_2SO_4 [3]. Both standards require dissolving the manufactured sea salt in 10.0 L of water, producing an ionic solution with ion concentrations similar to those in Table 2.3.

A sea water depositing 11% Na_2SO_4 is only possible if it is assumed that only sodium bonds with sulfate ions to produce a salt. All other cations listed in Table 2.3 must bond with chloride to form salts. This assumption is not justified. Usiglio developed a method to determine the order and amounts of salts that will deposit from seawater in experiments dating to 1849 (~ 100 years before HC studies began assuming seawater was nearly 11% sodium sulfate). In his method Usiglio evaporated water collected from the Mediterranean Sea into a dry atmosphere at 40°C . At intervals Usiglio would rapidly cool the water to 21°C to force salt precipitation. Following this procedure, Usiglio was able to measure salts as they precipitated in the reverse order of their

relative solubility in water. His results were reproduced by Clarke in 1924 as shown in Table 2.4. Many have reproduced Usiglio's work since, confirming the Usiglio sequence of salt deposition: first calcium carbonate, then gypsum, gypsum with halite, halite, and finally salts of magnesium and potassium [5]

Table 2.4: Order of precipitation of salts from seawater at 40°C as determined by Usiglio in 1849 [60]. Numerous studies since have replicated and confirmed Usiglio's findings. Sodium sulfate has not been found to precipitate from typical sea water.

Volume (liters)	Fe ₂ O ₃	CaCO ₃	CaSO ₄ ·2H ₂ O	NaCl	MgSO ₄	MgCl ₂	NaBr	KCl
1.00								
0.533	0.0030	0.0642						
0.3146		Trace						
0.245		Trace						
0.190		0.0530	0.5600					
0.1455			0.5620					
0.131			0.1840					
0.112			0.1600					
0.0905			0.0508	3.2614	0.0040	0.0078		
0.064			0.1476	9.6500	0.0130	0.0356		
0.039			0.0700	7.8960	0.0262	0.0434	0.0728	
0.0302			0.0144	2.6240	0.0174	0.0150	0.0358	
0.023				2.2720	0.0254	0.0240	0.0518	
0.0162				1.4040	0.5382	0.0274	0.0620	
Last Bittern				2.5885	1.8545	3.1640	0.3300	0.5339
Total Solids	0.0030	0.1172	1.7488	29.6959	2.4787	3.3172	0.5524	0.5339

Usiglio identified sulfate salts in his salt deposits, but did not include sodium sulfate. Table 2.5 shows a more recent analysis of the salts found in typical sea salt. Based on modern analysis, three sulfate salts can be found among the salts which account for 99.99% of sea salt and Na₂SO₄ is not among them. The final conclusion then, from those who study seawater, is that sodium sulfate will not deposit from a typical seawater. Therefore ingested seawater could not be a source of sodium sulfate to initiate HC.

Table 2.5: Major salts left from evaporated seawater based on modern analysis [71]. Just as in Usiglio’s experiment, sodium sulfate is not listed as a salt that will form from typical seawater.

Salt	wt % of sea salt
NaCl	77.74
MgCl ₂	10.88
MgSO ₄	4.74
CaSO ₄	3.60
K ₂ SO ₄	2.46
CaCO ₃	0.34
MgBr ₂	0.23
	99.99

Ignoring maritime studies dating to 1849, if it was assumed sufficient amounts of Na₂SO₄ were available from seawater, another problem arises. HC is not just a problem in maritime environments. HC is a recognized operational issue in environments far removed from the sea. For Na₂SO₄ to be the only cause of HC it would also have to be found in significant quantities in these other locations.

2.4.1.2.2 Non-Maritime Environments. Table 2.6 shows the most abundant minerals found in sedimentary rocks. The two most common forms of natural Na₂SO₄, mirabilite and thenardite, are not included in this list. Mirabilite and thenardite are not even listed among the top “rarely occurring” sedimentary minerals [62, 110].

Table 2.6: Major minerals found in sedimentary rocks [62, 110]. The only sulfate salt listed as a common mineral is gypsum. Sodium sulfate is not even abundant enough to be listed as a common rare mineral.

Very Common		Common	
Mineral	Composition	Mineral	Composition
Biotite	K, Mg, Al, Fe silicate (mica)	Actinolite	Ca-Mg-Fe-Silicate
Calcite	CaCO ₃	Andalusite	Al ₂ SiO ₅
Chalcedony	SiO ₂	Cassiterite	SnO ₂
Chlorite	Mg, Al, Fe, silicate (mica)	Chromite	FeCr ₂ O ₄
Garnet	Silicate of Ca, Mg, Fe	Corundum	Al ₂ O ₃
Hornblende	Na, Al, Ca, Mg, Fe silicate	Enstatite	MgSiO ₃
Ilmenite	FeTiO ₃	Epidote	HCa ₂ (Al, Fe) ₃ Si ₃ O ₁₃
Kaolinite	H ₄ Al ₂ Si ₂ O ₉	Glaucophane	Na, Al, Fe, Mg, silicate
Leucoxene	Alteration of Ilmenite or titaniferous magnetite	Gypsum	CaSO ₄ ·2H ₂ O
Limonite	Fe ₂ O ₃ ·nH ₂ O	Hypersthene	(Mg, Fe)SiO ₃
Magnetite	Fe ₃ O ₄	Kyanite	Al ₂ SiO ₅
Muscovite	H ₂ (K, Na)Al ₃ (SiO ₄) ₃	Microcline	KAlSi ₃ O ₈
Orthoclase	KAlSi ₃ O ₈	Monazite	CePO ₄
Plagioclase	Feldspar of NaAlSi ₃ O ₈ and CaAl ₂ Si ₂ O ₈	Pargasite	Ca, Mg, Fe, silicate
Pyrite	FeS ₂	Rutile	TiO ₂
Quartz	SiO ₂	Staurolite	Fe, Mg, Al, silicate
Zircon	ZrSiO ₄	Titanite	CaTiSiO ₅
		Topaz	Al ₂ (F, OH) ₂ SiO ₄
		Tourmaline	B, Al, silicate

Given the relatively low abundance of Na₂SO₄ across the globe, it could be expected that ingested Na₂SO₄ as an HC initiator would be limited to the few locations where natural Na₂SO₄ deposits may be found. Table 2.7 shows the primary Na₂SO₄ formations found on Earth. China is the top producer of natural and artificial Na₂SO₄ in the world, but is not included in the table because the amount of natural Na₂SO₄ in China is not currently known. Other countries with significant Na₂SO₄ deposits include Botswana, Egypt, Italy, Mongolia, Romania, and South Africa [57]. HC is not currently an issue at any of these locations. In fact, the major deposit of sodium sulfate in the United States is near the Great Salt Lake. A major US Air Force base is located in the same area, and to date, no known reports of HC have been made for DoD aircraft operating out of Hill Air Force Base.

Table 2.7: Major reserves of natural Na₂SO₄ [57]. HC is not a DoD concern at any of these locations.

Country	Reserves (tons)
United States	860,000
Spain	180,000
Mexico	170,000
Turkey	100,000
Canada	84,000
Other Countries	1,900,000

2.5 Real-World CMAS and HC

Sections 2.3.2 and 2.4.1 presented issues with the assumptions inherent within the current bodies of knowledge for CMAS and HC. This section will re-examine CMAS and HC to explain the two in terms of real-world observations presented in Section 1.1, instead of the assumptions of current literature.

2.5.1 CMAS - *Melting of Real Dusts.*

Arguably, the most important take away from current research into CMAS degradation of aviation GTE components is that the research does not account for the formation of CMAS glass. Instead current research starts with an artificial glass based upon the product found in fielded GTE after damage is already done. The consequence of this choice of starting point for academic study, along with the other issues raised with regard to test methods and the interpretation of the results of these tests brings into question the relevance, to the real-world problem, of more than twenty years of studies.

The difference in issues between western and eastern Saudi Arabia from Section 1.1 provide an example of why the starting point of CMAS is important. Despite both locations having all the ingredients to make CMAS, eastern Saudi Arabia does not have the level of reported issues as western Saudi Arabia. DSC data collected by AFRL provides insight into why sands from eastern Saudi Arabia cause less degradation. Figures 2.14 and 2.15 were collected by University of Dayton Research Institute (UDRI) personnel on a Netzsch 404 F1 heat-flux DSC with a temperature ramp rate of 20°C/min. Heat-flux DSC works by measuring the difference in heat flux into the sample

in question versus a reference (in all DSC runs presented in this document, a blank pan was used as the reference) as both the sample and reference are heated at a constant temperature rate [65]. Any event which causes a change in heat flux can be seen by DSC given sufficient sensitivity in the machine. Several typical DSC events are shown in Table 2.8

Table 2.8: Select events which can cause DSC peaks [114]. The most important changes for this study were fusion, vaporization, decomposition, and heat capacity transition.

	Enthalpic Change	Endothermic	Exothermic
Physical Changes	Crystalline transition	x	x
	Fusion	x	
	Vaporization	x	
	Sublimation	x	
	Adsorption	x	
	Glass transition	Change of baseline, no peaks	
	Liquid crystal transition	x	
	Heat capacity transition	Change of baseline, no peaks	
Chemical Changes	Chemisorption		x
	Desolvation	x	
	Decomposition	x	x
	Oxidative degradation		x
	Oxidation in gas atmosphere		x
	Reduction in gas atmosphere	x	
	Redox reaction	x	x
	Solid-state reaction	x	x
	Combustion		x

When a DSC sample goes through any of these events, the difference in measured heat-flux measured at the sample and at the reference for a give temperature will change. For example, in the case of melting (endothermic process), the sample temperature will not change until melting is complete, whereas the reference pan would rise in temperature given the same heat flux. In order to maintain the two cells at the same temperature ramp rate, the heat flux into the sample cell must be increased. Once the melting process concludes, the additional heat flux to the sample is no longer necessary to maintain the temperature ramp rate, and the sample cell begins to track to the reference cell again [74]. This difference in heat input between the cells results in a positive deviation in the

DSC plot. Conversely, an exothermic process produces its own heat flux so less heat must be added to the sample cell to maintain the temperature ramp rate, resulting in a negative deviation in the DSC plot.

The DSC used to collect data throughout this research effort outputs the difference between the heat capacity of the sample and reference cells based on the initial mass of the sample. Therefore any event, such as off-gassing or oxidation which could change the mass of the sample will affect the calculated heat capacity difference. For example, in off-gassing, some mass is lost. As a result of the assumption of constant sample mass used in the machine's calculations, the output heat capacity is less than the true heat capacity of the remaining sample. As sample mass continues to decrease, the calculated heat capacity continues to decline. As a result the DSC plot shows a shift in the baseline of the curve. Figure 2.13 is an example of a baseline shift due to the decomposition of gypsum beginning at 750°C.

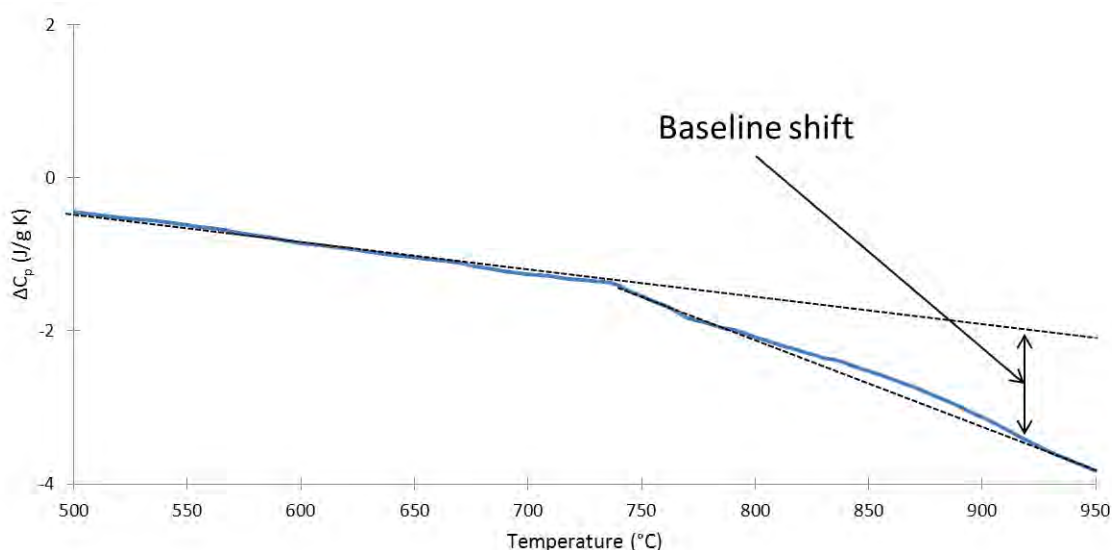


Figure 2.13: DSC curve showing the baseline shift for a gypsum sample due to the mass loss associated with decomposition. While the true heat capacity of gypsum has not changed, the DSC calculates heat capacity in reference to the original sample mass. Therefore calculated heat capacity is reported low.

As the events in Table 2.8 are all kinetic, the rate of scanning in DSC affects the output. Fast scans may make major events stand out as much of the noise from minor events is filtered

out. However, slow scans give more accurate outputs [65]. The trade-off caused by scan speed is especially important in samples, such as those that will be shown in AFRL's DSC runs, which are far from pure. For example, real-world samples may melt in phases instead of in one clean step. The ability to see these individual events occurring in the bulk is important to determining what happens in the system.

The primary peak for each curve shown in Figure 2.14 is the melting point of each respective sand collected around Saudi Arabia. As can be seen, both samples from eastern Saudi Arabia have a higher melting point than sands collected in the western area of the country. The difference in melting points helps explain why, despite having the four primary oxides to form a CMAS glass, sands from eastern Saudi Arabia are causing fewer issues than sands from western Saudi Arabia. In addition, it was explained in Section 1.1.1 that sands from western Saudi Arabia may have a lower melting point due in part to the presence of mica (melting point $\sim 1300^{\circ}\text{C}$) instead of dolomite (melting point exceeding 2300°C). The DSC plots confirm that sands from western Saudi Arabia melt at a lower temperature than eastern sands. However, the fact that the melting temperature is only $75\text{-}100^{\circ}\text{C}$ shows that the interaction between the various constituents has a large role in the melting of the bulk sand sample.

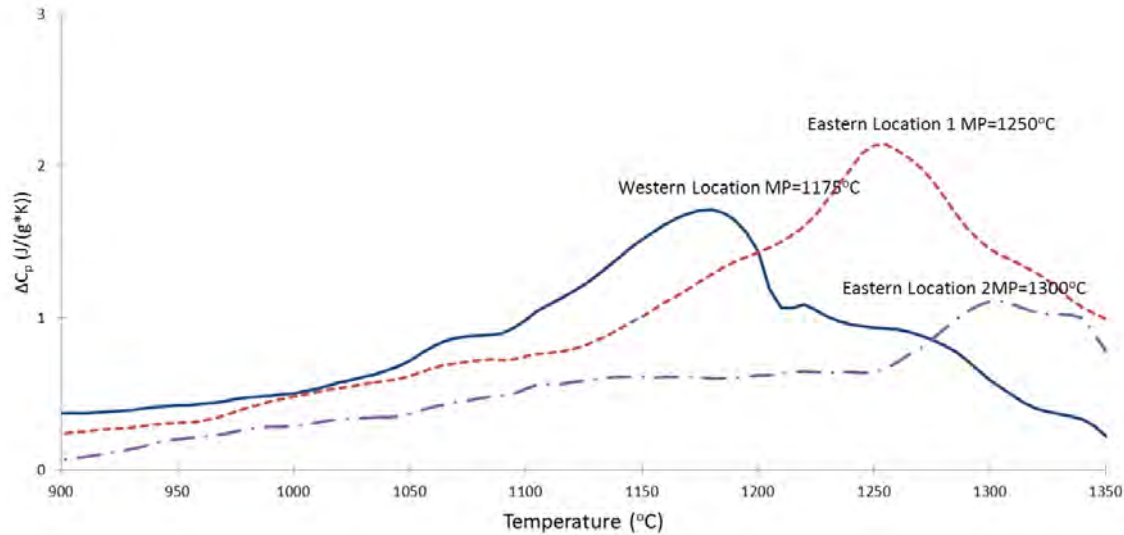


Figure 2.14: DSC curves of select sands collected in Saudi Arabia [83]. The effect of mica in place of dolomite in western sands (as mentioned in Figure 1.3) contributes to the lower melting point (denoted by the peak at 1175°C) of western sands. ΔC_p is the measured difference in heat capacity of the sample and the reference cell within the DSC. Shifts in baseline are due to compositional changes of the sample.

Though the locations are not identical, the AFRL DSC results are consistent with Stotts' study. Stotts shows samples from another location in western Saudi Arabia melting at $\sim 1200^\circ\text{C}$ while samples from Qatar and Bahrain (near eastern Saudi Arabia) melted around $1250\text{--}1275^\circ\text{C}$ [107]. Of particular note is how broad the melting peaks are for the Saudi Arabian samples. Melting of the bulk sample is a function of each individual component's melting point. The width of the peaks indicate melting of a sample with many components. The bulk's melting process begins when the lowest melting point component begins to melt and does not end until the highest melting point component has completely melted. The implication of this piecewise melting process is that an ingested dust may begin to soften, stick to, or even infiltrate GTE components (i.e. become a deposit) long before the bulk dust becomes molten.

DSC data (Figure 2.15) for sands collected at various Army Corps of Engineers sites in Afghanistan indicates why CMAS glass formation is possible across much of Afghanistan. Unlike the Saudi sands, the melting peaks for the Afghan samples are clustered in a tight temperature range at about the same temperature as sands from eastern Saudi Arabia, a known location for CMAS glass formation. Interestingly, the three Afghan samples have the same primary constituents

as eastern Saudi Arabia, yet melt at lower temperatures, suggesting that the exact ratios of the input constituents is important to glass formation. As was mentioned in Section 2.3.2, many have incorrectly used Borom's work to conclude that inputs do not matter in CMAS glass formation as long as the four necessary primary constituents are present. The difference in glass formation between the three Afghan samples and Dharhan sands prove this misinterpretation of Borom's work false.

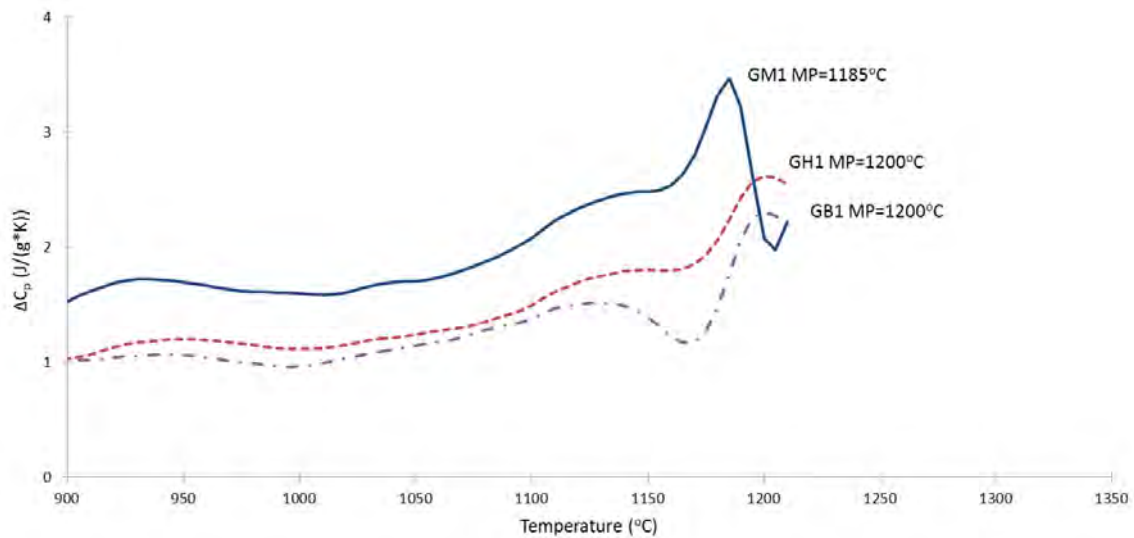


Figure 2.15: DSC curves of select sands collected in Afghanistan [83]. All three sands are known CMAS glass formers in DoD GTE and have similar melting points as sands from western Saudi Arabia. ΔC_p is the measured difference in heat capacity of the sample and the reference cell within the DSC. Shifts in baseline are due to compositional changes of the sample.

2.5.2 HC - An Environmental Initiator.

The discussion in Section 2.4.1 made the case that sodium sulfate cannot be the cause of HC issues the DoD is currently experiencing. It isn't available in sufficient quantities naturally at locations affected by HC. It may form by various chemical reactions, but not in the time allowed in an operational GTE. Finally, the choice of Na_2SO_4 confines the laboratory explanation of HC to temperatures lower than seen in fielded hardware with HC degradation.

Both Tables 2.5 and 2.4 show MgSO_4 to be more abundant than gypsum in seawater. However, analysis of actual evaporate deposits show gypsum to be the most abundant sulfate salt [60]. It is

hypothesized gypsum is more prevalent than MgSO_4 in evaporate deposits because MgSO_4 reacts with CaCO_3 (also an evaporate from seawater) to form dolomite and gypsum. This reaction serves to reduce the amount of MgSO_4 found while increasing gypsum in the deposit. Real world evidence to support this hypothesis is found in the fact that dolomite formations are commonly found under evaporate beds [60]. Therefore, due to this reaction process, MgSO_4 is not likely to be ingested in maritime environments. Only two sulfur containing minerals appear in Table 2.6: pyrite (FeS_2) and gypsum. Pyrite is 55% denser than other common sedimentary minerals [110] known to be ingested by aviation GTE. Therefore, pyrite will not be lofted by wind or ground disturbances as easily, making it unlikely to be ingested by GTE in appreciable quantities. However, gypsum has a density less than half that of pyrite (and 10% less than other common sedimentary minerals) [110], and as was discussed earlier, is found in many of the locations which currently show HC issues.

Instead, the sulfate salt gypsum appears to be a viable candidate as an initiator of HC in aviation GTE. It is the second most abundant salt in evaporate deposits [60]. It is readily found at many locations showing HC attack. It is the fourth most abundant salt to precipitate from sea water [71]. It has also been found in various studies along side molten glass deposits [18, 19, 101, 102] and melts at a similar temperature to natural CMAS glass forming sands. Finally, gypsum could provide not only the sulfate necessary to initiate HC but the calcium needed to form a CMAS deposit.

Smialek was able to show corrosive attack by gypsum at temperatures greater than 1000°C . Previous studies (and many since) had down-played the possibility of gypsum as a cause of HC attack because it shows less significant attack than sodium sulfate in a laboratory environment. However, the relative severity of HC caused by gypsum versus sodium sulfate is irrelevant to the discussion of HC in aviation GTE if, as shown in Section 2.4.1, sodium sulfate could not be a cause of HC in the real-world.

2.5.3 Potential Overlap Between CMAS and HC initiation.

Gypsum occurs naturally alongside calcite, dolomite, and quartz which are readily found in locations which have proven to be good CMAS formers. Therefore, it would not be unreasonable to suspect gypsum to be among the ingested minerals at locations showing CMAS formation on GTE components. In his studies, Smialek noted the presence of calcium sulfate in the glassy deposits

found on the Black Hawk HPT vanes [101, 102]. Stott, was able to find gypsum in dust samples collected near airports where aircraft were reporting glassing issues. In the case of Qatar samples, significant amounts of gypsum were reported [107]. Braue and Mechnic found significant deposits of anhydrite (gypsum stripped of water) beneath CMAS deposits, infiltrating the column gaps of a TC [18, 19]. The Afghan samples in Figure 2.15, where glassing is a current issue, contain gypsum, particularly the Helmand Basin samples which contain significant amounts of gypsum.

The significance of the preceding discussion of gypsum is important. In locations where gypsum is a known component in sand, ingested gypsum could provide calcium to aid the formation of CMAS while simultaneously providing the sulfur necessary to initiate HTHC. Given this possibility, it could be expected to find some instances of HTHC attack alongside CMAS deposits on GTE components. Therefore, it should not be surprising that AFRL investigations on field-returned HPT components have revealed the very phenomenon of simultaneous CMAS and HC degradation.

The implications of the possible overlap between HC and CMAS attacks are significant. CMAS dissolves YSZ which then precipitates as a yttria-depleted solid [43]. Yttrium found in the TC and MCrAlY EBCs readily reacts with sulfur [35]. CaO can readily displace yttria (Y_2O_3) in YSZ. Removal of yttria from YSZ TC destabilizes the TC. Sulfur decreases the adhesions between the TGO and the EBC. Therefore, in locations where gypsum is present, molten deposits could provide multiple attack modes for coating failure and removal. As was introduced in Section 2.2.4, much of the inherent environmental resistance of superalloys has been designed out in favor of mechanical properties. The superalloy still has sufficient aluminum to form a protective Al_2O_3 layer. However, CMAS has been shown to dissolve Al_2O_3 [43]. Therefore a gypsiferous CMAS, having already caused failure of the necessary protective coatings would be able to remove the little self-protection the superalloy could present, allowing direct access of sulfur from gypsum to initiate HC on the superalloy.

2.6 Conclusion

Molten deposits, CMAS glasses and sulfate salts especially, have been recognized as a significant problem for aviation GTEs by all DoD services. Current locations of GTE operation in sandy/dusty regions have greatly increased the likelihood of GTE exposure to the contaminants

necessary to form CMAS glass and initiate HC. The push for higher efficiency and performance has driven an increase in TIT, pushing turbine temperatures into the range favored for CMAS and HC attack. Today, these temperatures are limited to the hot sections of the GTE (the HPT and combustor) but may soon be found in the “cool” sections of the GTE as well.

Therefore, issues caused by CMAS and HC are only expected to grow. Despite decades of research into the two degradation mechanisms, they continue to be significant issues for DoD aviation GTEs. Continued problems with CMAS and HC degradation is undoubtedly due, in some part, to the fact that research of the two phenomena is disconnected from the operational environments they occur in. The two degradation mechanisms are inherently chemical processes, yet the chemistry used to study them does not conform to the chemistry of the real-world problem. It must be stressed that the extent of sulfate attack from molten deposits of ingested desert dusts will depend on the composition of the dust, when and how it melts, and the extent to which the dust sticks to and wets the component surface [7, 13, 98]. Current research methodology, quite simply, does not account for any of these issues.

The current CMAS recipes used for studies prevent any study of possible interactions between the two primary consequences of molten deposit formation. As far as the author can determine, this will be the *first* study to examine HC as a related phenomenon of CMAS formation. Beyond the significant fact that the lab chemistry of previous studies is not representative of the real world, the relevance of this research is directly tied to the questions raised during the discussion of current academic research. In summary, this research effort is relevant as it will answer the question: *what is the real-world process for CMAS and sulfate salt deposition and how does this process feed superalloy degradation due to sulfate attack?*

III. Materials and Facilities

This chapter introduces the materials and facilities which were necessary for this research effort into sulfate attack on nickel-based superalloy GTE components. First, test materials are described including details of processing and sample preparation. Then the experimental apparatus used for this investigation are described. Test procedures for each objective of this research study are described in detail in Chapters 4 (Objective 1), 5 (Objective 2), and 6 (Objectives 3 and 4).

3.1 Materials Studied

3.1.1 *Desert Dusts and Surrogates.*

As discussed in Chapters 1 and 2, the chemistry of the ingested dusts is one factor which determines whether a molten deposit forms on the GTE components leading to CMAS glass formation and/or HC. The following samples represent a small cross section of artificial desert dusts used in academic and military testing. Also included are a natural desert dust not known to cause CMAS or HC degradation, two natural desert dusts from locations with known CMAS and HC issues, and a newly developed artificial dust proposed by a tri-service engine test working group as a future test standard. Tables 3.1 and 3.2 show the weight percentage of minerals found in each mixture.

- **Oxide Mix** A laboratory oxide mixture based on a 2006 study into CMAS interactions with TBCs by Krämer et al [59]. This mixture is representative of those used in many academic studies of CMAS glass on GTE components. Reagent grade CaO and MgO (99.5% <20 μm) were obtained from Fisher Scientific. Silica flour #200 sieved (90% <75 μm) from Cincinnati Abrasive Supply provided the SiO_2 . S.S. White AccuBRADE 50 Blend #3 was used for Al_2O_3 . Accubrade contains >99% pure Al_2O_3 with a particle size <50 μm . The oxides were weighed and mixed in accordance with the composition shown in Table 2.2.
- **Oxide Glass** A crushed glass powder was produced from Oxide Mix in order to compare the DSC curves of Oxide Mix before and after a melt cycle. Oxide Glass test dust represents another method commonly used in CMAS studies: first a homogeneous glass is produced,

then crushed to a fine powder and applied to test samples as a paste. To prepare the glass powder, Oxide Mix was heated to 1350°C for 30 minutes, crushed, and heated again. The final glass was crushed in a ceramic mortar and pestle to a fine powder.

- **PTI Arizona Test Dust A2** A size standard artificial dust (64% of particles <10 μm and 100% <120 μm) manufactured by Powder Technology Inc (PTI) of Burnsville, MN. PTI A2 replaced the Arizona Road Dust which was developed as a General Motors standard for air cleaner testing [90] but eventually became a common standard for general sand ingestion testing, notably for the automotive industry. The composition presented in Table 3.1 was taken from the material safety data sheet (MSDS) available from PTI's website.
- **Aramco** A PTI mixture of 90% PTI A2 and 10% NaCl. The resulting particle distribution is the same as PTI A2. The composition presented in Table 3.1 was taken from the MSDS available from PTI's website.
- **QGCS** A standard artificial sand (90% of particles <50 μm) identified for sand ingestion testing in the Joint Service Specification Guide (JSSG-2007C). The composition presented in Table 3.1 was taken from the MSDS available from PTI's website.
- **AFRL02** One of two commercially available artificial dusts developed by AFRL for sand ingestion testing to mimic the chemistry of CMAS forming natural dusts. AFRL02 and AFRL03 were developed in response to many of the issues raised in Chapter 2 [82]. Opie's work [79] showed that the two artificial test dusts are an acceptable substitute for natural CMAS glass-causing sands, particularly sands found in Afghanistan. Additional testing by AFRL validated both AFRL02 and AFRL03 for use as surrogate test sands which will be the standards used to sand ingestion testing in an upcoming update to JSSG-2007C. AFRL02 has a particle distribution of 90% of particles <40.5 μm . The composition presented in Table 3.1 was obtained from PTI who manufactures AFRL02 and AFRL03.

Table 3.1: Composition of test samples used in Objective 1 crucible testing (along with samples in Table 3.2) to study melt progression of various dust chemistries.

Oxide Mix [59]			PTI A2 [93]		Aramco [91]		QGCS [92]		AFRL02 [82]	
Contributor		wt%	Contributor	wt%	Contributor	wt%	Contributor	wt%	Contributor	wt%
Ca	CaO	29.6	CaO	3.5	CaO	3.15	CaSO ₄ CaCO ₃	26 12	CaSO ₄ ·2H ₂ O	28.75
Mg	MgO	5.8	MgO	1.5	MgO	1.35	—	—	CaMg(CO ₃) ₂	13.33
Al	Al ₂ O ₃	21.2	Al ₂ O ₃	12.5	Al ₂ O ₃	11.25	—	—	Na(Si ₃ Al)O ₈	16.36
Si	SiO ₂	43.3	SiO ₂	72	SiO ₂	64.8	SiO ₂	60	SiO ₂	36.56
Salt	—	—	—	—	NaCl	10	NaCl	2	NaCl	5
Other	—	—	Fe ₂ O ₃	10.5	Fe ₂ O ₃	9.45	—	—	—	—
			Na ₂ O		Na ₂ O					
			K ₂ O		K ₂ O					
			TiO ₂		TiO ₂					

- **Gypsum** Pure gypsum was used to help determine a suitable loading technique for static furnace testing. Gypsum was obtained from Allied Custom Gypsum.
- **Sodium Sulfate** 99% pure sodium sulfate decahydrate (Na₂SO₄·10H₂O) was obtained from Fischer Scientific. The sodium sulfate crystals were milled to a fine powder and used as a comparison to pure gypsum during development of the loading technique.
- **.5CMAS, .3CMAS, and .1CMAS** Based on the recipe used for Oxide Mix, these test dusts were produced specifically for this research effort. The blends were used for all Objective 2 tests and several of the Objective 4 validation tests. For each blend, a certain percentage of CaO was replaced with gypsum to provide the sulfur content necessary to study HC. For example, the calcium content for .3CMAS was 30% gypsum and 70% CaO. The resulting sulfate mass fractions for .5CMAS, .3CMAS, and .1CMAS were 0.194, 0.129, and 0.0478 respectively. The blends were designed to have the same mass fractions of CaO, MgO, Al₂O₃, and SiO₂ as Oxide Mix post firing, assuming complete decomposition of gypsum according to Equations (4.2) and (4.3). The blends will produce the same eutectic glass composition at Krämer's glass. The presence of sulfate and water due to the substitution of gypsum for CaO in the starting blend do not change the eutectic glass formed as eutectic are point compositions (they do not change). The sulfate and water simply change the reactions possible before that eutectic glass forms.

- **GB1** A natural sand collected by the Army Corps of Engineers from the Helmand Province of Afghanistan. CMAS build-up and HTHC damage have been identified in GTEs operating in the area. The sand was sieved to a particle size $<55 \mu\text{m}$. A generic composition for GB1 was provided in Figure 1.2 and is copied to Table 3.1. The specific composition for GB1 will be determined using the procedures described below.
- **Mixed Afghan** A mix consisting of cast offs from AFRL's sieving process for a previous characterization effort which produced $<55 \mu\text{m}$ particle size lots of sands collected at the GB1, GH1, and GM1 sites identified in Figure 1.2.
- **Yuma Proving Grounds** Yuma Proving Grounds (YPG) is a Major Range and Test Facility Base and home to the DoD's desert natural environment testing. CMAS glass formation and HC are not currently known issues at YPG. The collected material was sieved to give an average particle size between 54 and 74 μm . The generic composition for the YPG samples was reported by Opie [79].
- **Mixed Yuma** A sample of the sand collected from YPG which had not been sieved.

Table 3.2: Composition of samples used in crucible testing and static furnace coupon testing. .5, .3, and .1CMAS were used in all Objective 2 testing to develop the sulfur degradation models presented in Chapter 6. GB1 and YPG were used in Objective 4 validation testing.

	.5CMAS		.3CMAS		.1CMAS		GB1 [79]		YPG [79]	
	Contributor	wt%	Contributor	wt%	Contributor	wt%	Contributor	wt%	Contributor	wt%
Ca	CaO	11.3	CaO	17.5	CaO	25.1	CaCO ₃		CaCO ₃	
	CaSO ₄ ·2H ₂ O	34.8	CaSO ₄ ·2H ₂ O	23.0	CaSO ₄ ·2H ₂ O	8.57	CaSO ₄ ·2H ₂ O			
Mg	MgO	4.44	MgO	4.90	MgO	5.47	CaMg(CO ₃) ₂		—	—
Al	Al ₂ O ₃	16.2	Al ₂ O ₃	17.9	Al ₂ O ₃	20.0	unspecified feldspars		NaAlSi ₃ O ₈ KAlSi ₃ O ₈	
Si	SiO ₂	33.2	SiO ₂	36.6	SiO ₂	40.8	SiO ₂		SiO ₂	
Salt	—	—	—	—	—	—	NaCl			

3.1.2 Substrates.

The following substrates were chosen to establish a progression from simple to fielded hardware representative.

- **Electroless nickel (EN)** is an inexpensive nickel alloy which was used to examine the loading methods in Section 5.1.1 and collect initial information on the reactions of gypsum with nickel. Coupons were prepared prior to use by progressive sanding at 120, 180, and 220 grit to remove surface irregularities and remove any surface film which may have been present. EN is reported to have a melting point between 880 and 1455°C depending on the amount of phosphorus present in the material. The melting point of EN decreases with increasing phosphorus up to 11 wt% [80]. EDS measurements of the EN samples used in this study showed no trace of phosphorus.
- **Nickel** Nickel coupons were used for static furnace tests described in Section 5.1.2. 99.5% pure nickel ¼" plate with a melting point of 1455°C was obtained from Alfa Aesar. The plate was sectioned into nominally ½" by 1" coupons using an aluminum oxide abrasive cut-off disk. As provided, the plate had a rough surface, so coupons were sanded with a high-speed orbital sander at 50 and 80 grit before hand sanding in the same manner as described for EN coupons.
- **NiCr-superalloy** A superalloy currently used in some DoD GTE. Dr. Zhu of NASA Glenn donated a polycrystalline block of a currently fielded NiCr-based superalloy to AFRL from which flat coupons, nominally ½" by 1", were cut for use in static furnace testing described in Sections 3.2.1 and 3.2.2. The samples did not have an EBC or TBC coating. The surface of the coupons were prepared in the same manner as the nickel coupons.

3.2 Test Apparatus

3.2.1 UDRI Static Furnace.

Figure 3.1 shows the Thermal Technologies LLC Laboratory Furnace used in this research. The model used has a 4" diameter, 6" tall graphite heating zone. The heating chamber is encased in a water-cooled thick-walled 6061-T6 extruded aluminum shell. This furnace model has a maximum operating temperature of 2500°C. All testing was performed under a N₂-blanketed reducing atmosphere to protect the graphite liner from oxidation at high temperature. This furnace, as currently configured, is only capable of static/batch heating cycles.



Figure 3.1: UDRI furnace used in all crucible and SR testing. The furnace was controlled manually using an optical pyrometer as a guide. All testing was completed in a N_2 atmosphere.

Past experience with this furnace has shown the built-in s-type thermocouple to consistently read low compared to the optical pyrometer described in Section 3.2.3. The low readings are due to the designed placement of the thermocouple in the heating zone. The thermocouple is only used as a guide for initial manual control of the furnace until the pyrometer can be used above $\sim 750^\circ\text{C}$. Actual test measurements are taken using the micro-optical disappearing filament pyrometer described in Section 3.2.3 aimed at a half-inch viewing port on the static furnace in conjunction with the built-in thermocouple to monitor chamber temperature during each run. Figure 3.2 shows thermocouple reading versus pyrometer for all static reducing (SR) test runs. Since the pyrometer can only read temperatures above 750°C , a second conversion curve (dashed line) was constructed based on a simple two-point line fit between the thermocouple reading at room temperature and the thermocouple reading when the pyrometer read 770°C (the lowest pyrometer reading recorded during testing with the UDRI static furnace).

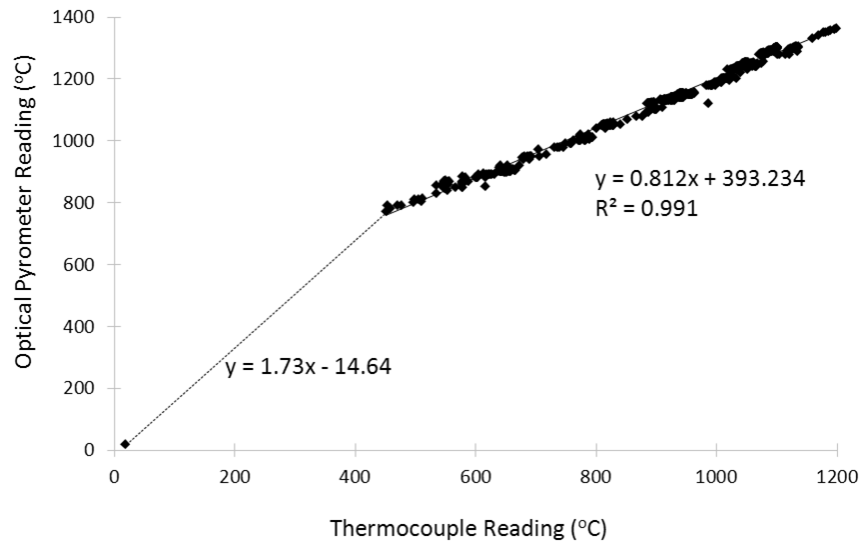


Figure 3.2: UDRI static furnace thermocouple versus pyrometer readings. While the thermocouple readings did not agree with pyrometer readings due to the factory placement of the thermocouple, readings were consistent between the two measurement devices.

3.2.2 AFRL Box Furnace.

Static oxidizing testing was performed in a Thermolyne 46100 High Temperature Furnace maintained by the Ceramic Branch of the AFRL Structural Materials Division (AFRL/RXCC). The furnace was controlled using Super Systems Inc. Realtime Screen Display v1.6.1.3 which can be programmed for automatic furnace control based on preconfigured run recipes. The furnace was last calibrated to 1700°C with a tolerance of $\pm 2^\circ\text{C}$ on Dec 10, 2014.

3.2.3 Major Analysis Equipment.

The following list describes major equipment used to perform sample analysis.

- Scanning electron microscopy (SEM)** Two separate FEI model 600FEG SEMs were used for imaging. The SEMs are maintained by the Materials Characterization Facility of AFRL. Back-scatter electron (BSE) images used for analysis were collected with one of two detectors provided by FEI. Images from testing described in Sections 5.1.1 and 5.1.2 were taken using a concentric detector array. Due to later malfunction of the array, a traditional two diode BSE detector was used to collect images from testing described in Sections 5.2 and 6.3. Elemental analysis was performed via EDS using Edax Inc.'s TEAMTM software.

- **Optical Pyrometer** A micro-optical disappearing filament pyrometer produced by the Pyrometer Instrument Company of Bergenfield, NJ with an 800-3200°C operating range. As can be seen from Figure 3.3, the agreement between the fit between thermocouple and pyrometer readings for all SR testing (solid line) and individual blocks of testing (dashed lines) was consistent through all testing with the UDRI static furnace. Temperature readings across all blocks were within 2.86% of the solid line. In addition, two physical phenomena confirmed pyrometer readings to be within 3.8% of furnace temperature within the range of temperature set-points used within this study: formation of a nickel-carbon eutectic melt (1309°C) as well bending of Orton SSB-3 (1167.8°C set-point) pyrometric cones.
- **DSC** A Netzsch 404 F1 operated by UDRI was used for all DSC runs. The DSC uses a PtRh/Al₂O₃ pan capable of operation to 1700°C [73]. All DSC runs were accomplished by UDRI personnel.
- **XRF** A Niton XL2-980 hand-held x-ray fluorescence (XRF) analyzer was used to confirm the composition of GB1 and YPG test samples listed in Table 3.2. The XRF was factory calibrated and included a chromoly steel (UNS K11572) sample with laboratory certification of composition which was used to reverify the XRF's function. XRF readings of the chromoly sample were within the laboratory certification's listed tolerances. Thermo Scientific NDT v8.4.2 software was used to collect data from the XRF.

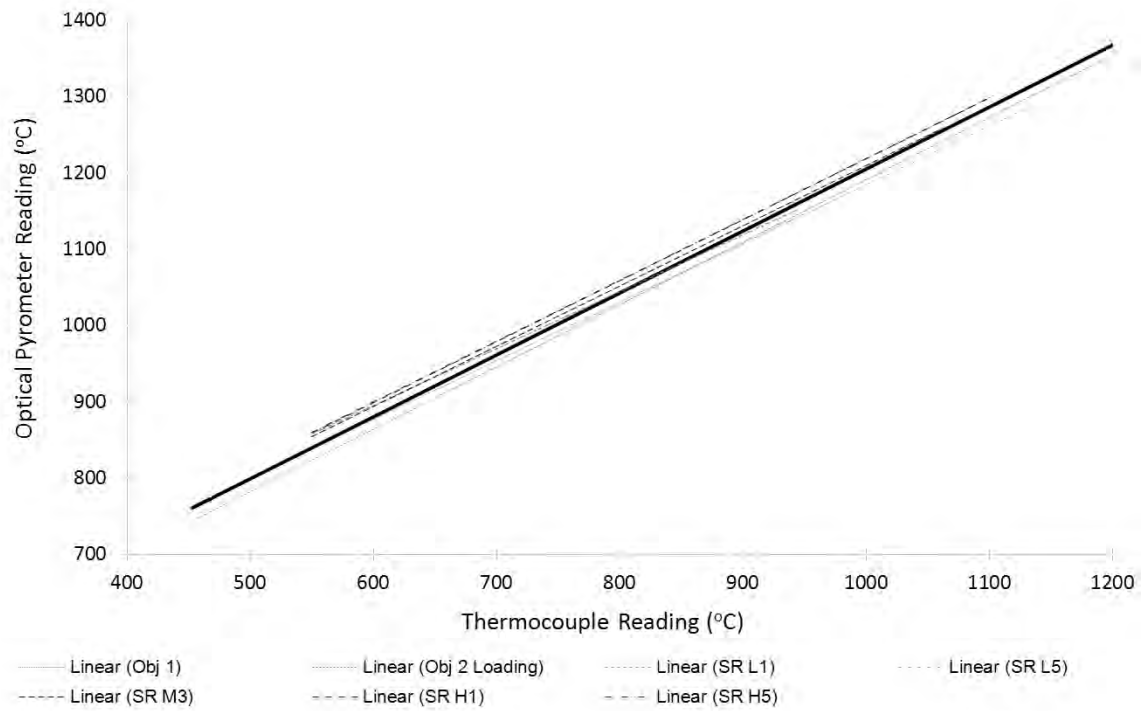


Figure 3.3: UDRI static furnace thermocouple versus pyrometer readings for successive testing blocks. The conversion curve plotted for the entire gamut of SR testing is shown with a solid line. Individual blocks of testing are plotted with various dashed lines as denoted in the legend. All temperature readings were within 2.86% of the solid line.

IV. Characterization of Desert Dust Chemistry

The first objective of this research effort was to characterize the evolution of select desert dusts and surrogates from loose powder to glass as a function of temperature. For this objective, the chemistry of select desert dusts and common artificial surrogates was studied as a function of temperature. Temperature of phase changes, softening, and melting, as well as species present at each stage are important to understanding what may or may not attack the substrates at operational temperatures.

4.1 Crucible Tests of Desert Dusts

Crucible testing of each sample dust identified in Tables 3.1 and 3.2 was accomplished to study the macroscopic changes of each dust with temperature. Mass loss measurements combined with known decomposition reactions for each component in the dusts allowed the determination of changes in dust composition with increasing temperature. In addition, thin-sections of select crucible samples allowed the determination of melt fraction of each sample as a function of temperature.

4.1.1 Methodology.

Media identified in Tables 3.1 and 3.2 were subjected to five minute soaks at peak temperatures ranging from 800-1300°C in the UDRI static furnace. Approximately 0.5 g of each media was measured into 12.5 mm diameter by 16 mm tall LECO® model 767 graphite crucibles. The mass of each sample was taken before and after each temperature run to determine mass loss due to off-gassing. Fresh dust charges were used for each temperature soak. Crucibles were loaded into the large graphite cup, as seen in Figure 4.1, for loading into the furnace. Empty graphite crucibles were added to fill the cup and ensure loaded crucibles did not fall during loading and testing.



Figure 4.1: Loaded crucibles in graphite cup. Two replicates of each dusts were loaded for each test run. Empty crucibles were used to fill gaps between test samples to ensure samples remained upright during testing.

Amperage control settings for a representative run are shown in Figure 4.2. The resulting furnace temperature profile is also included. The furnace was controlled using the built-in thermocouple until it read 550°C. The optical pyrometer was used for control above 550°C. Amperage was decreased starting ~20°C below the desired peak temperature to avoid overshooting the target temperature.

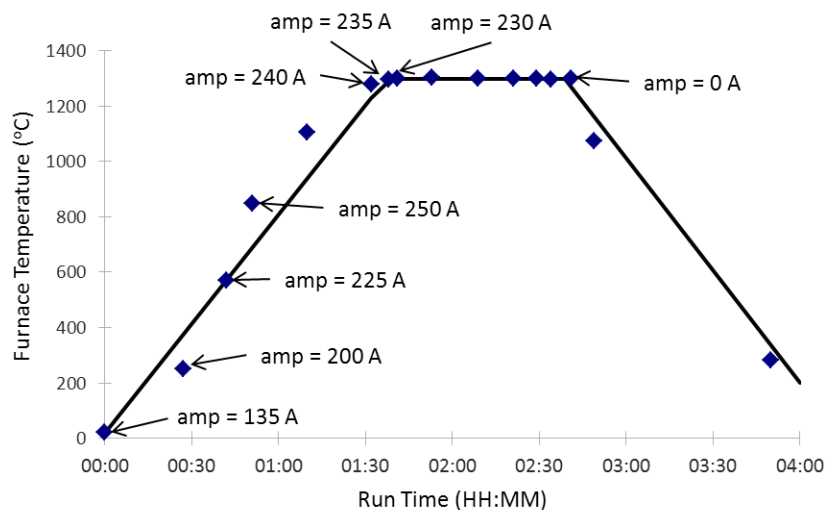


Figure 4.2: Static furnace amperage setting and resulting temperature profile for a typical SR run. Furnace amperage was changed at the same temperature for each run. The first three amperage settings were the same for each run. The next four settings were chose based upon the desired soak temperature.

Once the test chamber had been held at the target temperature for five minutes, the amperage controller was shut off to begin cool down. The furnace was not opened until the thermocouple read $\sim 200^{\circ}\text{C}$. The N_2 flow was maintained for the entire test run until just before opening the chamber to prevent oxidation of the graphite liner.

Once cool, the content of each crucible was stored in a polyethylene cup or bag until the sample could be prepared for analysis. Initially, not all the test media identified in Tables 3.1 and 3.2 were available. As a result, several temperature runs were accomplished in two batches. Due to the short run times of tests, most test days consisted of two or more runs. As noted in Section 4.1.1, once the thermocouple read 200°C on the furnace, the graphite cup was removed from the heating chamber. Samples were removed and samples for the next run loaded while the graphite cup was still warm. It was observed that the AFRL02 samples would expand dramatically when put into the warm graphite cup, likely due to the large amount of volatiles in AFRL02. No other sample displayed this behavior. AFRL02 samples were tapped if they began to expand upon placement into the graphite cup, to ensure the sample was sitting in the bottom of the crucible before loading the graphite cup into the heating chamber.

The following method used for thin-section preparation was adapted from standard methods found in literature [62]. Each pellet identified for sectioning was ground flat on one face with a wet bench grinder and then polished progressively on 30 micron, then 15 micron, and lastly 6 micron diamond lapping plates. The pellets were cleaned in an ultrasonic bath between each polishing step. Once polished, the flat side of the pellet was mounted to a 35 mm glass slide, then the other side of the pellet polished in the same manner until a $30\text{ }\mu\text{m}$ thin slice remained. A Meiji ML9000 transmittance optical microscope with a pair of polarized light filters was used to determine the percentage of glass formation for each sample as a function of heating temperature. Crystalline material allows the transmittance of light when the two polarizing filters are crossed. However, the amorphous structure of glass is optically isotropic and does not allow transmittance on light with the two filters crossed.

4.1.2 Results.

Two distinct physical states were identified in the evolution of test dusts: onset of sticking and onset of fusion. These two physical states were identified in all test dusts except QGCS which never progressed past a loose powder charge within the range of temperatures tested. Onset of sticking was defined as the temperature where a crucible load retained the shape of the crucible when removed from the crucible. At this point, individual particles had joined to make a single mass. Binding of the bulk sample may have occurred either by a sintering process or by melting. Sintering is a densification process which proceeds by neck formation between grains due to transfer of atoms within the grains to the grain boundary. The neck region grows in order to lower free energy by decreasing solid/vapor interfaces (i.e. reducing pores). Sintering can occur in the solid-state, whereby no portion of the bulk ever melts, or by a liquid-phase process. In liquid-phase sintering either an external liquid is added or the sintering process is accomplished at a temperature where some component in the bulk material can melt. In either case, the purpose of the liquid is to assist the transport of atoms to the necking region, thereby accelerating the rate of densification. Regardless of the mechanism, large scale melting of the entire sample had not yet begun as evidenced by the sharp edges and individual particles which can be seen in the samples at this state.

If the onset of sticking for a given dust is due to either constituent melting or liquid-phase sintering, then a liquid will be present in the sample. The presence of a liquid has an operational significance as this represents the temperature at which liquid-assisted adhesion could begin, resulting in some subset of an ingested dust sticking to GTE components. Once a single constituent can stick to GTE components, it can act as a glue to trap other dust constituents. This process leads to the initiation of a deposit within the GTE. Figure 4.3 shows an example of this physical state for the dusts studied.



Figure 4.3: Example of the physical appearance of a crucible charge at its onset of sticking (GB1 at 850°C). The onset of sticking represented the lowest temperature, in this study, at which a dust sample remained as a monolithic pellet upon removal from the crucible. This also indicates the lowest temperature at which a sand may begin to form a deposit within a GTE.

The onset of fusion was defined as the point where melting of the entire sample, not just individual constituents, had begun. At the onset of fusion, individual particles were no longer visible on the surface of samples, and the sample pellets no longer had sharp edges. The rounding of edges shown in Figure 4.4 is due to the influence of surface tension suggesting this state is due to bulk melting, not a sintering mechanism. The onset of fusion for each sample also has an operational significance. At this temperature, depending on the viscosity of the melt, a deposit based on a given dust can begin to infiltrate porous structures (such as TBCs) or wick into structural voids (such as cooling holes). In addition, the current understanding of HC (based on sodium sulfate) requires a molten deposit for HC degradation to occur. Therefore, according to the current literature, regardless of sulfate concentration, none of the dusts examined in this study should be able to cause HC until this onset of fusion. Figure 4.4 shows an example of this physical state for the dusts studied.



Figure 4.4: Example of the physical appearance of a crucible charge at its onset of fusion (GB1 at 1150°C). The onset of fusion represents the lowest temperature, in this study, at which a dust sample became molten during temperature soak. This also indicates the lowest temperature at which a sand may begin to infiltrate porous GTE structures.

As discussed in Section 2.3.2, a key issue with the manner in which current studies of molten deposits have been developed, is that the studies focus on the final melt only, ignoring the process (and implications) by which the melt forms. Table 4.1 shows the temperatures identified for onset of sticking and onset of fusion for each dust studied. Each of these dusts contain all four oxides required to form a CMAS glass, and if they had been heated sufficiently, they would have formed similar glasses, as Borom's studies had concluded. However, Table 4.1 shows that the process for how each dust will achieve a final glass melt is different, as denoted by the different temperatures each dust changes physical state. The operational significance of the two physical states shown in Table 4.1 shows that the process by which each dust forms a final glass must be considered as this process defines at what temperature, and in what manner, a given dust will cause degradation. As such, each individual dust's unique melting process defines how studies should properly be accomplished.

Table 4.1: Temperatures for onset of sticking and onset of fusion as determined by crucible temperature soaks for the identified test dusts. Onset of sticking represents the lowest temperature a given dust may begin to form a deposit within a GTE. Current HC studies rely on molten deposits so onset of fusion is the lowest temperature a given dust could potentially cause HC. Samples have been grouped to match the discussion presented in the following paragraphs.

Test Dust	Onset of Sticking (°C)	Onset of Fusion (°C)
PTI A2	850	1200
Aramco	800	1150
YPG	850	1150
Mixed Yuma	900	1150
GB1	850	1150
Mixed Afghan	1100	1150
AFRL02	800	1200
Oxide Mix	1100	1250

Both PTI A2 and Aramco began as light tan loose powders. Aramco’s onset of sticking and onset of fusion were both 50°C lower than found in PTI A2. Both samples contain K₂O which melts at 700°C. Aramco also contains NaCl which melts at 801°C. Therefore at the onset of sticking for both test dusts, a molten constituent was present, so ingestion of either sample could lead to deposit formation within the GTE. K₂O was only a few percentage points within both samples, but the addition of 10% NaCl gave Aramco a large fraction of low-temperature melting agents in which was responsible for the difference in temperature for onset of sticking between the two samples. PTI A2 gradually became darker brown with increasing temperature. Beginning at 1000°C, Aramco gradually took on a rust red tint with increasing temperature until its onset of fusing at 1150°C where its color became dark brown.

YPG and Mixed Yuma began as loose tan powders and gradually transitioned to dark brown pellets by 1200°C. A gold mottling on the surface of pellets of both samples became increasingly evident at 1250 and 1300°C. Both GB1 and Mixed Afghan began as light tan loose powders and gradually transitioned to dark gray pellets by 1300°C. Onset of fusion was the same in both pairs of samples, however for both pairs, the “pure” sample had a lower onset of onset of sticking than its mixed partner. For GB1, onset of sticking was 250°C lower than the mixed sample, for YPG, it was

50°C lower. The YPG and Mixed Yuma samples contain no constituents which could have been molten by the onset of sticking for the two samples. Therefore the sticking process for the Yuma sands must have been a solid-state sintering process. Therefore neither Yuma sample is expected to cause deposit initiation if ingested unless the GTE exceeds the temperature reported for their onset of fusion. In contrast, both GB1 and Mixed Afghan contain NaCl which will be molten at each onset of sticking. Therefore, both Afghan samples could lead to deposits within GTE if ingested at their respective onset of sticking temperatures. The larger particle size of the mixed samples should require more energy before individual particles can soften to begin the sticking process. The same theory holds true for the large scale melting denoted by the onset of fusion, therefore while both samples in each pair had the outward appearance of the onset of fusion at the same temperature, it was expected that the mixed samples would present a lower melt fraction when sectioned. The results which will be shown in Table 4.4 confirmed this expectation for the Afghan samples but not the Yuma samples. This finding suggests particle size distribution and chemistry provide distinct contributions to the melting process of a dust.

Oxide Mix and AFRL02 both dusts began as white loose powders. Oxide Mix remained white until its onset of fusion at 1250°C at which point it became dark gray. AFRL02 remained white until its onset of fusion at 1200°C where it became light tan. AFRL02 became gray at 1250°C and dark gray at 1300°C. Despite the additional volatiles in AFRL02 which should have aided its melting process, AFRL02 began to fuse only 50°C before Oxide Mix. However the results which will be shown in Table 4.4 confirmed that the volatiles in AFRL02 caused the melt fraction of AFRL02 to be substantially higher than that of Oxide Mix at each temperature set-point. Oxide Mix does not contain any constituent which could be molten at its onset of sticking, therefore it will not initiate a deposit at this temperature. AFRL02 contains NaCl which will melt and therefore AFRL02 could cause a deposit at its onset of sticking.

4.1.3 Discussion.

4.1.3.1 Glass Formation.

In order to determine the effect of the five minute soak versus the total heating time, two additional temperature runs were performed with GB1, Oxide Mix, and AFRL02. The first test

run (TP#1) was designed to determine if soak time affected glass formation. The second test run (TP#2) was designed to see if ramp rate and heating time affected mass loss. TP#2 will be discussed in Section 4.1.3.2. As shown in Figure 4.5, for TP#1, the three dusts were soaked at 1000°C for ~55 minutes instead of the typical five minute soak. The longer soak time caused the length of the run to be the same as a typical run at 1250°C. Table 4.2 shows GB1, Oxide Mix, and AFRL02 after the typical 1000°C and 1250°C runs, as well as after TP#1. The resulting pellets show that additional soak time, and total heating time, are not as critical as the actual peak soak temperature for glass formation.

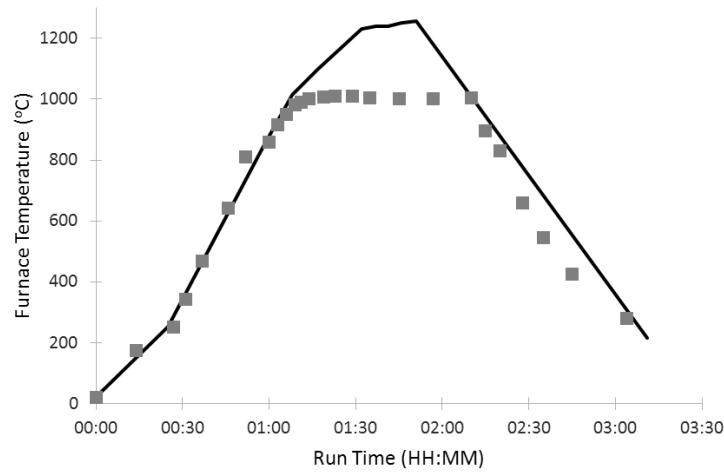











Figure 4.5: Static Furnace temperature profile for TP#1 (points) versus a typical 1250°C run (solid line). TP#1 was given a longer peak-temperature soak to see whether length of soak time affected melt progression.

Table 4.2: Sample appearance after heating under TP#1 versus 1000 and 1250°C. The final appearance of TP#1 test samples confirmed that peak temperature is more important than length of peak-temperature soak with regard to melt progression.

	1000°C	TP#1	1250°C
Oxide Mix			
GB1			
AFRL02			

Based on the physical appearance of samples after heating, it was not necessary to make thin-sections of all samples. Only samples which had begun to fuse were thin-sectioned. Images were captured of each thin-section at three different randomly selected locations. An example of a transmitted light and polarized light image for a single thin-section is shown in Figure 4.6.

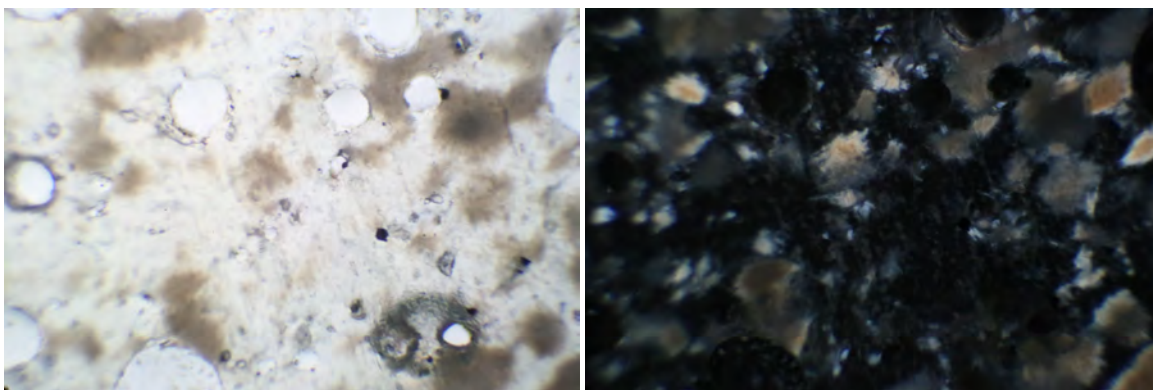


Figure 4.6: Unpolarized (left) and cross-polarized (right) transmitted light images of thin section GB1 pellet after 1200°C run. Glass has an amorphous structure so polarized light will not pass through it, resulting in glass appearing black in the right image. Cross-polarization reduces the total intensity of light passing through the entire thin-section so even non-glass regions will appear darker.

Each image was then edited using the GNU Image Manipulation Program (GIMP) v2.8.10 to isolate just the glass section of each thin-section. The image editing was necessary to allow for analysis of percent glass present in each sample. First all “black” areas of the polarized light image were selected using the “Select by Color” tool with a 5% color threshold. This tool selects pixels based upon their unique composite RGB-values within a defined threshold. The selected area was then collapsed into a single value of black and pasted into a new image with a pure white background. Figure 4.7 shows an example output of the image manipulation process. In this image, black represents glass and white represents all other phases present in the thin-section.

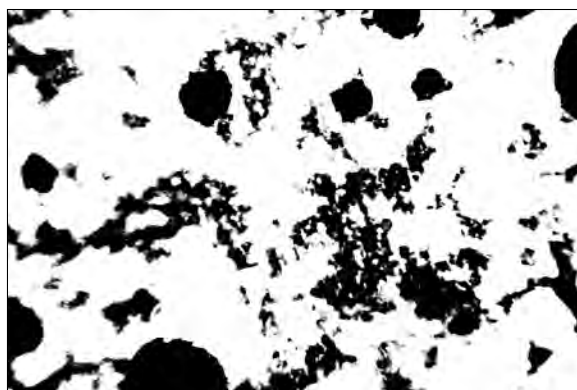


Figure 4.7: Initial processed image showing glass regions of thin-sectioned GB1 pellet from a 1200°C run. The image is of the same thin-section shown in Figure 4.6. In this image, black represents glass and white represents all other phases present in the thin-section.

Several thin-sections included voids left from bubbles formed from gases which escaped during heating. Also some images were taken near sample edges. In both cases the underlying glass slide showed through the subject thin-section and in cross-polarization appeared black. Therefore it was necessary to subtract these features so as not to skew glass measurement. Bubbles and sample edges were identified in the transmitted light images and selected using the “Select by Color” tool with a 5% color threshold. The selected area was then collapsed to a single value of gray and pasted into the previously edited glass images. Figure 4.8 shows an example of a final image used to calculate glass percentage in each thin-section. In this image, black represents only the glass which is part of the sample, gray represents the glass slide under the sample, which was not used in final calculations.

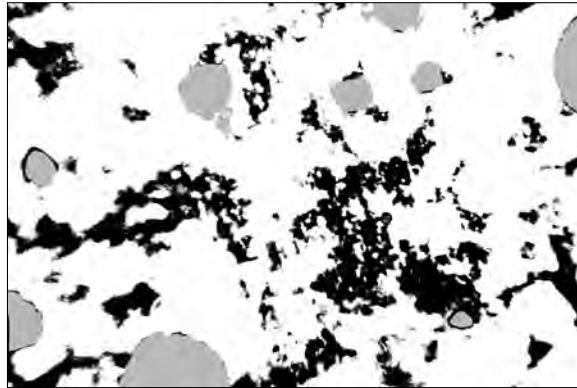


Figure 4.8: Final image showing glass regions of thin-sectioned GB1 pellet from a 1200°C run. The image is of the same thin-section shown in Figures 4.6 and 4.7. In this image, black represents only the glass which is part of the sample, gray represents the glass slide under the sample, which was not used in final calculations.

A histogram tool built into GIMP was used to determine the percent glass present in each image by determining the number of black pixels present versus the sum of white and black pixels. The percent of glass present in each sample is shown in Table 4.3.

Table 4.3: Percent of glass phase present in each thin-section as determined by GIMP. Images were taken at three random locations in each thin-section and processed as shown in Figures 4.7 and 4.8

	1150°C	1200°C	1250°C	1300°C
Oxide Mix	Not Sectioned	Not Sectioned	1.53 ± 1.57	21.3 ± 14.3
PTI A2	1.25 ± 0.927	2.94 ± 0.851	10.9 ± 3.39	22.2 ± 17.7
Aramco	1.99 ± 2.49	6.23 ± 6.46	1.18 ± 0.866	42.2 ± 6.05
QGCS	Not Sectioned	Not Sectioned	Not Sectioned	Not Sectioned
Mixed Yuma	Not Sectioned	16.2 ± 16.1	55.2 ± 14.5	71.0 ± 7.07
YPG	8.77 ± 3.24	7.76 ± 0.0377	41.6 ± 18.9	29.1 ± 14.4
Mixed Afghan	4.72 ± 4.33	2.56 ± 3.37	68.9 ± 23.1	71.3 ± 30.5
GB1	0.526 ± 0.103	15.8 ± 7.66	80.6 ± 9.82	89.3 ± 15.2
AFRL02	Not Sectioned	0.0718 ± 0.124	0.567 ± 0.666	96.4 ± 2.19

	1200°C	1250°C	1280°C	1320°C
.1CMAS	Not Sectioned	12.3 ± 7.77	24.2 ± 24.6	24.4 ± 15.8
.5CMAS	Not Sectioned	21.9 ± 20.9	12.6 ± 8.94	16.5 ± 13.7

However, when compared to the DSC curves presented in Section 4.2, the values shown in Table 4.3 did not correlate with the melting behavior depicted by the change in specific heat of each material. Review of thin-section images revealed the presence of mullite formations in several images for .1CMAS, .5CMAS, AFRL02, GB1, and the Oxide Mix. Mullite has been shown to form from kaolinite clay ($\text{Al}_2\text{Si}_2\text{O}_5(\text{OH})_4$) as low as 1100°C [23], but the presence of MgO can lower initiation to 1000°C [76]. Since .1CMAS, .5CMAS, AFRL02, GB1, and the Oxide Mix all contain MgO, and the raw ingredients for kaolinite, mullite formations from the samples heated above 1200°C in this study are a reasonable outcome. The formation of mullite ($\text{Al}_6\text{Si}_2\text{O}_{13}$) from Al_2O_3 and SiO_2 starting material available in the samples listed above proves the presence of a liquid phase transport mechanism suggesting glass fraction alone does not account for the full degree of sample melting.

Mullite has a crystalline structure so it will not block transmitted light under polarization. As a result the use of glass fraction caused the measure of melting progression to be low. Therefore it was necessary to reanalyze thin-sections showing the presence of mullite. Secondary mullite crystal formations were identified individually in thin-section images and manually painted black in GIMP. Secondary mullite is easy to identify in samples because its high aspect ratio (long, skinny

crystals) stands out from other crystal structures found in the samples. Primary mullite crystals could not be accounted for as their low aspect ratio (platelet crystals) was not distinguishable from other structures in the thin-sections. Figure 4.9 shows an example of an edited thin-section image before and after accounting for mullite formations. Based upon the inclusion of mullite formations, the melt fraction of each sample is shown in Table 4.4. The updated values in Table 4.4 track better with the melting behavior suggested by DSC runs. However, the updated values are still low because they do not account for primary mullite.



Figure 4.9: Measurement of glass fraction alone (middle image) proved to be insufficient to quantify melting behavior. Therefore, recrystallized phases were considered also. The image on the right includes mullite crystals to account for melt fraction. Images are of .5CMAS soaked at 1320°C (non-polarized image on left).

Table 4.4: Percent of melted phase present in each thin-section as determined by GIMP. Values which changed from Table 4.3 due to inclusion of secondary mullite are highlighted.

	1150°C	1200°C	1250°C	1300°C
Oxide Mix	Not Sectioned	Not Sectioned	5.60± 2.60	27.8± 19.4
PTI A2	1.25 ± 0.927	2.94 ± 0.851	10.9 ± 3.39	22.2 ± 17.7
Aramco	1.99 ± 2.49	6.23 ± 6.46	1.18 ± 0.866	42.2 ± 6.05
QGCS	Not Sectioned	Not Sectioned	Not Sectioned	Not Sectioned
Mixed Yuma	Not Sectioned	16.2 ± 16.1	55.2 ± 14.5	71.0 ± 7.07
YPG	8.77 ± 3.24	7.76 ± 0.0377	41.6 ± 18.9	29.1 ± 14.4
Mixed Afghan	4.72 ± 4.33	4.12± 4.01	68.9± 23.1	72.5± 28.5
GB1	0.526 ± 0.103	15.8 ± 7.66	80.6 ± 9.82	89.3 ± 15.2
AFRL02	Not Sectioned	5.12± 5.12	32.0± 6.69	96.4± 2.19

	1200°C	1250°C	1280°C	1320°C
.1CMAS	Not Sectioned	16.8 ± 6.75	32.5 ± 23.5	37.4 ± 9.93
.5CMAS	Not Sectioned	24.5 ± 22.3	19.4 ± 8.59	30.9 ± 12.7

4.1.3.2 Mass Loss.

As shown in Figure 4.10, for TP#2, GB1, Oxide Mix, and AFRL02 were soaked at 1000°C for the typical five minute soak. However, the initial heating rate was half of what was used for all other crucible test runs. The lower ramp rate caused the length of the run to be the same as a typical run at 1250°C.

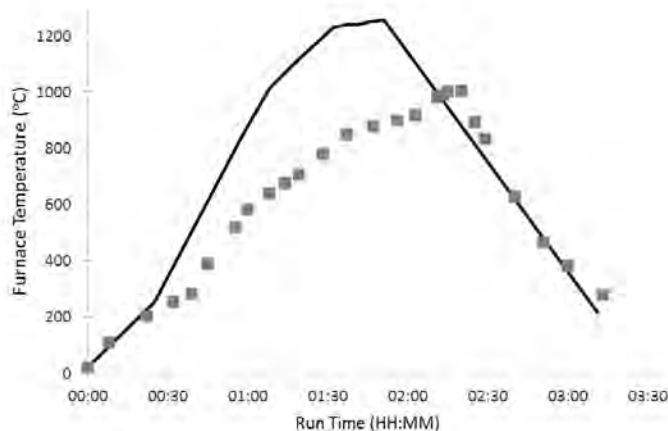


Figure 4.10: Static Furnace temperature profile for TP#2 (points) versus 1250°C run (solid line). The initial heating rate was lowered in TP#2 to provide the same total heating time as a typical 1250°C run. TP#2 was designed to determine if a slower heating rate would allow more volatiles to escape from the test samples.

Table 4.5 shows the mass loss for GB1, Oxide Mix, and AFRL02 after the typical 1000°C and 1250°C runs, as well as after TP#1. If the ramp rate used for typical runs was too high, it would be possible for volatiles to become trapped in the sample resulting in a lower reported mass loss. The results show that TP#2, with a slower ramp rate, as well as a longer total heating time, did not have any additional loss in mass. Therefore, the ramp rate used for the typical crucible tests was slow enough to not trap volatiles in the samples.

Table 4.5: Fraction mass loss of sample after heating under TP#2 versus 1000 and 1250°C. No difference in mass loss was noted between the three test runs, signifying that the typical heating rate used in crucible testing was sufficiently slow to prevent trapping of volatiles in test samples.

	1000°C		TP#2		1250°C	
	Sample 1	Sample 2	Sample 1	Sample 2	Sample 1	Sample 2
Oxide Mix	0.00	0.02	0.02	0.02	0.00	0.00
GB1	0.13	0.12	0.12	0.12	0.14	0.12
AFRL02	0.31	0.30	0.31	0.31	0.31	0.32

Figure 4.11 shows the mass loss versus temperature for the surrogate desert dusts tested as part of this research effort. Figure 4.12 shows the mass loss versus temperature for natural desert dusts. Considerable variance in measurement was found at several set-points. Given that many of the mass losses are due to chemical reactions, this fact is not surprising. Dashed lines have been added for each sample dust to help illustrate general trends in mass loss of each sample. End-points for the dashed lines are based on both measured mass at each temperature and the timing of the applicable chemical reactions described in the following paragraphs. The chemical reactions described in the following paragraphs represent the primary decomposition reactions expected in each test sample. Reactions with may simply rearrange the chemistry of the sample without a mass loss (for example the formation of mullite which was described in Section 4.1.3.1) are not included.

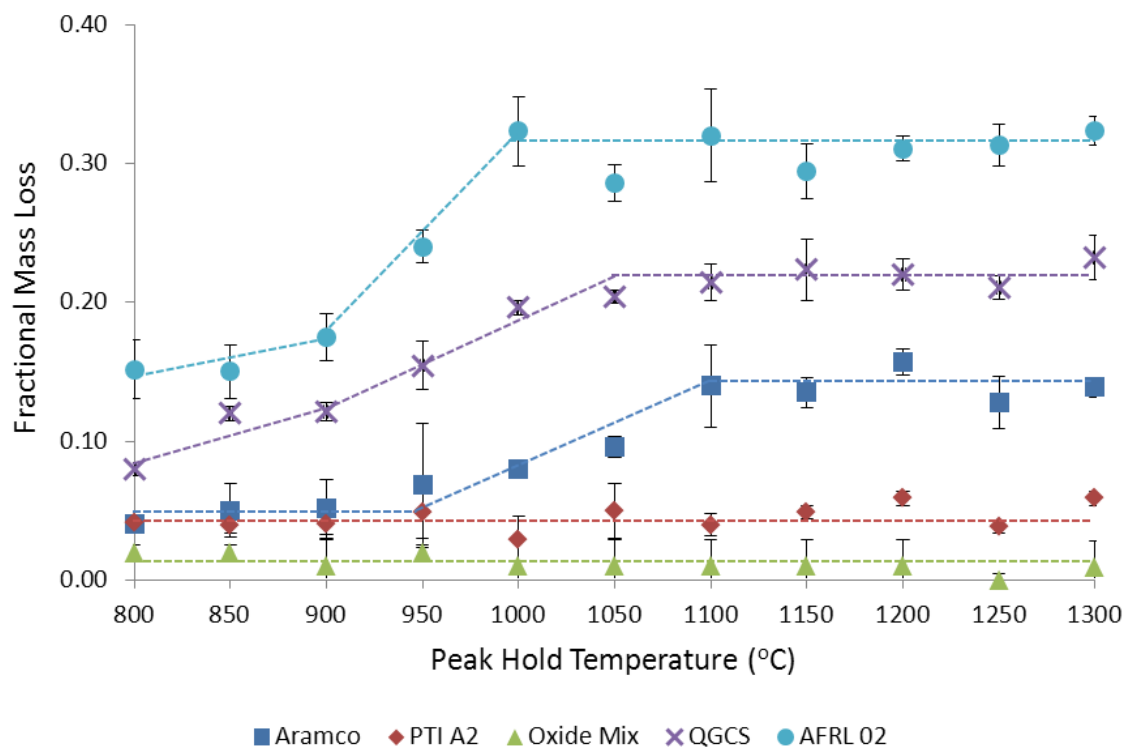


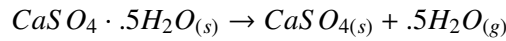
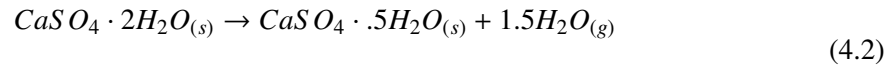
Figure 4.11: Average mass loss versus peak temperature in crucible testing (artificial dusts). The error bars denote the range of measured values about the average and include the measurement uncertainty for the scale used (0.005g). All the test dusts examined have the ability to absorb water from the atmosphere during storage at room temperature. Dehydration of these samples will occur starting near 200°C. Therefore all samples were expected to show mass loss even at the lowest crucible test run temperature (800°C). Data-points represent the average mass loss measured at each set-point, error bars denote the total range of measurement. Due to significant variance in measurement at some set-points, dashed lines representing the general trends in mass loss based on compositional changes in each sample have been included. The dashed lines do not imply any statistical significance.

4.1.3.2.1 Artificial Dusts. The primary loss of mass expected for the Oxide Mix or PTI A2 is from water absorbed by CaO during storage. The dehydration of both samples should be complete by ~200°C resulting in the unchanging mass loss shown over the temperature range depicted in Figure 4.11. PTI A2 will also experience mass loss due to the decomposition of K₂O beginning at approximately 350°C, accounting for some of the additional mass loss found in PTI A2 versus Oxide Mix. The only difference between PTI A2 and Aramco is the addition of 10% NaCl in Aramco. Like CaO, NaCl will absorb some water during storage which will also be lost by ~200°C. In addition, the mass loss for Aramco between 950°C and 1100°C can be attributed to the decomposition of

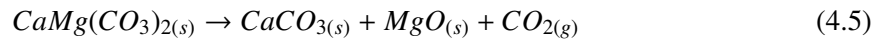
NaCl according to the following reaction.



QGCS will experience the same dehydration and decomposition of NaCl as Aramco. It will also lose mass from the dehydration of gypsum according to Equation (4.2) at ~200°C followed by decomposition of the dehydrated gypsum according to Equation (4.3). Figure 4.14 shows that decomposition of gypsum begins at 750°C. At 930°C the calcite in QGCS will decompose according to Equation (4.4). Resulting in the slightly steep mass loss noted in Figure 4.11 at 900°C. The decomposition of NaCl, gypsum, and calcite in QGCS accounts for QGCS's mass loss from 800 to 1100°C.



AFRL02 will also lose mass due to dehydration and decomposition of NaCl and gypsum. In addition, dolomite will decompose at 750°C into MgO and calcite according to Equation (4.5) followed by decomposition of calcite at 930°C. Figure 4.11 shows that despite experiencing the same decomposition reactions, plus the addition of the dolomite decomposition, AFRL02's mass loss occurs in a smaller temperature band (850 to 1000°C) than QGCS. The difference is likely due to the substantially smaller average particle size of AFRL02 versus QGCS.



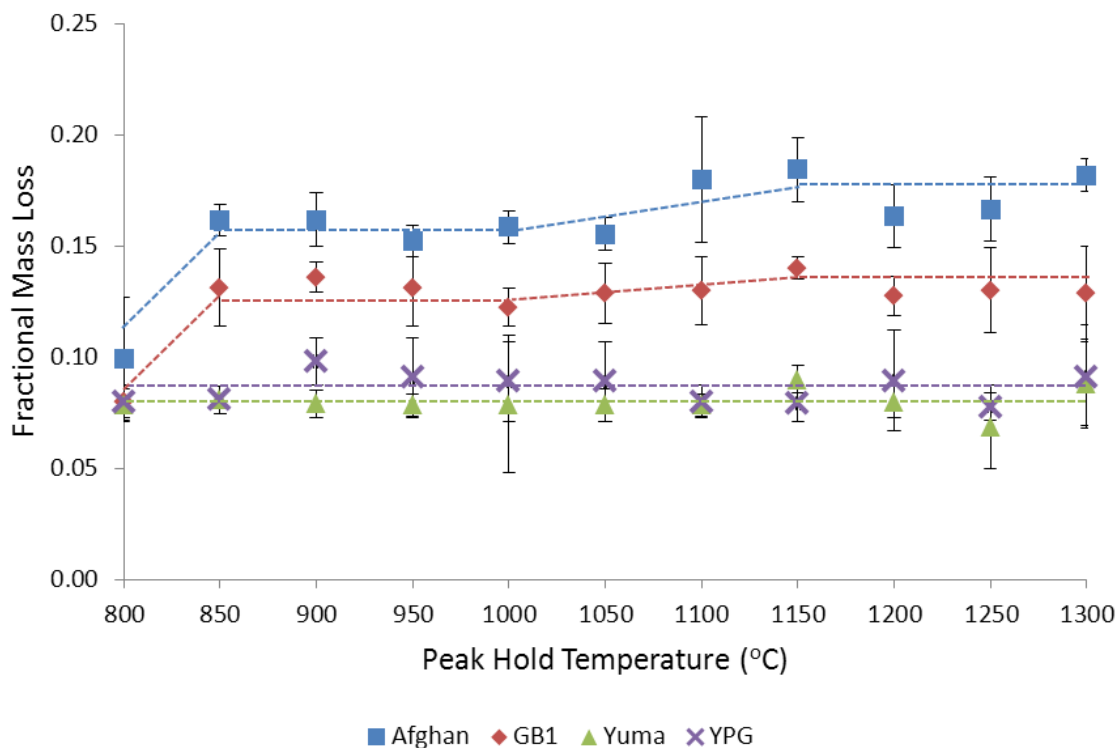


Figure 4.12: Average mass loss versus peak temperature in crucible testing (natural dusts). The error bars denote the range of measured values about the average and include the measurement uncertainty for the scale used (0.005g). All the test dusts examined have the ability to absorb water from the atmosphere during storage at room temperature. Dehydration of these samples will occur starting near 200°C. Therefore all samples were expected to show mass loss even at the lowest crucible test run temperature (800°C). Data-points represent the average mass loss measured at each set-point, error bars denote the total range of measurement. Due to significant variance in measurement at some set-points, dashed lines representing the general trends in mass loss based on compositional changes in each sample have been included. The dashed lines do not imply any statistical significance.

4.1.3.2.2 Natural Dusts. The Yuma samples were reported to contain calcite [79]. However, the relatively unchanged loss of mass shown in Figure 4.12 suggests calcite to be a minor component. The majority of mass loss for the two Yuma samples appears to be due to dehydration.

The loss of mass in the Mixed Afghan and GB1 samples can be attributed to the same dehydration and decomposition reactions identified for AFRL02. However, the timing of the mass losses in natural GB1 and Mixed Afghan is different. Whereas AFRL02 showed significant change in mass from 850 to 1000°C, the two Afghan samples showed a pronounced mass loss between 1000 and 1150°C. The difference in amount and timing of mass loss in the Afghan samples versus

AFRL02 also suggests AFRL02 has a higher concentration of volatiles (most likely gypsum and NaCl) since AFRL02's mass loss has been shifted to lower temperatures compared to the two Afghan samples.

4.2 DSC of Desert Dusts

Furnace testing can show whether or not a sample melted by the peak temperature achieved during the test run. However, without multiple runs, furnace testing cannot show how, at what temperature range, or how long it took the sample to melt. For example, if a dust melted at 800°C, tests run at 1000 or 1200°C would show the same result: a melted sample. Nor can furnace testing directly show any other changes a sample may have undergone during heating other than a final volume or mass change. In contrast, DSC can show melting and other thermal events or phase changes, as listed in Table 2.8, as they evolve. As was discussed in Section 2.5.1, DSC of a known sample mass will show not only the events which cause changes in heat capacity compared to the reference, but also changes which cause mass changes in the sample.

Due to the complex chemistry of most of the dusts used in this study, there may be multiple independent stages of melting, off-gassing, and compositional changes of individual phases within the bulk which contribute to overall properties of the melt. While furnace testing was useful to show discrete sample changes with increasing temperature, DSC can provide insights into how the sample got to those discrete points.

DSC measurement of the samples listed in Table 4.6 was performed at a heating rate of 20°C/min. A DSC run with a gypsum-salt blend was made. However, a run with a sodium sulfate-salt blend was not attempted because the $\text{Na}_2\text{SO}_4 + 5\% \text{NaCl}$ mixture exhibited deliquescent behavior. The sodium sulfate-salt blend was extremely water-phillic, and absorbed sufficient atmospheric moisture that it became a slurry at room temperature as shown in Figure 4.13.

Table 4.6: Samples subjected to DSC testing. The modified materials were included as a means of analyzing how melt response changes with the addition of additional variables.

Single-source Material	Modified Material
Gypsum	Gypsum + 5% NaCl
Sodium Sulfate	
GB1	Oxide Mix with gypsum instead of CaO
YPG	Oxide Mix + 5% NaCl
AFRL02	Oxide Mix with gypsum instead of CaO + 5% NaCl
PTI A2	Aramco
Oxide Mix	Oxide Glass (fired Oxide Mix)

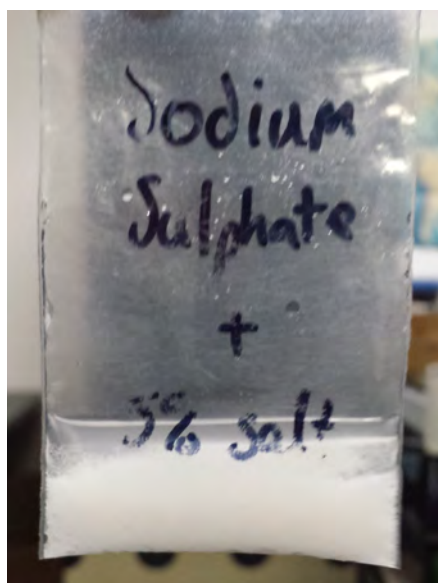


Figure 4.13: Result of a Na_2SO_4 /salt mixture deliquescing. The sample was not stable long enough to perform a DSC run.

4.2.1 Results - Single-Source Dusts.

Figure 4.14 shows the DSC curve obtained for the pure gypsum sample. The dehydration of gypsum shown in Equation (4.2) is a two step process. First gypsum ($\text{CaSO}_4 \cdot 2\text{H}_2\text{O}$) is transformed to basinite ($\text{CaSO}_4 \cdot .5\text{H}_2\text{O}$) then anhydrite (CaSO_4). Two peaks are seen in Figure 4.14 at 200°C representing these two dehydration steps. As was mentioned in Section 4.2, the output curve in DSC is due to change in heat capacity and/or mass of the sample. At $\sim 750^\circ\text{C}$ the

DSC curve for gypsum begins to decrease due to the decomposition of CaSO_4 , according to Equation (4.3), which releases SO_3 . Coincidentally, current literature cites HC beginning at approximately 750°C [35, 55, 58, 89, 94, 98]. HC at lower temperatures was not an objective of this research, but presents an interesting topic for future work. The sharp peak at 1225°C is the melting point of the gypsum sample.

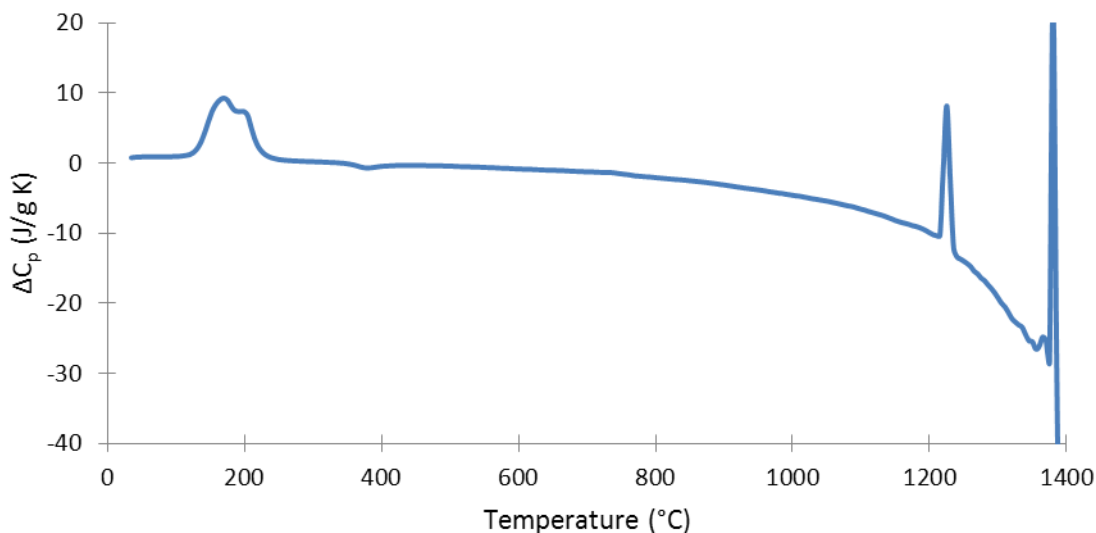


Figure 4.14: DSC plot for gypsum. A change in baseline is evident at $\sim 750^\circ\text{C}$ signifying the beginning of decomposition for gypsum. The current understanding of HC, based on lab study and field reports, indicates HC begins at $\sim 750^\circ\text{C}$. ΔC_p is the measured difference in heat capacity of the sample and the reference cell within the DSC. Shifts in baseline are due to compositional changes of the sample.

Figure 4.15 shows the DSC curve for sodium sulfate. The sodium sulfate sample used was the naturally occurring decahydrate form of the salt. Figure 4.15 shows a peak at 895°C representing the melting point of the sample. The melting point determined by DSC is in good agreement with the reported melting point of sodium sulfate of 884°C . Similar to the gypsum sample, the sodium sulfate DSC curve shows the decomposition of sodium sulfate according to Equation (4.6) starting well below the sample's melting point. Figure 4.15 shows the decomposition of sodium sulfate beginning at $\sim 290^\circ\text{C}$. As shown by Equation (4.6), sodium sulfate decomposes into three gaseous species. The boiling point of sodium is slightly lower (883°C) than the melting point of sodium sulfate. Therefore, as the molten sodium sulfate decomposes, sodium will vaporize into the gas

stream resulting in no residue. The lack of stability of sodium sulfate at higher temperatures explains why sodium sulfate-induced HC is minimal above 1000°C: there will be nothing left to cause attack.

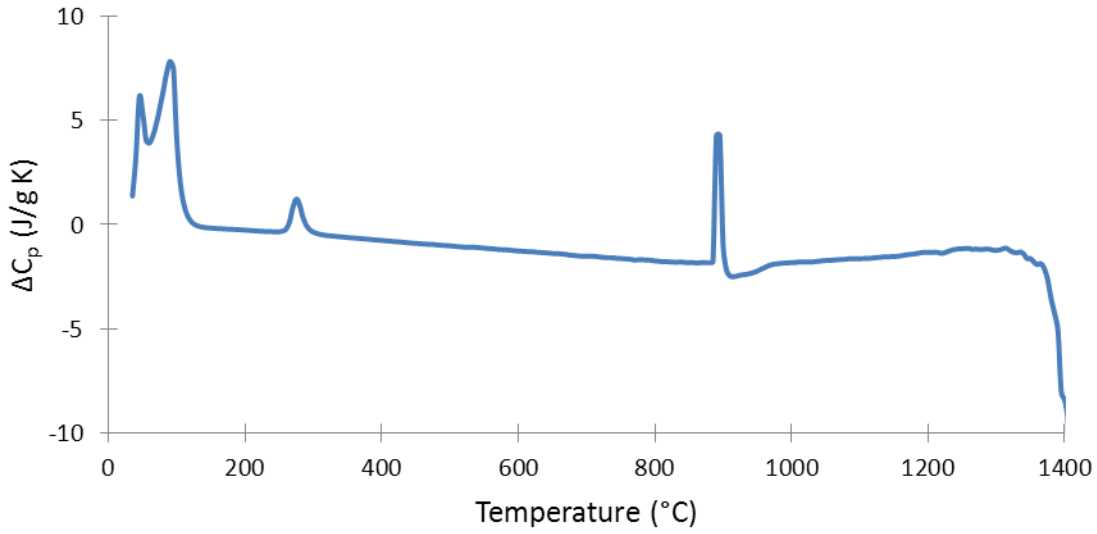
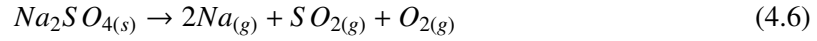


Figure 4.15: DSC plot for sodium sulfate showing that sodium sulfate melts at ~880°C. All the products of the decomposition of sodium sulfate vaporize at lower temperatures than this. Therefore, in an open atmosphere, there would be nothing present to cause attack at temperatures exceeding 1000°C. This helps explain why current lab study finds minimal degradation due to sodium sulfate-induced HC above 1000°C. ΔC_p is the measured difference in heat capacity of the sample and the reference cell within the DSC. Shifts in baseline are due to compositional changes of the sample.

Figure 4.16 shows the DSC curve obtained for Oxide Mix. Despite being a multicomponent mixture, Oxide Mix shows the simplest melting behavior of the dusts tested due to the fact that it is only comprised of stable oxides. The initial peak at 445°C is due to the loss of water absorbed from the atmosphere by CaO during storage. No other features are seen in Figure 4.16 until the extremely sharp melting peak at 1330°C.

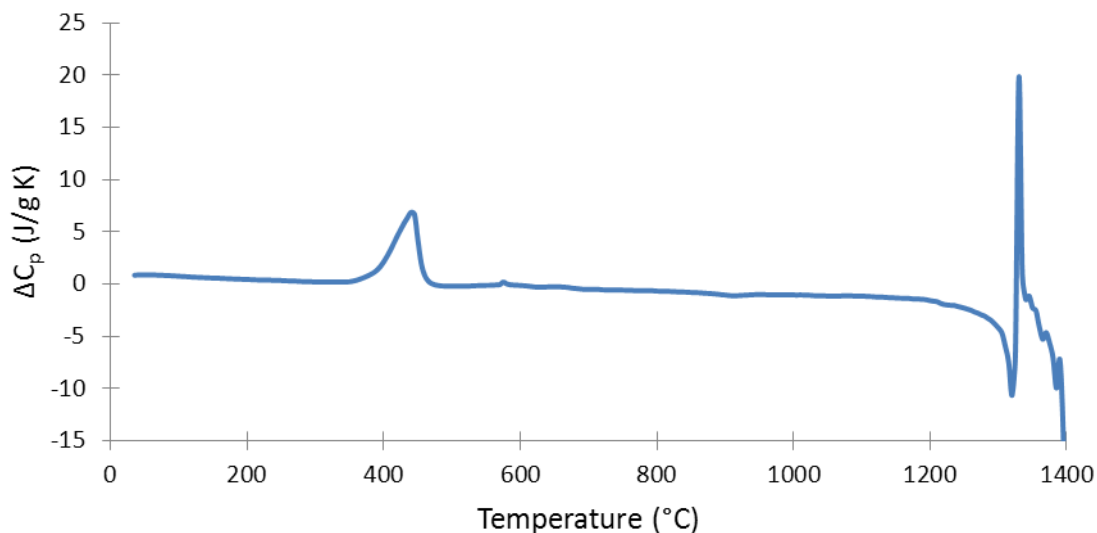


Figure 4.16: DSC plot for Oxide Mix. The melting peak at 1330°C is sharp due to the simplicity of the four constituents of Oxide Mix. ΔC_p is the measured difference in heat capacity of the sample and the reference cell within the DSC. Shifts in baseline are due to compositional changes of the sample.

Figure 4.17 shows the DSC curve for the PTI A2 sample. Like Oxide Mix, PTI A2 contains nothing but stable oxides. However, the large number of species in the PTI A2 sample causes a wide melting peak similar to GB1 or YPG. The peak near 700°C is due to the melting of K_2O in the sample. Figure 4.18 shows the DSC curve for the YPG sample. As with GB1, YPG shows a wide melting peak with its apex at 1190°C and onset of softening at 910°C.

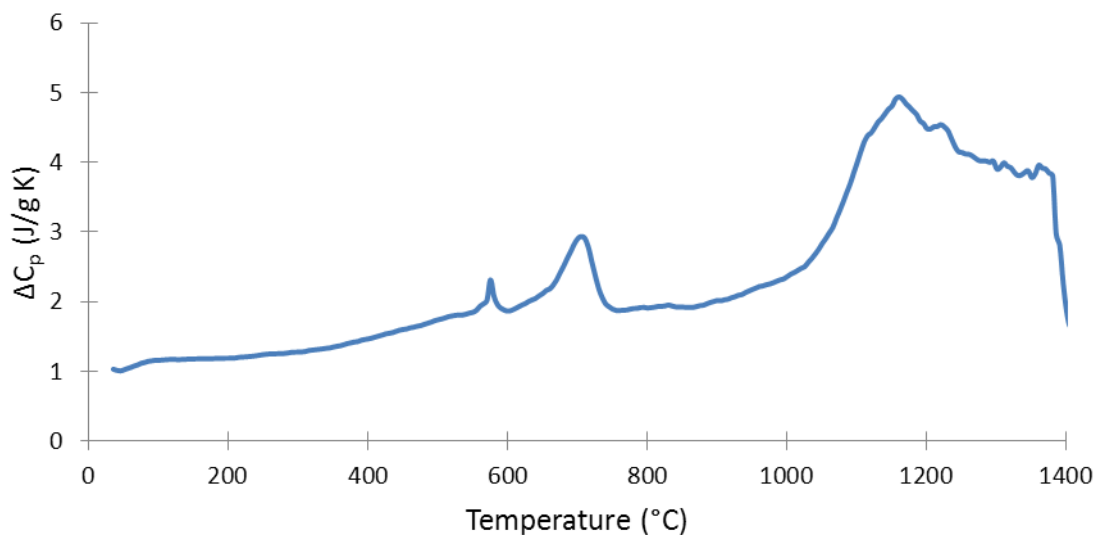


Figure 4.17: DSC plot for PTI A2. In contrast to the plot for Oxide Mix (Figure 4.16), PTI A2 shows a wide melting peak due to the large number of constituents in the sample. ΔC_p is the measured difference in heat capacity of the sample and the reference cell within the DSC. Shifts in baseline are due to compositional changes of the sample.

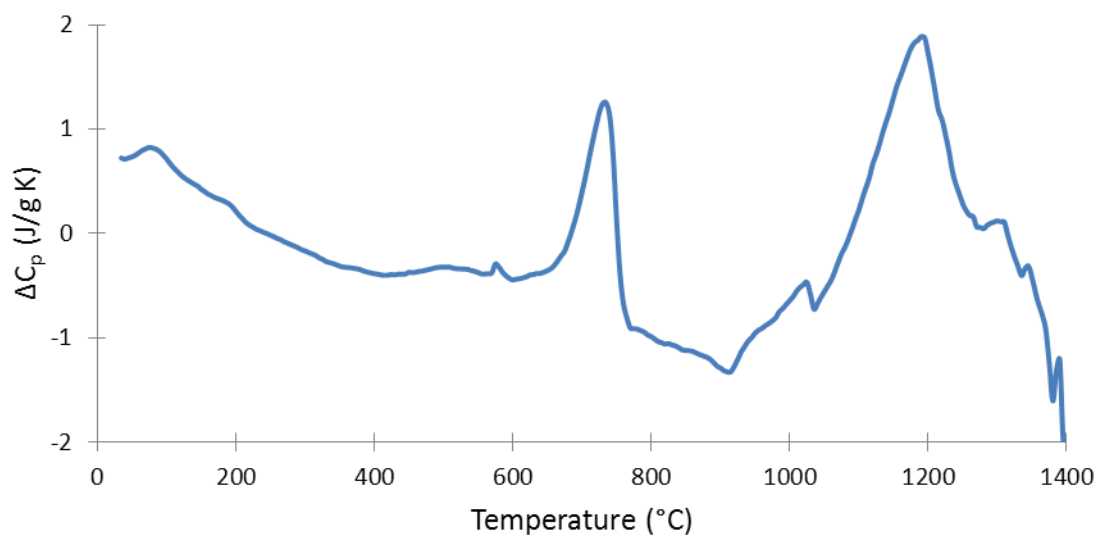


Figure 4.18: DSC plot for YPG. Unlike PTI A2, YPG's melting peak is wide due to the complexity of its constituents as opposed to the sheer number of them. ΔC_p is the measured difference in heat capacity of the sample and the reference cell within the DSC. Shifts in baseline are due to compositional changes of the sample.

Figure 4.19 shows the DSC curves for AFRL02 and GB1. The first peak at 765°C occurs with the decomposition of dolomite in accordance with Equation (4.5). Figures 4.14 and 4.15 showed the narrow melting peak associated with a simple compound. In comparison GB1 and AFRL02 are complex mixtures of compounds and therefore their DSC curves show wide melting peaks. The primary melting peak has its apex at 1200°C, however various compounds in the GB1 mixture begin to melt as low as 960°C. The onset of melting of individual components in the bulk sample is the softening point of the sample and is represented on the DSC curve as the point where the curve begins to climb to the melting peak.

AFRL02 was designed to mimic the bulk chemical behavior of GB1. In GB1 each component can be distributed in a wide range of particle sizes. The spread of particle sizes in GB1 causes peaks associated with various components to overlap each other since smaller particles will melt at slightly lower temperatures than large particles of the same component. In AFRL02 each component is present in a tight range of particles sizes, causing less spread in melting behavior for each individual component resulting in the melting peak for AFRL02 presenting as multiple distinct peaks.

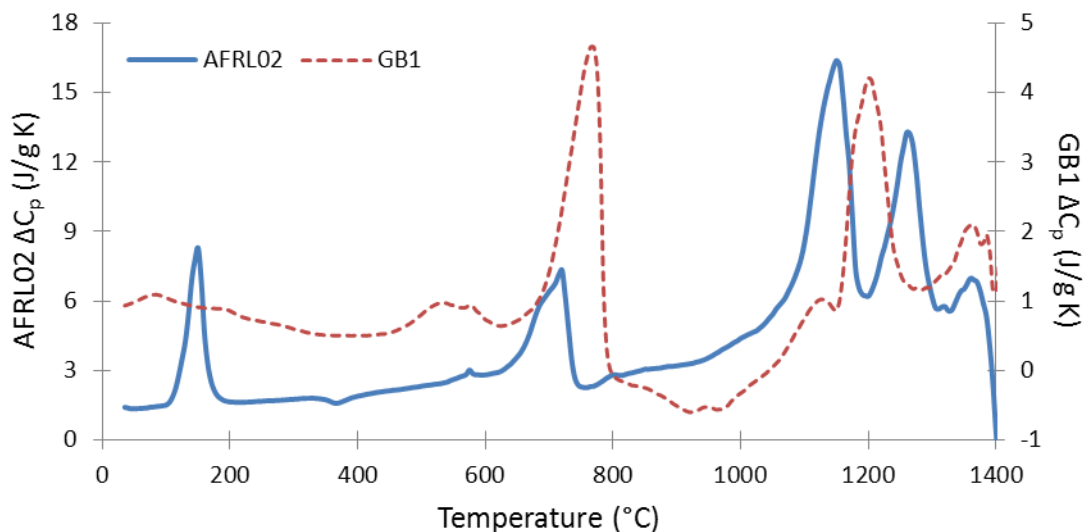


Figure 4.19: DSC plot for AFRL02 and GB1. AFRL02 was designed to mimic the final melt behavior of GB1. Though the end behavior of each sample is similar, a comparison of AFRL02's DSC to GB1's shows the route the two dusts take is different. ΔC_p is the measured difference in heat capacity of the sample and the reference cell within the DSC. Shifts in baseline are due to compositional changes of the sample.

4.2.2 Results - Modified Dusts.

Figures 4.16 - 4.19 helped explain the difference in DSC response due to the increasing complexity (from number or chemistry of components) of the sample. This section will show how modification of the sample by either heat treatment or addition of a fluxing agent (gypsum and/or NaCl) affects DSC response.

Figures 4.20 and 4.21 show the effect of prior melting of a sample on its DSC response. As discussed in Section 3.1.1, Oxide Mix was twice heated to 1350°C then crushed to produce Oxide Glass. Oxide Glass was produced to depict the effect of prior melting for two reasons. First, multiple iterations of melting and crushing to produce a homogeneous glass is common practice in CMAS studies. Second, the components used to produce Oxide Mix are already stable oxides, so no change in chemistry (which would also change DSC response) is expected due to melting. The lack of peaks for the fired sample in Figure 4.20 shows that Oxide Glass had not absorbed water after firing. Water is a key lubricating species in a dust mix which will lower the viscosity of the melt enabling the melt to infiltrate a porous substrate quicker. Therefore it is expected that a dry homogeneous glass powder produced in a similar manner would have different infiltration characteristics than the unfired powder of the same chemistry, which will skew test results.

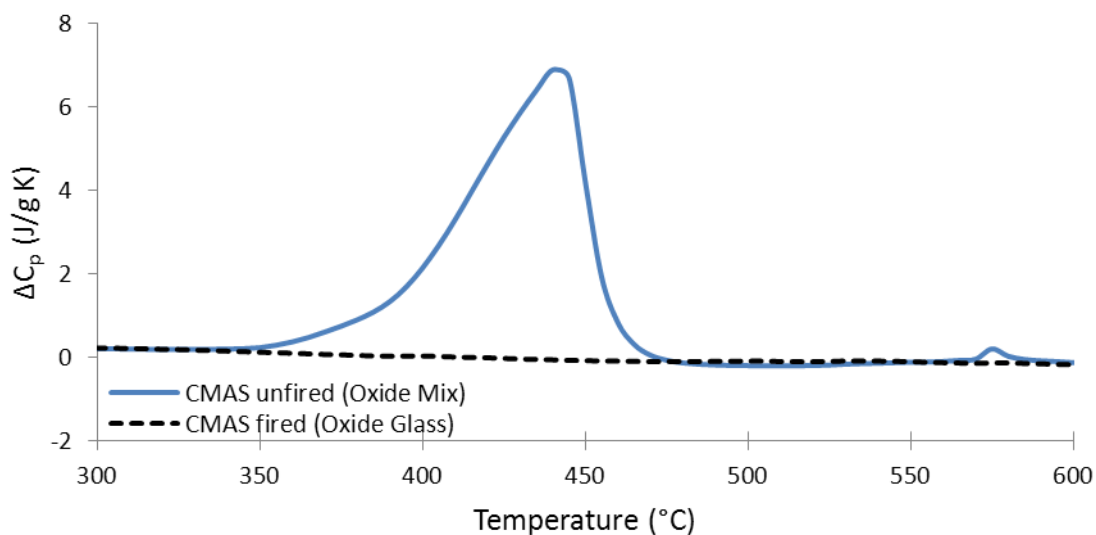


Figure 4.20: DSC plot comparing fired versus unfired CMAS mixtures from 300-600°C. Both MgO and CaO will absorb water from the atmosphere. The peaks for Oxide Mix are the dehydration of the sample. Oxide Glass did not absorb water, so lacks these peaks. ΔC_p is the measured difference in heat capacity of the sample and the reference cell within the DSC. Shifts in baseline are due to compositional changes of the sample.

Figure 4.21 shows an 80°C drop in melting temperature (1330°C versus 1250°C for unfired and fired respectively) due to prior melting of the sample. Oxide Glass melts at a lower temperature than Oxide Mix despite no change in chemistry because Oxide Glass has already been a glass. The particles of the crushed Oxide Glass are still tiny glass particles so the energy needed to fuse the sample into a bulk glass is lowered. The Oxide Glass sample was not milled to a consistent particle size before the DSC was taken. The larger spread in particle size as compared to the Oxide Mix caused the melting peak to be wider.

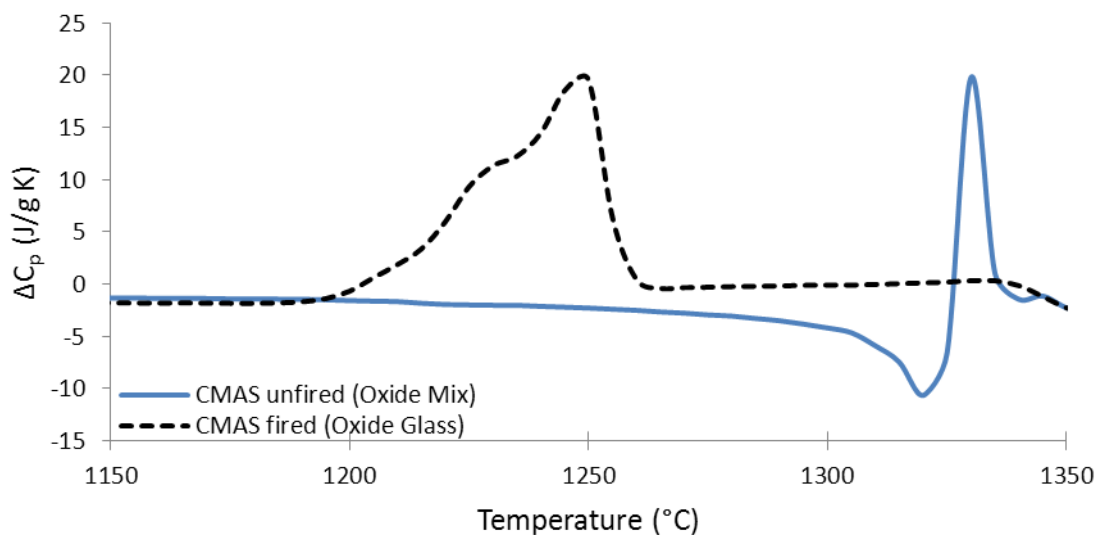


Figure 4.21: DSC plot comparing fired versus unfired CMAS mixtures from 1150-1350°C. Despite the exact same chemistry, the fired mixture melts 80°C lower due to the fact that it has already been a glass so less energy is required to fuse it into a glass pellet again. ΔC_p is the measured difference in heat capacity of the sample and the reference cell within the DSC. Shifts in baseline are due to compositional changes of the sample.

Figures 4.22 and 4.23 show the effect of adding gypsum as a single fluxing agent to Oxide Mix. For these figures, the four samples compared (in order of decreasing gypsum content) are pure gypsum, .5CMAS, .1CMAS, and Oxide Mix. Figure 4.22 depicts the temperature range over which the four samples dehydrate. The peaks on the left side of the figure represent change in heat capacity of the samples due to the dehydration of gypsum. The peaks become less pronounced with decreasing gypsum. The rightmost peaks are associated with the dehydration of CaO. As expected, these peaks become more pronounced with decreasing gypsum (and therefore increasing CaO).

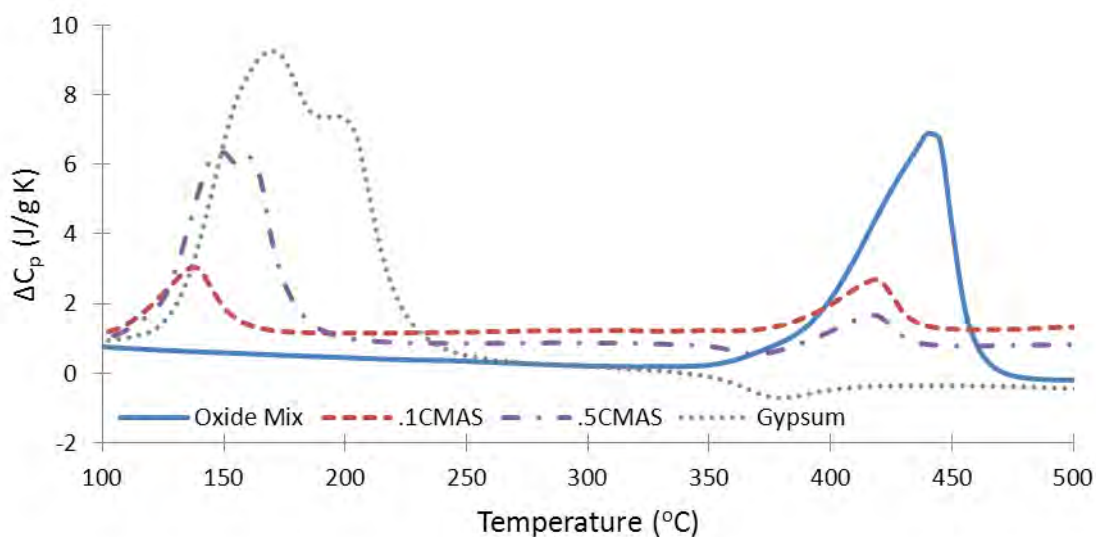


Figure 4.22: Change in CMAS DSC behavior due to increasing gypsum content from 100-500°C. Gypsum holds onto the water it absorbs less strongly than CaO. Therefore, increasing gypsum content in the sample, at the expense of CaO, shifts the primary dehydration peak to lower temperatures. ΔC_p is the measured difference in heat capacity of the sample and the reference cell within the DSC. Shifts in baseline are due to compositional changes of the sample.

Figure 4.23 shows the change in melting behavior of Oxide Mix as gypsum is substituted for CaO. The DSC curves show that Oxide Mix (0% sulfate) melts at 1330°C, .1CMAS (4.78% sulfate) melts at 1315°C, .5CMAS (19.4% sulfate) melts at 1295°C, and gypsum (55.8% sulfate) melts at 1225°C. The results show that gypsum works as a melting point depressant within a CMAS blend.

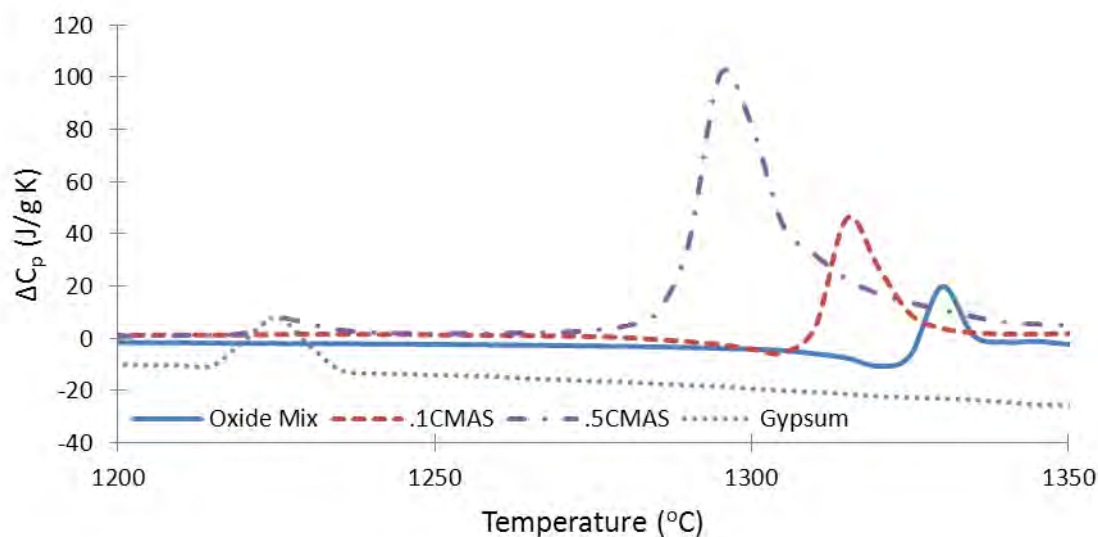


Figure 4.23: Change in CMAS DSC behavior due to increasing gypsum content from 1200-1350°C. The curves show that gypsum can work as a melting point depressant. ΔC_p is the measured difference in heat capacity of the sample and the reference cell within the DSC. Shifts in baseline are due to compositional changes of the sample.

Figures 4.24 - 4.26 show the effect of adding NaCl as a second fluxing agent to Oxide Mix. Oxide Mix, .1CMAS, .5CMAS, and gypsum are again depicted, both with, and without, the addition of 5% NaCl. In addition the DSC curve of PTI A2 is compared to the DSC curve for Aramco (PTI A2 + 10% NaCl). Figure 4.24 shows that the addition of NaCl has negligible impact to the dehydration of either gypsum or CaO in each respective sample. However, NaCl does affect the melting point of each sample. Figure 4.25 shows that the melting points of gypsum, .1CMAS, and Oxide Mix are decreased by 10, 5, and 30°C respectively. The melting point of .5CMAS increases 25°C.

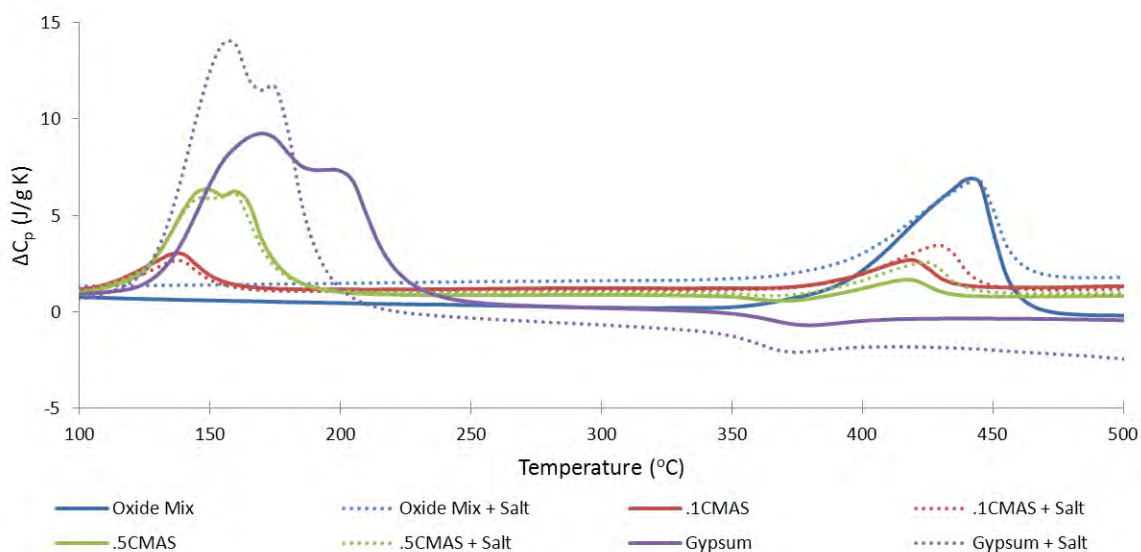


Figure 4.24: Effect of 5% NaCl added to various test dusts from 100-500°C. The addition of NaCl to the samples depicted in the plot does not appear to alter the dehydration temperature of the samples. ΔC_p is the measured difference in heat capacity of the sample and the reference cell within the DSC. Shifts in baseline are due to compositional changes of the sample.

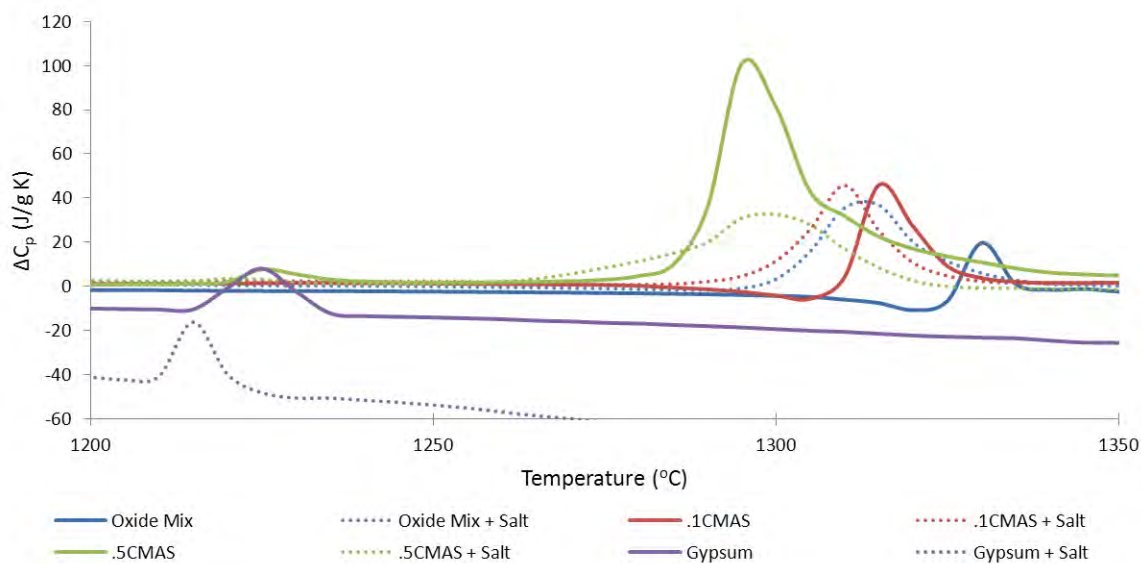


Figure 4.25: Effect of 5% NaCl added to various test dusts from 1200-1350°C. While the addition of NaCl did not affect the dehydration temperature of the samples, it did act as a melting point depressant for all samples except .5CMAS. ΔC_p is the measured difference in heat capacity of the sample and the reference cell within the DSC. Shifts in baseline are due to compositional changes of the sample.

Figure 4.26 shows that Aramco has a DSC peak which PTI A2 does not. This peak is associated with the decomposition of NaCl. In addition, the melting peak for Aramco starts at near the same temperature as PTI A2's. However PTI A2's melting curve peaks at 1160°C while Aramco's continues past the range of the DSC curve.

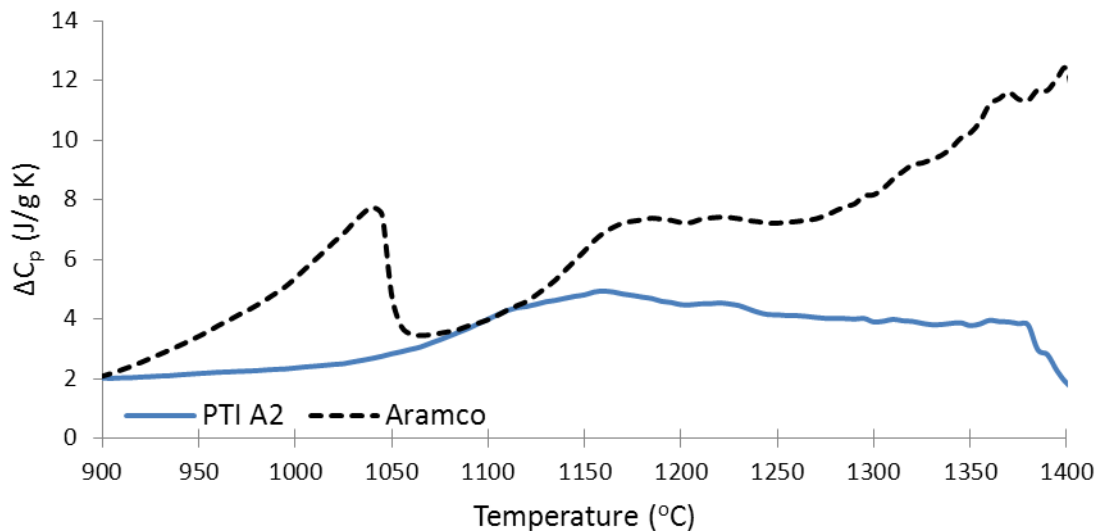


Figure 4.26: Difference in PTI A2 and Aramco DSC behavior from 900-1400°C which can be attributed to the presence of salt in Aramco. The peak at 1040°C is the melting of NaCl in the sample. ΔC_p is the measured difference in heat capacity of the sample and the reference cell within the DSC. Shifts in baseline are due to compositional changes of the sample.

4.3 Objective 1 Summary

Several important conclusions can be made from the results of the testing discussed in this chapter. First, as was mentioned in Section 2.4, one of the reasons studies into causes of HC other than Na_2SO_4 downplayed gypsum's role in HC due to gypsum's high melting point. However, as is shown in Figure 4.27, gypsum is molten at the same temperatures as GB1, and as was discussed in Chapter 3, DoD aircraft operating in the region of GB1 are currently experiencing HC issues.

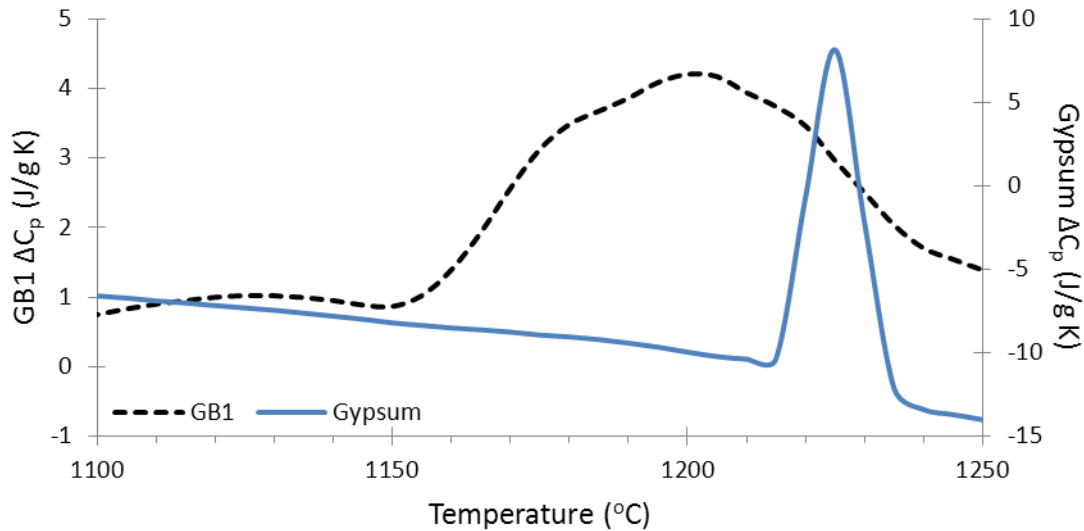


Figure 4.27: DSC plot comparing gypsum and GB1 from 1000-1500°C. Current literature argues that gypsum melts at too high of a temperature to cause HC. However, the plot shows that gypsum melts at a temperature within the melting range of a natural dust known to cause HC damage in DoD GTE. In addition, GB1 does not contain sodium sulfate. ΔC_p is the measured difference in heat capacity of the sample and the reference cell within the DSC. Shifts in baseline are due to compositional changes of the sample.

Second, Figures 4.22 and 4.23 showed the ability of gypsum to act as a melting point depressant. Gypsum's ability to lower the melting point of a dust sample is significant as gypsum's presence in certain operating locations, in addition to initiating HC, could act as an enabler for CMAS glass formation in GTE. Study of CMAS degradation without proper consideration for gypsum's effect on melting point is incomplete.

Third, Figures 4.24 - 4.26 showed NaCl to also affect sample melting behavior. However, the limited DSC samples runs were not sufficient to characterize the degree to which NaCl and gypsum contribute to any melting shift. Nor could it be inferred from the runs whether the individual contribution were additive, overlapping, or contradicting. Therefore, remaining testing under this research project will not examine the NaCl effect. Instead it is suggested as an area of future research.

Fourth, as was shown in Figure 4.21, the behavior of sample can change significantly based on previous thermal history. In order for the CMAS mixtures currently being used in academic studies to be relevant to current DoD operations, DoD aviation GTE would have to be ingesting glass

instead of dust. The undeniable fact that they are not has serious implications to not only current studies, but also efforts to develop new materials and coatings to combat the effects identified by those studies.

V. Quantification of Substrate Attack

The second objective of this research effort was to quantify the degradation of representative aviation GTE materials as caused by sulfur-containing artificial dusts. Substrate attack due to desert dust ingestion is affected by many variables in the real world. These variables are the result of the materials used, the operating parameters of the GTE, and properties of the specific dust ingested. In order to make the problem associated with quantifying substrate attack due to a sulfur-containing dust tenable, several decisions were made to limit the number of variables included in this study.

First, testing progressed from simple nickel to superalloy coupons. Second testing began with static loading in a reducing environment, which limited attack to sulfur corrosion only, before moving to a static oxidizing environment, which allowed for simultaneous oxidative and corrosive attack. Finally, a gypsiferous CMAS blend was used as the artificial dust. In order to attribute degradation to a single source (gypsum), the blend contained no other volatiles or highly reactive species typically found in natural dusts. The following sections provide details on the tests performed, and their results.

5.1 Static Reducing Furnace Flat Coupons

For all testing described in this section, gypsum, sodium sulfate, or the sulfur-containing CMAS blends identified in Section 4.1 were loaded onto coupons made of the EN, nickel, or superalloy substrates discussed in Section 3.1.2. To guarantee good surface contact between each media and the substrate, approximately 0.4 g of loose media was compacted into half-inch diameter compacted-powder cake approximately 1-2 mm thick. Dust compaction was accomplished with a ½" pellet-form loaded into a Carver Incorporated 10 ton hydraulic press as shown in Figure 5.1.



Figure 5.1: To prevent cross-contamination on test coupons, the dusts used for all SR and SO testing were pressed into thin wafers in a $\frac{1}{2}$ " form on a 10-ton press. The wafers were thin quartered and placed on test coupons.

The pressure required to form a stable wafer depended on the individual media. Gypsum and sodium sulfate wafers required 5000 psi. .5CMAS wafers were pressed at 7000 psi, while .1CMAS and .3CMAS wafers required 8000 psi. For the CMAS blends, as the amount of gypsum decreased in the media, more pressure was required to press a stable wafer, and the shelf-life of the wafer decreased. As an example, several pure gypsum wafers were still tightly packed more than six months after pressing, but .1CMAS wafers fell apart after only about two days. These pressures represent the minimum pressure necessary to create stable wafers was used for each dust. Minimal pressure was used to prevent wafer fusing due to sintering. The compacted wafers were then quartered so each test coupon could be loaded with multiple test dusts, as shown in Figure 5.2, without worry of cross contamination.

For all testing described in this section, the static furnace was controlled in the same manner as discussed in Section 4.1. The one exception was that nickel and superalloy coupons were loaded on sheets of molybdenum for low temperature runs or tungsten for runs above 1250°C. The use of molybdenum or tungsten sheets was necessary because nickel reacts with graphite at the temperatures the static furnace testing was accomplished. Molybdenum was initially used because it was already on hand so testing could continue while tungsten sheets were ordered. However, molybdenum could only be used for runs below 1250°C because it forms a binary eutectic with

nickel at 1309°C [77]. During trial runs before the testing described in the following sections, the eutectic melting behavior was actually noted to have begun by 1250°C, likely due to the presence of graphite and other impurities. Tungsten does not form a eutectic with nickel until 1495°C [78].

5.1.1 Development of Loading Method.

At the onset of this research effort, it was not known whether just the surface layer of a deposit directly in contact with the substrate or the entire deposit would contribute to surface attack. Two experiences, however, suggested that high media loading is detrimental to the sand melting process, and therefore this study of molten deposits. Testing associated with a multi-service test program showed incomplete glass formation on 1st stage HPT vanes in a T700 GTE at high media loading rates. Cross-sectioned vanes showed deposits with a granular structure topped with a thin glass film. Similar results were noted in Smialek's study [101]. Deposits formed in this two-phase manner suggest a self-insulation by thick deposits.

Expanding this hypothesis of self-insulation of dust deposits to the static loading tests described in this section, it would not be possible to increase attack media loading by simply loading more sand (i.e. using a thicker wafer) during a single heat run. Therefore, several methods (listed below) were reviewed to determine the best method to simulate the dynamic loading of dust in a static environment. The nature of batch testing required of the static furnace requires that a particular target dosage may require multiple thermal runs. Investigations were carried out on EN beginning with pure samples of gypsum to determine which of the methods listed below was most appropriate for use in the remainder of planned static furnace testing.

The loading methods examined included:

- a.** Apply a new dust wafer with each run after removing loose deposit.
- b.** Apply a dust wafer initially and leave it in place over several temperature excursions.
- c.** Method (a.) with the addition of a 30 second water rinse after after a temperature run.

For this initial investigation of loading method, only two parameters were varied in a simple 2² factorial design. High and low values for the peak temperature soak time parameter were 60 and 30 minutes respectively. The peak temperature soak was set at either 900 or 1200°C. Size limitations

within the Static Furnace allowed four 1'' square EN coupons, each with four sample locations to be loaded as shown in Figure 5.2. Each loading profile was run with two replicates resulting in the eight unique loading profiles shown in Table 5.1.

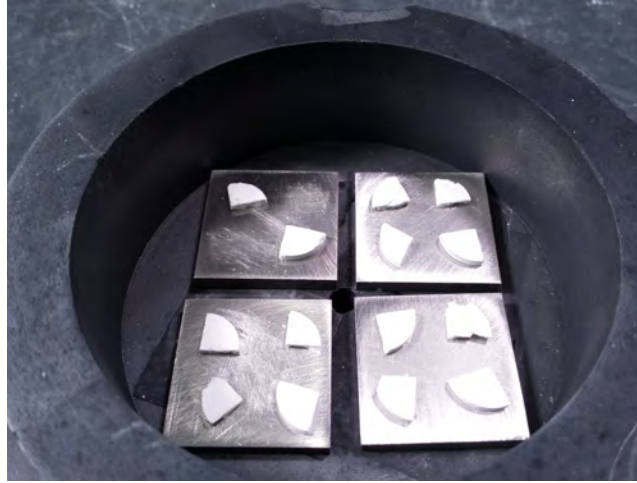


Figure 5.2: Gypsum samples on EN coupons. Multiple wafers from the press shown in Figure 5.1 were loaded on each coupon, providing at least two replicates for each test point.

Table 5.1: Profiles used for loading method determination.

Plate #	First Heating Cycle	Second Heating Cycle	Third Heating Cycle
1	¼ wafer	no gypsum loaded	—
	¼ wafer	previous wafer reused	—
2	¼ wafer	new ¼ wafer	no gypsum loaded
	¼ wafer	new ¼ wafer	new ¼ wafer
3	no gypsum loaded	—	—
	¼ wafer	—	—
4	¼ wafer (+ 30s wash)	no gypsum loaded	—
	¼ wafer (+ 30s wash)	new ¼ wafer	—

Mass loss of each gypsum wafer for the four time/temperature combinations are shown in Figure 5.3. The solid line on each plot is the theoretical mass loss expected, given an initial mass of gypsum, assuming complete decomposition according to Equation (5.1) which is the result of Equations (4.2) and (4.3). Recorded mass loss for each sample showed that at 1200°C, by 30

minutes, the samples should consist of only CaO. For 900°C runs, complete decomposition would not be expected until 60 minutes.

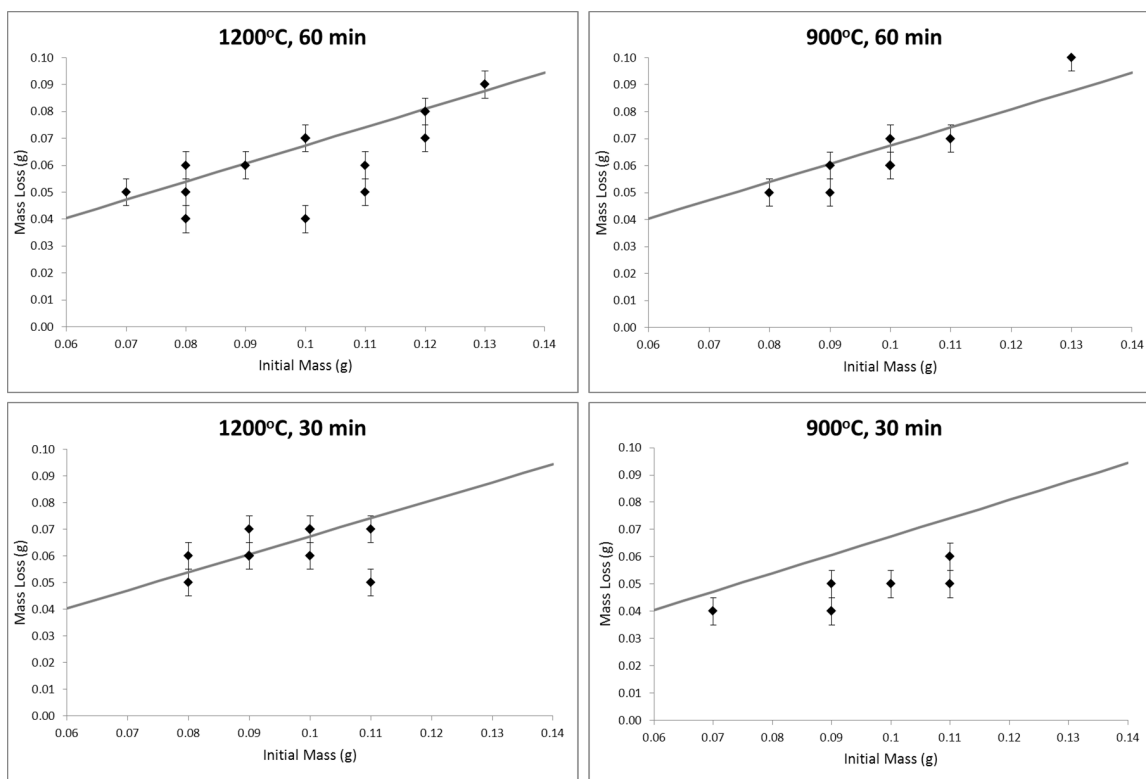
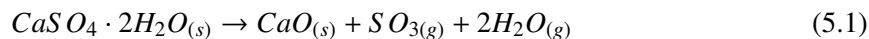


Figure 5.3: Sample mass loss for loading test runs. Solid lines represent the expected mass loss due to the complete decomposition of gypsum. The results showed that complete decomposition of gypsum could be expected within 30 minutes for temperatures near 1200°C.

No differences were noted in mass loss or wafers or change in external coupon appearance based upon the various loading methods. Following testing, the coupons were sectioned using a Struers Accuton-5 with a diamond cutting blade. Coupon sections were then mounted with either a Struers Durofast or Buehler Phenolic Powder mounting resin utilizing a Struers ProntoPress-20 set at 356°F and 4000 psi. The sample mounts were loaded into a six puck holder attached to a Struers TegraForce5 and polished with a Struers TegraPol-31 radial polisher with SiC paper at 320, 400, and 600 grit (300 rpm and 25 N down-force for 60 seconds each). The 600 grit run was followed

by a polish on a DAC wheel with #2 Dia pro Dac polishing fluid (150 rpm and 25 N down-force for 90 seconds) and a final polish on a MD Chem ops wheel with OPS polishing fluid (150 rpm and 10 N down-force for 90 seconds).

Final sample mounts were imaged using AFRL's SEMs described in Section 3.2.3. Figure 5.4 is a BSE cross-section of a gypsum-loaded coupon which was tested at 1200°C. EDS confirmed the presence of a sulfur-rich phase (light green bands in the image). Comparison of sodium sulfate and gypsum loaded coupons confirmed sodium sulfate to cause slightly worse degradation at 900°C. The depth of sulfur infiltration at 900°C was roughly equivalent for sodium sulfate and gypsum coupons, however the sodium sulfate coupons showed noticeable surface degradation which the gypsum coupons did not show. However, gypsum caused substantially more degradation, as measured by both depth of sulfur infiltration and significant surface degradation, at 1200°C. The minimal sulfur infiltration and lack of surface attack for sodium sulfate coupons at 1200°C was an expected result given that sodium sulfate decomposes into three vaporous species beginning well below 1000°C. DSC results for sodium sulfate discussed in Section 4.2.1 suggest this decomposition begins at only 290°C. Taken as a combination of sulfur infiltration and surface degradation, the gypsum coupon at 1200°C showed significantly more degradation than the other three test configurations. In addition, the current understanding of HC requires a molten deposit, yet the gypsum wafers caused degradation at both temperature set-points without melting. Further details of the results and implications of this subset of testing have been documented in a paper currently awaiting publication [61].

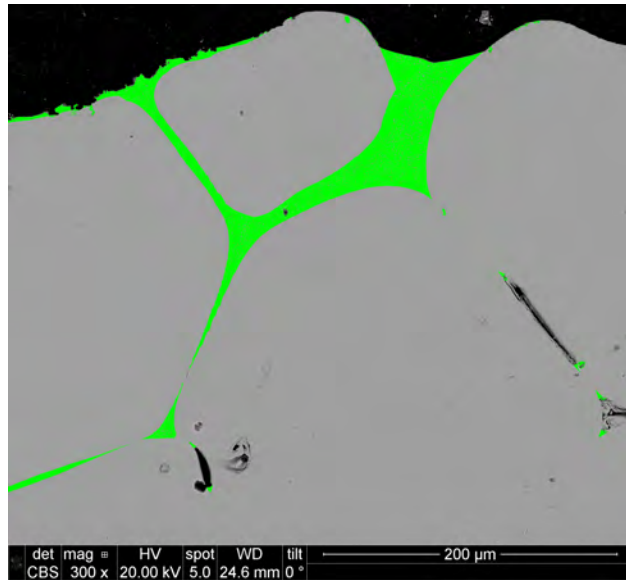


Figure 5.4: Depth profile for gypsum attack on EN coupon at 1200°C. The sodium sulfate coupon at the same temperature showed little infiltration of sulfur and no surface damage. The deep infiltration of sulfur (denoted by green bands) and significant surface damage (seen in the upper left corner of this image) suggest the literature argument that gypsum causes less severe degradation than sodium sulfate is incorrect at higher temperatures.

5.1.2 *Static Furnace Methodology.*

Table 5.2 shows the set-points used for the five initial static furnace test runs completed in UDRI's reducing furnace. The set-points were arranged in a 2^2 + center-point factorial design. This design was chosen as it is cited as an efficient design to collect data when curvature is expected in the response [69]. Typical studies of HC may extend to 100s of hours, however since there is no existing body of knowledge on gypsum-induced HC at elevated temperatures, it was decided to trade exposure time for the ability to test at multiple temperatures and sulfate concentrations to build an initial attack envelope.

Table 5.2: Static Reducing furnace testing set-points. The five temperature/sulfate concentration combinations represent a standard 2^2 + center-point DOE design. *Coupon collected for nickel only

Designation	Media	Temperature (°C)	Cycles
SR-L1	.1CMAS	1150	2, 4*, 8, 16
SR-L5	.5CMAS	1150	2, 4*, 8, 16
SR-M3	.3CMAS	1250	2, 4*, 8, 16
SR-H1	.1CMAS	1300	2, 4*, 8, 16
SR-H5	.5CMAS	1300	2, 4*, 8, 16

The temperatures in Table 5.2 were chosen based on DSC runs for .1CMAS and .5CMAS. According to the DSC curves neither sample had even begun to soften by 1150°C, so while chemistry would be different between the two samples, the physical state of the test dusts would be similar. At 1300°C, .5CMAS was just past the peak of its melting curve while .1CMAS was just approaching it. Therefore testing at 1300°C would account for different chemistry and different levels of melt progression. 1250°C was chosen slightly above the actual center-point between 1150 and 1300°C so that it would be between the melting point of gypsum and the CMAS blends.

The gypsum content of .1CMAS places it at the lower end of the geological definition of a gypsiferous dust. The gypsum content of .5CMAS is at the high end of the definition and just above the content in AFRL02. .3CMAS is simply the midpoint between .1CMAS and .5CMAS. Therefore the blends used bracket most natural environments where HC would be expected to be an issue, as well as a new DoD standard test dust for engine testing. It is worth noting that while the CMAS blends used in this study are described based on their gypsum content, the actual variable for study is the sulfate concentration of the dust. The sulfate ion is the reactive species which can directly lead to corrosion. It can also provide electron transport or act as an acidic species. Unfortunately, an anecdotal assertion exists which states calcium is a direct agent in HC due to the fact that calcium is often found alongside HC damage (this assertion would lead to the assumption that the concentration of gypsum should be the studied variable to account for both calcium and sulfate). However, calcium's presence near HC damage is mere coincidence due to the fact that

the most common sulfate dust is gypsum. Since sulfate is the direct causative agent of HC, the appropriate variable of study is the concentration of sulfate.

5.1.3 Results and Observations.

5.1.3.1 Appearance.

Tables 5.3 - 5.7 show the external change in appearance of coupons during SR furnace testing. At 1150°C the test wafers did not melt. However, from the initial heat run, a halo was observed around the wafer location on all coupons. The halo was used to place subsequent wafers to help contain loading to the same coupon location for each run. After heating, wafers stuck to the superalloy coupons requiring gentle prying with a razor blade to remove the wafer from the coupon. Wafers on nickel coupons stuck only slightly. In addition, the bottoms of wafers on superalloy coupons showed a grey discoloration from the initial heat run. Wafers on nickel coupons did not show discoloration until after several heat runs. Chromium sulfide has a brown-black coloration while nickel sulfide is black. The discoloration on the bottom of the test wafers is indicative of metal transfer to the wafers.

Table 5.3: Change in appearance of coupons for SR-L1 test runs.


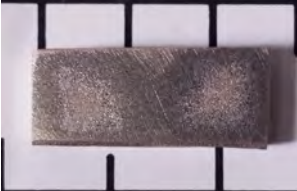
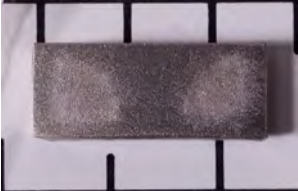






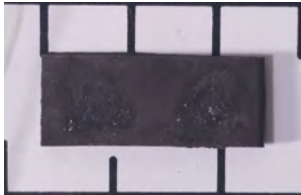

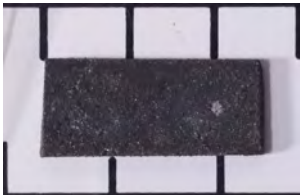
Material	2 cycles	8 cycles	16 cycles
Nickel			
Superalloy			

Table 5.4: Change in appearance of coupons for SR-L5 test runs.

Material	2 cycles	8 cycles	16 cycles
Nickel			
Superalloy			

Tables 5.5 - 5.7 show that the test wafers had begun melting at the higher temperature runs. Melted wafers would wet the surface of superalloy coupons. In addition, the melted wafers would pop off of the superalloy during cooling, but typically stayed in one piece. Wafer popping could occasionally be heard upon cooling past 400°C. However, most wafers did not pop off until after the furnace was opened. Melted wafers would bead on nickel coupons, and with subsequent runs, the bead caused a “crater” to form in the coupon surface. In addition, “bubbles” formed on the surface of the nickel coupons with corresponding depressions in the bottom of the wafer beads. The increased surface contact area between the bead and the nickel coupon due to the formation of these craters and bubbles made removal of the wafer beads from nickel coupons difficult. Beads formed at the SR-M3 set-point typically had to be pried from the coupon with a razor blade. Beads formed at the SR-H5 set-point required chiseling which often shattered the bead. During chiseling, care was taken not to contact the coupon with the chisel. The bottoms of beads which were not shattered showed a metallic sheen. The sheen was most pronounced for 1300°C runs.

Table 5.5: Change in appearance of coupons for SR-M3 test runs.




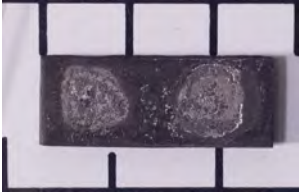

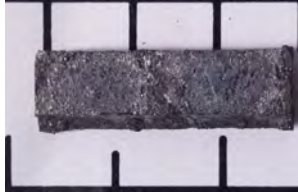
Material	2 cycles	8 cycles	16 cycles
Nickel			
Superalloy			

Table 5.6: Change in appearance of coupons for SR-H1 test runs.




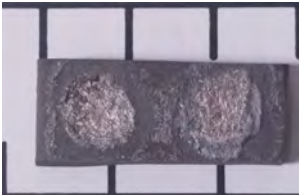
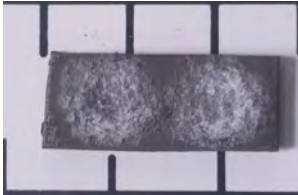
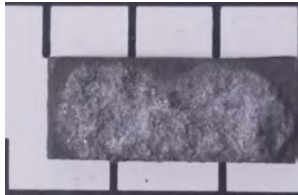

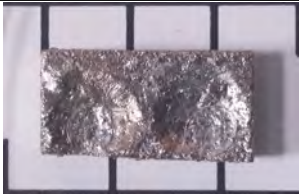

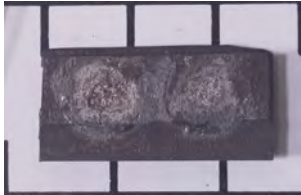


Material	2 cycles	8 cycles	16 cycles
Nickel			
Superalloy			

Table 5.7: Change in appearance of coupons for SR-H5 test runs.

Material	2 cycles	8 cycles	16 cycles
Nickel			
Superalloy			

The tungsten sheets also showed damage following test runs and had to occasionally be replaced. Individual sheets under each coupon typically lasted at least six runs at lower sulfate concentrations, but often were replaced after only two or three runs at the SR-H5 set-point.

5.1.3.2 Cross-Section Analysis.

Each coupon depicted in Tables 5.3 - 5.7 was cross-sectioned at multiple locations. Figure 5.5 shows a representative coupon and the location of cross-sections. Slight variations in coupons and the furnace meant the coupons were not always level. In temperature runs in which the test dust melted, the molten dust could move across the coupon surface. Therefore, the circles drawn on Figure 5.5 depict the location of the last wafers placed on coupon. The cross-sections were mounted and polished in accordance with procedures detailed in Section 5.1.1.

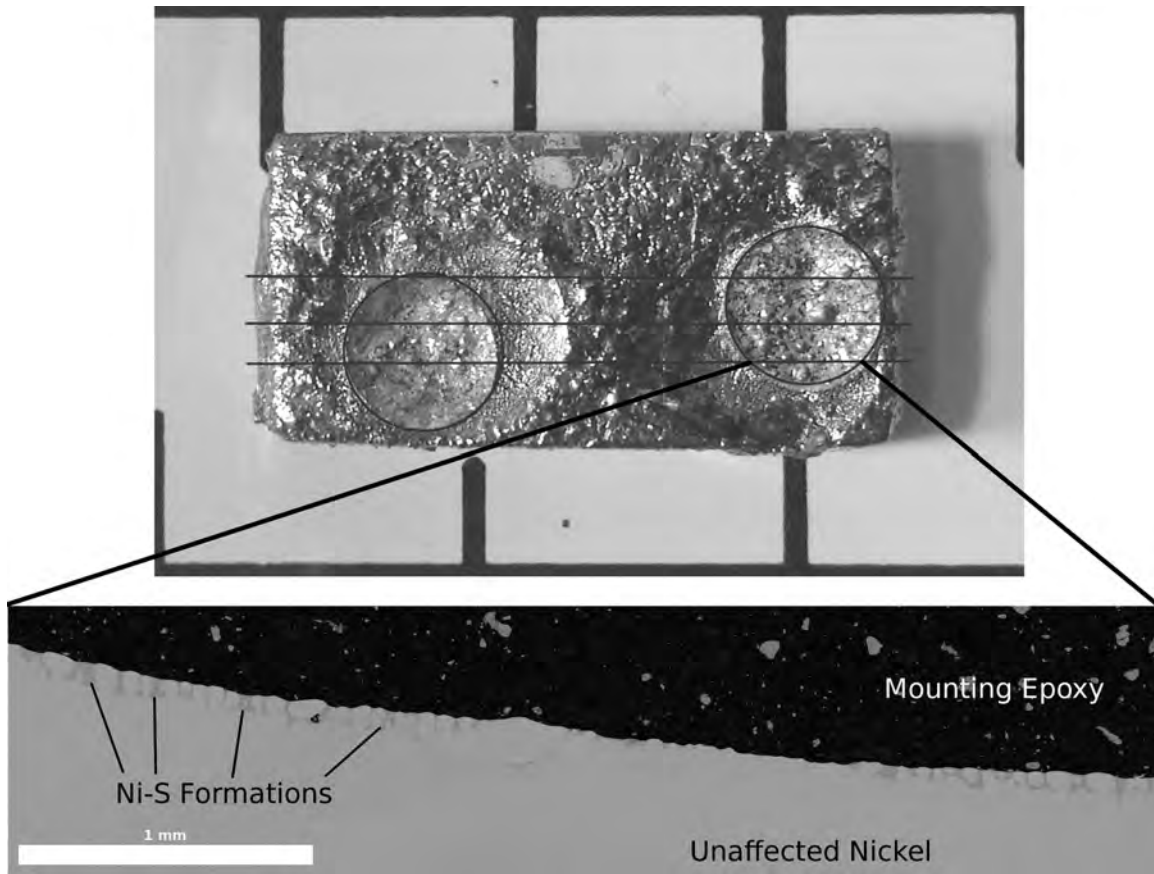


Figure 5.5: Surface image of representative coupon showing wafer and cross-section locations. When mounted for SEM imaging, the coupon cross-sections are reversed, as seen by the SEM detectors. Therefore the left edge of the SEM image is the right edge of the coupon as viewed from above.

BSE images were captured along the entire length of each cross-section and stitched together using GIMP. A thin line was added to each image, approximating the original coupon surface, to allow “leveling” of the cross-section to ensure measurements were taken normal to the original surface. The areas directly beneath the wafer position identified in Figure 5.5 were saved as new images for use in measuring depth of sulfur penetration and extent of damage. The inset BSE image in Figure 5.5 is an example of this process. As shown in Figure 5.5, nickel coupons from SR testing showed only two phases: unaffected nickel, and a Ni-S phase. Figure 5.6 depicts the complicated degradation identified in superalloy coupons during SR testing.

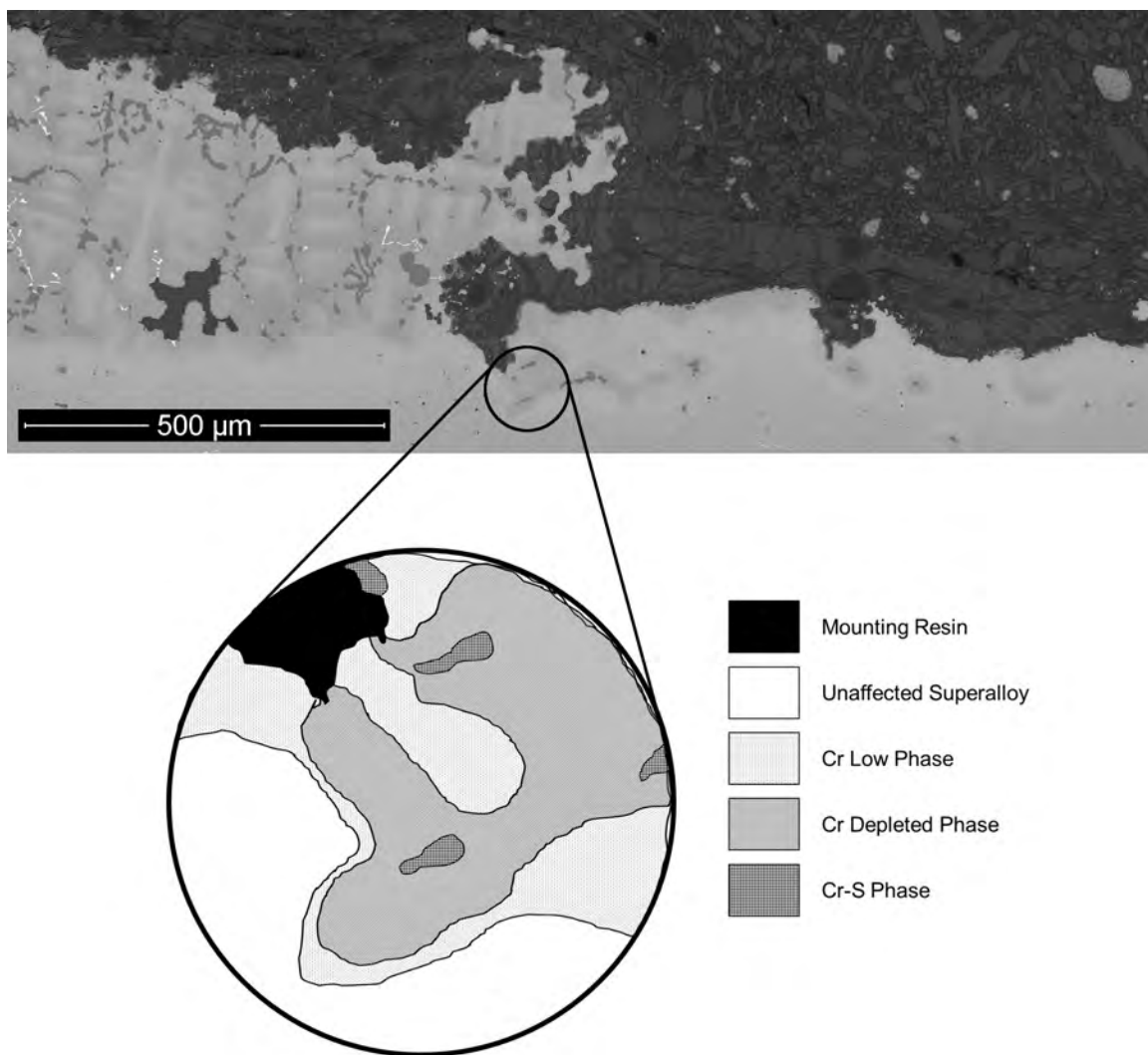


Figure 5.6: Chemical phases shown in BSE imaging of a cross-sectioned superalloy coupon exposed to sixteen heat soaks at the SR-M3 set-point. The illustration depicts the phases present in the circled region of SEM image.

5.1.3.3 *Extent of Degradation.*

Two outputs were used to quantify sulfur degradation to coupons. The first was thickness of the sulfur phase (as denoted by a Cr-S phase in superalloy coupons or Ni-S phase in nickel coupons) in the cross-sections produced according to the methods presented in Section 5.1.3.2. Thickness of sulfur phase was chosen as a degradation measurement as opposed to depth of sulfur penetration to remove potential measurement error due to the shift of coupon surface. The presence of sulfur in a substrate is necessary for HC to occur. In addition, the presence of sulfur, even if it has not

yet reacted with the substrate, affects material properties, especially if the sulfur is found at grain boundaries [72]. Area of degradation was chosen as it could relate to future mechanical testing of gypsum-degraded coupons. Using basic tension testing as an example, a low area of degradation would be indicative of a sharp degradation front approximating an edge crack. A high area of degradation would occur due to a consistently broad front, which in the limiting case would allow the coupon to be modeled as a multi-layered composite for the same tension testing.

5.1.3.3.1 Thickness of Sulfur Degradation. The thickness of sulfur degradation was measured using the “Measuring” tool in GIMP. The upper limit of the sulfur phase was defined as the top of the highest sulfur formation within the coupon. The lower limit was defined as the bottom of the lowest sulfur formation within the coupon. The two formations were not required to be continuous and often were separated laterally. Figure 5.7 schematically depicts the thickness measurement as taken on a superalloy coupon exposed at the SR-H5 set-point. A portion of the original BSE cross-section image is shown on the left. For simplicity, the right image only shows the sulfur-rich phase within the coupon. Location of measurements are superimposed on the right image. EDS analysis showed the “Cr-S” phase to be greater than 70% chromium and sulfur, the “Cr Depleted” phase to contain <15% of the chromium expected by the superalloy recipe, and the “Cr Low” phase to have <85% of the expected chromium.

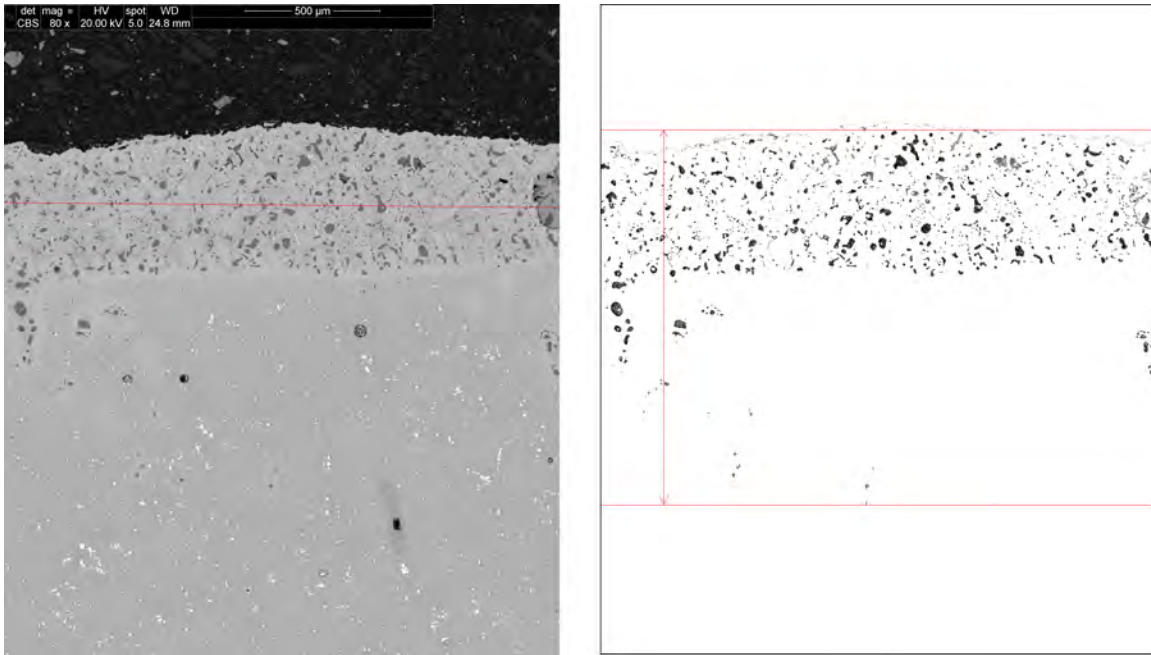


Figure 5.7: Measurement of sulfur-phase thickness for coupons tested in a SR environment. Thickness was defined as the difference in the highest sulfur-rich phase and lowest sulfur-rich phase as shown in the image on the right. The BSE image (left) of a superalloy cross-section was edited (right) to show only its Cr-S phases and associated limits for thickness measurement. The red line in the middle of the left image was for image alignment only, it was not used for measurement purposes.

Determination of the lower limit was simple in superalloy cross-sections. The grain structure of the superalloy used in this study was so fine that it was not visible at the magnifications used for measurements. In addition, the extremely fine grain structure removed an easy path of sulfur infiltration into the coupons. Instead sulfur had to diffuse across grains resulting in a relatively consistent degradation front in the superalloy. In contrast, the nickel coupons had a coarse grain structure which provided wide paths for infiltration so that sulfur did not have to diffuse across grains. Since sulfur followed the random grain structure in the nickel coupons depth of infiltration was not consistent. In addition, sulfur's presence in the grain boundaries did not necessarily translate to sulfur attack at the grain boundaries. Therefore, the low limit for sulfur degradation in nickel coupons was set at the lowest location where it appeared grain boundaries were widening due to sulfur's presence. Measurement according to this method discounted some sulfur infiltration in nickel coupons but also provided more consistent measurements.

The primary source of error in setting the upper limit was the possibility of selecting a sulfur formation within any residual deposit left on top of the sectioned coupon as opposed to a sulfur formation within the actual cross-section. This was an issue for all coupons, though more pronounced in superalloy coupons due to the large number of phases that could form due to the complex chemistry of the superalloy.

Assuming proper placement of the upper and lower limit, the resolution of the BSE images allowed the thickness measurements presented in Figures 5.8 - 5.16 to be accurate within 3.1×10^{-4} mm for 1150°C runs and 7.8×10^{-4} mm for 1250 and 1300°C runs. These accuracies translate to less than 0.1% measurement error in degradation thickness.

To normalize results across different wafer diameters, cross-section location within a wafer was translated into a position between zero at the wafer's center point, and unity at the wafer's edge. The damage under each wafer was assumed to be symmetric about its center point for position translation and subsequent analysis. Locations of cross-sections, in relationship to defined wafer position, were determined from the overhead images shown in Tables 5.3 - 5.7. Based upon the resolution of these images, assuming proper placement of coupon edges and wafer position, the cross-section radial position presented in Figures 5.8 - 5.11 and Figures 5.14 - 5.16 to be accurate within 2.5×10^{-2} mm for 1150 and 1250°C runs and 1.8×10^{-2} mm for 1300°C runs. These measurements account for approximately 2% error for radial position of cross-sections.

For SR runs, sometimes cross-sections did not overlap the defined wafer positions. Therefore some set-points in Figures 5.8 - 5.11 and Figures 5.14 - 5.16 have fewer data-points. Since three cross-sections were taken on each coupon, a maximum of six data-points per set-point was possible. In addition, at 200x magnification, degradation on the SR-L1 set-point nickel coupons was barely visible and sulfur infiltration could not be differentiated from residual sulfur in test dust deposits remaining on the coupons. Therefore degradation thickness on nickel coupons for the SR-L1 set-point was defined as zero for all cycle times. Figures 5.8 - 5.11 show the resulting measurements for thickness of sulfur infiltration for the nickel coupons at each set-point.

Second-order polynomial trend lines have been added for each set-point depicted in Figures 5.8 - 5.11 to allow discussion of general trends. These trend lines are simply curve fits, they are not

meant to imply any underlying physical phenomena. In general, the thickest degradation was found at the center-point of each wafer position and decreased with radial position. There did not appear to be any trend with regard to radial position at two cycles for any set-point, therefore a line depicting the average thickness of degradation for each set-point was included in Figure 5.11. Similarly, the SR-L5 set-point did not show a specific trend at any cycle time, so a line depicting the average thickness of degradation at the SR-L5 set-point was included for each cycle time. Figures 5.8 - 5.11 show significant scatter in the data about the trend line for each set-point, with no consistent trend in order of degradation among the set-points. The SR-H1 set-point showed the most degradation at every cycle time except four cycles. SR-L5 shows the least degradation at all cycle times. More degradation was measured at SR-M3 than SR-H1 for all cycle times except 16 cycles.

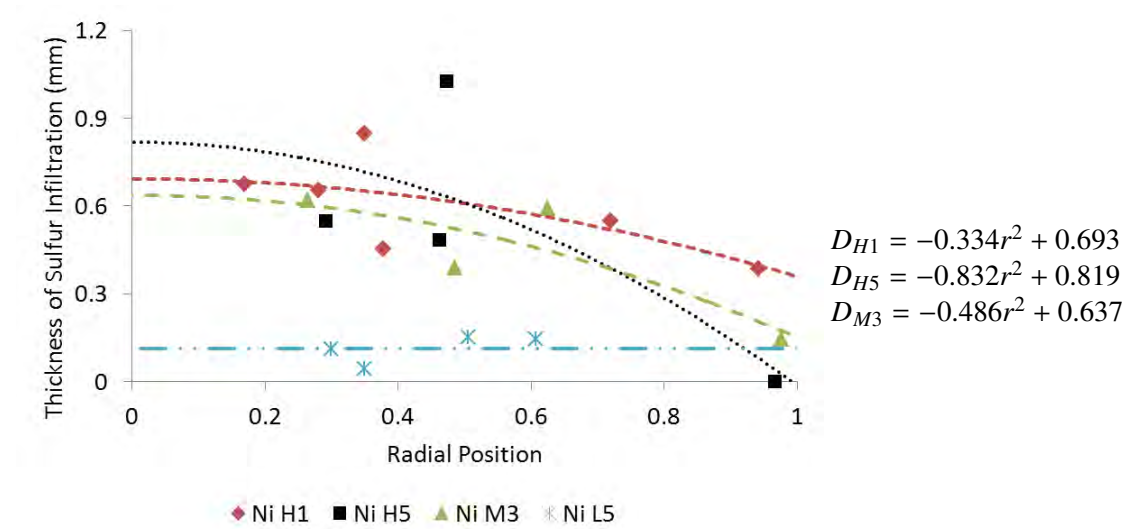


Figure 5.8: Thickness of sulfur degradation in nickel coupons in SR tests at 16 cycles. Dashed lines depict quadratic curve fits for experimental data (equations are included for each curve). No underlying physical phenomena is implied by the curve fits. In general degradation decreased radially from the center-point of the wafer position.

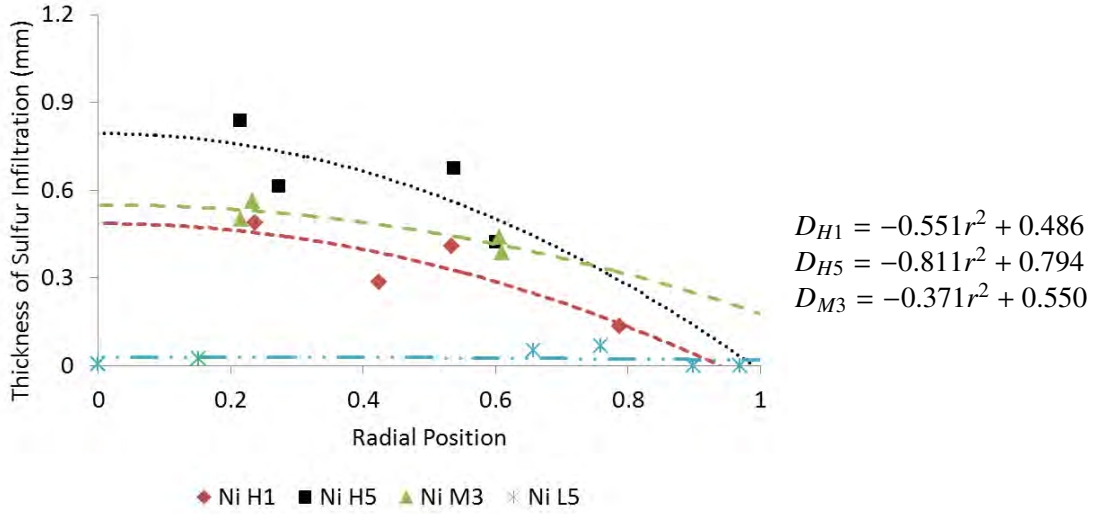


Figure 5.9: Thickness of sulfur degradation in nickel coupons in SR tests at eight cycles. Dashed lines depict quadratic curve fits for experimental data (equations are included for each curve). No underlying physical phenomena is implied by the curve fits. In general degradation decreased radially from the center-point of the wafer position.

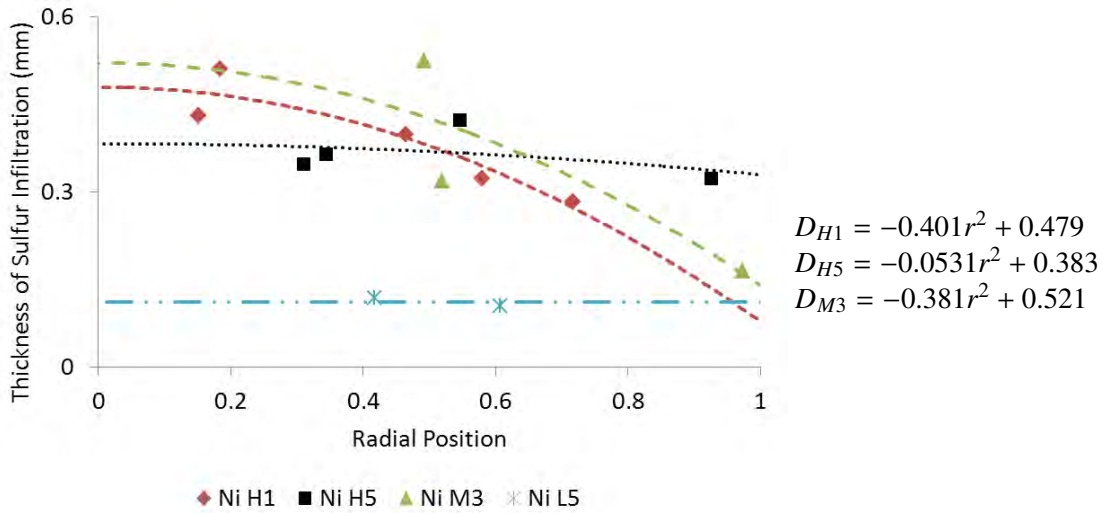


Figure 5.10: Thickness of sulfur degradation in nickel coupons in SR tests at four cycles. Dashed lines depict quadratic curve fits for experimental data (equations are included for each curve). No underlying physical phenomena is implied by the curve fits. In general degradation decreased radially from the center-point of the wafer position.

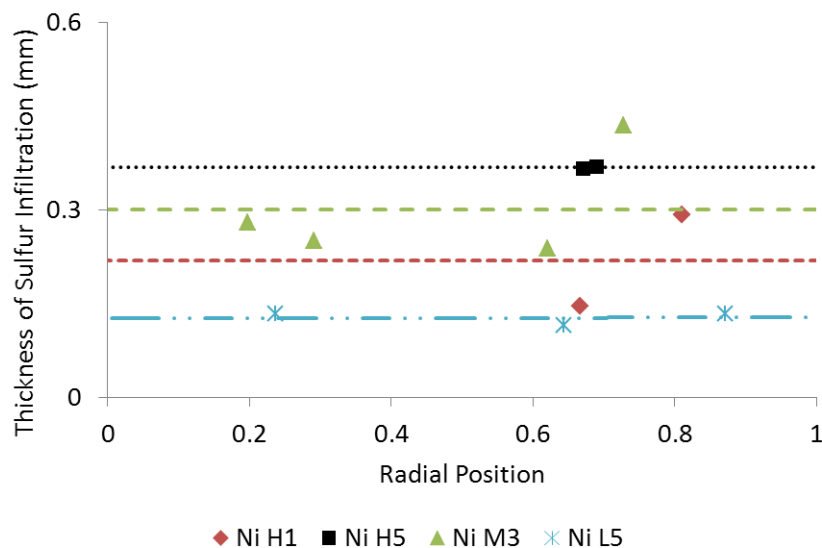


Figure 5.11: Thickness of sulfur degradation in nickel coupons in SR tests at two cycles. Dashed lines depict linear fits as no trend in radial position was found within experimental data at two cycles.

In order to compare changes in degradation at each set-point with time, a single thickness (with associated error) at $r = 0$ was calculated from each data point using the trend line equations shown in Figures 5.8 - 5.10 (the same procedure was also accomplished for the superalloy coupons in SR and static oxidizing (SO) testing to be discussed shortly). Figure 5.12 shows an example of this process. The equation shown in Figure 5.12 represents the curve fit for all data-points shown. The residual at each data-point between measured degradation and the curve fit is this used to shift the curve fit equation. The shifted equation for each data-point is then used to calculate the equivalent degradation at $r = 0$ for each data-point. The dotted line in Figure 5.12 represent the shifted curves for each data-point. Figure 5.13 depicts the trend in degradation as a function of time for each set-point. For all set-points except SR-L5, degradation increased with the natural logarithm of time. The trends in Figure 5.13 show the order of degradation is SR-H5, followed by SR-M3, SR-H1 (except at 16 cycles), and finally SR-L5.

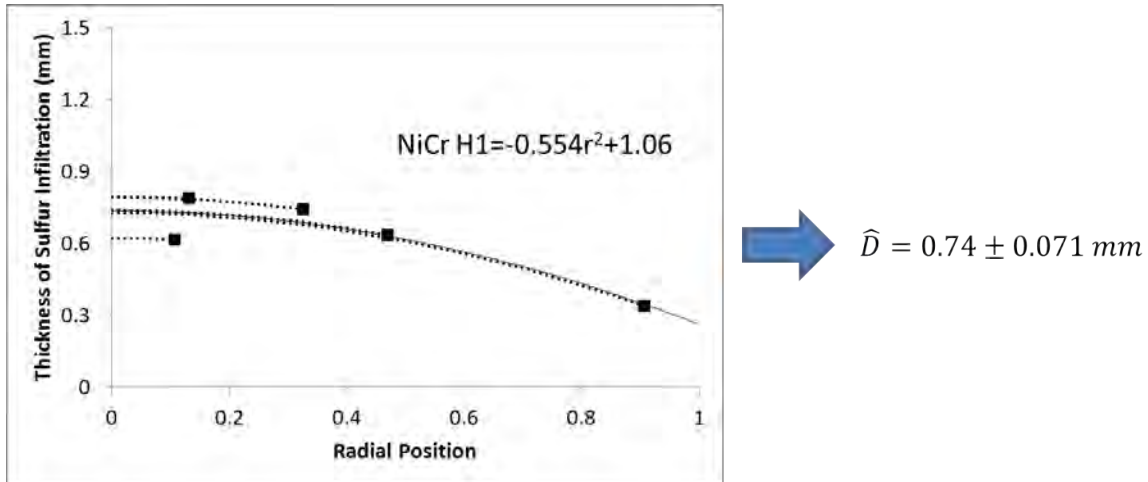


Figure 5.12: Measurements for each cross-section were reduced to a single equivalent thickness measurement at $r = 0$. The equation of the general curve fit (solid line) was used to trace each data-point back to $r = 0$ (dashed lines). In this manner a range of equivalent degradation for each set-point could be determined in order to plot degradation at each set-point against time.

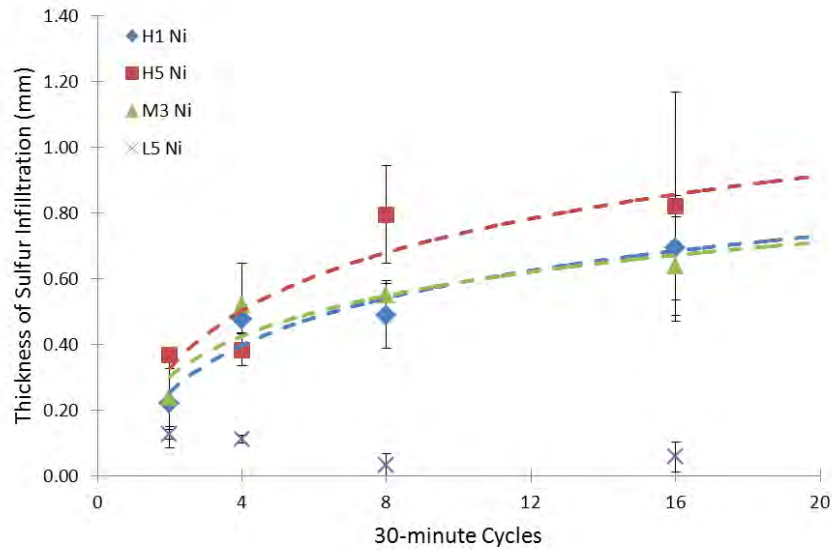


Figure 5.13: The equivalent degradation at $r = 0$ for each set-point plotted against time. In this figure, the average measured degradation at each set-point is depicted as a data-point. Error bars are for an 80% confidence interval of the standard error of measured degradation calculated at each set-point. Except for the SR-L5 set-point, equivalent degradation increased with the natural log of cycles. In general, the order of decreasing degradation was SR-H5, SR-M3, SR-H1, SR-L5.

For superalloy coupons, degradation was more clearly visible at the SR-L1 set-point than it had been for nickel coupons. However, the multitude of additional phases present in the superalloy, along with residual dust deposits at the surface, did not allow accurate determination of upper and lower limits for measurement. Therefore degradation at SR-L1 was defined as zero for all cycle times for superalloy coupons as well. Figures 5.14 - 5.16 show the resulting measurements for thickness of sulfur degradation for the superalloy coupons at each set-point. At all set-points the superalloy coupons showed thicker degradation than the nickel coupons due to the presence of chromium in the superalloy. Sulfur preferentially reacts with chromium over nickel. The variance in superalloy measurements is also smaller, especially at high temperature set-points, due primarily to the difference in infiltration modes (grain-boundary infiltration in nickel, diffusion in superalloy) discussed earlier.

Just as was done for the nickel coupons, second-order polynomial trend lines have been added for each set-point depicted in Figures 5.14 - 5.16 to allow discussion of general trends. These trend lines are simply curve fits, they are not meant to imply any underlying physical phenomena. In general, the thickest degradation was found at the center-point of each wafer position and decreased with radial position. There did not appear to be any trend with regard to radial position at the SR-L5 set-point for any cycle time or the SR-M3 set-point at two cycles, therefore a linear trend line for each of these set-points was applied. Figures 5.14 - 5.16 show less scatter in the data about the trend line for each set-point than had been found for nickel coupons. In addition, unlike in nickel coupons, a consistent pattern in level of degradation was found between the set-points. At all cycle times, the order of decreasing degradation was SR-H5, SR-H1, SR-M3, SR-L5.

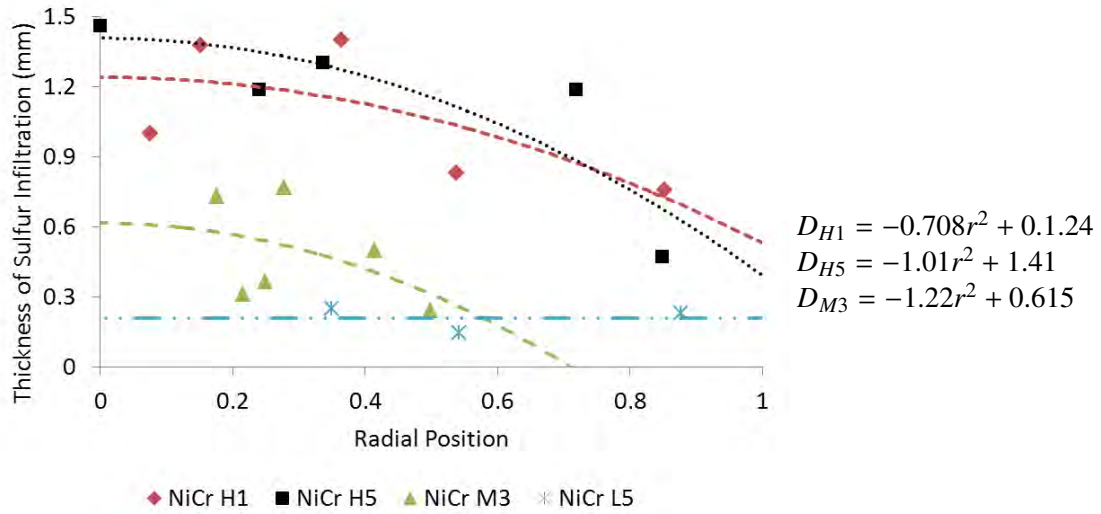


Figure 5.14: Thickness of sulfur degradation in superalloy coupons in SR tests at 16 cycles. Dashed lines depict quadratic curve fits for experimental data (equations are included for each curve). In general degradation decreased radially from the center-point of the wafer position. A linear fits was used for SR-L5 as no trend in radial position was evident. No underlying physical phenomena is implied by the curve fits.

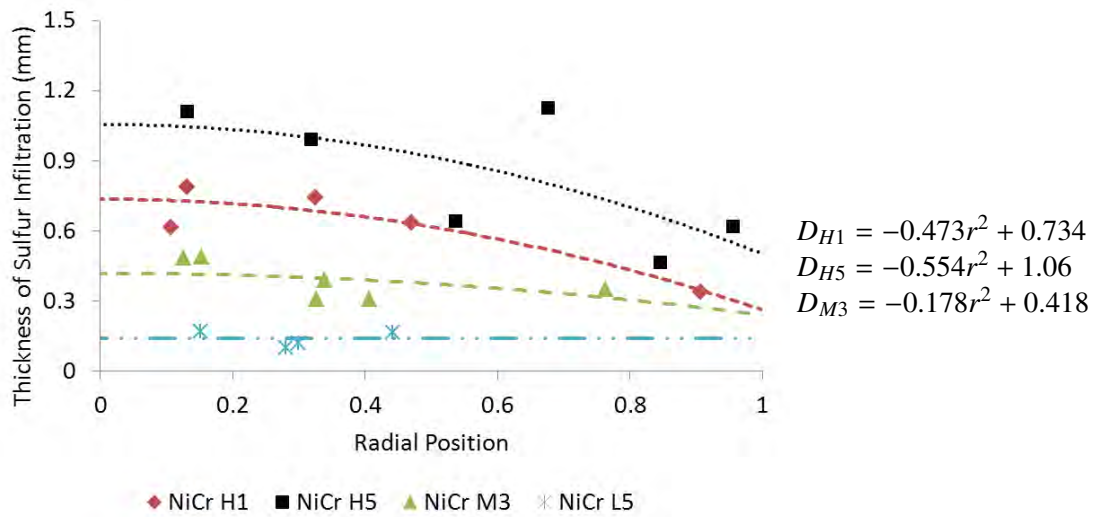


Figure 5.15: Thickness of sulfur degradation in superalloy coupons in SR tests at eight cycles. Dashed lines depict quadratic curve fits for experimental data (equations are included for each curve). In general degradation decreased radially from the center-point of the wafer position. A linear fit was used for SR-L5 as no trend in radial position was evident. No underlying physical phenomena is implied by the curve fits.

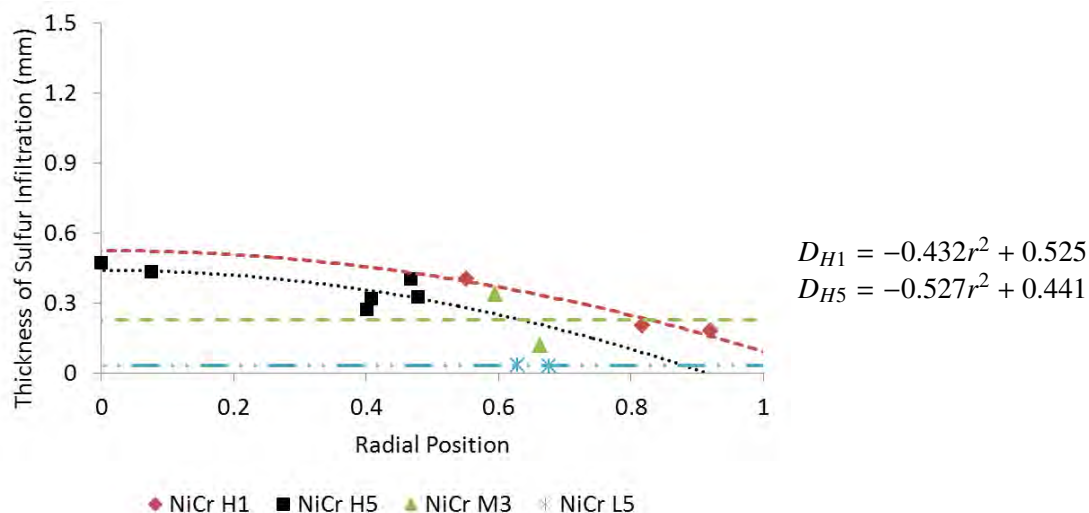


Figure 5.16: Thickness of sulfur degradation in superalloy coupons in SR tests at two cycles. Dashed lines depict quadratic curve fits for experimental data from the SR-H1 and SR-H5 set-points (equations are included for each curve). In general degradation decreased radially from the center-point of the wafer position. Linear fits were used for SR-M3 and SR-L5 set-points as no trend in radial position was evident. No underlying physical phenomena is implied by the curve fits.

The superalloy data-points were also reduced to single calculated values of equivalent degradation at $r = 0$ using the same procedure as was presented in Figure 5.12. Figure 5.17 clearly confirms the relationship of decreasing degradation with cycle time mentioned in the previous paragraph (SR-H5, SR-H1, SR-M3, SR-L5). In addition, just as was found for nickel coupons, equivalent degradation increased with the natural logarithm of time.

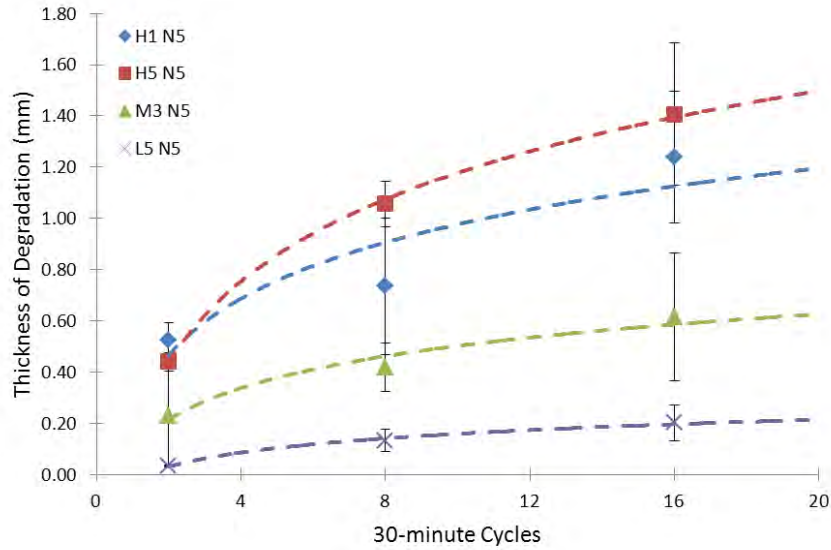


Figure 5.17: The equivalent degradation at $r = 0$ for each set-point plotted against time. In this figure, the average measured degradation at each set-point is depicted as a data-point. Error bars are for an 80% confidence interval of the standard error of measured degradation calculated at each set-point. For all set-points the equivalent degradation increased with the natural log of cycles. In general, the order of decreasing degradation was SR-H5, SR-M3, SR-H1, SR-L5.

5.1.3.3.2 Area of Degradation. The second measurement of degradation defined for this study was the fraction of the area (bounded by the same limits used to determine thickness of degradation) showing chemical degradation. To measure the area of degradation, the images produced in Section 5.1.3.3.1 were edited by replacing both the mounting resin and unaffected material with a transparent channel. Pixels in the transparent channel have no color value so they are not counted in GIMP's histogram tool. In this manner the resulting histogram data represents the fraction of degradation within the image area. Figure 5.18 schematically depicts the area fraction measurement for the same superalloy coupon depicted in Figure 5.7. The regions visible in the image on the right represent the chemically altered fraction of the affected area. The framed region represents the affected area.

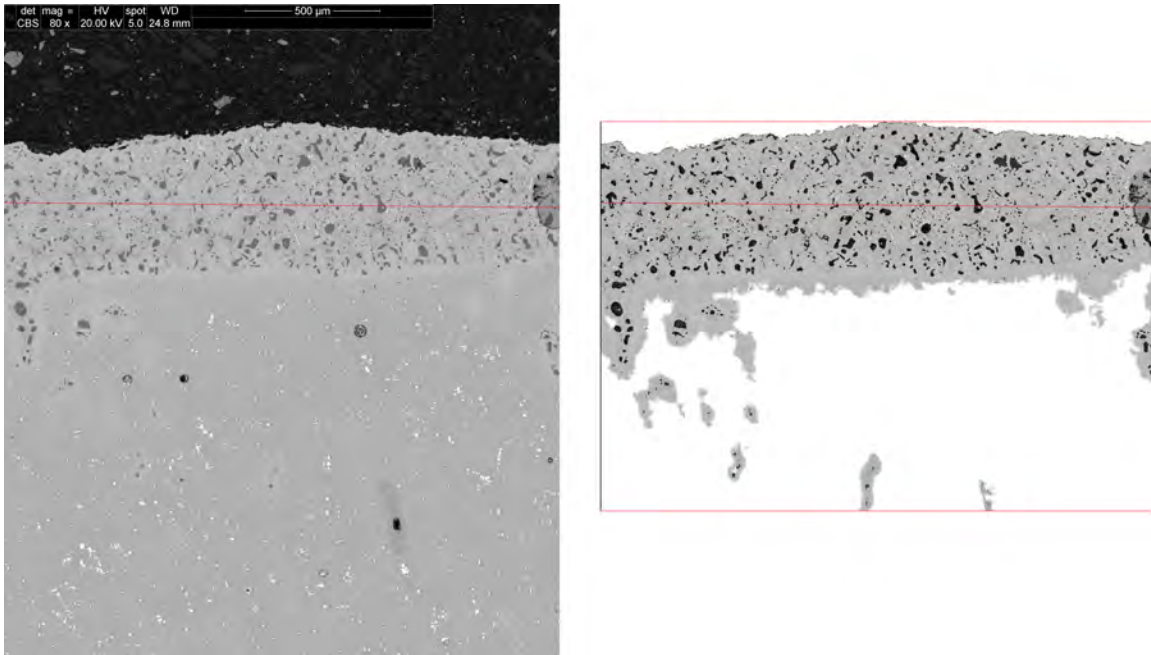


Figure 5.18: Measurement of area of chemical shift for coupons tested in a SR environment. Using the same boundaries set for thickness measurements (see Figure 5.7), all regions of the cross-section which did not show a shift in chemistry from the baseline superalloy (left) were deleted. GIMP's histogram tool was used to count the pixels remaining in the edited image (right), giving a fraction of the degradation thickness showing chemical degradation. The red line in the middle of the each image was for image alignment only, it was not used for measurement purposes.

Figures 5.19 and 5.20 show the resulting measurements for the area of degradation for the nickel coupons at each set-point. The plots show no discernible relationship between radial position, temperature, sulfate concentration, or cycles. In fact measurements appear to cluster around an average area fraction across all set-points except SR-L5 of 0.02 regardless of input values of any of these variables. Further, no consistent trend in area fraction with cycle time was found. These results suggest area fraction is not a significant measure of degradation and therefore does not warrant inclusion in the degradation models to be developed in Chapter 6.

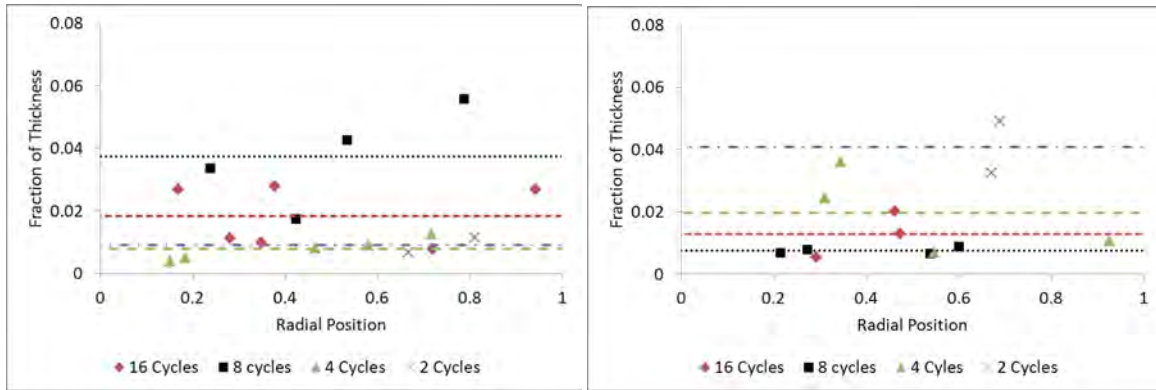


Figure 5.19: Area fraction of sulfur degradation in nickel coupons in SR tests at SR-H1 (left) and SR-H5 (right) set-points.

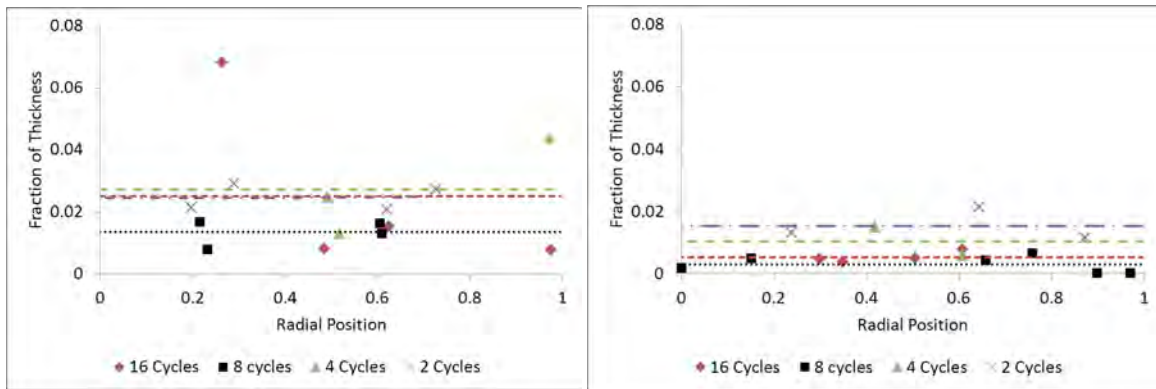


Figure 5.20: Area fraction in sulfur degradation on nickel coupons in SR tests at SR-M3 (left) and SR-L5 (right) set-points.

The superalloy coupons showed significantly higher area fractions of degradation than nickel coupons. The higher area fraction of degradation is related to the discussion of diffusion versus grain-boundary infiltration introduced in Section 5.1.3.3.1. Since sulfur traveled primarily along grain-boundaries in nickel coupons there is substantial unaffected space between each narrow sulfur-phase. Also the degraded nickel coupon is a binary system. The only phases possible are nickel (unaffected) and Ni-S (degraded). These two facts resulted in a low measurement of area fraction of degradation for nickel coupons. Figures 5.21 and 5.22 show the resulting measurements for the area of degradation for the superalloy coupons at each set-point. On the other hand, sulfur infiltration in the superalloy follows a diffusion front so progress is more uniform. In addition, the degraded

superalloy coupon can present multiple phases. The primary phases found in the superalloy were the superalloy (unaffected), low chromium (degraded), chromium depleted (degraded), Cr-S (degraded), and Ni-S (degraded). Therefore a higher area fraction of degradation in the superalloy compared to nickel coupons was expected.

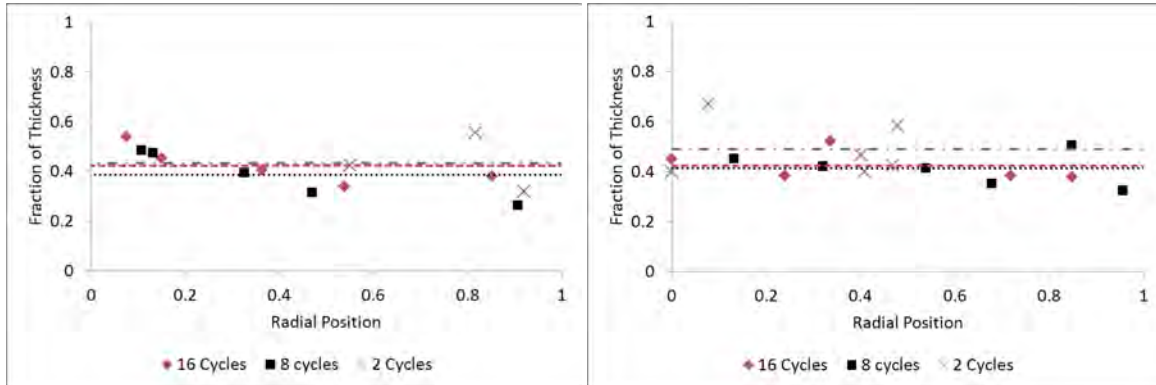


Figure 5.21: Area fraction in sulfur degradation in superalloy coupons in SR tests at SR-H1 (left) and SR-H5 (right) set-points.

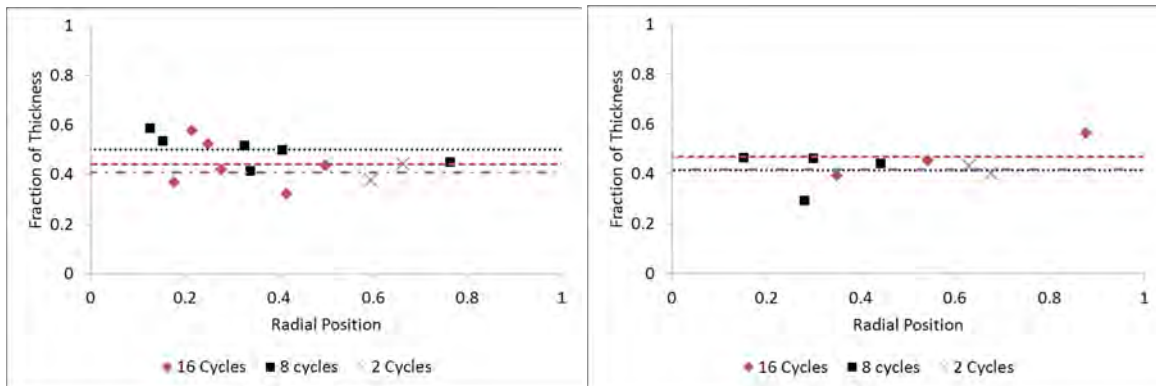


Figure 5.22: Area fraction of sulfur degradation in superalloy coupons in SR tests at SR-M3 (left) and SR-L5 (right) set-points.

Similar to the discussion for nickel coupons, area fraction of degradation does not appear to be a function of any of the measured input variables of this study. It does, however, appear to vary consistently with radial position showing a consistent parabolic shape with a maximum area fraction of ~ 0.50 at the wafer center point. Since there does not appear to be any predictive value

in a constant area fraction of degradation, this measurement will not be included in the degradation models developed in Chapter 6.

5.2 Static Oxidizing Furnace Flat Coupons

Testing was originally planned to progress from the SR environment described in Section 5.1 to a dynamic oxidizing (DO) environment utilizing a new test facility designed by AFRL to examine hot erosion and corrosion issues for the DoD. The AFRL Hot Rig has been described elsewhere [79]. However, initial review of the data obtained from testing in the static furnace showed significant variance. The Hot Rig was a new test facility which had not yet reached full operational capability so would have introduced its own variance. In addition, the move from SR to DO would have been a large leap in test environment. Therefore, it was deemed necessary to move to a SO test environment initially. The decision to move to SO testing instead of DO resulted in only one additional variable to account for, the step from a reducing to an oxidizing environment.

5.2.1 Oxidizing Furnace Methodology.

Testing in AFRL's oxidizing box furnace was completed according to the procedures presented in Section 5.1 except heating and cooling ramps rates were programmed at 20°C/min within the automatic furnace control. Table 5.8 shows the set points used for the test runs completed in AFRL's oxidizing furnace. Set-points were chosen to be as consistent with completed SR testing as possible to allow comparison across the two test environments. Following testing, coupons were sectioned and polished in the manner described in Section 5.1.1. Images were manipulated and analyzed in a manner similar to images gathered from Section 5.1 testing.

Table 5.8: Static Oxidizing furnace testing set-points. Analysis of nickel coupons for the SO-L1 and SO-M3 set-points did not show any sulfur degradation so nickel coupons were not used at any of the other set-points.

Designation	Media	Temperature (°C)	Cycles
SO-L1	.1CMAS	1150	2, 8, 16
SO-L5	.5CMAS	1200	8, 16
SO-M3	.3CMAS	1250	2, 8, 16
SO-H1	.1CMAS	1300	8, 16
SO-H3	.3CMAS	1350	4
SO-H5	.5CMAS	1300	8, 16

5.2.2 Results and Observations.

5.2.2.1 Appearance.

Tables 5.9 - 5.13 show the external change in appearance of coupons during SO testing. Wafers did not melt at the SO-L1, SO-L5, or SO-M3 set-points. Just as in SR testing, a halo was readily visible where the wafer had been placed prior to testing. The halo was used to help ensure wafers were placed in the same coupon position for each test run. Unlike SR testing, there was no adherence between nickel coupons and wafers post heating. The bottom of wafers showed a blue-green speckling beginning with the first cycle. Depending on valence state, nickel oxide can appear green (NiO) or dark grey (Ni₂O₃). The most common chrome oxide (Cr₂O₃) is green. Therefore the speckling is likely the result of the transport of metal oxides from the coupon surface to the wafers. The transport occurred without the wafer becoming molten.

Table 5.9: Change in appearance of coupons for SO-L1 test runs.

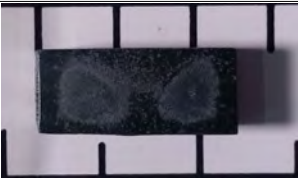
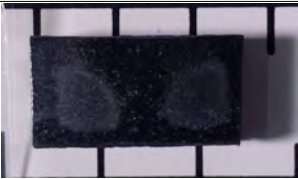




Material	2 cycles	8 cycles	16 cycles
Nickel			
Superalloy			

Table 5.10: Change in appearance of coupons for SO-L5 test runs.



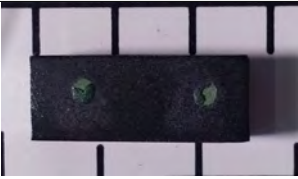
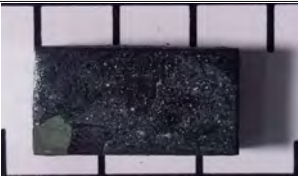
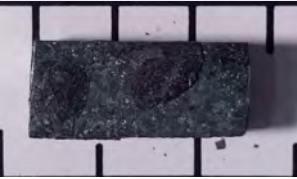

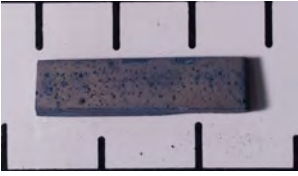

Material	8 cycles	16 cycles
Superalloy		

Table 5.11: Change in appearance of coupons for SO-M3 test runs.

Material	2 cycles	8 cycles	16 cycles
Nickel			
Superalloy			

Coupons showed a noticeable loss of volume as testing progressed at the SO-H1 and SO-H5 set-points. The loss of volume was most apparent at wafer locations where the coupon thickness was greatly reduced and the coupon width was tapered. Just as at lower temperatures, a halo effect was present, though not as readily identifiable. Coupons showed a lightly green-gray tint outside of halos with a slight blue tint under the halos. Unlike in reducing tests, the melted wafers were brittle and typically flaked apart with the slightest contact. The melted wafers also took the appearance of a thin film formed over a gas bubble as opposed to the fused pellets found in reducing tests.

Table 5.12: Change in appearance of coupons for SO-H1 test runs.



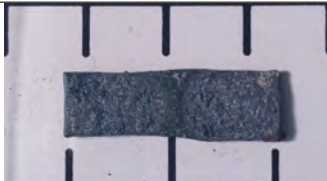
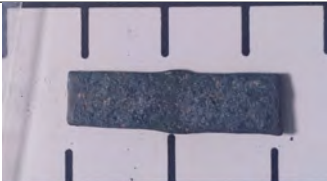
Material	8 cycles	16 cycles
Superalloy		

Table 5.13: Change in appearance of coupons for SO-H5 test runs.

Material	8 cycles	16 cycles
Superalloy		

5.2.2.2 *Extent of Degradation.*

Identification of sulfur-rich phases within SO tests was not as simple as it was for SR tests. Cross-sections from SR tests can be regarded as a “freeze-frame” of the sulfur attack. Without oxidization, there is little transport mechanism to remove the sulfides formed in SR tests, so the phases are readily visible on sectioning. In the SO tests, the sulfides are just an intermediary product

in route to oxide formation. In addition, as discussed in Sections 2.2.1 and 2.4, the oxides formed are volatile. Therefore the degradation products formed in SO tests may not be present in cross-sections to be measured. As a result degradation measurements for oxidizing test were defined differently.

5.2.2.2.1 Thickness of Degradation. SEM analysis of cross-sections of nickel coupons at the SO-L1 and SO-M3 set-points did not show the presence of a distinct sulfur phase. Only nickel oxide could be identified infiltrating the cross-sections. Therefore nickel coupons were not included in testing at any other SO set-point. Since sulfur phases were not easy to visibly identify, degradation thickness was measured based upon the appearance of physical damage to the superalloy. The presence of sulfur was found during EDS analysis of specific formation and EDS line scans into the depth of coupons. However the concentration of sulfur was lower than found in any SR test coupon, as would be expected by the fact that any sulfides formed are only intermediary products in the oxidizing environment. Figure 5.23 shows how the upper and lower limits were set for the thickness measurement. Since sulfur phases were not visible, unaffected regions were not removed from the right image of Figure 5.23 as had been done in Figure 5.7.

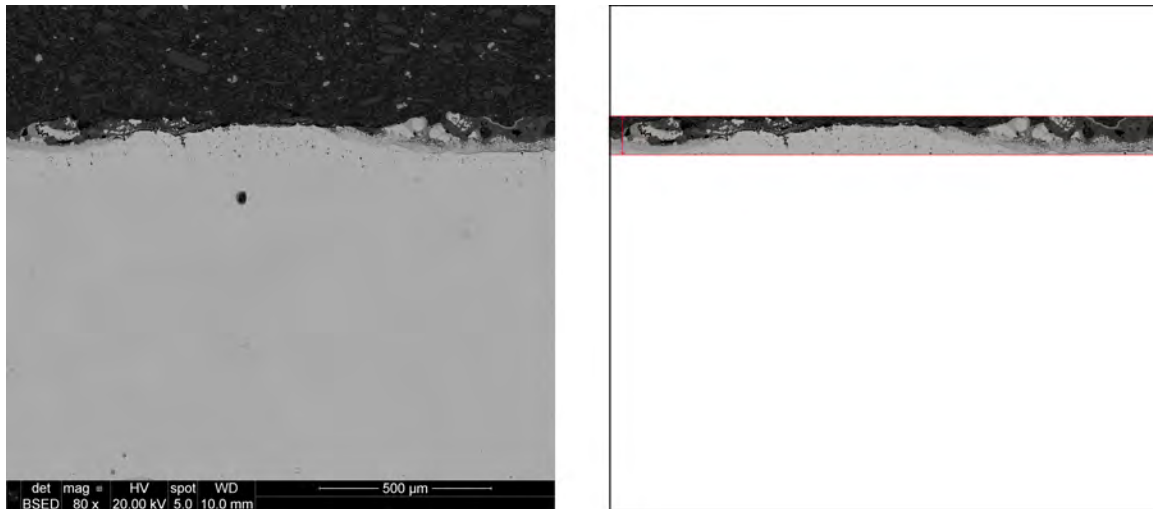


Figure 5.23: Measurement of degradation thickness for coupons tested in a SO. Sulfur phases were not visible in BSE images from SO testing (left image) as the nickel and chromium sulfides used to visibly identify degradation in SR testing were only intermediary steps in the SO environment. Therefore, the boundaries for thickness measurements (right image) were based on the upper and lower extents of physical degradation in cross-sections.

Figures 5.24 - 5.26 show the resulting measurements for thickness of degradation for the superalloy coupons at each oxidizing set-point. Just as was done for the SR testing coupons, second-order polynomial trend lines have been added for each set-point depicted in Figures 5.24 - 5.26 to allow discussion of general trends. These trend lines are simply curve fits, they are not meant to imply any underlying physical phenomena. In general, the thickest degradation was found at the center-point of each wafer position and decreased with radial position. There did not appear to be any trend with regard to radial position at the SO-L5 set-point for either cycle time it was tested at therefore a linear trend line for each of these set-points was applied. Figures 5.24 - 5.26 show less scatter in the data about the trend line for each set-point than had been found for nickel coupons in SR testing. When compared to SO testing only, SO-M3 showed the most scatter about its trend lines. In addition, a consistent pattern in level of degradation was found between the set-points. At both eight and 16 cycles, the order of decreasing degradation was SO-H1, SO-H5, SO-M3, SO-L5.

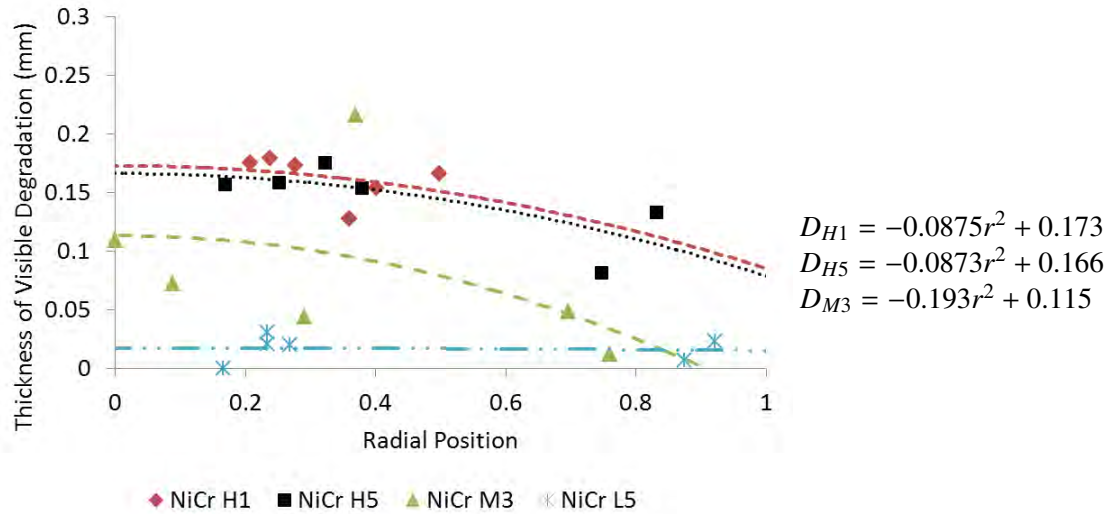


Figure 5.24: Thickness of physical degradation in superalloy coupons in SO tests at 16 cycles. Dashed lines depict quadratic curve fits for experimental data (equations are included for each curve). In general degradation decreased radially from the center-point of the wafer position. A linear fit was used for SO-L5 as no trend in radial position was evident. No underlying physical phenomena is implied by the curve fits.

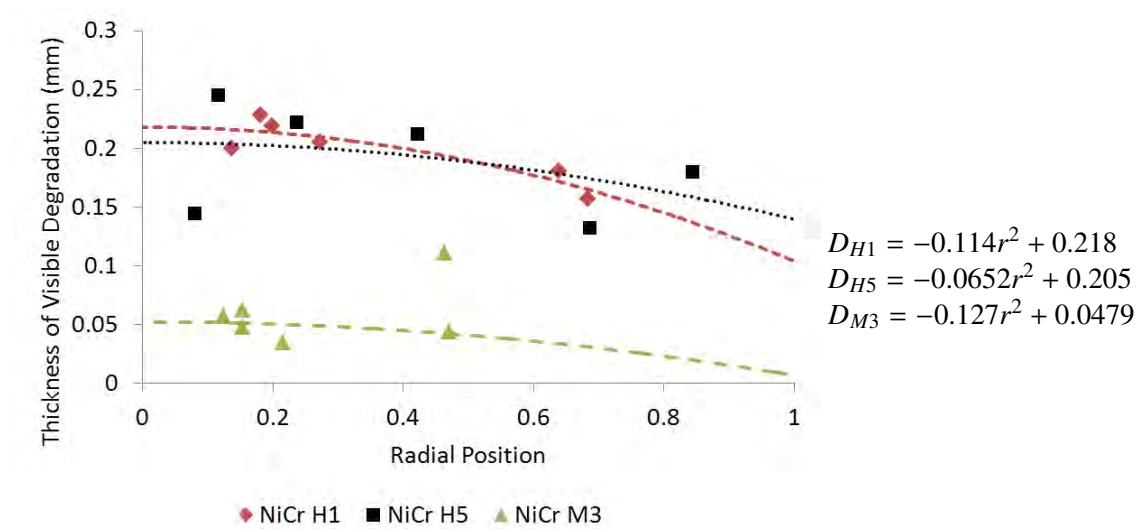


Figure 5.25: Thickness of physical degradation in superalloy coupons in SO tests at eight cycles. Dashed lines depict quadratic curve fits for experimental data (equations are included for each curve). In general degradation decreased radially from the center-point of the wafer position. A linear fit was used for SO-L5 as no trend in radial position was evident. No underlying physical phenomena is implied by the curve fits.

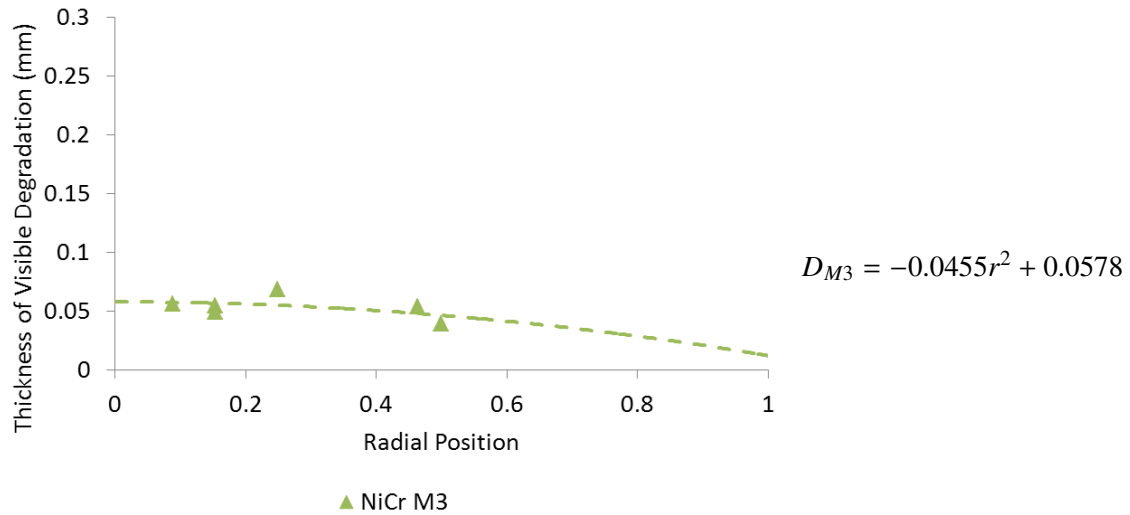


Figure 5.26: Thickness of physical degradation in superalloy coupons in SO tests at two cycles. Dashed lines depict quadratic curve fits for experimental data (equations are included for each curve). In general degradation decreased radially from the center-point of the wafer position. No underlying physical phenomena is implied by the curve fits.

5.2.2.2.2 Area of Degradation. As has been mentioned chemical degradation in SO coupons was not readily visible. In addition, physical degradation which could be seen often was

the result of voids left at the surface of cross-sections. Therefore an area fraction of degradation for SO set-points could not be readily measured.

5.2.3 Comparison to Static Reducing Tests.

As was introduced in Section 5.2.2.1, melted wafers from superalloy coupons had different appearances depending on whether they came from SR or SO testing. Melted wafers from SR were typically grayish with large regions of white (the initial color of the test dusts) at the center of the melt. The upper surfaces of melted wafer surfaces were smooth while the bottom surface, which had been in contact with the superalloy, was pocked as if the melt had trapped vapor pockets during the test run. However, the melted wafer still had a solid feel. In contrast, melted wafers from SO were typically a single blue-gray color. In addition, they were extremely thin and delicate and appeared to have formed on top of large vapor pockets. As discussed in Section 2.4, in an oxidizing atmosphere, the metal sulfides formed by reaction with sulfur, oxidize to metal oxides which are volatile at the temperatures used in SO testing. Vaporized metal oxides escaping the coupon account for the bubble-like appearance of the melted wafers in SO tests. In SR tests, no species off-gassed from the coupons. Figure 5.27 shows representative examples of melted wafers from SR and SO testing.

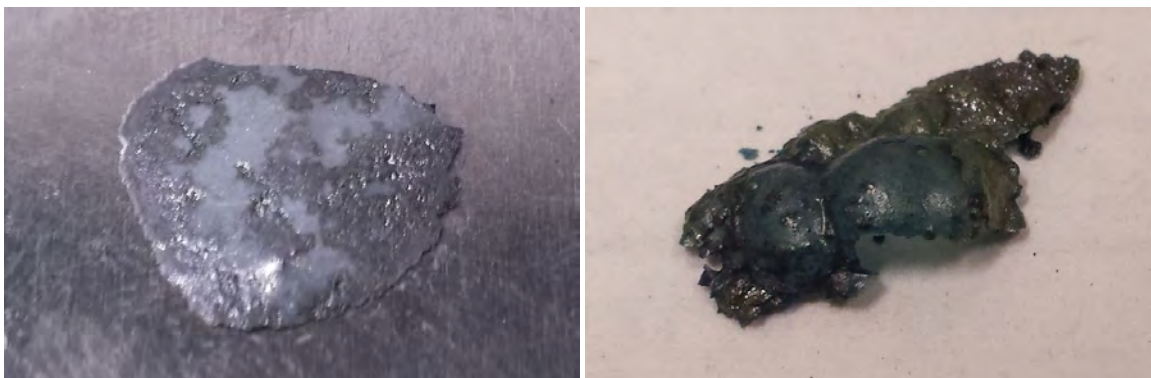


Figure 5.27: Representative melted wafers from SR-H1 (left) and SO-H5 (right) testing. Melted wafers from SR testing were solid gray masses. Melted wafers from SO testing were gray with a blue-green tint and appeared to have formed on top of a gas bubble, as such they were extremely thin and fragile.

Figures 5.28 and 5.29 depict the change in mass of superalloy coupons tested under SR and SO environments respectively. There is no significant change in mass for coupons where the test dust

did not melt for either environment. However, in SO testing, coupons on which the test dust melted showed significant mass loss. The mass loss for SO runs with melted wafers is due to a combination of two factors: the formation of volatile oxides of chromium and nickel, and the formation of a molten deposit which could act as a transport to flux the oxides away from the coupon. In fact, mass loss for the the SO-H3 set-point was so great that testing was halted after only four runs. Data collected at this set-point was not used to develop the models described in Chapter 6. Instead, the data collected was included as a validation point. The negligible change in mass at all SR and the SO-L1, SO-L5, and SO-M3 set-points suggest thickness of degradation may sufficiently quantify damage at these set-points. However, the substantial mass and volume changes of SO-H1 and SO-H5 coupons mean these thickness of degradation does not capture the entire extent of degradation. The ability of thickness of degradation to fully capture degradation at only some set-points will have significant consequences in the attempt to construct a model to predict damage due to gypsiferous dusts.

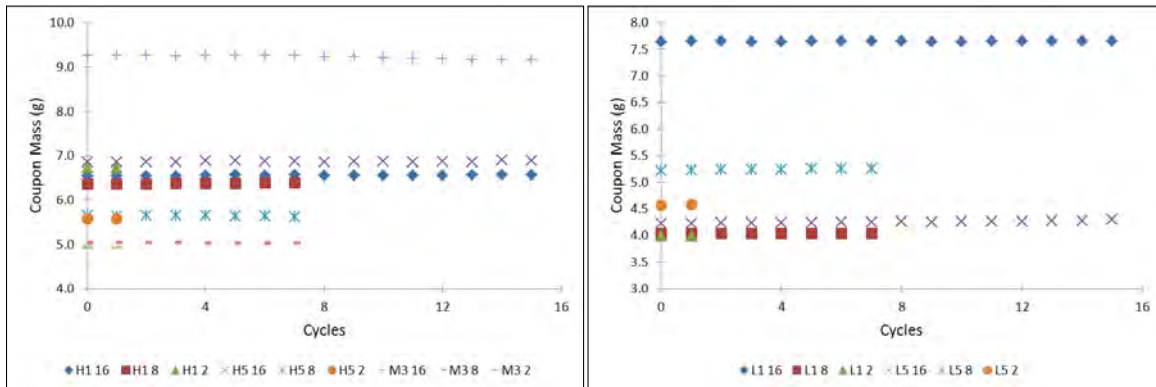


Figure 5.28: Coupon mass measured after each temperature run for SR environment set-points where test dust melted (left) and did not melt (right). No change in mass was evident for any SR set-point within the cycles tested.

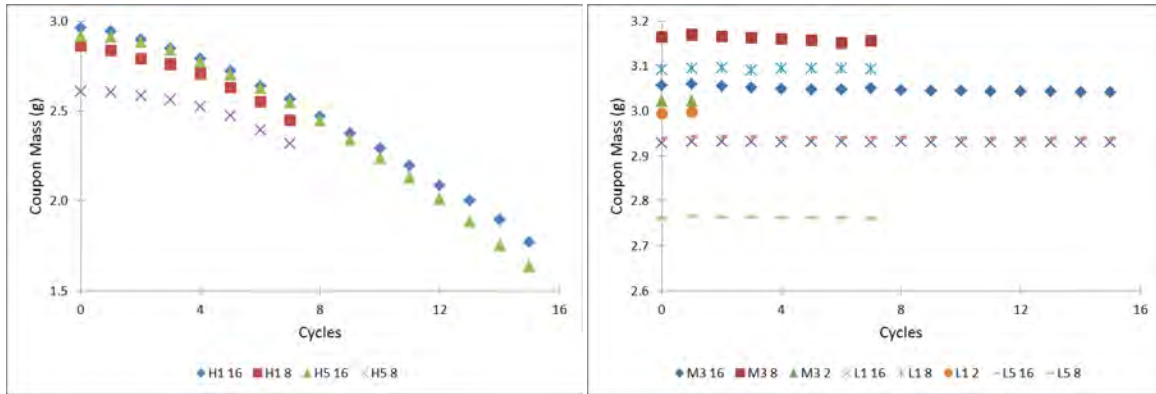


Figure 5.29: Coupon mass measured after each temperature run for SO environment set-points where test dust melted (left) and did not melt (right). No change in mass was found for SO set-points where the test dust wafers did not melt. However, substantial coupon mass loss was measured when the test wafers melted. The extreme mass loss accounts for an additional level of degradation in SO testing that the thickness of degradation measurement could not capture.

In the late 1930s Avrami adapted an equation originally derived by Kolmogorov to describe the rate at which a solid will undergo a phase transformation at constant temperature. A simplified version of the Avrami equation (also known as the Johnson-Mehl-Avrami-Kolmogorov, or JMAK, equation) is shown in Equation (5.2). The equation can be used to calculate the volume fraction of a solid, V , which has undergone phase transformation at a given time, t . k is a constant determined by the geometry of nuclei of phase change. n is time factor constant which also accounts for whether or how the nuclei growth is constrained in any direction. Both k and n must be determined experimentally [41, 100].

$$V(t) = 1 - e^{-kt^n} \quad (5.2)$$

All static furnace testing accomplished in this research effort included 30-minute isothermal soaks. It was assumed that the measured degradation for each test run occurred predominately during the isothermal soak. Therefore, the Avrami equation (Equation (5.2)) was applicable. The large mass loss found during testing at the SO-H1 and SO-H5 set-points was largely due to the formation of nickel and chromium oxides which off-gassed from the coupons (Figure 5.27 is evidence of this off-gassing). As the mass loss is directly tied to a phase change in the coupon, the Avrami equation suggests that mass loss should increase exponentially with time at a fixed

temperature. In fact experimental measurements found this relationship. The mass loss for all six coupons used for the SO-H1 and SO-H5 set-points, regardless of starting coupon mass, was found to increase exponentially with cycles.

Since the measured experimental data suggested that the Avrami equation may be applicable to this system, the constants k and n were determined by plotting the rearranged version of the Avrami equation shown in Equation (5.3). The slope of the linear fit to the resulting curve plotted using Equation (5.3) is n and the y-intercept will be $\ln(k)$.

$$\ln(-\ln(1 - V)) = \ln(k) + n\ln(t) \quad (5.3)$$

Figure 5.30 shows the resulting plots for the two set-points which had melted wafers: SO-H1 and SO-H5. From the plots, the values of k and n for SO-H1 were found to be 3.25×10^{-5} and 1.59 respectively. The values of k and n for SO-H5 were found to be 1.55×10^{-6} and 2.10 respectively. Three coupons were run at each set-point: two for 16 cycles and one for eight cycles. Each plot shows good overlap for its three coupons irrespective of starting coupon mass or final number of cycles. Both set-points were set at 1300°C for 30-minute temperature soaks on the same superalloy. The only difference between the two set-points is the attack media used. Therefore, it is reasonable that the primary cause of the different Avrami constants found for each set-point is the concentration of sulfate in the attack media. This suggests that the attack media does not just provide sulfate to initiate HC but changes the melting properties of the attacked substrate. Further testing with various gypsiferous dusts at other soak temperatures and soak durations is suggested to prove this hypothesis.

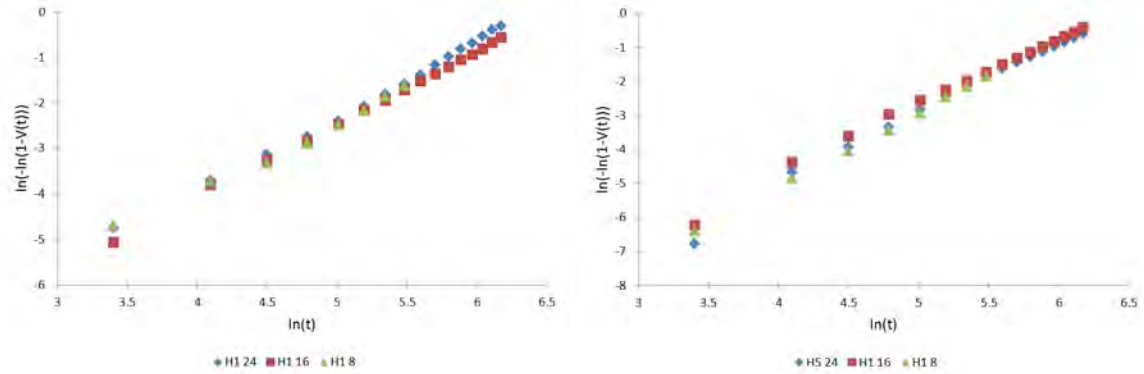


Figure 5.30: The Avrami constants for SO-H1 (left) and SO-H5 (right) were determined using these plots. The slope of the linear lines in each plot give n . The y-intercept of each plot gives $\ln(k)$. Both test runs were at 1300°C with 30-minute soaks. The only difference between the two test runs was the concentration of sulfate loaded for each temperature soak (0.0478 for .1CMAS and 0.1942 for .5CMAS).

Mass loss at the SO-H1 and SO-H5 set-points was transformed into an equivalent thickness of degradation by use of the superalloy density and wafer area. In order to identify trends between total degradation, the degradation shown in Figures 5.24 - 5.26 was reduced to equivalent degradation at $r = 0$ as had been done for SR tests and the equivalent thickness due to mass loss was added to these results. Figure 5.31 shows the total degradation at each set-point plot against time. At the SO-M3 and SO-L5 set-points, where there was no mass loss, degradation increased with the natural logarithm of time just as was found in SR testing. However for SO-H1 and SO-H5 set-points, the degradation increased exponentially with time.

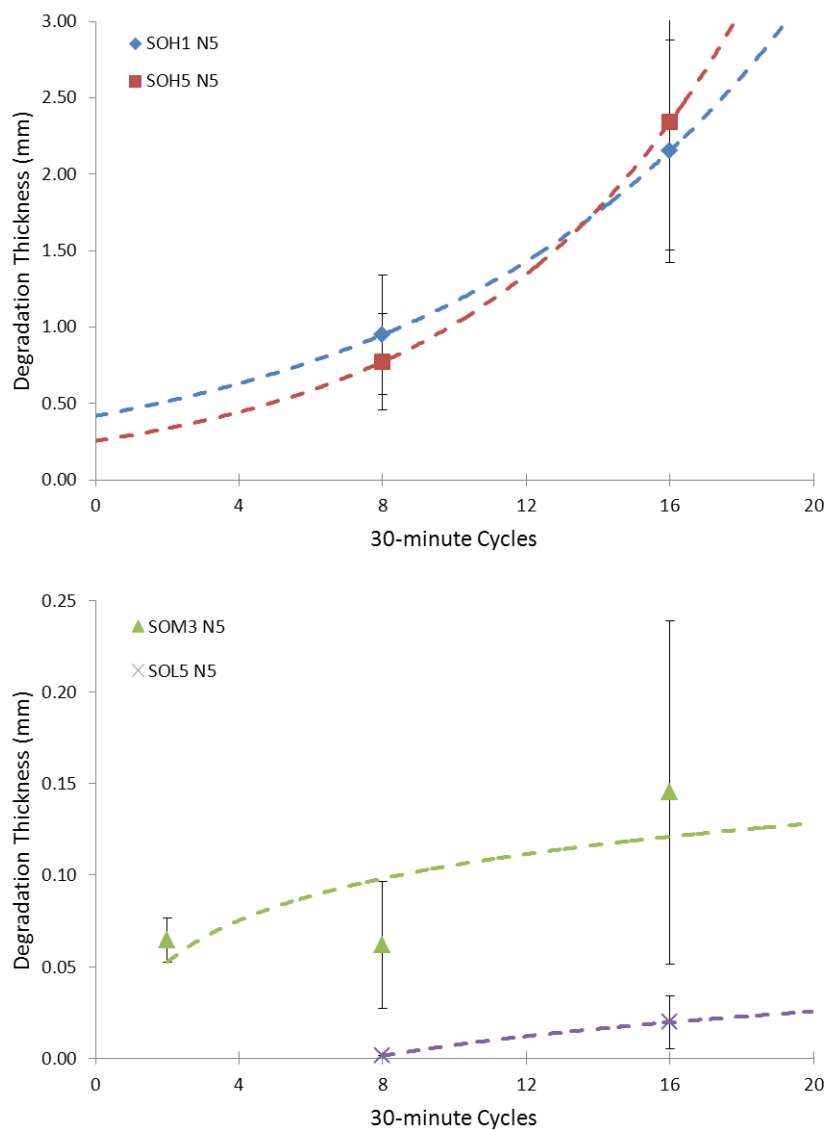


Figure 5.31: The equivalent degradation at $r = 0$ for each set-point plotted against time. In this figure, the average measured degradation at each set-point is depicted as a data-point. Error bars are for an 80% confidence interval of the standard error of measured degradation calculated at each set-point. For the SO-H1 and SO-H5 set-points (top image) which showed significant mass loss, the equivalent degradation increased exponentially with cycles. For the SO-L5 and SO-M3 set-points (bottom image) the equivalent degradation increased with the natural log of cycles. In general, the order of decreasing degradation was SR-H1, SR-H5, SR-M3, SR-L5. However, for higher cycles, the SR-H5 trend predicts it will have the most degradation.

Figure 5.32 shows an example of the difference in presentation of sulfur degradation between tests run in a oxidizing environment (left image) and a reducing environment (right image). An image of HTHC damage (middle image), representing the accepted presentation of HC damage

at high temperatures, is included for comparison. The two images taken from this research effort compare favorably with the accepted presentation of HTHC. The notable exception being that “Zone 1” is not present in the reducing image as the formation of the porous metal oxide layer associated with “Zone 1” is not possible without an oxidizing environment. The “Zone 2” chromium-depleted zone is readily visible for both images taken from the current research effort.

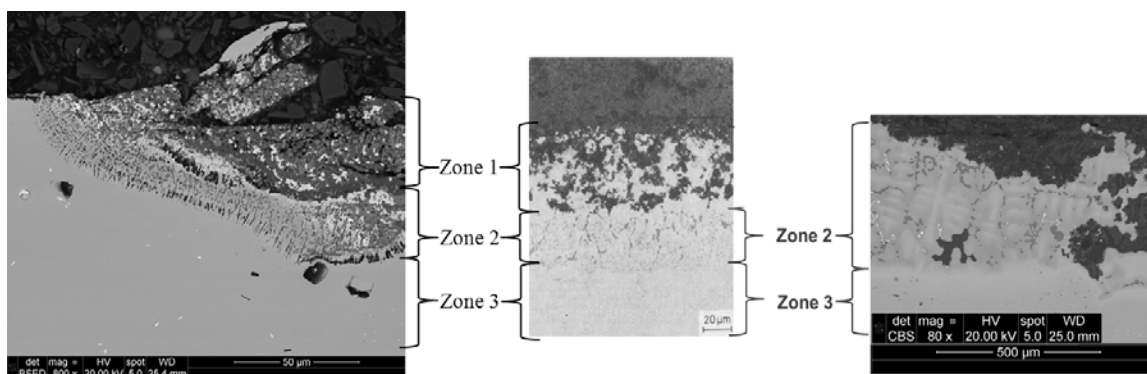


Figure 5.32: Comparison of sulfur degradation noted in oxidizing (left) and reducing (right) environments in this study. The image in the middle is a depiction of sulfur degradation caused by sodium sulfate [96]. The images from this study confirm that gypsum can cause sulfur degradation which presents similarly to HC as currently defined in literature. The images also confirm that gypsum-induced HC can occur at temperatures beyond the current temperature range cited for sodium sulfate-induced HC.

Figure 5.32 depicts another difference between degradation in oxidizing and reducing environments. The conversion of sulfides to oxides, which was only possible in the oxidizing environment, seems to provide a transport mechanism of chemical phases formed in the coupons. Without a transport mechanism, the various new phases formed by the introduction of sulfur into the superalloy are allowed to grow *in situ*. The lack of movement in SR testing causes the large, distinct phases seen in the coupon in the right image of Figure 5.32. With the oxidizing transport mechanism, these phases cannot grow, instead the species formed by reaction with sulfur are removed from the coupon.

5.3 Objective 2 Summary

Chapter 2 concluded with the assertion that sodium sulfate cannot be the cause of HC issues currently experienced in DoD aviation GTE. Instead, gypsum was proposed as the initiator, largely

due to the fact that, unlike sodium sulfate, it is present in the environments HC has proven to be an issue for the DoD. Testing introduced in this chapter, showed that in SR testing, at a temperature favored by sodium sulfate, sulfur infiltration into a nickel coupon is comparable whether the sulfur source is gypsum or sodium sulfate. However at a temperature sodium sulfate is known to cause minimal damage (and is closer to current operating temperatures in current DoD aviation GTEs) gypsum causes significantly more sulfur infiltration and substrate damage. The remainder of this chapter therefore examined degradation caused by a gypsiferous test dust and found damage to approximate the degradation currently associated with HC.

The “bubble” formation mentioned in Section 5.1.3.1 on nickel coupons were determined to be nickel sulfides during EDS analysis. Superalloy cross-sections reveal the growth of new Ni-Cr phases above the original coupon surface. The transport of metal from the substrate into molten CMAS deposits is significant because it shows the beginning of the fluxing associated with HC even without the presence of an oxidizing environment despite the fact that current literature attributes the oxidizing of metal sulfides as the cause of metal fluxing out of the substrate. In SO testing the transfer of metal from the substrate into deposit was more pronounced with metallic phases penetrating far into dust deposits at the surface of coupons. The transfer of metal from SO superalloy coupons created a porous structure at the coupon surface. The fluxing of metals (particularly nickel and chromium) from the substrate to the gas/deposit interface matches the current definition of HC.

The discoloration of the bottom of unmelted wafers from both SR and SO tests suggested that nickel and chromium from the test coupons were leaching into the test wafers. The fact that leaching occurred without the test wafers becoming molten is significant as the current explanation of HC relies on a molten deposit for metal transport out of the substrate. The ability of a gypsiferous dust to remove metal from the substrate without being molten raises the possibility of gypsum-induced HC degradation below the melting point of gypsum.

SR coupons revealed the leaching of chromium from surrounding areas into a Cr-S formation. At all but the SR-L1 set-point, a region almost completely depleted of chromium could be found surrounding the Cr-S formations. EDS analysis of SO coupons showed a region (though not visibly identifiable) just below the physical degradation that was measured in Section 5.2.2.2.1 which had

a lower concentration of chromium than expected for the recipe of the particular superalloy studied in this effort. At the SO-H1 and SO-H5 set-points, the metal fluxing had progressed to the point that separate nickel and nickel-sulfur formations could be found at the top of glass deposits at the surface of the coupons. The fact that nearly pure nickel phases existed on superalloy coupons suggests complete localized chromium depletion followed by sulfur attack on nickel. The presence of a chromium-depleted zone beneath a porous metal structure matches the current definition of HC.

In conclusion, the damage depicted in Figure 5.32 serves as a summary of the arguments presented in this paper. The damage in the middle image was caused by sodium sulfate at 830°C. The damage seen in the other two images in Figure 5.32 were caused by gypsum at 1250°C. As discussed in Chapter 2, current literature states that gypsum does not cause HC and HC does not occur at temperatures exceeding 1000°C. Therefore, these images are a direct contradiction to current research and a clear indication of the need to reexamine the current body of HC knowledge in light of the operational reality of today's GTEs. As a start, Chapter 6 will present an initial model based upon this research to predict damage caused by a gypsiferous dust on a superalloy.

VI. Sulfate Attack Model

The last objectives of this research effort were to develop a model for sulfur attack on superalloy components and then evaluate the efficacy of the model using select natural desert dusts. An initial set of models was developed to describe the phenomenological relationship between extent of degradation and temperature, sulfate concentration, and cycle time. The initial models were simple polynomial equations based on statistical curve fitting. The initial statistical models were used to develop the final model which was designed in the form of a kinetic rate law equation.

6.1 Initial Model Development

The initial models developed for this research effort is based upon three primary variables: the coupon surface temperature, the concentration of sulfate ion in the attack media, and the cumulative exposure time at the peak surface temperature. Similar to the concept introduced in Figure 2.9, degradation due to desert dust ingestion (even if it does not form a CMAS glass), follows a sequence of probabilistic events. A generic timeline for degradation due to desert dust ingestion is presented in Figure 6.1

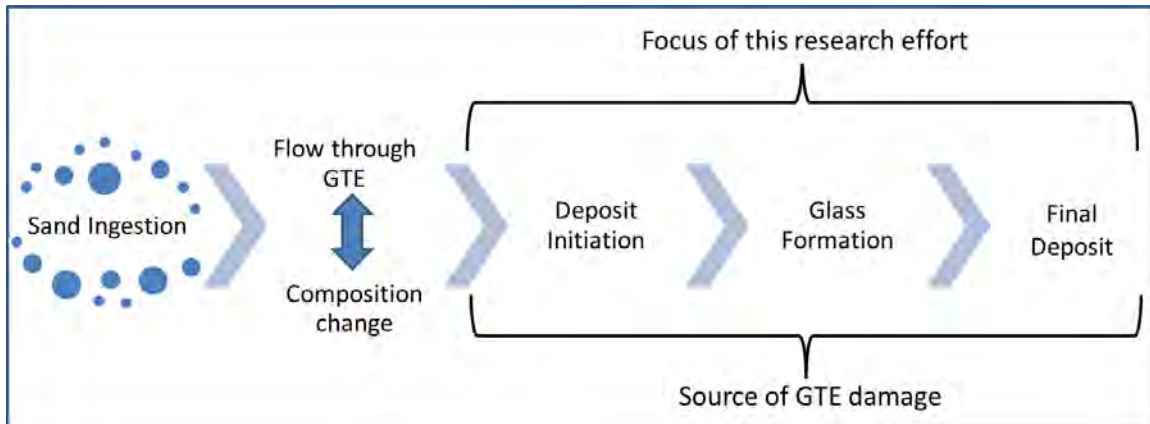


Figure 6.1: Example sequence of events for degradation due to gypsiferous desert dust ingestion accounting for the issues raised in Chapters 2 and 4. GTE component damage is likely the result of the three steps bracketed in the figure, therefore, this research effort has examined all three steps. The other steps shown in this figure are highly influenced by the specific design of a particular GTE and therefore beyond the scope of this research effort.

The initial three steps depicted in Figure 6.1 are primarily dependent upon the specific configuration of the GTE affected and therefore beyond the scope of this research effort. Instead the models discussed in this chapter were developed with the intent of making them as broadly applicable as possible. In that vein, several functions were developed to predict degradation due to an attack media of a specific composition (following whatever changes may have occurred in Step 2) impacting a substrate with a known surface temperature, at Step 3 of Figure 6.1. The variables examined to create the initial model are described in the following sections.

6.1.1 Position.

The measurements presented in Figures 5.8 - 5.11 and Figures 5.14 - 5.16 showed that degradation varied with radial position when temperature, sulfate concentration, and cycle time were held constant. Therefore, initially attempts were made to include radial position as an independent variable in developing the degradation model. However, using JMP v10.0.2 statistical analysis software, if temperature and sulfate concentration were included as variables, no statistically significant treatment of radial position could be found within the limited data obtained during testing. The most significant treatment of radial position had p-values of 0.57 and 0.20 ($p < 0.05$ is typically used to signify significance) for first-order and second-order radial position terms respectively. The interaction terms between radial position and either temperature or sulfate concentration were found to be even less significant. At the same time, all temperature and sulfate concentration terms (other than those involving interaction with radial position) had p-values less than 0.05. Therefore, a single thickness (with associated error) at $r = 0$ was calculated from each data point using the trend line curve's equation (as discussed in Section 5.1.3.3.1). The removal of radial position as a potential variable meant the model would not be able to predict a depth profile of attack, only a maximum level. However, it also allowed the inclusion of peak temperature soak time as a variable within the numbers of data-points already collected during testing. Tables 6.1 and 6.2 show the average calculated \hat{D} for each set-point measured in this study. The tolerance values given are the sample deviation of measured values at each set-point. In the tables "not tested" means a particular set-point was not tested. A dash means that the value at that set-point was defined as zero as described in Section 5.1.3.3.1

Table 6.1: The average equivalent degradation at $r = 0$ (denoted \hat{D}) for each SR set-point calculated as described in Section 5.1.3.3.1. Tolerance bands were calculated at the 80% confidence level using the standard error of measured values at each set-point. Calculated tolerance bands may be outside of actual precision of measurement.

\hat{D} (mm) for nickel coupons				
Set-Point	16 cycles	8 cycles	4 cycles	2 cycles
H1	0.693 \pm 0.160	0.486 \pm 0.098	0.477 \pm 0.042	0.219 \pm 0.133
H5	0.819 \pm 0.349	0.794 \pm 0.149	0.383 \pm 0.049	0.368 \pm 0.004
M3	0.637 \pm 0.149	0.550 \pm 0.044	0.521 \pm 0.125	0.237 \pm 0.088
L5	0.0570 \pm 0.0462	0.0307 \pm 0.0361	0.112 \pm 0.012	0.126 \pm 0.014
\hat{D} (mm) for superalloy coupons				
H1	1.24 \pm 0.28	0.735 \pm 0.091	not tested	0.524 \pm 0.036
H5	1.41 \pm 0.26	1.06 \pm 0.27	not tested	0.441 \pm 0.070
M3	0.615 \pm 0.249	0.418 \pm 0.094	not tested	0.229 \pm 0.197
L5	0.202 \pm 0.070	0.132 \pm 0.043	not tested	0.0339 \pm 0.0031

Table 6.2: The average equivalent degradation at $r = 0$ (denoted \hat{D}) for each SO set-point calculated as described in Section 5.1.3.3.1. Measurements shown do not include degradation thickness calculated due to mass loss. Tolerance bands were calculated at the 80% confidence level using the standard error of measured values at each set-point. Calculated tolerance bands may be outside of actual precision of measurement.

\hat{D} (mm)			
Set-Point	16 cycles	8 cycles	2 cycles
H1	0.173 \pm 0.023	0.218 \pm 0.014	not tested
H5	0.166 \pm 0.028	0.205 \pm 0.052	not tested
M3	0.125 \pm 0.083	0.0479 \pm 0.0310	0.0578 \pm 0.0102
L1	0.0725 \pm 0.0335	—	—
L5	0.0176 \pm 0.0144	—	not tested

6.1.2 Peak Temperature Soak Time.

Within the initial models, cumulative soak time (variable t) was defined as the cumulative time (in minutes) the coupons were soaked at the peak temperature set-point. For example, a coupon subjected to eight 30-minute cycles experienced a total peak soak time of 240 minutes.

6.1.3 Temperature Dependence.

The temperature dependence of attack can be separated into at least two components: effect on the attacked substrate and effect on the attacking dust. In polycrystalline substrates, grain boundaries can widen as a result of the CTE of the substrate. Wider boundaries provide an increased opportunity for infiltration of the attack dust. This research effort did not examine sufficient substrate material types to develop a relationship to account for this temperature effect. Ignoring the temperature effect on the substrate is a potential source of error identified as an item of future work to refine the models developed later in this chapter.

For the remaining temperature effect, it was initially proposed that temperature should be expressed as a function of attack dust. The following illustration explains this decision. Using the simple gypsiferous CMAS blends of this research effort as a starting point, it would be possible to add additional fluxing agents to lower the melting point of the test dusts. In fact, the dust recipe could be modified in a manner that sulfate concentration was unaffected but melting point was decreased. As the current accepted mechanism of HC relies on a molten deposit, it is logical that a gypsiferous CMAS, and a gypsiferous CMAS with additional fluxing agents, would produce different levels of sulfur degradation at the same temperature.

Figure 6.2 shows the relationship between fraction of melt formation and normalized temperature for the samples tested in Section 4.1. The values of fraction melt formed were reported in Table 4.3. For each test dust, the data points shown in Table 6.3 were identified. The onset of softening was defined as the nadir of the last valley before the final melting curve. The end of melting was defined as the nadir of the last valley before DSC run termination at 1400°C. The melting peak was defined as the temperature of the highest peak between these two points. Temperature was normalized for each test dust setting the softening point to zero and the end of melting to unity.

Table 6.3: Data points, obtained from DSC data, used to develop melting relationship of select dusts.

Dust	Softening Point (°C)	Primary Melting Peak (°C)	End of Primary Melting (°C)
GB1	920	1200	1375
YPG	910	1190	1380
AFRL02	755	1150	1325
Oxide Mix	1200	1330	1385
Aramco	815	1370	1380
PTI A2	865	1160	1350
.1CMAS	1135	1315	1380
.5CMAS	1105	1295	1400

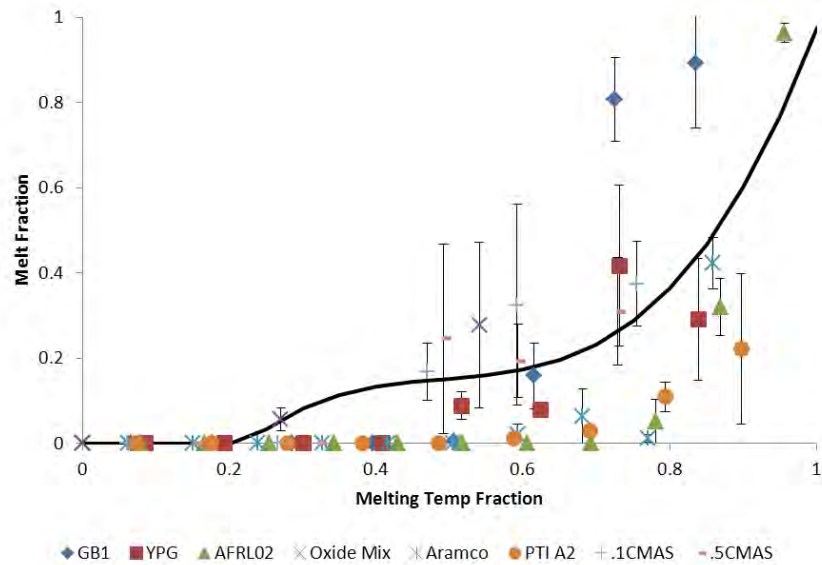


Figure 6.2: Relationship between fraction melt formed and normalized temperature. The solid curve is the best data fit given by Equation (6.1). Though the fitted curve was statistically significant, the test data contained significant noise. As a result the curve fit was a poor predictor of melt fraction.

The data-points, as shown in Figure 6.2, were analyzed in JMP to give a relation between normalized temperature (variable \hat{T}) and melt fraction (variable FM). The relationship developed using JMP is presented in Equation (6.1). The relationship was determined to be statistically significant with $p < 0.001$, however the equation could only account for 29% of the variance in melt fraction, and most importantly the lack of fit of the model was also deemed significant. However,

the relationship was better than expressions developed for melt fraction using temperature directly.

$$FM(\hat{T}) = -0.607 + 4.33\hat{T} - 8.49\hat{T}^2 + 5.74\hat{T}^3 \quad (6.1)$$

Without a better predictor of melt fraction, it was decided to leave temperature unmodified as the input variable for degradation. However, development of a better relationship for melt fraction is suggested as a future area of study to better tie exposure temperature to attack dust response and hopefully provide a more accurate degradation model. Two primary additional variables are suggested for further study to improve the melt fraction function: particle size distribution and presence of volatiles. The amount of energy needed to melt a dust sample is related to the sample's particle size distribution. Smaller particles can obtain uniform temperature in less time than large particles at the same energy input. Volatiles act as fluxing agents which can depress melting temperature of a sample. This behavior is captured directly by DSC measurements (as evidenced by the shift in melting point due to the addition of gypsum shown in Figures 4.22 and 4.23). However, volatiles also cause sample compositional changes as the volatile off-gases. Therefore it would be possible for a volatile to allow the onset of melting at a depressed temperature then off-gas leaving a sample whose melting progression shifts to approach the melt progression that would be expected of a sample which never had volatiles. As an example, .1CMAS begins to melt at 1135°C. If all of .1CMAS's sulfate off-gassed before the sample was fully melted, .1CMAS should begin to behave like Oxide Mix with .1CMAS's melt progression tracing Oxide Mix's.

6.1.4 Sulfur Dependence.

For the initial model, concentration of sulfate (assigned the variable s) was not translated through any additional formula. The input values of s were 0.0478, 0.129, or 0.194 for .1CMAS, .3CMAS, and .5CMAS respectively.

6.1.5 Thickness of Degradation in a Reducing Environment.

Based upon the discussion presented in Sections 6.1.1 - 6.1.4 an initial model of degradation was developed. This model was only based on the results of SR furnace testing and accounted for nickel and superalloy coupons separately. An "Effect Screening" module built into JMP

was used to determine what combination of independent variables accounted for the most significant contributions to the variance in measured degradation. The curve fit described in Equation (6.2) was developed based on JMP's outputs to describe the phenomenological relationship measured in testing between degradation (output) and temperature, sulfate concentration, and cycles (independent variables). Logarithmic values were used for the three input variables due to the five order-of-magnitude spread in variables (T on the order of 10^3 , \hat{D} and s on the order of 10^{-2} - 10^{-1}). The constants determined for Equation (6.2) are listed in Table 6.4.

$$\hat{D}(T, s, t)_{SR} = c_0 + c_1 \ln(T) + c_2 \ln(s) + c_3 \ln(t) + c_4 \ln(T) * \ln(t) + c_5 (\ln(T))^2 \quad (6.2)$$

Table 6.4: JMP was used to determine the constants for thickness of degradation in nickel (left) and superalloy (right) coupons in a SR environment. The constants are used in Equation (6.2).

Constant	Value	Constant	Value
c_0	-1350	c_0	4210
c_1	387	c_1	-1180
c_2	0.0730	c_2	0.105
c_3	-15.1	c_3	-20.7
c_4	2.14	c_4	2.95
c_5	-27.7	c_5	82.2

The constants listed in Table 6.4 can then be used to plot a response surface for any combination of temperature, sulfate concentration, and cycles. As an example, Figure 6.3 was plotted using Matlab to show maximum sulfur infiltration into coupons loaded with .5CMAS as a function of temperature and cycles. The statistical model for nickel coupon degradation was determined to be statistically significant with $p < 0.0001$ and a root-mean-square error (RMSE) of 0.111. RMSE is a measure of the standard deviation between predicted and measured values. A good value of RMSE should be low in comparison to the range of measured values. For example, the RMSE for nickel degradation was 0.111 which is low when compared to the measured range of degradation

of 1.03 mm. The measurement of lack-of-fit (LOF) was high ($LOF = 0.0664$), but not significant (defined as $LOF < 0.05$). The model for superalloy degradation was also found to be statistically significant with $p < 0.001$ and RMSE of 0.157 compared to a measurement range of 1.46 mm. RMSE can be used to compare two models when the range of the dependent variables of each model are equal. Therefore the error in these two models is nearly equivalent with RMSE accounting for approximately 10.8% error in each. LOF was higher for the superalloy ($LOF = 0.0566$), though still not considered significant.

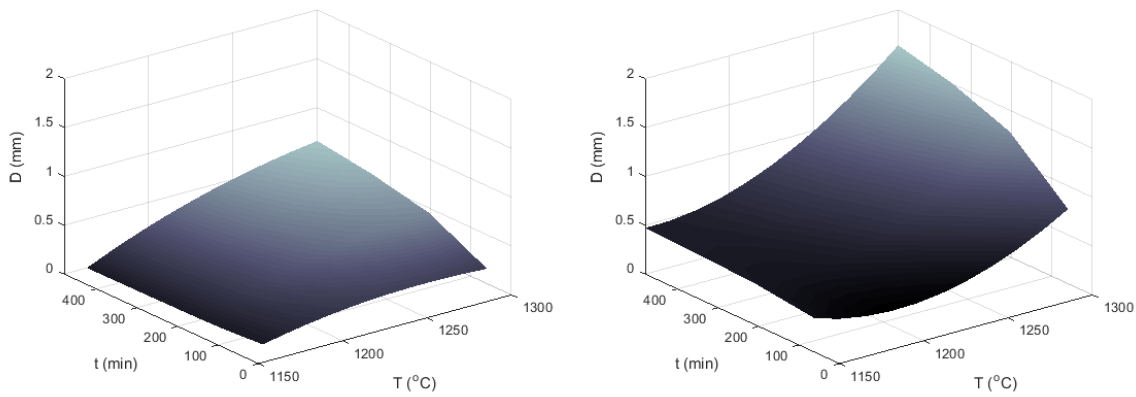


Figure 6.3: Predicted thickness of sulfur phase due to .5CMAS loading on nickel (left) and superalloy (right) coupons in SR testing.

6.1.6 Thickness of Degradation in an Oxidizing Environment.

The curve fit described in Equation (6.3) was developed using JMP to describe the phenomenological relationship measured in testing between degradation (output) and temperature, sulfate concentration, and cycles (independent variables). As with the SR models, logarithmic values were used for the three input variables due to the five order-of-magnitude spread in variables. Equation (6.3) was built in the same form as the two SR models. However, the constants were different. The constants determined for Equation (6.3) are listed in Table 6.5.

$$\hat{D}(T, s, t)_{NiCr,SO} = c_0 + c_1 \ln(T) + c_2 \ln(s) + c_3 \ln(t) + c_4 \ln(T) * \ln(t) + c_5 (\ln(T))^2 \quad (6.3)$$

Table 6.5: JMP was used to determine the constants for thickness of degradation in nickel (left) and superalloy (right) coupons in a SO environment. The constants are used in Equation (6.3).

Constant	Value
c_0	991
c_1	-283
c_2	-0.0106
c_3	3.14
c_4	-0.438
c_5	20.1

Figure 6.4 was plotted using Matlab to show maximum sulfur infiltration into a superalloy coupon loaded with .5CMAS as a function of temperature and cycles. The statistical model for SO degradation was determined to be statistically significant with $p < 0.0001$ and a RMSE of 0.0384 on a range of 0.245. RMSE was not as good for the SO model compared to either SR model since RMSE represented 15.7% of the measurement range. LOF was relatively high ($LOF = 0.0689$), though still not significant. LOF for the SO model was lower than either SR model.

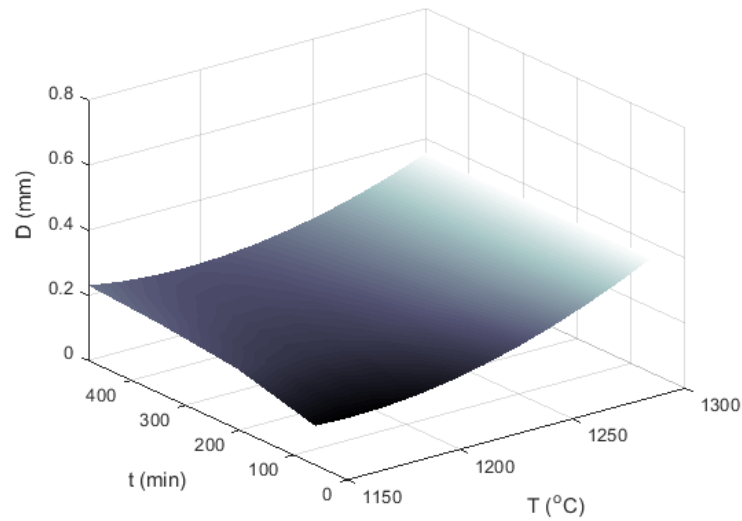


Figure 6.4: Predicted thickness of sulfur phase due to .5CMAS loading on superalloy coupons in SO testing.

6.1.7 Mass Loss in an Oxidizing Environment.

The measured thickness of degradation in SO testing matches what would have been expected: the highest temperatures show more degradation than the lowest. However the plots of coupon mass versus cycles presented in Section 5.2.3 show that thickness of degradation under-reports degradation in SO testing when the test media melts. Mass loss of SO coupons was analyzed against temperature, sulfate concentration, and time in JMP. The curve fit described in Equation (6.4) was developed to describe the phenomenological relationship measured in testing between degradation (output) and temperature, sulfate concentration, and cycles (independent variables). As with the other three JMP models, logarithmic values were used for the three input variables due to the five order-of-magnitude spread in variables.

For the other statistical models, it was found that some higher-order-terms could be neglected without appreciably affecting the overall curve fit. This was true regardless of the significance of correlation for an individual term found by JMP. Ignoring certain higher-order-terms allowed construction of the previous three models in the same mathematical form. A single mathematical form was desired as it was believed it would allow the models to be merged into a single model at a later date. The statistical curve fit for mass loss, however, required every second-order term JMP deemed as significant. Therefore, Equation (6.4) is significantly more complex than Equations (6.2) and (6.3). In addition, the constants determined for Equations (6.2) and (6.3) could be truncated after only two decimal places without causing a significant change in predicted values. Truncating at fewer than three decimal places for the mass loss model constants caused significant changes in predicted values. These two issues suggest the mass loss model to be less tolerant to measurement error than the other three models. The constants determined for Equation (6.4) are listed in Table 6.6.

$$M(T, s, t)_{NiCr,SO} = c_0 + c_1T + c_2s + c_3t + c_4T * s + c_5T * t + c_6s * t + c_7T^2 + c_8t^2 \quad (6.4)$$

Table 6.6: JMP was used to determine the constants for mass loss in superalloy coupons in a SO environment. The constants are used in Equation (6.4).

Constant	Value	Constant	Value
c_0	100.0	c_5	2.38
c_1	-0.163	c_6	-0.002 81
c_2	16.9	c_7	6.60
c_3	-0.0287	c_8	1.75
c_4	-0.0126		

Figure 6.5 was plotted using Matlab to superalloy coupon mass loss due to loading with .5CMAS as a function of temperature and cycles. The statistical model for mass loss was determined to be statistically significant with $p < 0.0001$ and a RMSE of 0.00471 on a range of 0.0829. RMSE and LOF for the mass loss model were significantly better than the other three models with RMSE representing only 5.68% of the measurement range and $LOF = 0.880$. The better fit of the mass loss model as compared to the three thickness models was an expected outcome of polynomial curve fitting. Polynomial curve fits are generally expected to improve with increasings numbers of higher order terms.

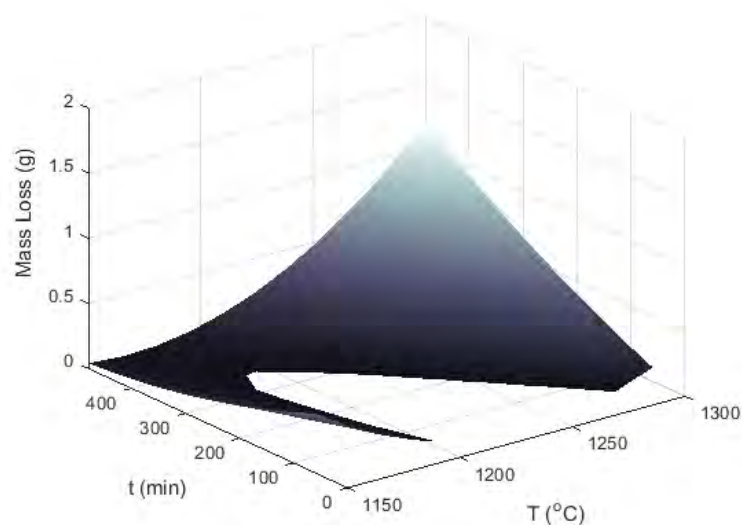


Figure 6.5: Predicted coupon mass loss due to .5CMAS loading on superalloy coupons in SO testing. The parabolic nature of the response surface due primarily to the quadratic terms of T cause the JMP model to deviate from measured values of mass loss at lower temperatures. A new model form is identified in Section 6.2 to correct this issue.

Despite fitting test data well, Equation (6.4) presented two significant issues. First, the white cut-out within the response surface shown in Figure 6.5 occurs because the polynomial curve fit predicts negative mass loss in this region. Measured mass loss was non-negative on the entire range depicted in the figure. Second, the quadratic nature of Equation (6.4) begins to predict increasing mass loss as temperature decreases and cumulative soak time approaches zero. These two issues in the modeled response surface are not expected for a typical chemical reaction and pointed to the need for a different form for the models.

6.2 Final Model Development

The initial models presented in Equations (6.2) - (6.4) proved to be good representation of the phenomenon observed in testing within the range the input variables used to create the models. However, in the case of temperature in particular, once the expressions in Equations (6.2) - (6.4) were plotted over a wider range, the limitations of the polynomial fits were apparent. Figure 6.6 (plotted using Equation (6.3)) is representative of this issue. As shown by the RMSE calculated for each JMP model in Section 6.1.6, the resulting curve fits experimental measurements well between

1150 and 1300°C. However, when temperatures below 1150°C are considered, the parabolic nature of the model predicts degradation rapidly increasing with decreasing temperature. This result is not expected for a typical chemical reaction.

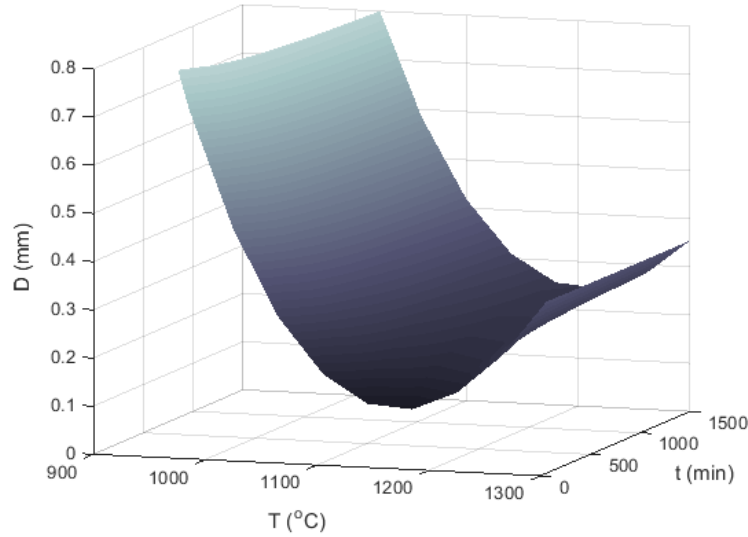


Figure 6.6: Plot of predicted thickness of degradation from 900 to 1300°C. The three thickness of degradation models showed the same issue as the mass loss model, however it was not apparent without the temperature range studied. Once the models were plotted over a wider temperature range, the parabolic nature of the models showed increasing degradation with decreasing temperature. The new model form presented in Equation (6.5) was used to correct this issue.

In order to make the model applicable to variable ranges outside those used in this study, a model based on rates of reaction was examined. The mathematical models presented in Equations (6.2) - (6.4) provided the necessary quantity of data points to develop rate models. The rate of a general chemical reaction will take the form shown in Equation (6.5).

$$r = \frac{d[\text{reactant}]}{dt} = k * f([\text{reactants}]) \quad (6.5)$$

where $k = c * e^{-E_a/RT}$

In Equation (6.5), k is known as the Arrhenius rate constant. The term “[x]” found in Equation (6.5) and Equations (6.8) - (6.11) is standard chemistry notation meaning *concentration of x*. Assuming the various degradation measurements recorded during testing is the result of

chemical reactions involving nickel, chromium, and sulfur only, degradation will be proportional to the extent of these reactions as calculated by a rate equation integrated over time as shown in Equation (6.6). Therefore, the final form of the degradation models was assumed to be of the form given by the last expression shown in Equation (6.6). This expression is comprised of a constant and three independent functions of temperature, sulfate concentration, and time respectively. R is the gas constant (8.314 J/molK) and E_a is the activation energy, which is reaction specific. For generic chemical reactions, $f(s)$ takes the simple form of reactant concentration(s) raised to a power. The exponent cannot be determined by the stoichiometry of the reaction, it must be found experimentally.

$$\hat{D} \propto \int_0^t r * f(s) dt \propto r * f(s) * t = c * e^{\frac{-E_a}{RT}} * f(s) * f(t) \quad (6.6)$$

6.2.1 Thickness of Degradation in a Reducing Environment - Nickel.

The only reaction to cause degradation in the nickel coupon in a SR environment is the reaction to form nickel sulfide. Degradation in the superalloy coupons adds the reaction to form chromium sulfide, and degradation in the superalloy coupons in the SO environment adds the oxidation of both nickel and chromium sulfides. Therefore, the thickness of degradation for nickel coupons was the starting point for final model development because the other models were expected to build upon it.

Initially it was believed dividing both sides of Equation (6.6) by t to produce a function dependent on temperature and sulfate concentration would allow determination of $f(s)$ and E_a . However, \hat{D} remained on the order of 10^{-1} while cycle time increased from an order of 10^1 to 10^2 , resulting in up to a three order-of-magnitude difference in variables. Therefore \hat{D}/t was not consistent when plotted against sulfate concentration and temperature. Instead, $\hat{D}/\ln(t)$ was used. Surface plots of $\hat{D}/\ln(t)$ as a function of sulfate concentration and temperatures were similar regardless of cycle time suggesting this treatment removed most of the time dependence of degradation. In addition, as was shown in Figure 5.13SRNiCrTimeSONiCrTime, degradation was noted to increase with the natural logarithm of time. As an aside, use of $\ln(t)$ instead of t in the rate law equation is not without precedent [14, 15] and the term $\ln(t)$ will retain the units of minutes.

Next, sulfate concentration was held constant and Equation (6.6) manipulated into the form shown in Equation (6.7) which allowed the graphing of the Arrhenius plots, for each value of s , as

shown in Figure 6.7. The Arrhenius plot allows the determination of E_a from the slope of the lines. The constant is the y-intercept of the plot. In an ideal system, the Arrhenius plot would consist of straight lines. Chemical systems typically result in curves similar to those in Figure 6.7, therefore the slope of the line is taken as the best fit with the linear portion of the curve.

$$\ln\left(\frac{\hat{D}}{\ln(t)}\right) = \ln(c) - \frac{E_a}{RT} + \ln(f(s)) = \text{constant} - \frac{E_a}{R} * \frac{1}{T} \quad (6.7)$$

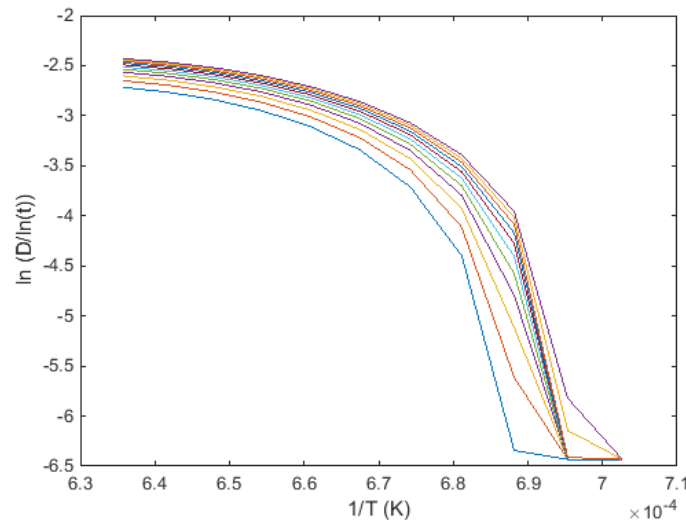


Figure 6.7: Arrhenius plots for nickel degradation at various sulfate concentrations. Activation energy (E_a) can be determined from the slope of the linear portions of the curves. “constant” in Equation (6.7) is found as the y-intercept extrapolated from the linear portions of the curves from 6.3 to $6.8 \times 10^{-4} \text{ K}^{-1}$.

The slopes of the linear portion of each curve in Figure 6.7 were averaged to find E_a . The values of “constant” determined for each sulfate concentration in the Arrhenius plots in Figure 6.7 were then plotted as a function of sulfate concentration. A logarithmic curve was fit to the data points to find c and $f(s)$. This procedure gave all the functions and constants identified in the right-hand expression in Equation (6.6). Since \hat{D} is only proportional, not equal, to the right-hand expression of Equation (6.6) an additional expression was needed to fit the model to the experimental data. An expression was found in the same form as the Arrhenius rate constant expression. The final expression for the thickness of degradation in a nickel coupon in a SR environment is shown in

Equation (6.8). A plot of this expression for .5CMAS is shown in Figure 6.8. In Equation (6.8), the units of \hat{D} are mm, the units for E_a are J/mol, T is in K, the units for s are wt%, and $\ln(t)$ is in units of minutes.

$$\hat{D}_{Ni,SR} = 1.89 \times 10^{10} * e^{-3.31 \times 10^5 / RT} * s^{0.243} * \ln(t) \quad (6.8)$$

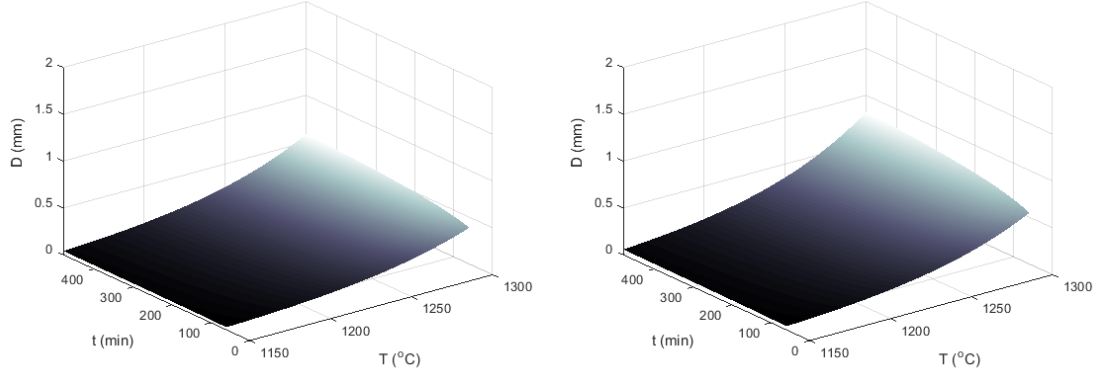


Figure 6.8: Plot of the mean thickness of degradation predicted by Equation (6.8) due to .1CMAS (left) and .5CMAS (right) loading on a nickel coupon in SR environment. The model increases with $\ln(t)$ and exponentially with $1/T$.

Equation (6.8) shows the mean value for each calculated constant. The 80% confidence interval for E_a was 3.03×10^5 - 3.59×10^5 J/mol, for the pre-exponential term it was 1.55×10^{10} - 2.32×10^{10} , and for n it was 0.145 - 0.341. RMSE was calculated for the model presented in Equation (6.8) in accordance with Equation (6.9). In the equation, n represents the number of measurements taken. RMSE for Equation (6.8) was calculated at 0.155 (12.8% of measured range) which was slightly higher than what was calculated for the JMP model of nickel degradation (RMSE was only 10.8% of the measured range). However, the model presented in the form of Equation (6.8) corrected the issue of the JMP model predicting increasing degradation with decreasing temperature.

$$\sqrt{\frac{\sum_{i=1}^n (\text{predicted}_i - \text{measured}_i)^2}{n}} \quad (6.9)$$

Figure 6.9 depicts the performance of the model against measured values at each set-point. Equation (6.8) showed good agreement with experimental values particularly at eight and 16

cycles. The difference in predicted and measured values at low cycle times suggest an initial degradation period in which “simple” degradation pathways are exploited (i.e. pre-existing surface impurities or irregularities). More extensive polishing of coupons, beyond the 220-grit sandpaper used in this study, could confirm this theory. Once these “simple” pathways are exploited, the experimental degradation settles into a logarithmic degradation with time. The primary exception to the model’s performance was at the SR-M3 set-point. The model was within the measurement range of experimental data only at two cycles. This was likely a coincidence due to the issue with degradation at low cycles just mentioned. It is worth noting that for both SR and SO superalloy testing, the M3 set-point showed less degradation than the H1 set-point. Only for nickel SR testing was this not the case, suggesting measurement error as the primary contributor to the discrepancy between measured and predicted values.

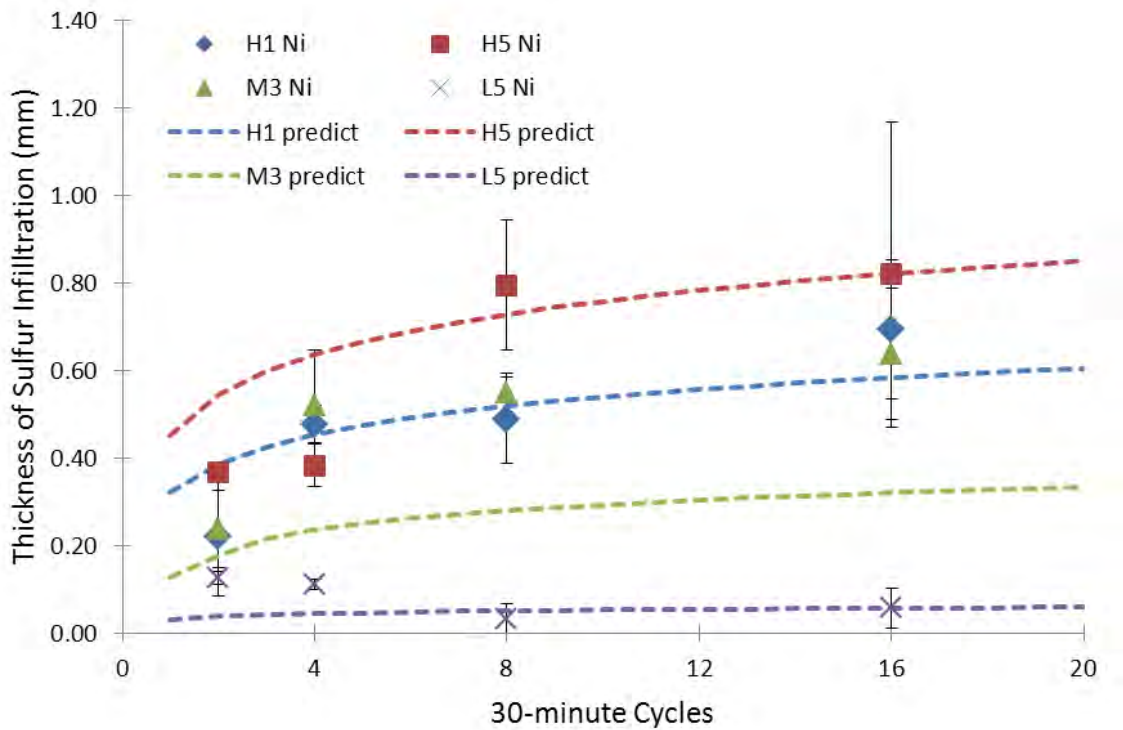


Figure 6.9: Comparison between measured and predicted degradation for nickel in SR testing. In this figure, the average measured degradation at each set-point is depicted as a data-point. Error bars are for an 80% confidence interval of the standard error of measured degradation calculated at each set-point. Mean degradation predicted by the model is shown by dashed lines.

In addition, Equation (6.8) showed $E_a = 3.31 \times 10^5$ J/mol. Blaszczyzyn reported values of E_a for diffusion of sulfur into nickel ranging from 24.9 kcal/mol (1.04×10^5 J/mol), for nickel with no previous sulfur coating, to 84.3 kcal/mol (3.52×10^5 J/mol), for nickel with 100% prior sulfur surface coverage [14]. As mentioned in Section 5.1.3.3.1, the thickness of sulfur degradation in nickel coupons is primarily affected by diffusion. After the first thermal cycle, some level of sulfur is present at the surface of the nickel coupons, so the E_a calculated in this research should fall between the two extreme values found by Blaszczyzyn. Therefore, E_a , as shown in Equation (6.8), is in agreement with expected values.

6.2.2 Thickness of Degradation in a Reducing Environment - Superalloy.

In NiCr superalloys, sulfur will preferentially attack chromium. Once chromium is sufficiently depleted in the alloy, sulfur begins to attack nickel. Therefore the rate constant for degradation in superalloy coupons was modeled as the sum of the rate constant for nickel (see Equation (6.8)) and a rate constant for chromium's reaction. The final rate constant is then multiplied by the same $f(s)$ and $f(t)$ shown in Equation (6.8). To calculate the rate constant for chromium, the degradation to nickel predicted by Equation (6.8) was subtracted from the JMP model for NiCr degradation (Equation (6.2)). This value was assumed to be the degradation due to chromium's presence. Figure 6.10 illustrates this process at a single value of temperature and sulfate concentration (the actual calculated difference is a three-dimensional array which does not lend well to printing in 2-D). Values of E_a and c were then calculated for chromium using the same procedure outlined in Section 6.2.1.

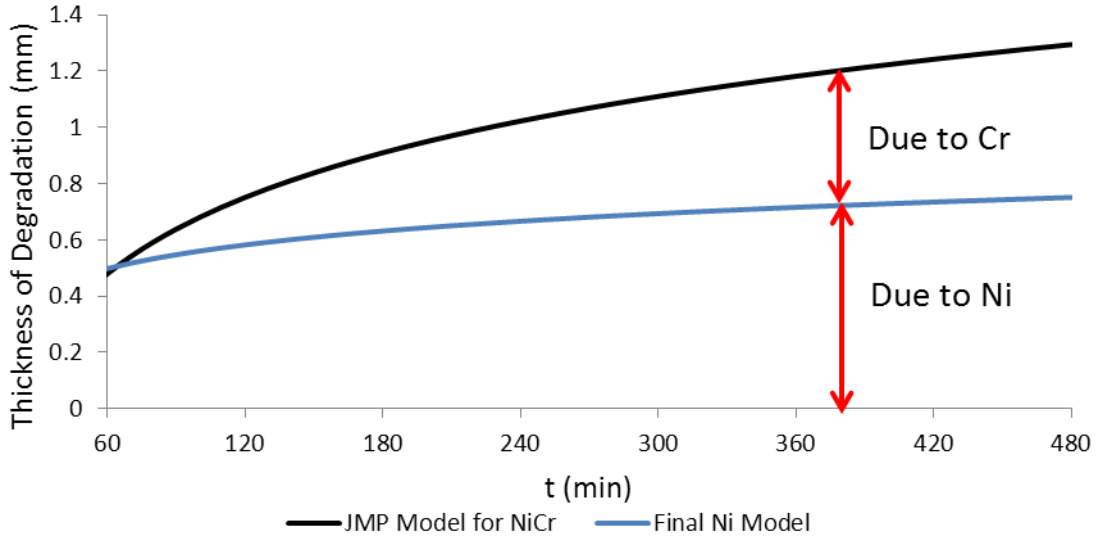


Figure 6.10: Plot of the assumed contribution of chromium to degradation of the superalloy coupon in SR testing. Chromium's contribution was assumed to be the difference between measured degradation, depicted by the curve fit calculated by JMP (Equation (6.2)), and the degradation predicted for nickel by Equation (6.8). The plot depicts the difference as a function of time at

An inherent assumption in this summation of rate constants is that the nickel-sulfur and chromium-sulfur reactions are the only causing degradation. Study of other NiCr superalloys would be necessary to confirm the assumption that reactions involving the other alloying elements is minimal. In addition, for the development of the model for the particular superalloy used in this study, it was assumed that the degradation due to the chromium-sulfur reaction was only responsible for the difference in the measured degradation and the degradation calculated by Equation (6.8). This is a gross simplification. However, without studying other superalloys with other concentrations of chromium, it is not possible at this point to determine the actual ratio of chromium to nickel degradation. The final expression for the thickness of degradation in a superalloy coupon in a SR environment is shown in Equation (6.10). A plot of this expression for .5CMAS is shown in Figure 6.11. The units for Equation (6.10) are the same as listed for Equation (6.8).

$$\hat{D}_{NiCr,SR} = \left(1.89 \times 10^{10} * e^{-3.31 \times 10^5 / RT} + 6.80 \times 10^4 * e^{-1.66 \times 10^5 / RT} \right) * s^{0.243} * \ln(t) \quad (6.10)$$

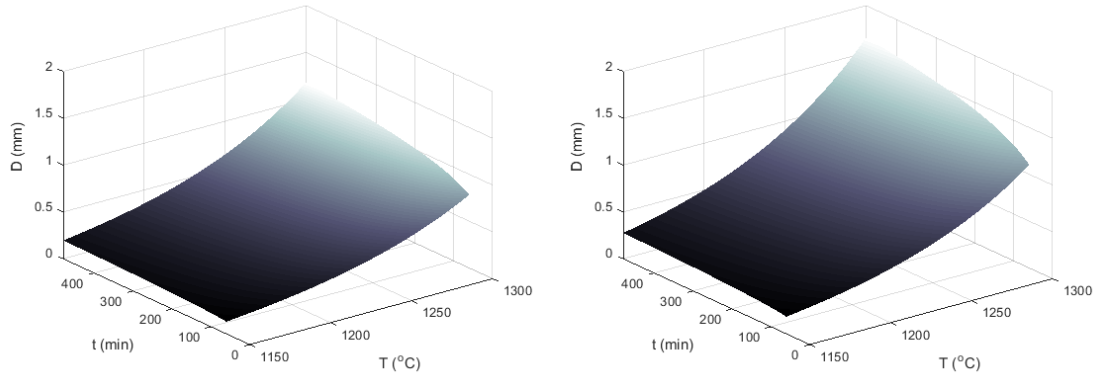


Figure 6.11: Plot of the mean thickness of degradation predicted by Equation (6.10) due to .1CMAS (left) and .5CMAS (right) loading on a superalloy coupon in SR environment. Mean degradation increases with $\ln(t)$ and exponentially with $1/T$.

Equation (6.10) shows the mean value for each calculated constant for chromium's contribution to degradation. The 80% confidence interval for E_a was 1.22×10^5 - 2.11×10^5 J/mol and for the pre-exponential term it was 5.94×10^4 - 7.78×10^4 . RMSE for Equation (6.10) was calculated to be 0.317 (18.6% of measured range) which was significantly higher than calculated for the JMP model (10.8% of measured range). The increased error is attributed to the two simplifying assumptions presented in the previous paragraph. However, as with Equation (6.8), the model presented in Equation (6.10) has the temperature response, expected for a chemical degradation reaction, which the JMP model could not replicate. Therefore, while the accuracy of predicted degradation was less than the JMP model within the temperature range used in this research effort, the Equation (6.10) is expected to provide more accurate predictions for the complete range of temperatures over which HC occurs.

Figure 6.12 depicts the performance of the model against measured values at each set-point and shows that the error in the model reported in the previous paragraph is distributed evenly across all set-points. This is in contrast to Equation (6.8) only the predicted degradation for SR-M3 varied significantly from measured values. If the error had been concentrated into one set-point, it would have proven that the assumptions used to build Equation (6.10) were not the primary cause of error in this model and therefore study of other NiCr superalloys would not improve Equation (6.10).

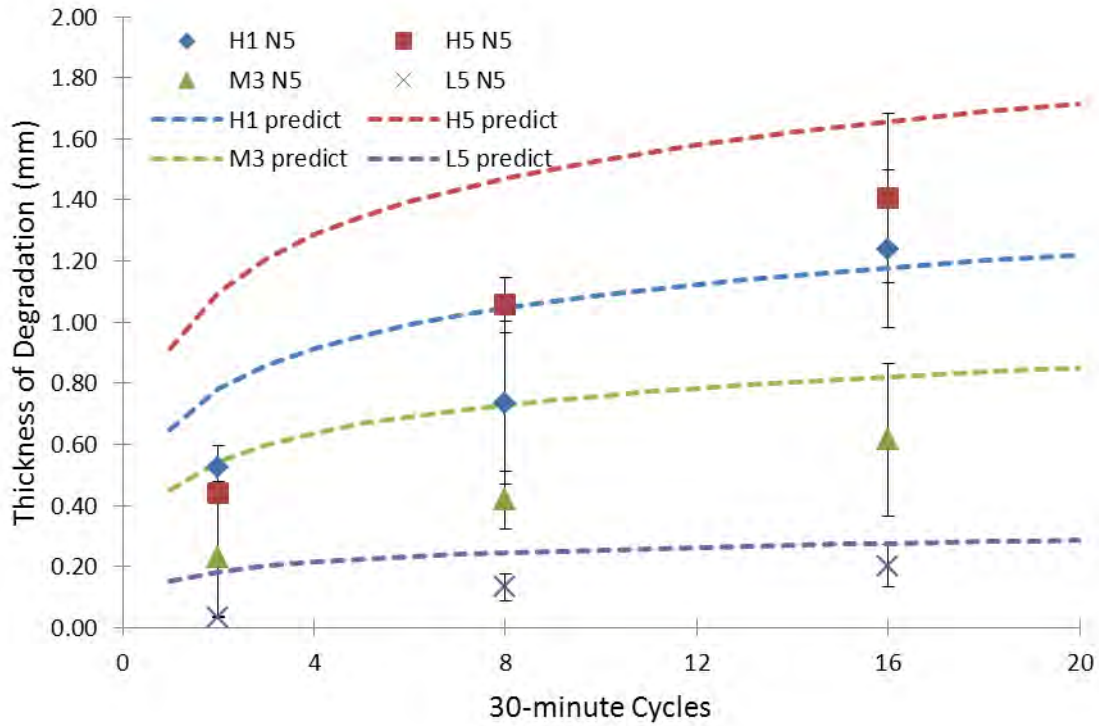


Figure 6.12: Comparison between measured and predicted degradation for superalloy in SR testing. In this figure, the average measured degradation at each set-point is depicted as a data-point. Error bars are for an 80% confidence interval of the standard error of measured degradation calculated at each set-point. Mean degradation predicted by the model is shown by dashed lines.

Despite the larger error measured for Equation (6.10), the value of E_a calculated for the sulfidation of chromium in this equation (1.66×10^5 J/mol) agrees well with the value of 1.47×10^5 J/mol reported by Chandler and McQueen [22]. The agreement in activation energies for chromium and nickel diffusion (from Section 6.2.1 suggest the rate constant expression in Equation (6.10) does not contribute significantly to the error depicted in Figure 6.12. Figure 6.12 shows larger relative errors for the SR-L5 and SR-H5 set-points than the SR-M3 set-point, which shows larger error than the SR-H1 set-point. In other words, error is increasing with sulfate concentration. This issue was not found in Figure 6.9 which suggests that some amount of error appears to be based on the fact that only the concentration of sulfate is included in Equation (6.10). The study of other NiCr superalloys suggested earlier in this section will allow additional term(s) to account for the concentration of chromium and/or nickel in the attacked substrate which will contribute to reducing

the error currently found in Equation (6.10). In addition, with increasing cycles, the error at all set-points decreases as measured degradation begins to approach a natural logarithm function of time. This suggests an initial incubation period for the sulfate reaction with NiCr. The length of the incubation period is likely related to the concentration of chromium in the superalloy. As the concentration of chromium increases, at the expense of nickel, the probability of sulfate coming into contact with chromium (which sulfate preferentially attacks) increases so the incubation period is expected to decrease. The study of other NiCr superalloys will be necessary to validate this hypothesis.

6.2.3 Thickness of Degradation in an Oxidizing Environment - Superalloy.

Equation (6.10) was used as the basis for the final model of degradation in an oxidizing environment. For sulfate attack in an oxidizing environment, the sulfides formed (which were studied in SR testing) are only an intermediary step to final oxides of nickel and chromium. Therefore, the rate constant developed to account for sulfide formation would be multiplied by a separate rate constant for the oxidization reaction to provide a measure of the total chemical degradation. As discussed in Section 6.1.7, measurements of thickness of degradation in oxidizing tests did not completely capture the degradation caused by the gypsiferous test dusts. Once the test dusts melted, the coupons showed significant mass loss with each successive cycle. Therefore, development of the final model for the oxidizing environment involved two steps. First, it was assumed that all mass loss per cycle could be attributed to the loss in volume over each wafer position. Using the dimensions of the wafers and the density of the particular superalloy studied, mass loss could be converted to an equivalent thickness. A boundary condition was applied to the predicted mass loss given by Equation (6.4) so that mass loss was zero if $T < T_c$. As shown in Figure 6.13, T_c was defined as the linear curve fit to the average of melting point and softening point for sample dusts as a function of the dusts' sulfate concentration. Additional testing of various gypsiferous dusts at multiple temperatures between their softening and melting points will be necessary to determine a better equation for T_c . The dusts used to develop Figure 6.13 were Oxide Mix (0% sulfate), .1CMAS (4.78% sulfate), .5CMAS (19.4% sulfate), and pure gypsum (55.8% sulfate). The resulting step function for mass loss was then converted into a thickness.

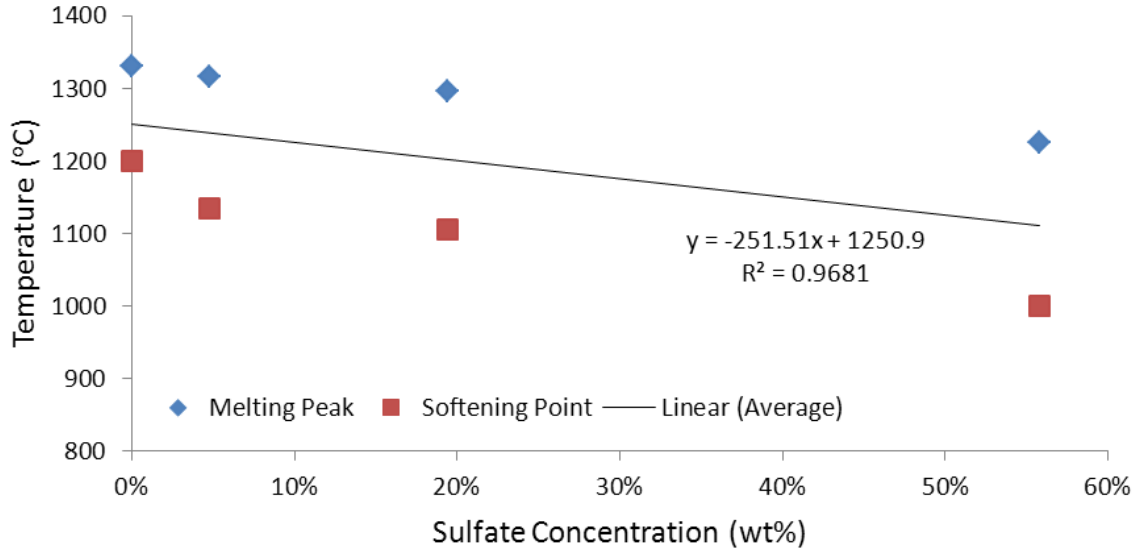


Figure 6.13: Relationship between T_c and dust sulfate concentration. During SO testing it was noted that mass loss only occur if test temperature was greater than T_c as calculated for the attack media. The expression for T_c (shown as y in the figure) provides the boundary for the step function which accounts for equivalent thickness of degradation due to mass loss.

Second, the resulting step function for equivalent degradation due to mass loss was added to the results of Equation (6.10) and fit to data-points obtained from the mathematical model developed for the SO runs (Equation (6.3)). The fit involved the use of a multiplier expression which was a function of temperature, sulfate concentration, and time. The multiplier expression was determined in a similar manner as described in Section 6.2.1. However, the multiplier was also a step function due to the fact that the mass loss step function is embedded in the multiplier. Other than the constants calculated for each expression in the step-function, the primary difference in the two is that the $f(t)$ for the expression used at $T > T_c$ is exponential as opposed to logarithmic. Plots of all six coupons which were tested above T_c showed the same exponential loss of mass. The relationship developed in Equation (6.11) is plotted in Figure 6.14. The units for Equation (6.11) are the same as listed for Equation (6.8).

$$\begin{aligned}\hat{D}_{NiCr,SO} &= \hat{D}_{NiCr,SR} * 1.35 \times 10^{-8} * e^{1.98 \times 10^5 / RT} * \ln(t), T < T_c \\ \hat{D}_{NiCr,SO} &= \hat{D}_{NiCr,SR} * 3.79 \times 10^8 * e^{-2.67 \times 10^5 / RT} * e^{0.003t}, T > T_c\end{aligned}\tag{6.11}$$

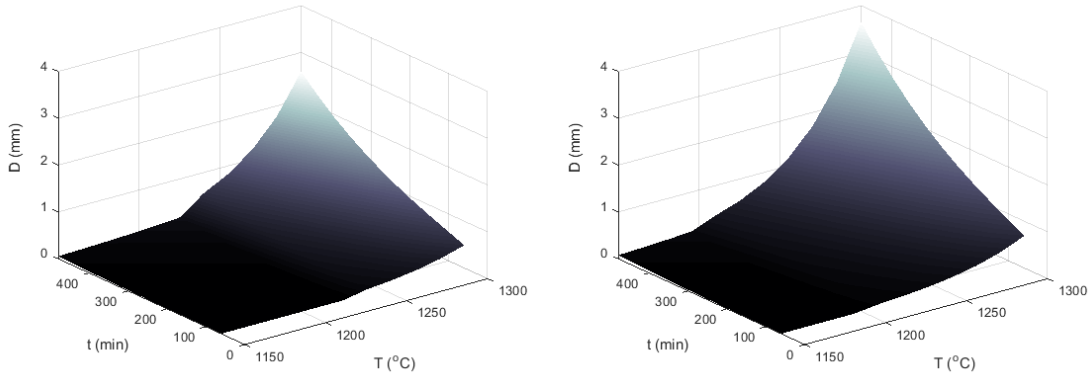


Figure 6.14: Plot of the mean thickness of degradation predicted by Equation (6.11) due to .1CMAS (left) and .5CMAS (right) loading on a superalloy coupon in SO environment. The response surface includes the thickness of degradation calculated from the predicted mass loss of a coupon. Mean degradation increases exponentially with $1/T$. At $T < T_c$, mean degradation increases with $\ln(t)$, but at $T > T_c$ it increases exponentially with t .

The expression in Equation (6.11) for $T < T_c$ shows both a negative E_a and small pre-exponential term. Neither of which is typically found in an Arrhenius rate constant. However, they match observations from SEM analysis of low temperature SO coupon cross-sections. In these coupons an Al_2O_3 layer was identified at the cross-section surface. This alumina layer helps slow (but not stop) sulfur attack of the superalloy. Therefore the thickness of sulfur degradation was found to be lower in runs at 1150 and 1250°C in SO tests versus SR tests. The negative E_a and small pre-exponential term in the multiplier for $T < T_c$ allow Equation (6.11) to predict less degradation at low temperatures, in agreement with experimental measurements.

Equation (6.11) shows the mean value for each calculated constant. The 80% confidence interval for E_a was -2.03×10^5 - -1.94×10^5 J/mol and for the pre-exponential term it was 1.05×10^{-8} - 1.72×10^{-8} for $T < T_c$. The 80% confidence interval for E_a was 2.07×10^5 - 3.27×10^5 J/mol and for the pre-exponential term it was 3.33×10^8 - 4.31×10^8 for $T > T_c$. RMSE for Equation (6.11) was calculated to be 0.316 (11.2% of measured range) which was lower than calculated for the JMP model (15.7% of measured range). Figure 6.15 depicts the performance of the model against measured values at each set-point and shows that model performs worst at the SO-H5 set-point. It was discussed in Section 5.2.3 that mass loss in SO testing when the attack

dust melts may be predicted by the Avrami equation (but that further testing was necessary to prove the hypothesis). Figure 6.16 depicts the predicted melt fraction as a function of time using the Avrami constants calculated in Section 5.2.3. The plot shows the same inversion of the SO-H1 and SO-H5 set-points between eight and 16 cycles (240 and 480 minutes). If further testing proves that the mass loss on a superalloy coupon attacked by a gypsiferous dust does follow the Avrami equation, then use of this function of time instead of the simple exponential function of time shown in Equation (6.11) may improve the model significantly.

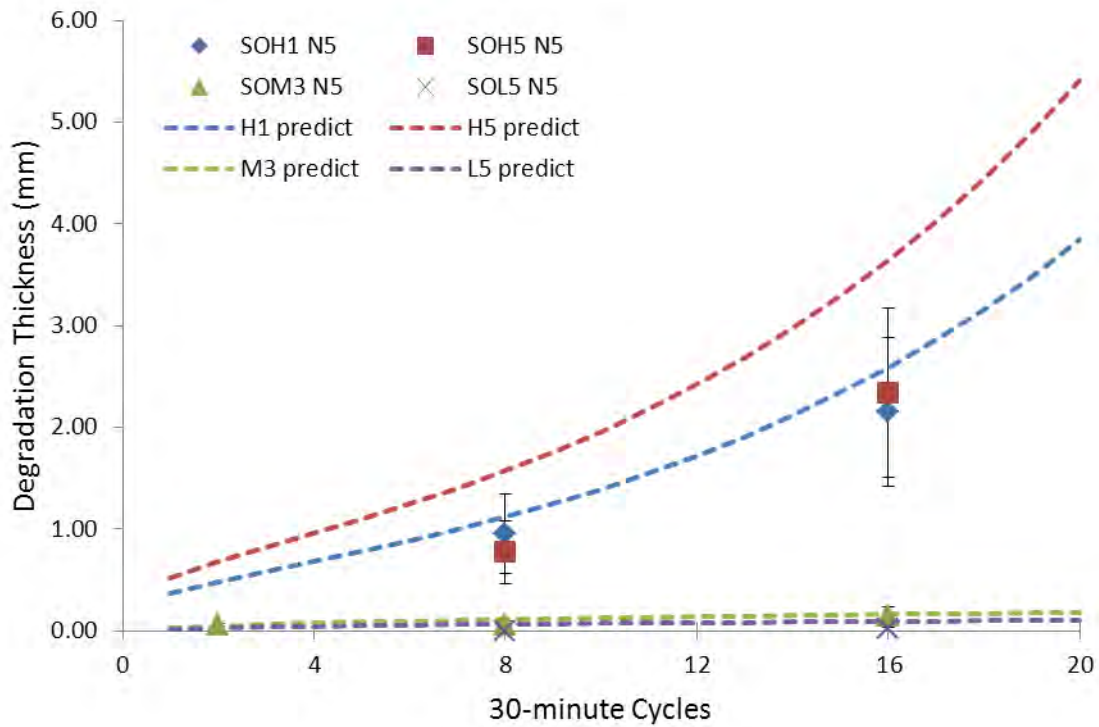


Figure 6.15: Comparison between measured and predicted degradation for superalloy in SO testing. In this figure, the average measured degradation at each set-point is depicted as a data-point. Error bars are for an 80% confidence interval of the standard error of measured degradation calculated at each set-point. Mean degradation predicted by the model is shown by dashed lines.

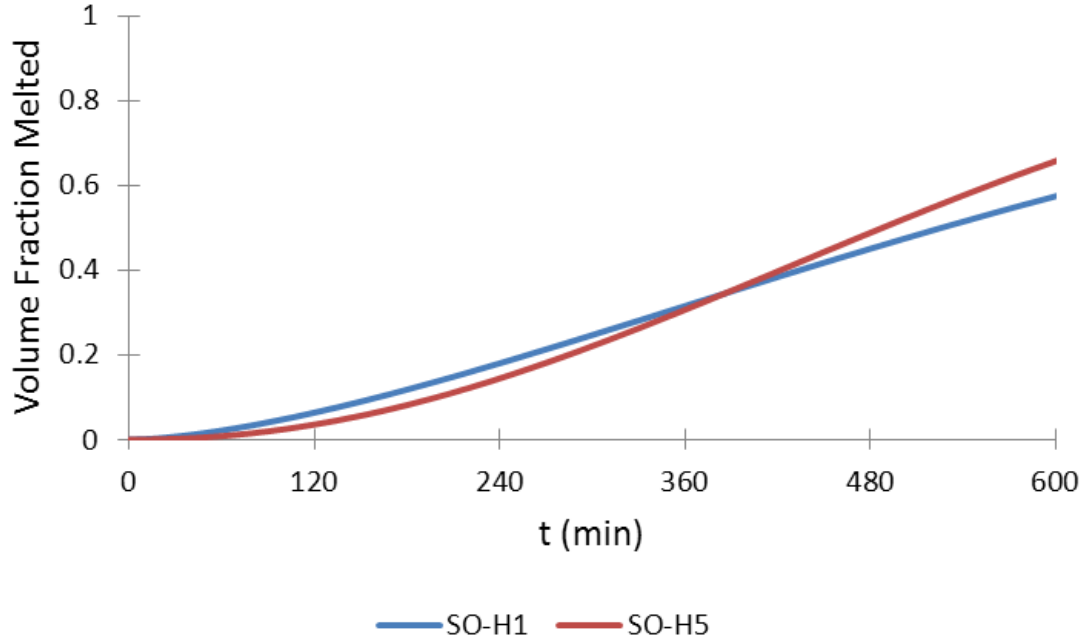


Figure 6.16: Plot of Avrami melt curves for SO-H1 and SO-H5 set-points using the constants calculated in Section 5.2.3. The Avrami plots show the same inversion of SO-H1 and SO-H5 degradation between 240 and 480 minutes as can be seen in Figure 6.12. This suggests the use of an Avrami relationship for $f(t)$ in Equation (6.11) may improve the model. However the applicability of the Avrami model to the modeled system must first be proven.

The activation energy for the oxidation of chromium obtained carrying out the multiplication in Equation (6.11) for $T > T_c$ was calculated to be 4.33×10^5 J/mol (80% confidence interval of 3.29×10^5 - 5.38×10^5). A value of 2.56 to 3.00×10^5 J/mol for oxidation of chromium in a NiCr superalloy containing 13% chromium was reported by Encinas-Oropesa et al. [36]. The reported value is not a direct comparison, however, because the superalloy used in this study had a considerably higher chromium content. Though likely high, the value of E_a calculated in this study is roughly comparable to the Encinas-Oropesa study suggesting extensive modifications are not necessary to improve the accuracy of Equation (6.11).

6.3 Model Validation

The last objective of this research effort was to attempt to validate the models presented in Sections 6.2.1 - 6.2.3 using input variables outside the range of values used to build the models,

including the use of natural dusts with complex chemistry. Additional parameters were identified for consideration as future work to improve the model.

6.3.1 Methodology.

Table 6.7 depicts the samples and set-points used for validation runs of the model. As mentioned in Section 5.2.3, testing was planned at the SO-H3 set-point during oxidizing tests. However, the mass loss measured in coupons required testing at the SO-H3 set-point to be halted after only four cycles. Therefore data from SO-H3 was not used in model development and therefore represented a temperature/sulfate concentration out-lier for validation of the model. SR-MG and SR-MY represented new sulfate concentration points to test the models' extrapolation potential. They also introduced complex chemistry which was expected to alter the damage mechanisms identified from testing with simple gypsiferous dusts. As was discussed in Section 5.2.2.2, oxidation removes much of the direct evidence of sulfur infiltration by allowing sulfides to oxidize into volatile species which readily leave the attacked substrate. Since GB1 and YPG represent far more complex chemistries than the CMAS blends used to develop the model, it was decided to test GB1 and YPG in a SR environment so that the effect of different chemistries could be directly studied in the coupons. In a SO environment, the difference may have been obscured by continued oxidation. GB1 and YPG were also chosen because the results of crucible testing Section 4.1 showed similar melt behavior despite different chemistries. In addition, GB1 was reported to have significant levels of gypsum while YPG is reported to have none. Therefore testing at 1250°C (where both had begun to melt in crucible testing) would allow the separation of damage due to melting of the test dust from damage due to sulfate attack.

Table 6.7: Set-points used for validation testing of SR and SO models. These set-points represent a temperature (SO-M3) and two sulfate concentrations (SR-MG and SR-MY) outside the input range of variables used to develop the models in Sections 6.1 and 6.2.

Designation	Media	Temperature (°C)	Cycles
SO-H3	.3CMAS	1350	4
SR-MG	GB1	1250	8
SR-MY	YPG	1250	8

6.3.2 Results.

Figure 6.17 shows the final appearance of a coupon from the SR-MG validation run, and a portion of the SEM image taken of a cross-section from the coupon. After only two thermal soaks, bubbles of metal could be seen at the surface of the dust melt. Two examples of these metal bubbles can be seen in the cross-section in Figure 6.17. The metal bubbles made complete removal of the melted dust wafer impossible, so change in mass of the coupon could not be analyzed. The areas of the coupon where GB1 was not loaded had similar appearance to unloaded areas of coupons from the SR-M3 testing described in Section 5.1.2.

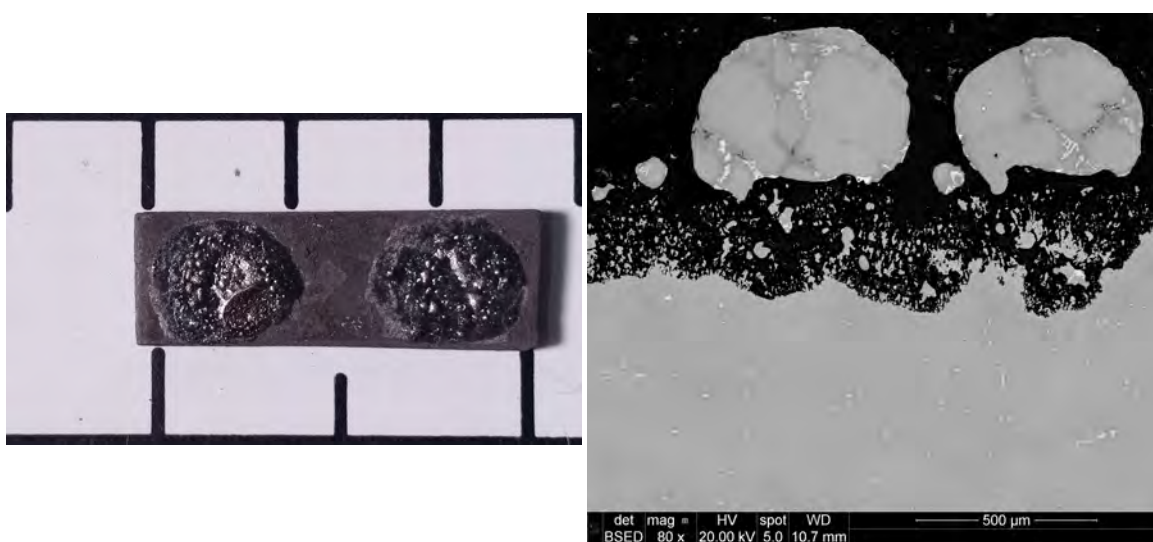


Figure 6.17: Change in appearance of a superalloy coupon (left) and cross-sectional damage (right) due to loading with GB1 for eight cycles at 1250°C. Cross-sections showed sulfur degradation concentrated in “bubbles” suspended above a porous superalloy layer.

The measured thickness of degradation for the SR-MG coupon is shown in Figure 6.18. SEM imaging revealed two zones of degradation in the SR-MG cross-sections. The upper zone presented the same chemical phases as were found in Section 5.1.2 tests. However, a second zone was also identified which did not show the presence of sulfur. This zone had the same appearance as areas identified on coupons from Section 5.2 testing where coupon substrate metal had fluxed into molten dust deposits. The similarity in degradation between this zone and SO coupons is significant as this zone formed without the presence of oxygen. Chlorine is a strong oxidizing

agent, and the only oxidizing agent in the sample other than sulfur. Since sulfur had not caused this presentation of damage in previous SR testing, the lower degradation zone is likely due to the chlorine which can be found in the GB1 sample. Measurements revealed that total degradation thickness for SR-MG falls between H1 and H5 degradation, for the same number of cycles, despite running at 50°C lower and at a significantly lower sulfate concentration. Degradation, due to sulfur only, falls between M3 and H1 degradation. .3CMAS had significantly more sulfur than the GB1 sample used in these tests yet exhibit less sulfur degradation. However, at 1250°C, GB1 was nearly 80% melted whereas .3CMAS had not even begun to melt according to Section 4.1 testing. These results suggest that degree of dust melting, given a certain minimum amount of sulfur present, may aid sulfur infiltration into the substrate allowing an attack media to cause damage as if it had a higher concentration of sulfur. Second, the results may suggest that much of the sulfur present in the dusts with high sulfur concentrations escaped into the atmosphere instead of infiltrating the test substrates. Degradation predicted by Equation (6.10) was 0.428 mm as compared to average measured degradation of 0.532 mm (19.5% low). However, as shown in Figure 6.18 the error associated with the predicted value and measured value suggest no significant difference between measured and predicted degradation.

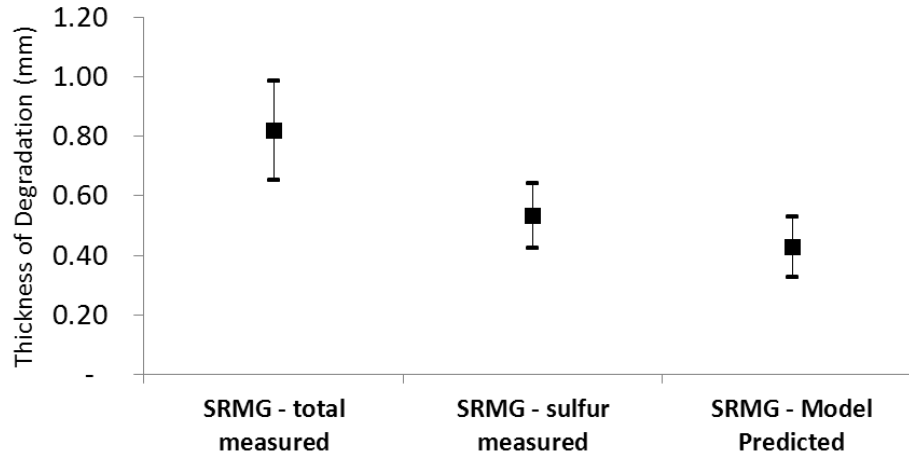


Figure 6.18: Plot of the degradation thickness for SR-MG testing. Degradation due to sulfur was only a portion of total degradation measured in the coupon. Predicted sulfur degradation correlates well with measured sulfur degradation. For the first two columns, the average measured degradation is depicted as a data-point with error bars denoting an 80% confidence interval of the standard error of measured degradation. The model predicted value (third column) is the model prediction of mean degradation with associated error for an 80% confidence interval based on the RMSE of the model.

Figure 6.19 shows the final appearance of a coupon from the SR-MY validation run, and a portion of the SEM image taken of a cross-section from the coupon. Like SR-MG, metal bubbles appeared at the top of the dust wafer melt preventing complete removal of the melted wafer. However, the metal bubbles were not identified until after four thermal cycles. Like SR-MG tests, the areas of the coupon where YPG was not loaded had similar appearance to unloaded areas of coupons from the SR-M3 testing.

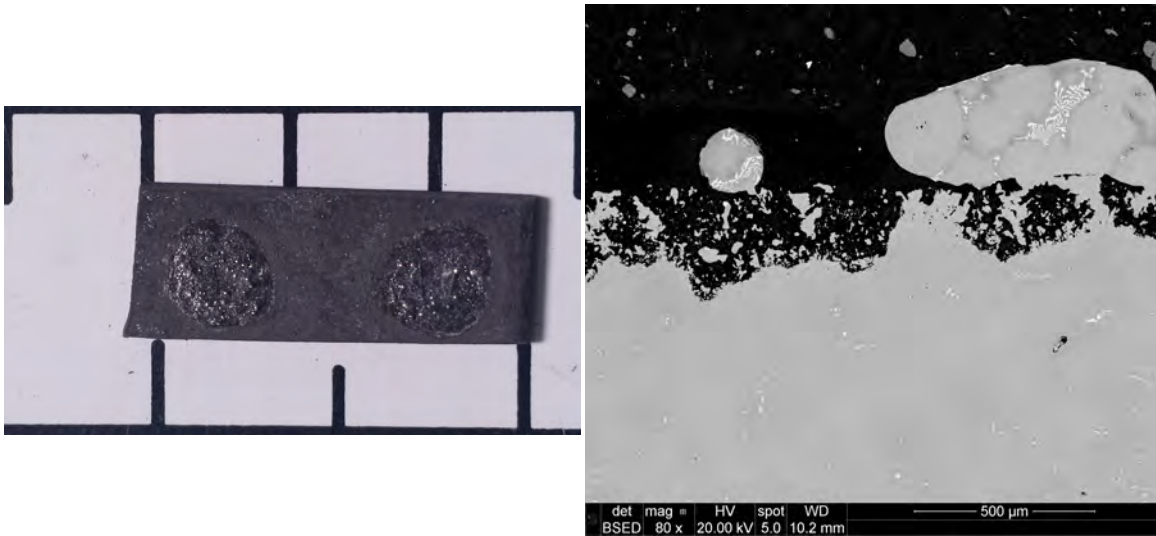


Figure 6.19: Change in appearance of a superalloy coupon (left) and cross-sectional damage (right) due to loading with YPG for eight cycles at 1250°C. Cross-sections showed sulfur degradation concentrated in “bubbles” suspended above a porous superalloy layer.

The measured thickness of degradation for the SR-MY coupon is shown in Figure 6.20. Measurements revealed that total degradation thickness for SR-MY falls between M3 and H1 degradation, while degradation due to sulfur only was less than M3 degradation. Degradation predicted by Equation (6.10) was 0.353 mm as compared to average measured degradation of 0.289 mm (12.4% high). As shown in Figure 6.20, considering the errors associated with the predicted value and measured value the difference between measured and predicted degradation is not significant.

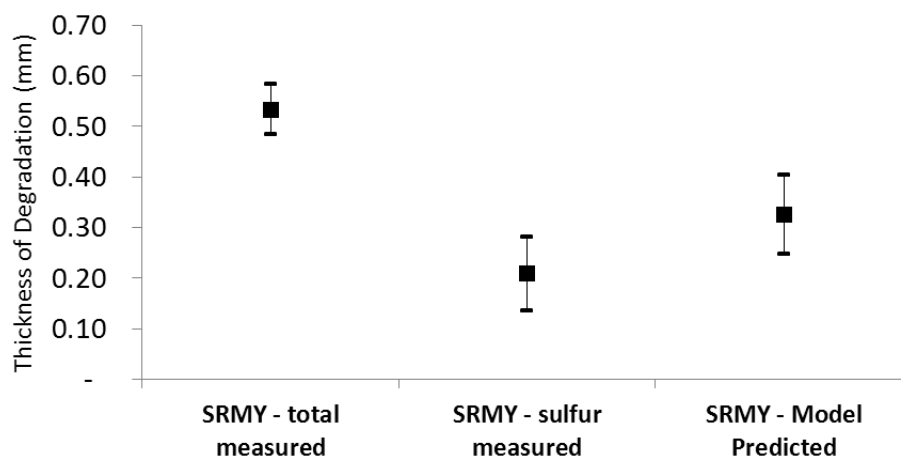


Figure 6.20: Plot of the degradation thickness for SR-MY testing. Degradation due to sulfur was only a portion of total degradation measured in the coupon. The model over-predicted sulfur degradation, likely due to the low concentration of sulfate in YPG. For the first two columns, the average measured degradation is depicted as a data-point with error bars denoting an 80% confidence interval of the standard error of measured degradation. The model predicted value (third column) is the model prediction of mean degradation with associated error for an 80% confidence interval based on the RMSE of the model.

It is worth noting that the presentation of degradation for both the SR-MG and SR-MY runs vindicated the decision to run these two tests in a SR environment instead of a SO environment. The degradation zones in each set of cross-sections attributed to chlorine bear a significant resemblance to the damage seen in SO testing of the gypsiferous CMAS blends. In a SO environment, the sulfur degradation identified in the “bubbles” shown in Figures 6.17 and 6.19 would have proceeded to the same end-point of all degradation due to sulfur in Section 5.2. In other words, sulfur-initiated degradation would have been impossible to distinguish from chlorine-initiated degradation in a SO environment. Testing GB1 and YPG in a SR environment allowed to identification of the two separate layers of degradation shown in Figures 6.17 and 6.19.

Figure 6.21 shows the final appearance of a coupon from the SO-H3 validation run, and a portion of the SEM image taken of a cross-section from the coupon. Depth of degradation was difficult to measure for SO-H3 cross-sections because in some locations damage was evident from both the bottom and top of the cross-section. In two cross-sections, a vertical fissure traveled the entire depth of the cross-section. To allow consistent measurement, the lower boundary for degradation measurement was set at the deepest sign of damage at a horizontal surface outside the

fissures. Damage predicted by Equation (6.11) was 2.97 mm as compared to average measured degradation (including due to mass loss) of 1.76 mm (69.2% high).

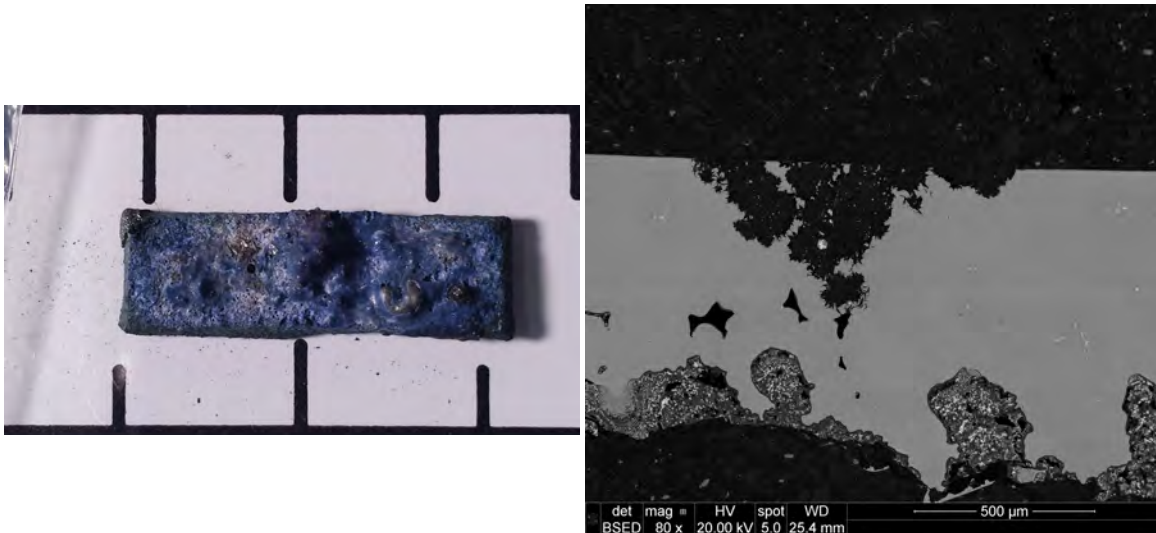


Figure 6.21: Change in appearance of a superalloy coupon (left) and cross-sectional damage (right) due to loading with .3CMAS for four cycles at 1350°C. Measurement of degradation was difficult because damage was found coming from both the top and bottom of the coupons.

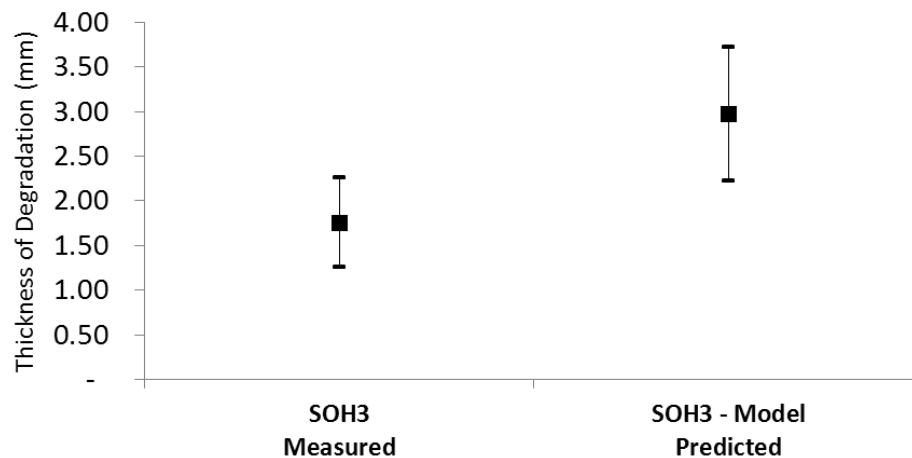


Figure 6.22: Plot of the degradation thickness for SO-H3 testing. The model over-predicted sulfur degradation, however, the temperature of this run represents an extreme temperature for surface temperatures within a GTE. For the first column, the average measured degradation is depicted as a data-point with error bars denoting an 80% confidence interval of the standard error of measured degradation. The model predicted value (second column) is the model prediction of mean degradation with associated error for an 80% confidence interval based on the RMSE of the model.

6.3.3 Discussion.

The three validation runs presented in this section provide several key insights in the models developed for sulfate degradation. First, as judged by three set-points outside the range of input variables used to develop the models, Equation (6.10) and Equation (6.11) are good predictors of degradation. Improvements are necessary to increase the accuracy of all three physical models, however, considering these models represent the first attempt ever to build a predictive model for gypsum-induced HC at elevated temperatures, the results are encouraging.

Second, the error in prediction for SR-MY is attributable to the trace sulfate concentration in YPG, as measured by XRF. Figure 6.23 shows that below 1% concentration, the response due to sulfate rapidly decreases to zero. The concentration of sulfate in YPG (0.464%) lies in this zone. Therefore the model should be limited to dusts with sulfate concentrations greater than 1%. As a logical aside, HC is likely a minor concern compared to other degradation mechanisms in areas where the local dusts only contain trace levels of sulfate.

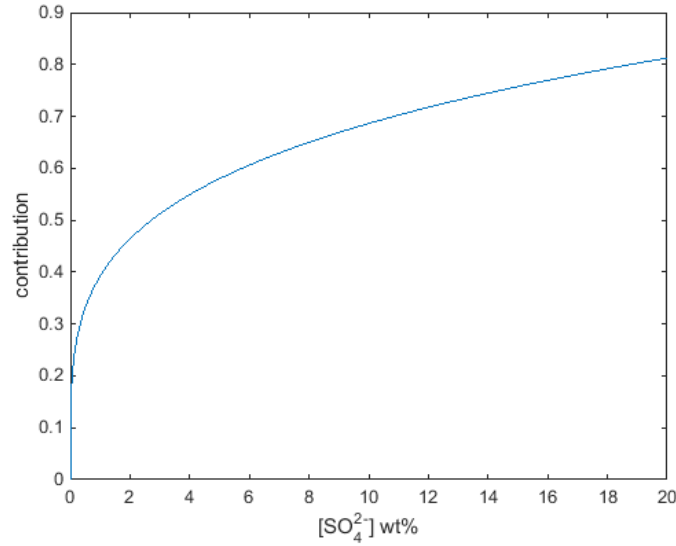


Figure 6.23: Plot of the contribution of $f(s)$ to the predicted degradation (\hat{D}) at 1250°C as a function of sulfate concentration. The concentration of sulfate in YPG fell into the nearly vertical portion of the plot, which may explain why the predicted degradation for YPG was poor compared to the other predictions.

Third, when the range of measured values and error uncertainty of the model are considered, the results at SO-H3 are better than the 69.2% difference in average measured and mean predicted values would suggest. In addition, the temperature at the SO-H3 set-point represented an extreme surface temperature for current DoD GTEs. Current superalloy material and component design cannot operate at this extreme surface temperature. Therefore, the lack of accuracy above 1300°C does not currently have a real-world impact. However, if engine temperature continue to rise and new materials are developed with higher temperature capacities, additional testing will be necessary at temperatures above 1300°C to improve the model's accuracy at these temperatures.

Finally, the results of testing with GB1 and YPG show that the presence of other volatiles in the attacking dust does not diminish the expected degradation due to sulfur. This suggests that other agents, for example chlorine in the case of GB1 and YPG, do not degrade the superalloy by a competing mechanism. If chlorine had caused damage by a competing mechanism, the amount of sulfur degradation would have been expected to be less.

6.4 Summary of Findings from Objective 3 and 4

Chapter 5 concluded that the degradation analyzed in SR and SO testing met the literature definition of HC. This chapter presented the systematic construction of a first-of-its-kind model to predict the degradation caused by a gypsiferous dust. The implications of this model are immediate and significant. From the stand-point of current DoD operations, the life of uncoated GTE components (or components stripped of protective coatings by other damage mechanisms) can be predicted based on the specific operating conditions of an aircraft. The model shows clearly the trade-off between exposure time and surface temperature. For example, assume a damage tolerance of 2 mil was acceptable before component replacement. The final model presented in Equation (6.11) predicts that a GTE with component surface temperatures of 1000°C would require component replacement after 30 hours of operation in an environment containing 4.78% sulfate. A GTE operating with component surface temperatures of 1200°C would require component replacement after only 10 hours. This knowledge would allow more efficient maintenance planning.

From the stand-point of academic study, the model developed in this chapter provides the starting point to build future studies of gypsum-induced HC. It predicts that gypsum-induced HC

occurs over a wide range of temperature and sulfate concentrations. Significantly, it predicts that gypsum can cause HC degradation at temperatures traditionally explained by sodium sulfate. Given that this research effort also disproved sodium sulfate as the cause of DoD HC issues, it will be necessary to study gypsum attack at lower temperatures to determine how, and to what extent, it can explain damage once attributed to sodium sulfate. The model also shows that melting of the gypsiferous dust contributes to a large increase in degradation. Therefore additional attention needs to be addressed to better determine the melting boundary as a function of temperature and sulfate content.

Validation testing proved the models can be used to extrapolate predicted damage outside the boundaries of the temperature and sulfate concentration set-points used to construct the model. However, it was identified that concentrations of sulfate <1% may cause large error in predicted degradation. An additional damage mechanism, likely associated with chlorine, was identified in samples loaded with YPG and GB1. The chlorine damage mechanism appears to occur parallel to the sulfur degradation mechanism and warrants further study.

VII. Concluding Remarks

Despite decades of research, little progress has been made in the mitigation of the affects of molten deposit (specifically sulfate salt and CMAS glass) attack on DoD GTE in the operational environment. Much knowledge has been gained in the laboratory, but as stated in the opening motivation of the document, and shown repeatedly in Chapter 2, little of this knowledge has proven applicable to the real-world problem. Worse, the problem of molten deposits will only grow as DoD operations continue or grow in dusty desert environments. Today only hot-section components are affected, but the push for increased GTE operating temperature will soon introduce HC issues into the “cold” sections of the GTE. Therefore it is imperative that a lifing model be developed to account for molten deposits.

Often the DoD must follow the lead of its industry partners and the academics they fund. The DoD’s reliance on the industry’s lead has often resulted in knowledge which could be beneficial to the entire community being locked into one proprietary solution. However, the DoD is leading the current shift of thought on molten deposits. The DoD has been the first to publicly acknowledge the gap between laboratory study and operational reality discussed throughout this document. Over the past several years, a tri-service working group has developed two artificial sands to mimic naturally ingested dusts (AFRL02 and AFRL03), developed new engine qualification standards for sand ingestion (contained in the next release of the Joint Service Specification Guide for GTE), and built a one-of-a-kind test bed for corrosion and erosion testing due to ingested environmental matter (the AFRL Hot Rig). The efforts of the tri-service working group have put the DoD in a unique position where its industry suppliers are currently following the DoD’s lead.

7.1 Contributions

This research effort is among the first to take advantage of the DoD’s current lead role in molten deposits. This research tackled only a small part of the molten deposit problem: sulfate attack. However, sulfate attack has proven to be a significant problem because it not only occurs over a wide operating range, but can be detrimental to coated and uncoated superalloy GTE components.

Perhaps more importantly, this study of sulfate attack, based on realistic dusts, is a first step toward the end goal of a relevant lifing model. It is also the first step in correcting a disconnect between laboratory study and operational reality which has needed correction for several decades.

Chapter 2 of this work examined the disconnect between real-world experience and the manner in which HC is studied in the laboratory. Notably, while literature based on lab study states HC to be minimal at temperatures exceeding 1000°C, real-world examples are readily available of HC above 1000°C. Additionally, while CMAS and HC are studied as separate issues, real-world examples often find sulfate deposits alongside CMAS. In addition, DSC testing conducted in this effort showed not only could gypsum provide calcium to enable a CMAS deposit, gypsum acts as a melting point depressant allowing a CMAS blend to melt at temperatures below those cited by academic studies of CMAS. However, the most significant contribution from the discussion in Chapter 2 is the proof that sodium sulfate is not the cause of HC in the environments in which the DoD operates. This conclusion has serious implications as to the applicability of more than 40 years of HC research to the DoD problem.

The remainder of this research effort built upon the discovery that sodium sulfate cannot be the cause of DoD HC issues. Gypsum was identified as the most likely cause of DoD HC issues and the degradation caused by gypsum was quantified over a range of temperatures and sulfate concentrations. In addition, the two primary arguments against gypsum-induced HC cited by current literature were disproved.

Current literature argues that gypsum melts at too high of a temperature to cause HC. However, DSC results presented in Section 4.2 showed gypsum melts at a temperature within the melting range of a natural dust known to cause HC. In addition, even before melting, gypsum begins to decompose (at ~ 750°C) releasing sulfur which could initiate HC. Further, testing in Sections 5.1.1 and 5.1.2 showed significant sulfur infiltration and coupon degradation even at temperatures below the melting point of the gypsiferous test dusts used. The degradation was identified in less than eight total hours of temperature exposure while typical HC testing is carried out for hundreds of hours. These four findings prove the high melting point of gypsum (as compared to sodium sulfate) is not an impediment to gypsum's ability to act as an HC initiator.

Current literature also argues that (in nickel alloys) gypsum causes less severe degradation than sodium sulfate. The studies which presented this argument accomplished testing at temperatures lower than 900°C. This argument was already proven moot by the fact that sodium sulfate is not present in any environment the DoD is experiencing HC issues. However, testing in Section 5.1.1 showed comparable sulfur infiltration due to sodium sulfate or gypsum loading into EN coupons at 900°C, but significantly deeper infiltration and greater degradation for gypsum-loaded coupons at 1200°C. Therefore, not only is the literature argument invalid, it is also incorrect at temperatures the DoD has noted HC issues.

Having proven sodium sulfate cannot be the initiator of HC degradation found by the DoD, a first-of-its-kind model was developed to account for the HC damage caused by gypsum. The model can predict the thickness of degradation in both reducing and oxidizing environments as a function of surface temperature, sulfate concentration, and time. Prediction of damage in a reducing environment will be especially important to the future laboratory study of gypsum-induced HC which will be required to fully understand the gypsum degradation mechanism. Little study of gypsum degradation has been accomplished to date because more than forty years of study have assumed gypsum does not cause appreciable degradation. Testing in a reducing environment will be necessary as sulfide chemistry quickly oxidizes and is removed from samples coupons in an oxidizing environment. Prediction of damage in an oxidizing environment is important because the real-world phenomenon of HC happens in an oxidizing environment.

An additional significant outcome of the model is that it predicts gypsum-induced degradation at temperatures where HC degradation is currently attributed to sodium sulfate. The prediction of gypsum-induced degradation at low temperatures is important, because if sodium sulfate is not the cause of HC, as was shown in this work, an alternate cause is necessary. Further, the model shows that even without the attack dust becoming molten, significant degradation can occur, given sufficient exposure time. The degradation, however, will not include significant mass change. Traditionally the extent of HC degradation has been measured in terms of mass change. The model shows that mass change alone is insufficient to quantify damage and therefore prior claims that gypsum does not cause HC may have been the result of incomplete analysis of test samples.

As discussed in Section 2.4.1.1, current literature has shown, in a lab environment, NaCl must be present for sodium sulfate to be corrosive to superalloys. The testing described in Chapter 5 of this document proved gypsum to be corrosive, to the superalloy tested, without the aide of NaCl. Additional SR testing validated that the models developed in this research effort could predict degradation at two sulfate concentrations outside the range used to build the models. However, the most significant finding from this validation testing was that the addition of NaCl did not affect gypsum's ability to initiate HC. In other words, yet another weakness in the explanation of sodium sulfate as the cause of HC does not apply to gypsum-induced HC.

7.2 Future Work

During the course of this research effort, several opportunities were identified to refine the model developed in Chapter 7. This research effort measured thickness of degradation, however depth of degradation would likely better capture extent of damage to the coupons. Depth of degradation could not be captured in this research effort, however, because coupon dimensions changed during testing, with some thinner coupons even bowing at the most severe set-points. In addition, some degradation sites showed evidence of new crystal growth which resulted in a coupon surface raised above the initial surface. Since the coupon surface could not be definitively located, a depth measurement could not be made. To overcome this limitation, future testing must use machined coupons of consistent size. Measurements of all dimensions should be made at multiple locations after each thermal cycle. In addition, coupon surface area should be large in comparison to wafer area to provide an unaffected surface which can be used as a reference. It was discovered that gypsum can cause degradation even outside of the wafer boundaries so coupons used in this research effort proved to be too small to have unaffected surface areas.

This research effort only looked at one loading level ($\sim 0.16\text{g/cm}^2$). Other loading concentrations will need study to fully quantify the attack envelope of gypsum. However, care must be taken before testing with higher concentrations of test media. It was mentioned in Chapter 1 that Smialek noted glass deposits with inner granular zones. Similar results were noticed in T700 tests discussed in Chapter 5. Some deposits were found during this research effort which also appeared to be granular near the coupon surface with a smooth monolithic glass on top of the granules. The

interior granules suggest that the bottom of the test dust wafer was at a lower temperature than the top. Since the portion of the wafer in contact with the coupon surface was cooler, the measured degradation at those locations is attributable to a different temperature. The error in temperature should be minimal with thin wafers but will grow with increasing loading concentration.

Superalloys containing other concentrations of chromium should be studied to determine the effect of chromium concentration in the initiation and extent of sulfur attack. In addition, coupons of pure chromium should be included. The actual form of the expression given in Equation (6.10) should be a weighted average of attack on pure nickel and attack on pure chromium. Testing with superalloys of various chromium concentrations will allow the determination of the weighting parameters.

It was suggested in Section 5.2.3 that mass loss at the SO-H1 and SO-H5 set-points (the only which showed mass loss) may have followed an Avrami curve. It was also suggested that the concentration of sulfate within the attack media affects the Avrami constants at a given temperature. Since only two set-points were available which showed mass loss, the Avrami equation was not used in the model developed in Section 6.2.3. Use of the Avrami equation to model mass loss instead of the simple exponential curve used in Section 6.2.3 looks promising to reduce some error found in the model. Further testing is necessary at additional set-point combinations of temperature, soak duration, and sulfate concentration to determine if mass loss in SO environment indeed follows the Avrami equation and determine if this expression improves the model shown in Section 6.2.3.

This work focused on degradation that could occur to an unprotected superalloy. The unprotected superalloy could exist because it was never coated due to the fact that designers used the results of HC study, now disproved in this research effort, to assume an EBC to protect against sulfur attack was not necessary. Alternatively, the unprotected superalloy could exist because its designed protective coating had been removed by any of the damage mechanisms briefly cited in Section 1.2. In either case, the models have been shown to be good predictors of degradation due to sulfur. However, the models developed in this work may also be applicable to superalloys with EBCs. Typical diffusion EBCs are NiAl, therefore Equation (6.8) is already directly applicable to testing in a SR environment. Additional SR testing of diffusion EBCs will be required to update Equation (6.8)

to account for EBC degradation within an oxidizing environment. Equations (6.10) and (6.11) may already be applicable to testing of NiCrAlY and CoNiCrAlY overlay EBCs. However, since the concentration of nickel and chromium in these two coating types is different from the concentrations in the superalloy tested in this research effort, the constants identified in Equations (6.10) and (6.11) will not be updated.

Future work should progressively add other volatile components to the dust mix such as NaCl and carbonates. These agents can act as melting point depressants just as gypsum can and may affect the damage mechanism itself. In addition chlorine is a strong oxidizing agent, just as sulfur is, so its presence may greatly increase degradation levels. Limited testing with two NaCl containing dusts, GB1 and YPG, showed that chlorine did not appear to either enhance, or detract from, sulfur degradation. Instead, chlorine attack provided an additional mechanism of degradation. Additional testing is necessary to confirm that chlorine attack is neither a complimenting or competing attack mechanism to sulfur attack.

Validation test runs showed the possibility that, assuming a minimal amount of sulfur was present in the sample, a lower melting attack dust could cause more degradation than a dust with higher melting point and sulfate concentration. It was hypothesized in Section 6.1.3 that temperature should be split into two input functions: one a function of attack media, and one a function of attacked substrate. The results of the validation tests with GB1 and YPG lend credence to this hypothesis. Additional testing of various attack dusts formulated with equal sulfate concentrations, but different melting points is necessary to determine whether the temperature variables used in the final models presented in Chapter 6 should be replaced with temperature functions.

Future testing will need to progress to dynamic loading. All tests in this research effort were based on static loading of attack media. The model developed in this study assumed that the concentration of sulfate in the attack media was constant during each thermal cycle. As the degradation measured is the result of chemical reactions, this assumption is obviously not valid. As sulfate reacts with either nickel or chromium in the test coupons, the concentration of sulfate will drop, as will the reaction rate. Therefore, it is possible with continuous loading of test dust (even with an equivalent mass load) could result in higher levels of degradation.

Finally, DSC results suggest gypsum's decomposition starting at 750°C could release sulfur to initiate HC attack. The model developed in this effort predicts degradation at temperatures lower than were tested in this research effort. Therefore, while much effort is still needed to fully quantify gypsum-induced HC at temperatures greater than 1000°C, temperatures below 1000°C must also be studied.

Bibliography

- [1] *The Engine Handbook*. Technical report, Oklahoma City Air Logistics Center, 2011.
- [2] Akuezue, H. C. *Calcium Sulfate-Induced Accelerated Corrosion*. Master's thesis, University of California, 1979.
- [3] ASTM D1141-98 "Standard Practice for the Preparation of Substitute Ocean Water", 2013.
- [4] Aygun, A., A. L. Vasiliev, N. P. Padture, and X. Ma. "Novel thermal barrier coatings that are resistant to high-temperature attack by glassy deposits". *Acta Materialia*, 55(20):6734–6745, 12 2007.
- [5] Babel, M. and B. C. Schreiber. *Geochemistry of Evaporates and Evolution of Seawater*, 483–560. Treatise on Geochemistry. Elsevier, 2nd edition, 2014. URL <http://dx.doi.org/10.1016/B978-0-08-095975-7.00718-X>.
- [6] Balint, D. S. and J. W. Hutchinson. "An analytical model of rumpling in thermal barrier coatings". *Journal of the Mechanics and Physics of Solids*, 53(4):949–973, 4 2005.
- [7] Balsone, S. "The Effect of Stress and Hot Corrosion on Nickel-Base Superalloys", 1985.
- [8] Barkalow, R. H., J. A. Goebel, and F. S. Pettit. *Erosion-Corrosion of Coatings and Superalloys in High-Velocity Hot Gases*, 163. Erosion: Prevention and Useful Applications. American Society for Testing and Materials, 1979.
- [9] Bartlett, A. H. and R. Dal Maschio. "Failure Mechanisms of a Zirconia-8 wt% Yttria Thermal Barrier Coating". *Journal of the American Ceramic Society*, 78(4):1018–1024, 1995.
- [10] Batchelor, A. W., L. N. Lam, and M. Chandrasekaran. *Materials: Degradation and its Control by Surface Engineering*. Imperial College Press, London, England, 2nd edition, 2002.
- [11] Beele, W., G. Marijnissen, and A. van Lieshout. "The evolution of thermal barrier coatings - status and upcoming solutions for today's key issues". *Surface and Coatings Technology*, 120-121:61–67, 1999.
- [12] Bennett, I. J., J. M. Kranenburg, and W. G. Sloof. "Modeling the Influence of Reactive Elements on the Work of Adhesion between Oxides and Metal Alloys". *Journal of the American Ceramic Society*, 88(8):2209–2216, 2005.
- [13] Birks, N., G. H. Meier, and F. S. Pettit. *Introduction to the High-Temperature Oxidation of Metals*. Cambridge University Press, New York, 2nd edition, 2006.
- [14] Blaszczyzyn, M. "Surface self-diffusion of sulfur covered nickel". *Surface Science*, 136(1):103–110, 1/1 1984.
- [15] Blaszczyzyn, M., R. BÅaszczyszyn, R. Mclewski, A. J. Melmed, and T. E. Madey. "Interactions of sulfur with nickel surfaces: Adsorption, diffusion and desorption". *Surface Science*, 131(23):433–447, 9/1 1983.

- [16] Borom, M. P., C. A. Johnson, and L. A. Peluso. "Role of environment deposits and operating surface temperature in spallation of air plasma sprayed thermal barrier coatings". *Surface and Coatings Technology*, 86-87:116–126, 1996. ID: 02578972/v86-87inone.p1/116-roedaoapstbc.
- [17] Boyer, K. and A. J. Rolling. "Jet Engines 101: An Introduction to Aircraft Gas Turbine Engines", 2009.
- [18] Braue, W. and P. Mechnich. "Recession of an EB-PVD YSZ Coated Turbine Blade by CaSO_4 and Fe, Ti-Rich CMAS-Type Deposits". *Journal of the American Ceramic Society*, 94(12):4483–4489, 2011.
- [19] Braue, Wolfgang. "Environmental stability of the YSZ layer and the YSZ/TGO interface of an in-service EB-PVD coated high-pressure turbine blade". *Journal of Materials Science*, 44(7):1664–1675, 04/01 2009. J2: J Mater Sci.
- [20] Brown, G. F., D. L. Schmidt, and A. C. Huffman. *Geology of the Arabian Peninsula: Shield Area of Western Saudi Arabia*. Technical Report 560-A, U.S. Geological Survey, 1963.
- [21] Casanova, M. "Corrosion Problems in Turbines". *Second Turbomachinery Symposium*. 1973. URL <http://turbolab.tamu.edu/proc/turboproc/T2/T2pg83-90.pdf>.
- [22] Chandler, J. and H. J. McQueen. "Sulfidation of a Complex Nickel-Based Alloy-Inconel 713C". *Corrosion*, 25(3):126–129, 1969.
- [23] Chen, C. Y., G. S. Lan, and W. H. Tuan. "Microstructural evolution of mullite during the sintering of kaolin powder compacts". *Ceramics International*, 26:715–720, 2000.
- [24] Chen, X., M. Y. He, I. Spitsberg, N. A. Fleck, J. W. Hutchinson, and A. G. Evans. "Mechanisms governing the high temperature erosion of thermal barrier coatings". *Wear*, 256(7-8):735–746, 4 2004.
- [25] Chen, X., J. W. Hutchinson, M. Y. He, and A. G. Evans. "On the propagation and coalescence of delamination cracks in compressed coatings: with application to thermal barrier systems". *Acta Materialia*, 51(7):2017–2030, 2003. ID: 13596454/v51i0007/2017_otpacowattbs.
- [26] Chevalier, J., L. Gremillard, A. V. Virkar, and D. R. Clarke. "The Tetragonal-Monoclinic Transformation in Zirconia: Lessons Learned and Future Trends". *Journal of the American Ceramic Society*, 92(9):1901–1920, 2009.
- [27] Clarke, D. R. and S. R. Phillpot. "Thermal barrier coating materials". *Materials Today*, 8(6):22–29, 6 2005.
- [28] Commercial Aviation Safety Team. "The Gas Turbine Cycle". URL http://www.cast-safety.org/pdf/3_engine_fundamentals.pdf.
- [29] Cumpsty, N. *Jet Propulsion: A Simple Guide to the Aerodynamic and Thermodynamic Design and Performance of Jet Engines*. Cambridge University Press, Cambridge, United Kingdom, 2nd edition, 2003.

- [30] Darolia, R. “Thermal barrier coatings technology: critical review, progress update, remaining challenges and prospects”. *International Materials Reviews*, 58(6):315–348, 08/01; 2014/02 2013. Doi: 10.1179/1743280413Y.0000000019; M3: doi: 10.1179/1743280413Y.0000000019; 23.
- [31] Darolia, R., B. A. R. Boutwell, and M. D. Gormann. “Method for depositing gamma-prime nickel aluminide coatings”, May 3 2006. URL <http://www.google.com/patents/EP1652959A1?cl=en>. EP Patent App. EP20,050,256,516.
- [32] Donachie, M. J., R. A. Sprague, R. N. Russel, K. G. Boll, and E. F. Bradley. *Sulfidation of Hot Section Alloys in Gas Turbine Engines*, 85–104. Hot Corrosion Problems Associated with Gas Turbines, ASTM STP 421. American Society for Testing and Materials, 1967.
- [33] Drexler, J. M., A. L. Ortiz, and N. P. Padture. “Composition effects of thermal barrier coating ceramics on their interaction with molten Ca-Mg-Al-silicate (CMAS) glass”. *Acta Materialia*, 60(15):5437–5447, 9 2012.
- [34] Drexler, J. M., K. Shinoda, A. L. Ortiz, D. Li, A. L. Vasiliev, A. D. Gledhill, S. Sampath, and N. P. Padture. “Air-plasma-sprayed thermal barrier coatings that are resistant to high-temperature attack by glassy deposits”. *Acta Materialia*, 58(20):6835–6844, 12 2010.
- [35] Eliaz, N., G. Shemesh, and R. M. Latanision. “Hot corrosion in gas turbine components”. *Engineering Failure Analysis*, 9(1):31–43, 2 2002.
- [36] Encinas-Oropesa, A., G. L. Drew, M. C. Hardy, A. J. Legget, J. R. Nicholls, and N. J. Simms. “Effects of Oxidation and Hot Corrosion in a Nickel Disc Alloy”. *Superalloys*, 609–618, 2008.
- [37] Erickson, G. L. “Superalloy Developments for Aero and Industrial Gas Turbines”. *Proceedings of ASM 1993 Materials Congress Materials Week*, 29. 1994.
- [38] Evans, A. G., D. R. Clarke, and C. G. Levi. “The influence of oxides on the performance of advanced gas turbines”. *Journal of the European Ceramic Society*, 28(7):1405–1419, 2008.
- [39] Evans, A. G., M. Y. He, and J. W. Hutchinson. “The Ratcheting of Compressed Thermally Grown Thin Films on Ductile Substrates”. *Acta Materialia*, 48:2593–2601, 2000.
- [40] Evans, A. G., D. R. Mumm, J. W. Hutchinson, G. H. Meier, and F. S. Pettit. “Mechanisms controlling the durability of thermal barrier coatings”. *Progress in Materials Science*, 46(5):505–553, 2001.
- [41] Fanfoni, M. and M. Tomellini. “The Johnson-Mehl-Avrami-Kolmogorov model: A brief review”. *Il Nuovo Cimento D*, 20(7-8):1171–1182, 1998.
- [42] Glassman, I. and R. A. Yetter. *Combustion*. Elsevier Inc., United States, 4th edition, 2008.
- [43] Gleeson, B. “Thermal Barrier Coatings for Aeroengine Applications”. *Journal of Propulsion and Power*, 22(2):375–383, 03/01; 2014/02 2006. Doi: 10.2514/1.20734; M3: doi: 10.2514/1.20734; 23.
- [44] Goebel, J. A. and F. S. Pettit. “Na₂SO₄-Induced Accelerated Oxidation (Hot Corrosion) of Nickel”. *Metallurgical Transactions*, I(July):1943–1954, 1970.

- [45] Goebel, J. A., F. S. Pettit, and G. W. Goward. “Hot Corrosion Mechanism in Stationary Gas Turbines”.
- [46] Goward, G. W. “Progress in coatings for gas turbine airfoils”. *Surface and Coatings Technology*, 108-109(0):73–79, 10/10 1998.
- [47] Graham, L. D., J. D. Gadd, and R. J. Quigg. “Hot Corrosion Behavior of Coated and Uncoated Superalloys”. *The Sixty-Ninth Annual Meeting of the American Society for Testing and Materials*, 105. 1966.
- [48] Hanby, V. I. “Sodium Sulfate Formation and Deposition in Marine Gas Turbines”. *Journal of Engineering for Power*, 129–133, 1974.
- [49] Hancock, P., J. R. Nicholls, and D. J. Stephenson. “The mechanism of high temperature erosion of coated superalloys”. *Surface and Coatings Technology*, 32(1-4):285–304, 11 1987.
- [50] Harada, H. “High Temperature Materials for Gas Turbines: The Present and Future”. *International Gas Turbine Congress*. 2003.
- [51] Hillery, R. V., N. Bartlett, H. L. Bernstein, R. F. Davis, H. Herman, L. L. Hsu, W. L. Hsu, J. C. Murphy, R. A. Rapp, J. S. Smith, and J. Stringer. *Coatings for High-Temperature Structural Materials: Trends and Opportunities*. The National Academies Press, 1996.
- [52] INSG Secretariat. “Nickel-Based Super Alloys”, 2013.
- [53] Karlsson, A., T. Xu, and A. Evans. “The effect of the thermal barrier coating on the displacement instability in thermal barrier systems”. *Acta Materialia*, 50(5):1211–1218, 2002. ID: 13596454/v50i0005/1211_teottbdiitbs.
- [54] Karlsson, A. M., J. W. Hutchinson, and A. G. Evans. “The displacement of the thermally grown oxide in thermal barrier systems upon temperature cycling”. *Materials Science and Engineering: A*, 351(1-2):244–257, 2003. ID: 09215093/v351i1-2/244_tdottgtbsutc.
- [55] Khajavi, M. R. and M. H. Shariat. “Failure of first stage gas turbine blades”. *Engineering Failure Analysis*, 11(4):589–597, 8 2004.
- [56] Kim, H. “Investigation of Critical Issues in Thermal Barrier Coating Durability”, 2005.
- [57] Kostick, D. S. *Mineral Commodity Summaries: Sodium Sulfate*. Technical Report 2014, US Geological Survey, 2014. URL http://minerals.er.usgs.gov/minerals/pubs/commodity/sodium_sulfate/mcs-2013-nasul.pdf.
- [58] Koul, A. K., J. P. Immarrigeon, R. V. Dainty, and P. C. Patnaik. “Degradation of High Performance Aero-Engine Turbine Blades”. *Proceedings of ASM 1993 Materials Congress Materials Week*, 69. 1994.
- [59] Krämer, Stephan, James Yang, Carlos G. Levi, and Curtis A. Johnson. “Thermochemical Interaction of Thermal Barrier Coatings with Molten CaO-MgO-Al₂O₃-SiO₂ (CMAS) Deposits”. *Journal of the American Ceramic Society*, 89(10):3167–3175, 2006.
- [60] Krauskopf, K. B. *Introduction to Geochemistry*. McGraw-Hill Book Company, United States, 2nd edition, 1979.

- [61] Krisak, M. B., B. I. Bentley, A. W. Phelps, and T. C. Radsick. "A Review of Calcium Sulfate as an Alternative Cause of Hot Corrosion", 2015.
- [62] Krumbein, W. C. and F. J. Pettijohn. *Manual of Sedimentary Petrography*. Society of Economic Paleontologists and Mineralogists, Tulsa, OK, 1988.
- [63] Lau, M. "U.S. Army Perspective on Sand and Volcanic Ash Ingestion", 2012.
- [64] Lavigne, O., M. P. Bacos, J. M. Dovaux, R. Mevrel, M. Poulain, C. Rio, and M. H. Vidal-Setif. "Performance and Degradation Mechanisms of Thermal Barrier Coatings for Turbine Blades: A Review of Onera Activities". *The Onera Journal*, (3), 2011.
- [65] Leng, Y. *Materials Characterization: Introduction to Microscopic and Spectroscopic Methods*. Wiley, 1st edition, 2009.
- [66] Levi, C. G. "Emerging materials and processes for thermal barrier systems". *Current Opinion in Solid State and Materials Science*, 8(1):77–91, 1 2004.
- [67] Mattingly, J. D., W. H. Heiser, and D. T. Pratt. *Aircraft Engine Design*. American Institute of Aeronautics and Astronautics, Inc., Reston, VA, 2 edition, 2002.
- [68] McDonald, E. and T. Caldwell. *Geochemical and Physical Characteristics of Iraqi Dust and Soil Samples*. Technical report, Desert Research Institute, 2004.
- [69] Montgomery, D. C. *Design and Analysis of Experiments*. John Wiley & Sons, Inc., 8th edition, 2013.
- [70] Muan, A. and E. F. Osborn. *Phase Equilibria Among Oxides in Steelmaking*. Addison-Wesley Publishing Co., Reading, Massachusetts, 1965.
- [71] Myers, J.J., C.H. Holm, and R.F. McAllister (editors). *Handbook of Ocean and Underwater Engineering*. McGraw-Hill Book Company, New York, 1969.
- [72] National Materials Advisory Board. *Hot Corrosion in Gas Turbines: Mechanisms; Alloy and Coating Development; Environmental Effects; Evaluation*. Technical Report AD-870 745, National Research Council, 1970. URL <http://www.ntis.gov/search/product.aspx?ABBR=AD870745>.
- [73] Netzsch. "DSC 404 F1 Pegasus - High Temperature DSC". URL <https://www.netzsch-thermal-analysis.com/us/products-solutions/differential-scanning-calorimetry/dsc-404-f1-pegasus/>.
- [74] Netzsch. "Principle of a Heat-Flux DSC". URL <https://www.netzsch-thermal-analysis.com/en/landing-pages/principle-of-a-heat-flux-dsc/>.
- [75] Nicholls, J. R., M. J. Deakin, and D. S. Rickerby. "A comparison between the erosion behaviour of thermal spray and electron beam physical vapour deposition thermal barrier coatings". *Wear*, 233-235(0):352–361, 12 1999.
- [76] Nour, W. M. N. and H. M. Awad. "Effect of MgO on Phase Formation and Mullite Morphology of Different Egyptian Clays". *Journal of the Australian Ceramic Society*, 44(2):27–37, 2008.

- [77] Okamoto, H. “Mo-Ni (Molybdenum-Nickel)”. *Journal of Phase Equilibria*, 12(6):703, 1991.
- [78] Okamoto, H. “Ni-W (Nickel-Tungsten)”. *Journal of Phase Equilibria*, 12(6):706, 1991.
- [79] Opie, N. *A Comparison of Afghanistan, Yuma, AZ, and Manufactured Sands Melted on EB-PVD Thermal Barrier Coatings*. Master’s thesis, Air Force Institute of Technology, 2014.
- [80] Parkinson, R. *Properties and applicaions of electroless nickel*. Technical Report 10081, Nickel Institute, 2011. URL http://nickelinstitute.org/~Media/Files/TechnicalLiterature/PropertiesAndApplicationsOfElectrolessNickel_10081_.pdf.
- [81] Pettit, F. S. and G. H. Meier. “Oxidation and Hot Corrosion of Superalloys”. *Superalloys (Fifth International Symposium)*, 651–687. 1984. URL http://www.tms.org/superalloys/10.7449/1984/Superalloys.1984_651_687.pdf.
- [82] Pfledderer, L. and A. Phelps. “Manufactured Source for CMAS Creation and Ingestion in Gas Turbine Engines”, 2013.
- [83] Phelps, A. “Desert Dust DSC”, 2013.
- [84] Phelps, A. W. Senior Research Scientist, University of Dayton Research Institute. Personal Communication. December 2013.
- [85] Pias, J. *Formations Superficielles et Sols D’Afghanistan*. Technical report, Orstom, 1976.
- [86] Pokluda, J. and M. Kianicova. *Damage and Performance Assessment of Protective Coatings on Turbine Blades*, 283–306. Gas Turbines. InTech, 2010.
- [87] Pollock, T. and S. Tin. “Nickel-Based Superalloys for Advanced Turbine Engines: Chemistry, Microstructure, and Properties”. *Journal of Propulsion and Power*, 22(2):361, 2006.
- [88] Pollock, T. M., D. M. Lipkin, and K. J. Hemker. “Multifunctional coating interlayers for thermal-barrier systems”. *MRS Bulletin*, 37(10):923–931, 2012.
- [89] Pomeroy, M. “Coatings for gas turbine materials and long term stability issues”. *Materials and Design*, 26:223, 2004.
- [90] PTI Inc. “Test Dust History”. URL <http://www.powdertechologyinc.com/test-dust-contaminants/test-dust-history/>.
- [91] PTI Inc. “Aramco Test Dust [Material Safety Data Sheet]”, 2011. URL <http://www.powdertechologyinc.com/wp-content/uploads/2012/11/MSDS.03.Aramco-Test-Dust.21-Jun-2011.pdf>.
- [92] PTI Inc. “Quartz, Gypsum, Calcite, and Salt Blend [Material Safety Data Sheet]”, 2011. URL http://www.powdertechologyinc.com/wp-content/uploads/2012/11/MSDS.06.QGCS1_11-March-2011.pdf.
- [93] PTI Inc. “Arizona Test Dust [Material Safety Data Sheet]”, 2012. URL <http://www.powdertechologyinc.com/wp-content/uploads/2012/08/MSDS.01.Arizona-Test-Dust.4-April-2012.pdf>.

- [94] Rapp, Robert A. "Hot corrosion of materials: a fluxing mechanism?" *Corrosion Science*, 44(2):209–221, 2 2002.
- [95] Saudi Geological Survey. "Sedimentary Rocks". URL <http://www.sgs.org.sa/English/Geology/Phanerozoic/Pages/default.aspx>. Accessed:23 Aug, 2015.
- [96] Saunders, S. R. J. and J. R. Nicholls. "Hot salt corrosion test procedures and coating evaluation". *Thin Solid Films*, 119(3):247–269, 9/21 1984.
- [97] Segersall, M. *Nickel-Based Single-Crystal Superalloys*. Ph.D. dissertation, Linköping University Institute of Technology, 2013.
- [98] Shrier, L. L., R. A. Jarman, and G. T. Burnstein. *Nickel and its Alloys*, 7:91. Corrosion: Metal/Environment Reactions. Butterworth-Heinemann Ltd, Oxford, United Kingdom, 3rd edition, 1994.
- [99] Sims, C. T., N. S. Stoloff, and W. C. Hagel. *Superalloys II*. John Wiley & Sons Inc., United States, 1987.
- [100] Sinah, I. and R. K. Mandal. "Avrami exponent under transient and heterogeneous nucleation transformation conditions". *Journal of Non-Crystalline Solids*, 357(3):919–925, 2011.
- [101] Smialek, J., F. Archer, and R. Garlick. "The Chemistry of Saudi Arabian Sand: A Deposition Problem on Helicopter Turbine Airfoils". *SAMPE Conference*. 1992.
- [102] Smialek, J., F. Archer, and R. Garlick. "Turbine Airfoil Degradation in the Persian Gulf War". *Journal of Materials*, December:39–41, 1994.
- [103] Sourmail, T. "Coatings for High Temperature Applications: The Gas Turbine", 2009.
- [104] Spitsberg, I. T., D. R. Mumm, and A. G. Evans. "On the failure mechanisms of thermal barrier coatings with diffusion aluminide bond coatings". *Materials Science and Engineering: A*, 394(1-2):176–191, 3/15 2005.
- [105] Stott, F. H., D. J. de Wet, and R. Taylor. "The effects of molten silicate deposits in the stability of thermal barrier coatings for turbine applications at very high temperatures". *3rd International SAMPE Metals Conference*, M92–M101. 1992.
- [106] Stott, F. H., D. J. de Wet, and R. Taylor. "The Degradation resistance of thermal barrier coatings to molten deposits at very high temperatures". *Advanced Materials*, 14A:135–140, 1993.
- [107] Stott, F. H., D. J. de Wet, and R. Taylor. "Degradation of Thermal-Barrier Coatings at Very High Temperatures." *MRS Bulletin*, 19(10):46–49, 1994.
- [108] Strangman, T, D Raybould, A Jameel, and W Baker. "Damage mechanisms, life prediction, and development of EB-PVD thermal barrier coatings for turbine airfoils". *Surface and Coatings Technology*, 202(4-7):658–664, 2007. URL http://journals.ohiolink.edu/ejc/article.cgi?issn=02578972&issue=v202i4-7&article=658_dmlpadtbcfta. ID: 02578972/v202i4-7/658_dmlpadtbcfta.

- [109] Streets, W. L. *Gas Turbine and Jet Engine Fuels: Progress Report No.1*. Technical Report 2873-61R, Armed Services Technical Information Agency, 1961.
- [110] Tickell, F. G. *The Examination of Fragmental Rocks*. Stanford University Press, Stanford, CA, 4th edition, 1950.
- [111] Toriz, F.C., A.B. Thakker, and S.K. Gupta. “Thermal Barrier Coatings for Jet Engines”. *ASME 1988 International Gas Turbine and Aeroengine Congress and Exposition*, volume 5. 1988.
- [112] Vidal-Setif, M. H., N. Chellah, C. Rio, C. Sanchez, and O. Lavigne. “Calcium-magnesium-alumino-silicate (CMAS) degradation of EB-PVD thermal barrier coatings: Characterization of CMAS damage on ex-service high pressure blade TBCs”. *Surface and Coatings Technology*, 208(0):39–45, 9/15 2012.
- [113] Wellman, R., G. Whitman, and J. R. Nicholls. “CMAS corrosion of EB PVD TBCs: Identifying the minimum level to initiate damage”. *International Journal of Refractory Metals and Hard Materials*, 28(1):124–132, 1 2010.
- [114] Wendlandt, W. *Thermal Analysis*. Wiley-Interscience, 3rd edition, 1986.
- [115] Wright, P. K. and A. G. Evans. “Mechanisms governing the performance of thermal barrier coatings”. *Current Opinion in Solid State and Materials Science*, 4:255–265, 1999.

REPORT DOCUMENTATION PAGE					<i>Form Approved</i> OMB No. 0704-0188	
The public reporting burden for this collection of information is estimated to average 1 hour per response, including the time for reviewing instructions, searching existing data sources, gathering and maintaining the data needed, and completing and reviewing the collection of information. Send comments regarding this burden estimate or any other aspect of this collection of information, including suggestions for reducing this burden to Department of Defense, Washington Headquarters Services, Directorate for Information Operations and Reports (0704-0188), 1215 Jefferson Davis Highway, Suite 1204, Arlington, VA 22202-4302. Respondents should be aware that notwithstanding any other provision of law, no person shall be subject to any penalty for failing to comply with a collection of information if it does not display a currently valid OMB control number. PLEASE DO NOT RETURN YOUR FORM TO THE ABOVE ADDRESS.						
1. REPORT DATE (DD-MM-YYYY) 18-09-2015		2. REPORT TYPE Dissertation			3. DATES COVERED (From — To) Oct 2012-Sep 2015	
4. TITLE AND SUBTITLE Environmental Degradation of Nickel-Based Superalloys due to gypsiferous desert dusts					5a. CONTRACT NUMBER 5b. GRANT NUMBER 5c. PROGRAM ELEMENT NUMBER 5d. PROJECT NUMBER 5e. TASK NUMBER 5f. WORK UNIT NUMBER	
6. AUTHOR(S) Krisak, Matthew B., Major, USAF					8. PERFORMING ORGANIZATION REPORT NUMBER AFIT-ENY-DS-15-S-066	
7. PERFORMING ORGANIZATION NAME(S) AND ADDRESS(ES) Air Force Institute of Technology Graduate School of Engineering and Management (AFIT/EN) 2950 Hobson Way Wright-Patterson AFB, OH 45433-7765					10. SPONSOR/MONITOR'S ACRONYM(S) AFRL/RXSS	
9. SPONSORING / MONITORING AGENCY NAME(S) AND ADDRESS(ES) Air Force Research Lab, Materials and Manufacturing Directorate Materials Durability and Sustainment Branch Ms. Lynne Pfladderer, lynne.pfladderer@us.af.mil 2179 12 th st, Bldg 652 Wright-Patterson AFB, OH 45433					11. SPONSOR/MONITOR'S REPORT NUMBER(S)	
12. DISTRIBUTION / AVAILABILITY STATEMENT DISTRIBUTION STATEMENT A: APPROVED FOR PUBLIC RELEASE; DISTRIBUTION UNLIMITED						
13. SUPPLEMENTARY NOTES This work is declared a work of the U.S. Government and is not subject to copyright protection in the United States.						
14. ABSTRACT Despite decades of research, little progress has been made to mitigate the effects of hot corrosion degradation to engine components. A ground-up review of real-world incidents revealed that sodium sulfate, cited as the cause of hot corrosion in all current academic study, is not present in any operational environment where hot corrosion is an issue, raising serious concerns as to the real-world applicability of current laboratory study. An alternative species was identified which is found in locations with known hot corrosion issues. Further, gypsum was proven to initiate hot corrosion at temperatures associated with modern gas turbine engine operation, which are beyond the range at which sodium sulfate could cause degradation. A novel model was developed to predict degradation caused by gypsiferous dusts as a function of temperature, sulfate concentration, and time. The model, based on rate law equations, was validated by additional testing. Further, the model predicted that gypsum could cause degradation at temperatures lower than studied in this effort (750 to 1000°C). This prediction is important as an alternate cause of hot corrosion is necessary at these temperatures given that sodium sulfate is not present in the operational environment to initiate hot corrosion at any temperature.						
15. SUBJECT TERMS CMAS, hot corrosion, sulfur-attack, GTE, superalloy, dust ingestion, gypsum						
16. SECURITY CLASSIFICATION OF:			17. LIMITATION OF ABSTRACT		18. NUMBER OF PAGES	
a. REPORT	b. ABSTRACT	c. THIS PAGE	UU		208	
U	U	U	19a. NAME OF RESPONSIBLE PERSON Capt Brook I. Bentley (ENY)			
						19b. TELEPHONE NUMBER (include area code) (937) 255-3636 x7478 brook.bentley@us.af.mil